Soft, Stretchable, and Conductive Hydrogel Composites

Submitted in partial fulfillment of the requirements for

the degree of

Doctor of Philosophy

in

Mechanical Engineering

Yunsik Ohm

B.S., Biomaterials Engineering, Seoul National University

B.S., Mechanical Engineering, Seoul National University

M.S., Mechanical Engineering, Carnegie Mellon University

Acknowledgements

Doctoral committee:

Dr. Carmel Majidi (chair), *Carnegie Mellon University*

Dr. Philip LeDuc, *Carnegie Mellon University*

Dr. Rahul Panat, *Carnegie Mellon University*

Dr. Christopher Bettinger, *Carnegie Mellon University*

Abstract

Hydrogels, crosslinked polymeric networks mostly filled with water, have unique mechanical properties, including extreme compliance, stretchability, and conformability. However, their intrinsic ionic conductivity (10^{-5} to 10^{-1} S cm^{-1}) limits their use in soft electronics, wearable technologies, or bioelectronics. One way to improve their electrical properties is to introduce conductive fillers into a soft hydrogel matrix. In turn, the high concentrations of metallic fillers required to achieve adequate conductivity for digital circuit applications degrade hydrogel's desirable mechanical properties. To overcome this limitation, we need a new material architecture that maintains the soft ($< 10^2$ kPa) and stretchable ($> 50\%$ strain) properties of hydrogels while also enabling high electrical conductivity (> 100 S cm^{-1}).

This dissertation introduces various soft conductive composites that achieve low electrical resistance through percolating networks of embedded silver particles. Most of this work focuses on a novel material architecture and a processing method in which silver flakes are suspended with a tough hydrogel. By controlling the water content inside, the composite functions as either a conductor or an insulator. Moreover, this property is reversible so that it can reconfigure the conductive pathways within the composite. Overall, this dissertation contributes to the diversity of hydrogel-based conductors for soft and stretchable electronics.

Contents

List of Tables

List of Figures

xiii

Chapter 1

Introduction

1.1 Motivation

Current electronic devices heavily rely on rigid and brittle materials, such as silicon wafers or metals [1, 2, 3, 4]. Although circuit technologies related to silicon microelectronics have been significantly developed [5], they are still limited for emerging applications, including soft electronics, wearable technologies, and bioelectronics. This is because existing circuit materials have inherent rigidity, which causes problems related to mechanical mismatch with soft surfaces [1].

Progress within these emerging application domains depends on the development of soft conductors to complement silicon-based technologies. These materials can still be functional in soft and stretchable applications without losing their electrical properties. For example, electronics with similar mechanical properties to biological tissues can be directly implemented on/in human bodies to enhance or help human sensory systems [6]. There are at least two core requirements for those soft conductive materials: i) mechanical properties, including compliance, stretchability, or conformability, and ii) electrical properties, such as conductivity [7].

There are several methodologies to create soft stretchable conductors, including inorganic

materials using deterministic structures [8, 9] and intrinsically soft and stretchable materials engineered with conductive fillers [10]. Although promising, those techniques usually lack some of the desired mechanical or electrical properties for soft conductors, such as conformability, softness, high conductivity, reprogrammability, or self-repair. A new material architecture with all of these properties would open up new possibilities in soft electronics, wearable technologies, and bioelectronics.

1.2   Overview of Soft and Stretchable Conductors

Recently, there have been pioneering works in soft, stretchable, and conductive materials utilizing a variety of soft material architectures. Figure 1.1 shows four representative methods to fabricate those materials, including deterministic structure, metal/carbon-filled composites, liquid metal-based composites, and conductive polymers/gels.

Before the emergence of soft and stretchable conductors, electronic devices heavily relied on thin silicon wafers and metals, such as gold (Au), silver (Ag), or Copper (Cu). These devices are usually not stretchable or deformable but instead are rigid and brittle. Beginning with the work by Bowden *et al.* [11], researchers have created deterministic or wavy structures of intrinsically rigid and brittle materials to achieve structural deformability (Figure 1.1a). Rigid materials (usually conductive components made of metals) are selectively attached to pre-stretched elastomer substrates, which will eventually cause shape changes of the rigid parts out of the plane. The shape changes that are generated by mechanical buckling enable the device to handle mechanical deformation, including stretching, bending, or twisting. Kim *et al.* [12] showed a noncoplanar structure combined with serpentine bridge designs, enabling a conductive layer of rigid material to be stretchable. This design opens up the usage of conventional rigid metals in the application of stretchable electronics with high electrical conductivity, rubber-like stretchability, and low electromechanical coupling.

Another way to create conductive and stretchable materials is to introduce conductive

Stretchable and conductive materials

Deterministic structures

Metal/carbon-filled composites

Liquid metal-based composite

Conductive polymers/gels
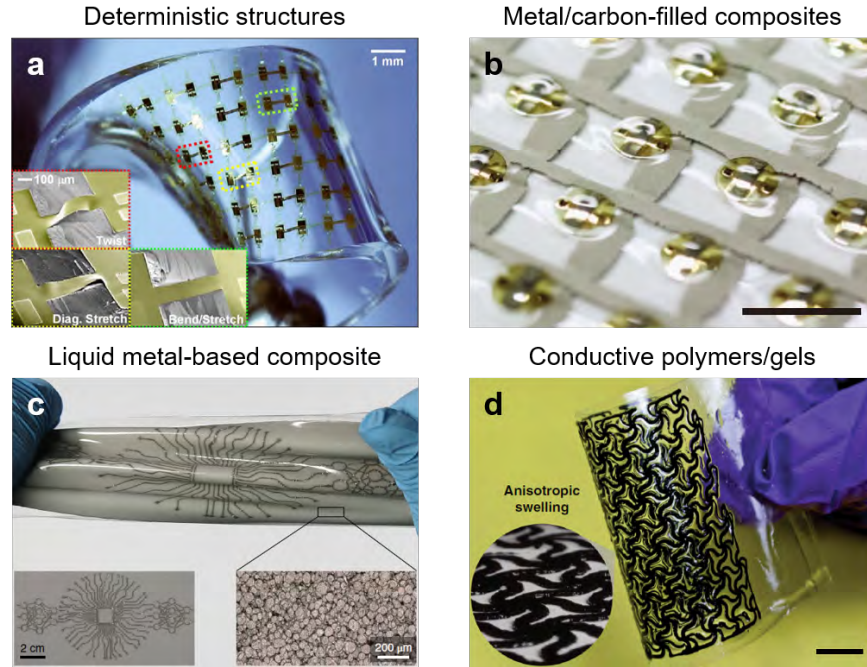
Figure 1.1: Overview of soft and conductive materials. **a**, Deterministic structured wavy electronics. Kim *et al.* [12] showed a structural design that enables rigid conductive materials (for example, gold (Au), silver (Ag), and copper (Cu)) to be resilient to mechanical deformations. Scale bar: 1 mm. **b**, Metal/carbon-filled elastomer composites. Matsuhisa *et al.* [13] introduced a printable elastic conductor which is composed of silver flakes, a fluorine rubber, and a fluorine surfactant. Scale bar: 10 mm. **c**, Liquid metal-based composites. Markvicka *et al.* [14] reported a material architecture that is composed of liquid metal droplets suspended in a soft elastomer. Scale bar: 200 µm. **d**, Conductive polymers or gels. Lu *et al.* [15] fabricated a free-standing poly(3,4-ethylenedioxythiophene):poly(styrene sulfonate) (PEDOT:PSS) hydrogel. Scale bar: 8 mm.

fillers into elastic materials. Figure 1.1b shows a representative work of metal/carbon-filled elastomers. Matsuhisa *et al.* [13] introduced a fabrication method of printable elastic conductors composed of silver flakes, a fluorine rubber, and a fluorine surfactant. The composite has a high initial conductivity of $738 \, \text{S} \, \text{cm}^{-1}$ and can be strained up to 215% without losing its electrical properties. This method does not need highly customized equipment or special fabrication methods; therefore, it is relatively easy to reproduce and scale up.

Recently, there has been an exciting development in stretchable conductors using liquid metal. Liquid metals (LMs) are metals that are liquid at or near room temperature [16]. Gallium-based liquid metals, such as eutectic Gallium-Indium (EGaIn; 75% of Gallium and

25% of Indium by weight) [17] and Gallium-Indium-Tin (Galinstan; 68% of Gallium, 22% of Indium, and 10% of Tin by weight) [18], are especially popular because of their high electrical conductivity ($\sigma = 3.4 \times 10^4$ S cm^{-1}), low viscosity ($\eta = 2$ mPa s), a melting point lower than room temperature (EGaIn: 15°C and Galinstan: -19°C), and low toxicity with negligible vapor pressure [19]. By utilizing these properties, Park & Majidi *et al.* [20] introduced microfluidic channels of EGaIn into a silicone rubber matrix to fabricate a hyperelastic pressure sensor. Fassler *et al.* [21] and Markvicka *et al.* [14] presented another method of making LM-based composites by dispersing LM microdroplets into a poly(dimethylsiloxane) (PDMS) substrate. Mechanical pressure can create electrical pathways in the polymeric matrix by rupturing oxide layers of LM microdroplets, which is the basic principle of its 'self-healing' functionality. Although promising, the cytotoxicity of LMs is not fully proven yet [22] and sealing of LM microdroplets with elastomer could cause smearing out or coalescence of LM particles.

The last approach to stretchable electronics is to utilize conductive polymers or gels. Gels usually have lower Young's moduli than other materials [23], which represents a potential advantage compared to the abovementioned material architectures. In some specific applications, such as bioelectronics or wearable electronics, having mechanical properties that are similar to those of the surrounding soft environment is critical for biocompatibility and comfort. To fabricate stretchable conductors with low Young's modulus (< 100 kPa), researchers have used intrinsically stretchable and electrically conductive polymers, for example, conductive hydrogels. Keplinger *et al.* [24] reported a stretchable and transparent ionic conductor made of a polyacrylamide hydrogel with sodium chloride (NaCl). This ionic hydrogel shows excellent mechanical properties including high stretchability (strain limit > 1000%) and high transmittance (> 98%); however, it has lower conductivity than other stretchable conductors since the electrical properties are dependent on the flow of ions. To improve their electrical properties, hydrogels have been filled with conductive materials such as conducting polymers. Lu *et al.* [15] presented a pure poly(3,4-ethylenedioxythiophene) polystyrene sulfonate (PE-DOT:PSS), which has 35% of strain limit and a volumetric conductivity of approximately 40
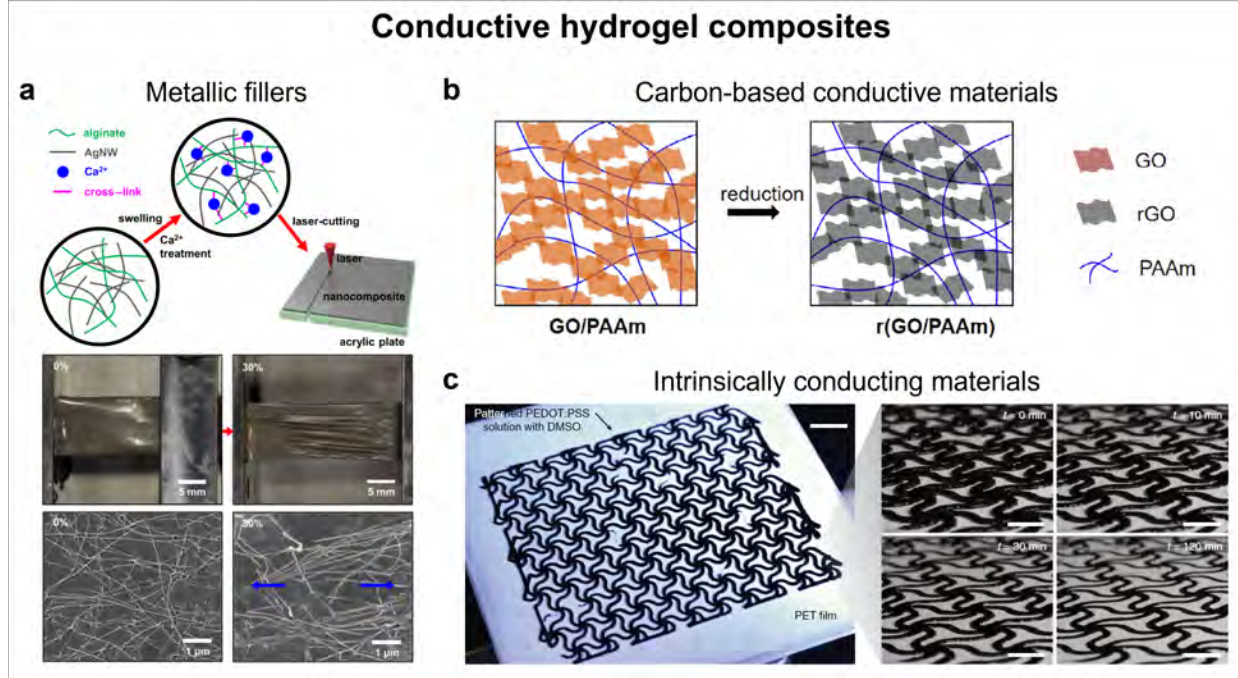
Figure 1.2: Overview of conductive hydrogel composites. **a**, Conductive hydrogels embedded with metallic fillers. Lim *et al.* [25] showed a soft conductive nanocomposite using alginate hydrogels and silver nanowires. **b**, Carbon-based conductive hydrogels. Jo *et al.* [26] introduced conductive hydrogels consisting of reduced graphene oxide and polyacrylamide hydrogel. **c**, Intrinsically conducting hydrogels. Lu *et al.* [15] fabricated a free-standing poly(3,4-ethylenedioxythiophene):poly(styrene sulfonate) (PEDOT:PSS) hydrogel.

S cm^{-1}. This represents a significant improvement over prior work, and yet this material class still needs better electrical (> 100 S cm^{-1}) and mechanical properties to be practically used in applications such as bioelectronics, soft robotics, and wearable electronics.

1.3   Overview of Conductive Hydrogel Composites

Hydrogels are a promising candidate for soft electronics since they have similar mechanical properties to a range of biological materials and soft tissues [24]. Researchers have highlighted various features of hydrogels, including their high fracture toughness, tissue-like Young's modulus (10^2 kPa), a large amount of water ($> 75\%$ by volume), ionic conductivity, bioactivity, and biocompatibility [27, 28]. These properties enable unique applications in bioelectronics [29] and soft robotics [30]. However, hydrogels have an intrinsic ionic conductivity

5

(10^{-5} to 10^{-1} S cm^{-1}) that is $6-9$ orders of magnitude lower than the conductivity of metals.

To improve their electrical conductivity, researchers have composited hydrogels with conductive materials such as metallic fillers (e.g., nanowires or micro/nanoparticles) [31, 32, 25, 33], carbon-based conductive materials (e.g., carbon nanotubes or graphene) [34, 26], and intrinsically conducting polymers (e.g., PEDOT:PSS or PANI) [35, 15, 36, 37], as shown in Figure 1.2. These composites demonstrate the potential for engineering hydrogels that are both conductive ($\sim 10^{-5} - 10^1$ S cm^{-1}) and have tissue-like mechanical compliance. However, there is a trade-off between improved electrical conductivity and lowered compliance and deformability in these conductive hydrogel composites. For instance, a pure PEDOT:PSS hydrogel [15] has been developed with electrical conductivity (~ 40 S cm^{-1}) but high Young's modulus (~ 2 MPa) and low maximum strain limit ($< 35\%$ strain), while a soft graphene hydrogel [26] has been synthesized with favorable mechanical properties (Young's modulus of 50 kPa) but low electrical conductivity ($\sim 10^{-4}$ S cm^{-1}).

The percolated electrical networks allow hydrogels to achieve high electrical conductivity while preserving their unique mechanical properties. However, the conductive pathways cannot usually be modified without rebuilding the entire material or sample. The ability to reconfigure percolating networks within hydrogel matrices can close this gap by allowing for the controlled modification between conductive and non-conductive states [38, 39, 40, 14]. For example, Park *et al.* [39] demonstrated a poly(ethylene glycol) diacrylate (PEGDA) hydrogel embedded with eutectic gallium indium (EGaIn) particles. Mechanical stimuli (e.g., friction) can activate percolating pathways in the composite by rupturing native oxide layers of the EGaIn particles. Moreover, the conductive networks can be erased when the hydrogel matrix is rehydrated and swollen by water. Although these unique material architectures show potential for reconfigurable and reversible electrical pathways in soft materials, there are clear limitations in terms of practical cases. For the conductors that can be reconfigured through mechanical activations, the materials should be reachable to recreate the conductive pathways, which could not always be the option when a device is placed in the human body.

To overcome the abovementioned limitations, we need a new material architecture whose electrical networks can be reconfigured or reversible through non-mechanical sintering in safe environments.

1.4 Objectives and Dissertation Overview

Soft and stretchable conductors have great potential to fill the gap between conventional rigid, brittle electronics and soft, deformable surfaces. Although promising, those materials still have limitations to overcome. They usually lack either the mechanical compliance necessary to conform well to soft environments, the high electrical conductivity required for digital and power electronics, or the ability to restore their mechanical/electrical properties under damage without being replaced. There needs to be a new material architecture with a low Young's modulus of less than 100 kPa, a conductivity higher than 100 S cm^{-1}, and mechanical or electrical reconfigurability. The dissertation focuses on (i) a conductive hydrogel composite that has high compliance, suitable electrical properties for digital circuitry, and reversible electrical networks, (ii) characterization of mechanical, electrical, and electromechanical properties, and (iii) demonstrations utilizing this composite in soft electronics, wearable technologies, and bioelectronics.

The research questions this dissertation covers are:

1. How does silver influence stretchable and flexible electronics as an anchor material between soft silicone substrates and liquid metal?

2. How do different morphologies of silver flakes affect a thermoplastic elastomer's mechanical and electrical behaviors?

3. Can we enhance the electrical conductivity of a self-healing material by adding conductive fillers while preserving the material's original properties?

4. Can microstructural shape changes of an elastomeric matrix decrease the percolation threshold of silver fillers while preserving mechanical properties of the elastomer?

5. How can we tailor percolation of silver fillers to enhance the electrical properties of hydrogels without compromising their low Young's modulus and high stretchability?

6. Can we introduce reversible or reconfigurable percolation pathways within conductive hydrogel composites by controlling the microstructure of silver fillers?

The dissertation follows the structure below:

In Chapter 2, I introduce four types of soft and stretchable conductors: (i) an electronic tattoo made of a commercial temporary tattoo film, silver nanoparticles ink, and eutectic gallium indium, (ii) a bi-phasic ink composed of micro-sized silver flakes, eutectic gallium indium alloy, and styrene isoprene tri-block copolymer, (iii) a poly(vinyl alcohol)-sodium borate composite embedded with silver micro-flakes and microscale droplets of gallium-based liquid metal alloy, and (iv) a phase-segregated silver-silicone composite composed of silver-coated poly(dimethylsiloxane) beads and various types of silver particles, including silver flakes, silver microparticles, and silver nanoparticles.

In Chapter 3, I present the 'Ag-hydrogel,' architecture, which is an electrically conductive hydrogel composite with high electrical conductivity, low Young's modulus, and high stretchability. The composite is composed of a tough polyacrylamide-alginate double network hydrogel and silver flakes.

In Chapter 4, I expand the functionality of the material architecture introduced in Chapter 3. This chapter focuses on reconfigurable electrical networks within the conductive hydrogel composite by controlling water content.

Lastly, Chapter 5 concludes this dissertation with possible future directions that may overcome the materials' limitations, contributions, and lessons learned from each project.

Chapter 2

Soft, Stretchable, and Conductive Composites using Silver Particles

- M. Tavakoli, M. H. Malakooti, H. Paisana, **Y. Ohm**, D. G. Marques, P. A. Lopes, A. P. Piedade, A. T. de Almeida, and C. Majidi, "EGaIn-Assisted Room-Temperature Sintering of Silver Nanoparticles for Stretchable, Inkjet-Printed, Thin-Film Electronics," *Advanced Materials*, vol. 30, no. 29, p. 1801852, 2018.

- C. Pan, **Y. Ohm**, Y. Wang, M. J. Ford, K. Kumar, S. Kumar, and C. Majidi, "Silver-Coated Poly (dimethylsiloxane) Beads for Soft, Stretchable, and Thermally Stable Conductive Elastomer Composites," *ACS Applied Materials & Interfaces*, vol. 11, no. 45, pp. 42561-42570, 2019.

- W. Zu, **Y. Ohm**, M. R. Carneiro, M. Vinciguerra, M. Tavakoli, and C. Majidi, "A Comparative Study of Silver Microflakes in Digitally Printable Liquid Metal Embedded Elastomer Inks for Stretchable Electronics," *Advanced Materials Technologies*, 2022.

- Y. Zhao, **Y. Ohm**, J. Liao, Y. Luo, H. Cheng, P. Roberts, P. Won, M. Islam, and C. Majidi, "Self-healable Electrically Conductive Organogel Composite," 2022, *Manuscript in preparation*.

2.1 Introduction

Stretchable electronics have the potential for transformative impact for emerging applications in wearable computations [41, 42, 7, 43, 44, 45, 46, 47], soft robotics [48, 24, 49], stretchable displays [50, 51, 52, 53], energy storage/harvesting devices [54, 55, 56, 57, 58, 59], and biocompatible devices [60, 61, 62, 63, 64]. Such technologies demand electrically conductive materials for robust circuit wiring along with mechanical compliance and deformability. Maintaining reliable electrical conductance during mechanical deformation can be achieved through a variety of techniques, including (i) wavy or serpentine microstructures of ultrathin silicon or metallic films on an elastic substrate [65, 12], (ii) soft microfluidics with conductive fluids such as gallium-based liquid metal alloy [66, 16], and (iii) electrically conductive polymers and gels [15, 37, 67]. Another popular strategy for developing stretchable conductors is to disperse conductive fillers into an elastomer. The elastomeric materials (e.g., silicone, epoxy, and polyimide) provide physical and mechanical compliance and deformability, while conductive particles, including metallic fillers (e.g., silver (Ag), gold (Au), nickel (Ni), and copper (Cu)), provide electrical conductivity enabled by percolating networks of conductive inclusions. [68, 69, 14, 70, 71, 72].

Among these materials, silver has been selected as one of the most promising conductive fillers due to its lowest electrical resistivity [73], inert chemical reactivity [74], abundance than other noble metals, and antimicrobial/antibacterial properties [75]. For example, Larmagnac *et al.* [76] showed a stretchable and conductive composite made of silver microparticles and an elastomer called poly(dimethylsiloxane) or PDMS. However, using a single dispersion phase might require unnecessarily large amount of conductive fillers, which could not be cost-effective. The limitation of this method can be overcome by (i) creating composites with multiphase inclusions to form conductive bridge between conductive fillers [13, 77, 78, 79], or (ii) creating heterogeneous material architectures with controlled micro-structures that reduce the required amount of conductive fillers to create percolation networks [80, 81, 82, 83].

In this chapter, I will introduce several Ag-based soft conductors that I have co-developed with other members of the Soft Machines Lab. This includes a room temperature "sintering" technique that drastically improves the conductivity and mechanical deformability of Ag-based conductive ink circuits printed on temporary tattoo paper [84]. Similar to other sinter-free techniques [85, 86], this approach also makes use of a secondary ink and the application of a chemically reducing vapor or liquid. The circuit is produced by printing silver nanoparticles (AgNP) ink on tattoo film using a desktop photo inkjet printer, and then coating the printed ink with eutectic gallium-indium (EGaIn) using a simple deposition and cleaning technique. EGaIn is a nontoxic metal alloy that is liquid at room temperature and mixes with silver to form thin, highly conductive (4.8×10^6 S m^{-1}) and mechanically robust semisolid circuit traces. In contrast to conventional sintering, the silver nanoparticles interact with the liquid alloy to form a heterogeneous substance composed of AgNP-In-Ga clusters surrounded by a Ga-rich film. These traces maintain high electrical conductivity and low electromechanical coupling (gauge factor ≈ 1) for axial strains up to 80% and can withstand strains above 110% prior to complete electrical or mechanical failure. Since the fabrication process is performed in ambient conditions and inert chemical environment, circuits can be printed on a wide range of substrate including polymeric thin films.

Another example of a conductive material embedded with multiphase inclusions is a bi-phasic ink synthesized by mixing silver microflakes, EGaIn alloy, and styrene isoprene (SIS) tri-block copolymer as a soft elastomer binder [87]. This ink is promising for printed soft electronics because of its high stretchability, high conductivity, elimination of sintering or other forms of post-processing steps, and compatibility with low-cost extrusion-based printers. Without any sintering by heat or pressure, this ink overcomes the additional post-processing steps required for previous inks composed of percolating liquid metal droplets. In this way, it is particularly well-suited for applications in printed soft electronics that require rapid and scalable manufacturing. However, there still remains a gap in the systematic study of these AgInGa-SIS inks and further study is required to develop a stronger understanding

of how the composition of inks, specifically the choice of Ag microflakes, influences their electrical and electromechanical properties. My contributions have focused on examining the influence of material composition on the performance of these conductive elastomer inks. This systematic study leads to the discovery of a digitally printable biphasic composite with an exceptional combination of high electrical conductivity (highest value: 6.38×10^5 S m^{-1}), high stretchability (>1000%), extremely low electromechanical coupling (<2% resistance change at 100% strain), and promising durability on stretching. The stretchable SIS block copolymer is used as a soft elastomeric binder for embedding solid phase Ag microflakes and liquid phase EGaIn alloy that electrically anchors to the Ag microflakes. This enables rapid and automatic fabrication of stretchable printed circuit boards through the direct ink writing (DIW) technique.

The next study I will present in this chapter is a self-healing hydrogel composite. In this work, my collaborators and I introduced an enhanced electrical conductivity into a self-healing material architecture (poly(vinyl alcohol)-sodium borate, PVA-Borax) by adding silver (Ag) micro-flakes and gallium-based liquid metal (LM) alloy. The composite exhibits high electrical conductivity (7×10^4 S m^{-1}) along with rapid and highly efficient self-healing properties. The composite also shows desired mechanical properties such as a low Young's modulus (~ 20 kPa), a high stretchability (> 400% strain), and an anti-dehydration property (the weight increases by 2% (w/w) within 24 hours in the ambient environment and does not change afterward). We chose PVA-Borax as the hydrogel matrix due to its non-toxicity, favorable biocompatibility, and well-recognized self-healing ability. The PVA-Borax hydrogel is highly viscoelastic and easy to deform since it is crosslinked through hydrogen bonding. To tune the mechanical and rheological properties for the purpose of applications, we conduct the freeze-thaw approach, which introduces physical entanglements between polymer chains [88] and alters the mechanical and rheological properties of the composite. To avoid the rapid dehydration of hydrogel, as commonly observed at room temperature, we replaced water with Ethylene Glycol (EG) as the solvent since the EG has a negligible evaporation rate in

the ambient condition. For electrical conductivity, we incorporate a low volume fraction of silver (Ag) flakes and liquid metal (eutectic Gallium-Indium) microdroplets as conductive elements. The high conductivity is achieved by a partial dehydration process in an elevated temperature (100°C) to remove a moderate portion of liquid and accelerate the formation of electrical percolated pathways. Since the inclusions are low in volume, the composite exhibits low stiffness (Young's modulus ~ 20 kPa) and excellent self-healing property both mechanically and electrically (heal up to 96% of original maximum strain property within 5 minutes and heal up to 95% of original conductivity instantaneously).

Lastly, I will cover collaborative work on exploring how Heterogeneous material microstructures can help to improve electrical conductivity of composites with limited amount of conductive fillers. In this chapter, I will present a core-shell silver-coated poly(dimethylsiloxane) (PDMS@Ag) bead-based material architecture for elastic conductors [89]. The material exhibits an enhancement in electrical conductivity, good thermal stability, and high mechanical compliance. The effects of the presence of PDMS@Ag are studied in terms of enhancement in electrical conductivity and suppression in the change of temperature-dependent conductivity relative to the composites without PDMS@Ag. The electromechanical properties of the conductive composite are also presented. The Ag-coated PDMS beads in the composite introduce microstructural changes to the host matrix. This allows conductive fillers to get physically closer than the case of composites without beads, which results in smaller filler concentrations to reach percolation threshold shown in Appendix B.1. Two potential applications of thermally stable elastic conductors for wearable devices and soft robotics will be demonstrated by a highly stretchable antenna for a "smart" furnace glove in Appendix B.3 and B.4.

2.2 EGain-Assisted Sintering of Silver Nanoparticles

2.2.1 Contribution to AgNP-Ga-In Thin-Film Composite

This project was a joint project between the Soft Machines Lab at CMU and Soft and Printed Microelectronics at University of Coimbra. I fabricated and developed the fabrication method of AgNP-Ga-In Thin-Film composite. I also contributed to the project by conducting and analyzing electromechanical characterization. I also participated in preparation for demonstration. This work is an example of composites with multiphase inclusions to reduce the amount of conductive fillers for percolation threshold.

2.2.2 Fabrication of AgNP-Ga-In Thin-Film Composite

As illustrated in Figure 2.1A, circuits are produced with the following processing steps: First, an inkjet printer is used to deposit an AgNP ink on a polymeric film (i). Next, drops of EGaIn are deposited (ii) and rubbed onto the circuit using a lint-free cloth (iii) to cover the entire circuit (iv). Then, the excess EGaIn is removed by applying a weak aqueous solution of acetic acid (v). Once fully cleaned (vi), the circuit can be populated with surface mount chips (vii). The final circuit is ready to be released from its carrier film (viii) and transferred over 3D surfaces or human skin. Prior to EGaIn deposition, the Ag ink is nonconductive due to the low AgNP density and lack of percolation (Figure 2.1B). When EGaIn is added, it causes the nanoparticles to aggregate and fills in the gaps to form a continuous metallic film (Figure 2.1C). The system silver-indium-gallium was investigated over five decades ago, in which authors found out that the ternary eutectic alloy with a melting temperature of 14.5 °C forms by adding 2% of Ag to the Eutectic Ga-In alloy [90]. This material composition may justify the existence of a liquid phase alloy within the printed Ag-Ga-In circuit that contributes to the stretchability of the circuits. EGaIn deposition leads to a six order-of-magnitude increase in volumetric conductivity from 3.6 to 4.85×10^6 S m^{-1} for printed circuits and more than a $25 \times$ increase in the maximum failure strain of the thin-film circuits from 4.5% to 118%

strain, as shown in Figure 2.1D. Moreover, such circuits are highly flexible and can support enough strain to be transferred to curved, highly textured, nondevelopable 3D surfaces like the model brain and headphones presented in Figure 2.1E and 2.1F, respectively. Additional details on the circuit printing, EGaIn deposition and cleaning are presented in Appendix A.1.

2.2.3   Electromechanical Characterization of AgNP-Ga-In

In order to demonstrate the functionality of conductive AgNP-Ga-In traces under large mechanical deformations, the electromechanical behavior of printed circuits are studied. Tensile specimens are prepared by placing the conductive traces on temporary tattoo paper (TTP) substrate between two layers of poly(dimethylsiloxane) (PDMS) and cutting them into a standard "Dogbone" shape following ASTM D412 criteria. The specimen is then subjected
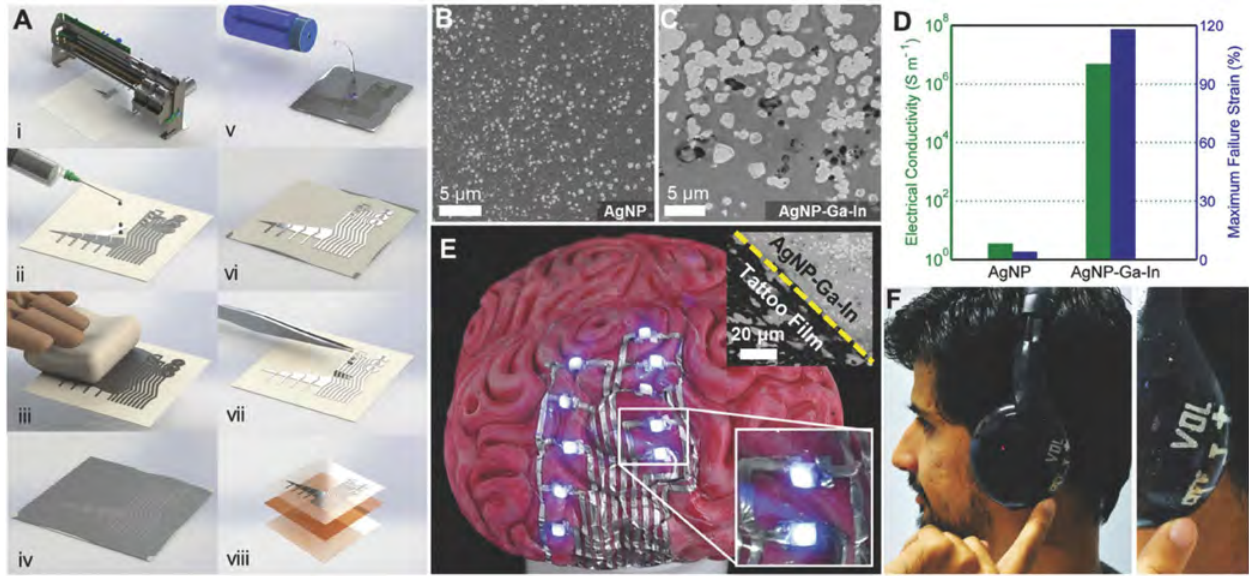
Figure 2.1: Soft, stretchable, and ultrathin printed electronics for 3D hydrographic printing. **A**, printing procedure of conductive traces. **B**, SEM of inkjet-printed silver nanoparticles. **C**, SEM of "sintered" silver nanoparticles and liquid metal alloy. **D**, volumetric electrical conductivity and maximum failure strain of AgNP coating prior and after EGaIn deposition. **E**, Hydrographically transferred electronic tattoo on a model brain; (top inset: micrograph of AgNP-Ga-In circuit trace and exposed tattoo film, bottom inset: Light-emitting diodes (LEDs) having different orientation on the highly textured surface). **F**, Conformal capacitive touchpad on a headphone created using hydrographic transfer technique.

to uniaxial tensile loading to replicate the mechanical loading conditions for electronic tattoo transfer on human skin. As shown in Figure 2.2A, the samples maintain their high electrical conductivity under applied strains up to above 80% and demonstrate a repeatable and reliable electromechanical response. However, in some cases, we have measured failure strains of the specimens as high as 118% for the same loading condition and fabrication process. Also, as shown in Figure 2.3, changing the speed of tensile test or using different width of conductive traces have only minor effect on the electromechanical response of conductive AgNP-Ga-In traces. The conductive traces maintain their low resistance, in the range of 20–30 Ω, after being stretched from 0% to 20% strain for 400 cycles (Figure 2.2B). The ability for the specimens to remain electrically conductive and maintain moderate electromechanical coupling during continuous mechanical cycling suggests that these electronic tattoos could have adequate durability for daily use on the human body.

To better understand the influence of mechanical deformation on electrical conductivity, we examine the cyclical response more closely. Figure 2.2C shows the changes in electrical resistance of the conductive AgNP-Ga-In trace during the first four stretching cycles. While the displacement is accurately controlled to linearly vary between 0 and 12 mm, the measured resistance shows a different behavior for the first cycle of stretching and the following cycles. In the first half cycle (points 1–2 in Figure 2.2C), the resistance increases with increased displacement. However, in the second half of the first loading cycle (points 2–3 in Figure 2.2C), the resistance initially drops but then increases to its peak value when the strain returns to zero. Except for the first loading cycle, the peak resistance always appears at 0% strain, when the sample is fully relaxed. This negative piezoresistive effect has a few potential explanations. One possible reason is related to the formation of permanent wrinkles that are observed in TTP film after being initially stretched. As illustrated in Figure 2.2D and 2.2E, when a "virgin" sample (state 1; previously unloaded) is stretched (state 2) and then relaxed (state 3), the film will undergo inelastic deformation; in contrast, the PDMS remains elastic, as shown by the uniform peak force in Figure 2.2B. Since its deformation

16
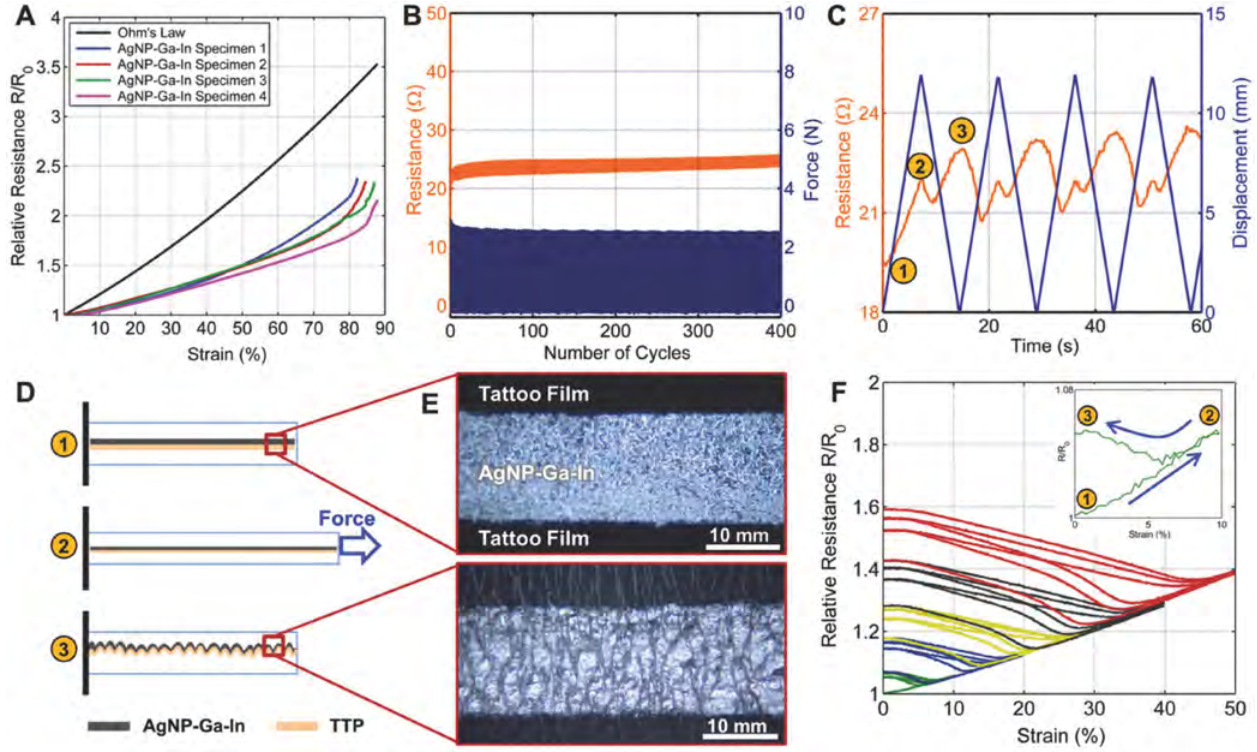
Figure 2.2: Electromechanical behavior of the conductive AgNP-Ga-In traces sandwiched between poly(dimethylsiloxane) (PDMS) layers. **A**, Relative resistance versus strain of conductive traces subjected to uniaxial strain with a displacement rate of 20 mm min^{-1}. **B**, Absolute electrical resistance under cyclic loading with controlled 0–20% strain. **C**, Electrical resistance versus time during the first four cycles of stretching from 0% to 20% strain, **D**, Schematic illustration of AgNP-Ga-In and temporary tattoo paper (TTP) in: (1) unstrained, (2) stretched, (3) and relaxed states. **E**, Optical images of the AgNP-Ga-In printed on TTP film before and after being stretched with apparent wrinkles. **F**, relative resistance versus applied strain during an incremental cyclic loading representing the hysteresis behavior of the conductive traces; inset shows the first cycle.

is not fully reversible, the film is permanently elongated and will form wrinkles when the PDMS substrate relaxes back to its natural (unloaded) length (as shown in Figure 2.2E). In this wrinkled state, the AgNP-Ga-In trace is subject to internal residual stresses that could cause microcracks, degradation of conductive networks, and a higher electrical resistance. Subsequently stretching the sample (i.e., going from state 3 to 2) could reduce electrical resistance by smoothing out the wrinkles, relieving the residual stress, and closing the microcracks.

The mechanisms for electromechanical hysteresis and negative piezoresistivity may also explain the incremental loading response presented in Figure 2.2F. This plot shows the

17

dependency of electrical resistance on applied strain as the cyclical strain limit increases in increments of 10%. The sample is loaded three times at each strain until a cyclical strain of 50% is reached. Each time the strain limit increases to a new value, the electromechanical response follows a "master curve" that is similar to what was measured for the virgin samples in Figure 2.2A. However, subsequent loadings at that strain limit follow a separate curve that exhibits the negative piezoresistivity effect. This electromechanical response was previously observed for other biphasic thin metal films composed of gallium, which indicates the crucial role of Ga-rich regions in increasing conductivity and stretchability of the circuits [91]. Similar to the constant strain cyclic test (Figure 2.2C), decreasing the strain in each step of incremental cyclic loading also leads to an initial drop in resistance followed by a steady increase (Figure 2.2F inset). Despite this highly nonmonotonic behavior, such electromechanical response is still relatively modest when compared to predictions based on Ohm's law, with only a 40–60% increase in electrical resistance under a 50% strain.

In order to ensure that the changes in the resistivity of the AgNP-Ga-In traces is not governed by the stretch rate of electronic tattoos, electromechanical characterizations are performed at different displacement rate. As shown in Figure 2.3A, changing the displace-
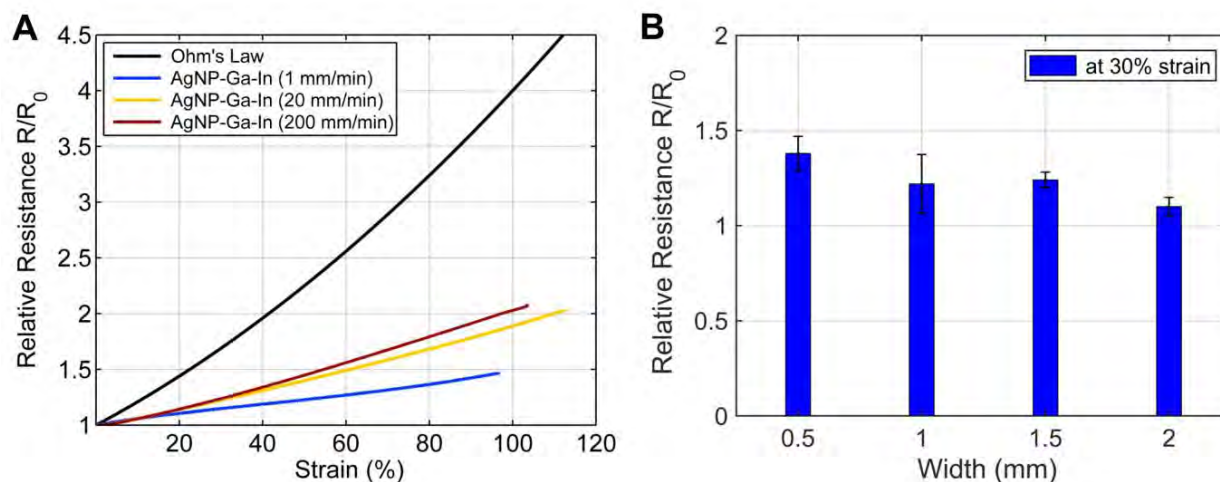
Figure 2.3: Electromechanical response of conductive AgNP-Ga-In traces. **A**, Effect of test rate on the electromechanical response of conductive traces embedded in PDMS tensile specimen under different displacement rates; 1, 20, and 200 mm min^{-1}. **B**, Relative resistance of traces at 30% tensile strain versus width of traces.

ment rate from 1 mm min^{-1} to 20 mm min^{-1} and subsequently 200 mm min^{-1} does not significantly affect the resistance of AgNp-Ga-In traces. In fact, for all different velocities, a gauge factor less than 1 was achieved with a maximum strain up to approximately 100%. The presented data in the manuscript is based on the displacement rate of 20 mm min^{-1} during the tensile test.

In order to demonstrate the resolution of conductive AgNP-Ga-In traces, straight lines with varying width and spaces between traces are printed. After deposition of EGaIn and
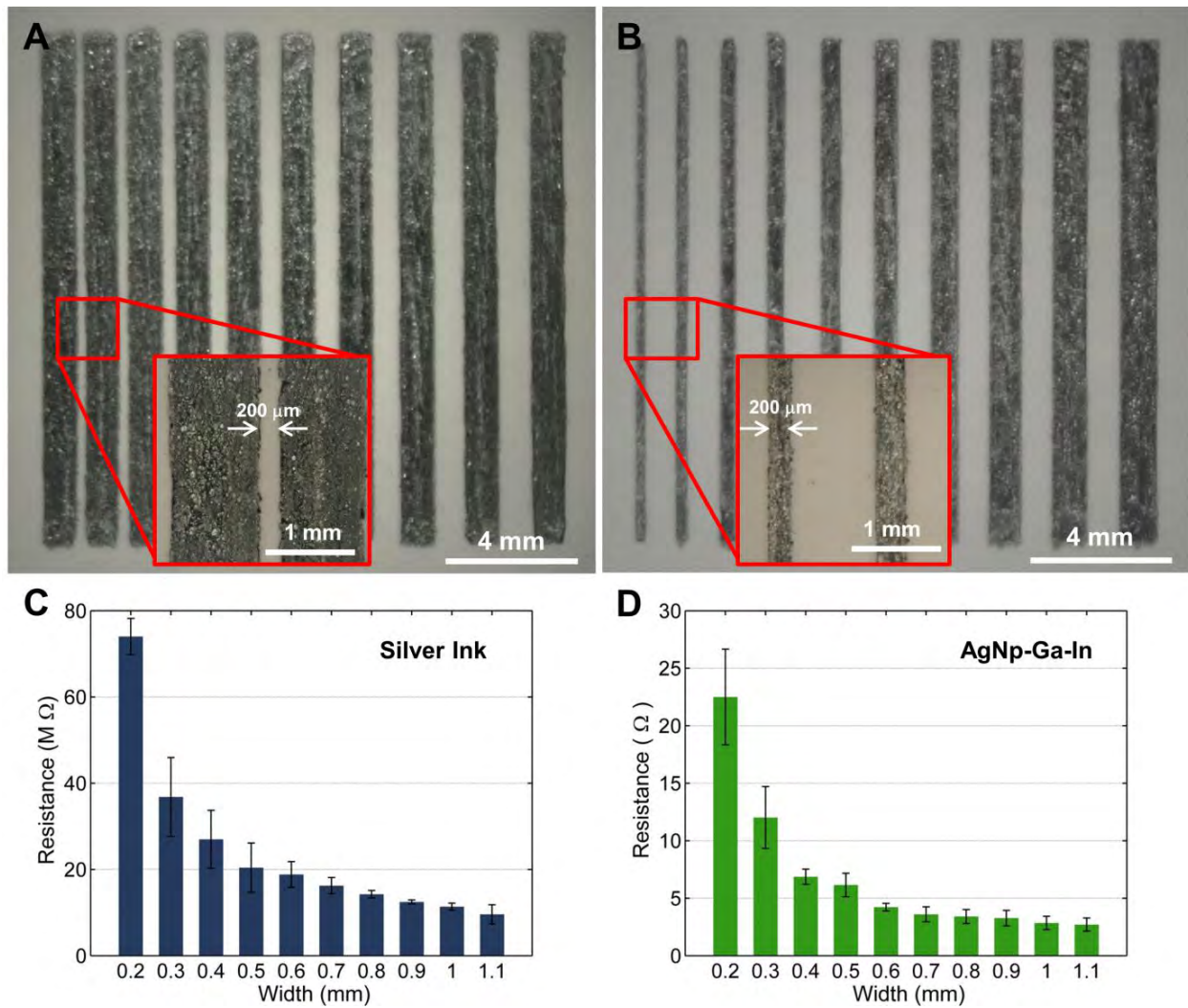
Figure 2.4: Optical images of 10 mm long, conductive AgNP-Ga-In traces and measured resistance of traces. **A**, Fabricated traces with the width of 1 mm and minimum distance of 200 µm up to 1 mm. **B**, Fabricated traces with varying width from 200 µm up to 1.1 mm with increments of 100 µm. **C**, Resistance of printer silver ink versus line width in the range of mega ohm. **D**, Resistance of traces after EGaIn deposition in the range of ohm.

cleaning the excess materials, the resistance of each line is measured. Figure 2.4 shows optical images of 10 mm long AgNP-Ga-In traces with varying width and spacing. The spacing between these traces can be as small as 200 μm and there will be no residue between them. At smaller gaps, there might be a chance to have excess EGaIn between traces which can cause a short electrical circuit. Moreover, 200 μm is the smallest width for the thin film traces with high conductivity. Although it is possible to fabricate traces that have a smaller width, the conductivity will increase and thus the reliability of electrical circuit will reduce. The variation of the electrical resistance versus width of traces before and after deposition of EGaIn is shown in Figure 2.4C and 2.4D. In all different case, the resistance of pure silver ink (AgNP) is in the mega-ohm range while the average resistance of traces after EGaIn deposition varies between 3 to 23 Ω for various widths.

2.2.4   Conductive AgNP-Ga-In Traces for Flexible Electronics

The AgNP-Ga-In traces, with maximum resolution of 200 μm (Figure 2.4), allow for surface-mounted microelectronic chips to be "soldered" to the circuit terminals. This objective is accomplished using a corrosive vapor exposure technique similar to what had recently been reported by Ozutemiz et al. [92]. Referring to Figure 2.5A, we begin with a bare AgNP-Ga-In circuit (left image) fabricated using the aforementioned fabrication method. Next, the circuit is populated with surface mounted microelectronic components and HCl vapor is blown over the circuit. The HCl vapor removes the Ga_2O_3 skin from the liquid metal and enables it to self-align and wet with the pins of the chip [92]. As shown in the middle image in Figure 2.5A, the metal wetting layer holds down the liquid metal so that the EGaIn does not bead up or rinse away when vapor is applied. Finally, the populated circuit is coated with a thin layer of PDMS (right image in Figure 2.5A).

Using hydrographic transfer, the circuit can be placed on 3D objects like the toy lemon shown in Figure 2.5B. It can also function as an electronic tattoo with on-board microelectronic chips for visual display and power regulation (Figure 2.5C). Electromechanical testing

on conductive AgNP-Ga-In traces with a 0 Ω resistor in the middle of specimen revealed the resistance of these stretchable electronics up to 80% strains (Figure 2.5D). As expected, all the samples failed at the interface between rigid microchip and compliant PDMS due to the high stress concentrations. Moreover, the stretchability of the ultrathin conductive traces is also demonstrated on the highly textured brain-shaped foam with mounted light-emitting diodes (LEDs). As shown in Figure 2.5E, squeezing the foam deforms the circuit but does not interfere with the operation of the LEDs remain functional. These circuits are only a few examples to demonstrate mechanical robustness and functionality of stretchable AgNP-Ga-In
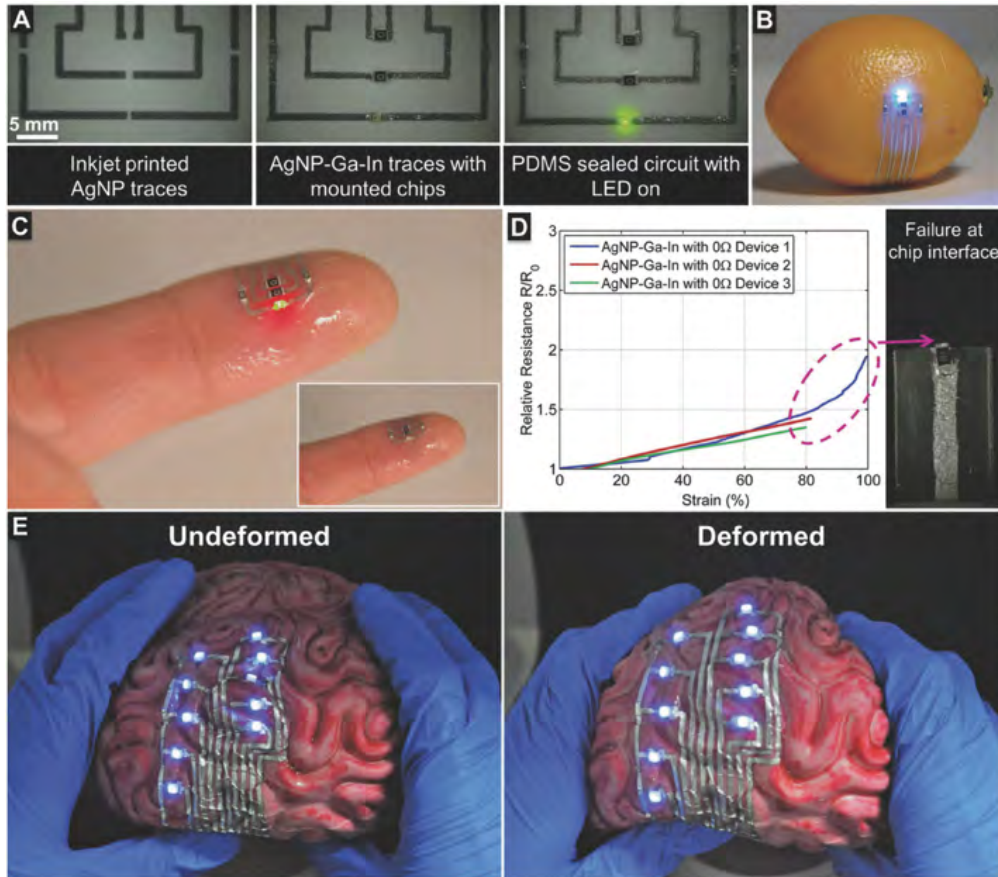
Figure 2.5: Conductive AgNP-Ga-In traces for flexible electronics. **A**, Process for populating AgNP-Ga-In circuit with surface mounted components. **B**, Circuit placed on a toy lemon using hydrographic transfer. **C**, Circuit functioning as electronic tattoo on human skin with an integrated LED on finger print, inset: LED is off on the same circuit. **D**, Relative resistance versus strain of conductive traces with a 0 Ω resistor in the middle of specimen, subjected to uniaxial strain until mechanical failure, inset: failed specimen at the interface between chip and PDMS. **E**, Functioning LEDs on a soft brain-shaped toy before and after deformation.

conductors.

2.3 Digitally Printable Elastomer Inks Embedded with Silver and Liquid Metal

2.3.1 Contribution to AgInGa-SIS Ink

This project was led by Wuzhou Zu. I conducted and analyzed the electromechanical tests of the conductive inks with different types of silver flakes. I helped the project by brainstroming and designing compelling demonstrations to show the originality of the work. I edited manuscript as the second author of this project. This material is another example of composites with multiphase inclusions using silver flakes and eutectic gallium indium.

2.3.2 Fabrication of AgInGa-SIS Ink

The conductive ink was fabricated by dissolving styrene isoprene (SIS) block copolymer in toluene. SIS block copolymer is chosen as the elastomer binder because of its high elasticity and adhesive properties. Silver (Ag) microflakes were added as the conductive filler because of the high electrical conductivity and aspect ratio, which results in improved percolation behavior at lower particle concentration when compared to other conductive fillers such as
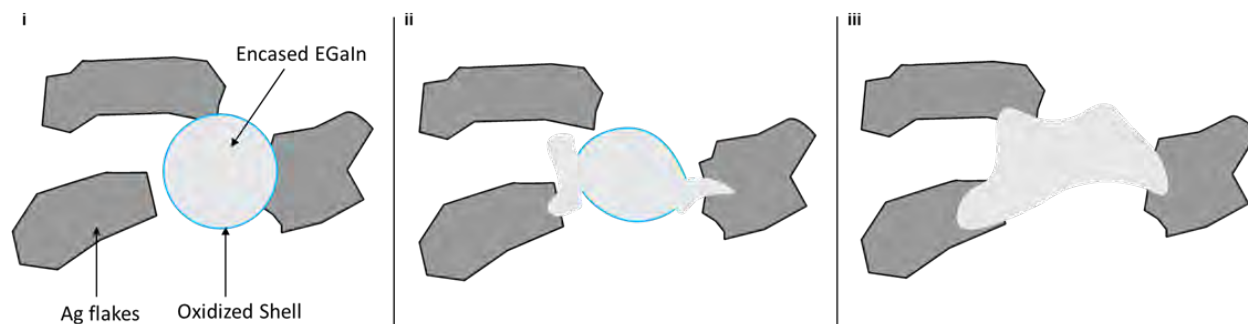
Figure 2.6: Schematic of ruptured oxidized layer of EGaIn. **i**, Ag microflakes and EGaIn composite in their original state. **ii**, Under mechanical shear, the oxidized shell of EGaIn fractures to release encased EGaIn. **iii**, Released EGaIn forms additional pathways between the Ag flakes.

Table 2.1: Detailed electrical and electromechanical properties of the AgGaIn-SIS inks made of five different commercially available microflakes

Ag flakes	Maximum strain	Relative resistance [Ω] (@100% strain)	Relative resistance [Ω] (@Max strain)	Average conductivity [10^5 S m^{-1}]	Maximum conductivity [10^5 S m^{-1}]
SF87	>1050%	0.87	16.46	2.13±0.21	2.31
SF94	>1050%	1.01	8.85	5.10±1.14	6.38
SF98	>1050%	0.76	6.98	2.11±0.40	2.60
SF163	330%	1.49	7.41	5.02±0.92	6.10
Sigma-Aldrich 327077	465%	1.98	25.55	4.32±0.52	5.17

microspheres. Eutectic gallium indium (EGaIn) is added to the Ag-SIS blend in order to form electrically conductive liquid bridges between the Ag microflakes and hence to improve the conductance of the elastomer under stretching. Under uniaxial stretch, the oxidized (Ga_2O_3) layer coating the surface of the EGaIn droplets will fracture and allow the EGaIn to flow [93] and make contact with adjacent Ag particles, as Figure 2.6 shows. Due to the distinction of the Zeta potential for EGaIn and Ag microflakes, the EGaIn droplets with positive charge [94] are easily adsorbed on the surface of the negatively charged flat Ag microflakes [95]. Without Ag flakes, however, LM droplets remain separated and do not form conductive pathways within the printed ink. As previously described in Lopes *et al.* [87], the formation of an $AgIn_2$ intermetallic component between the Ag flakes and the EGaIn alloy results in the formation of continuously conductive pathways within the ink. This composite addresses all challenges against printing liquid metal itself, including low-viscosity, lack of adhesion to the underlying substrate, and smearing and permits the ink to be printed using low-cost paste extrusion printers.

2.3.3 Electromechanical Properties of AgInGa-SIS Ink

In order to explore how the choice of Ag flakes influences the conductivity behaviors, we synthesized the ink with five different Ag flakes that are commercially available (SF87, SF94, SF98, SF163; Ames Goldsmith and 327077; Sigma-Aldrich) and recorded the electrical and electromechanical properties of the printed conductive traces. The detailed results of the conductivity testing can be found in Table 2.1, and the important morphological properties of these Ag flakes are presented in Table 2.2. Among all samples of five commercial silver flakes, the average initial conductivity is 3.74×10^5 S m^{-1}, with a maximum value of 6.38×10^5 S m^{-1} for the sample filled with SF94 Ag flakes. The variance of initial conductivity of all the samples is 1.51×10^5 S m^{-1}, which suggests that each of the Ag flakes contributes to adequate conductivity for digitally circuit applications.

On the other hand, the results of electromechanical coupling characterization show significant variance between these Ag flakes (Figure 2.7a). The electromechanical coupling of the elastic conductor is measured by monitoring the change in relative resistance R/R_0 as a function of uniaxial strain. Here, R is the resistance under mechanical strain and R_0 is the original resistance in unloaded state for conductive traces printed on a dogbone-shaped SIS rubber substrate. The maximum strain of the sample ranges from 325% to over 1000% for

Table 2.2: Important morphological properties of five commercially available silver microflakes

Ag flakes	Surface area [m²g⁻¹]	Tapped density [g cm⁻³]	Average size [μm]
SF87	0.82	3.80	4.05
SF94	0.67	4.00	5.44
SF98	1.04	4.00	3.58
SF163	1.34	2.10	3.49
Sigma-Aldrich 327077	N/A	N/A	N/A
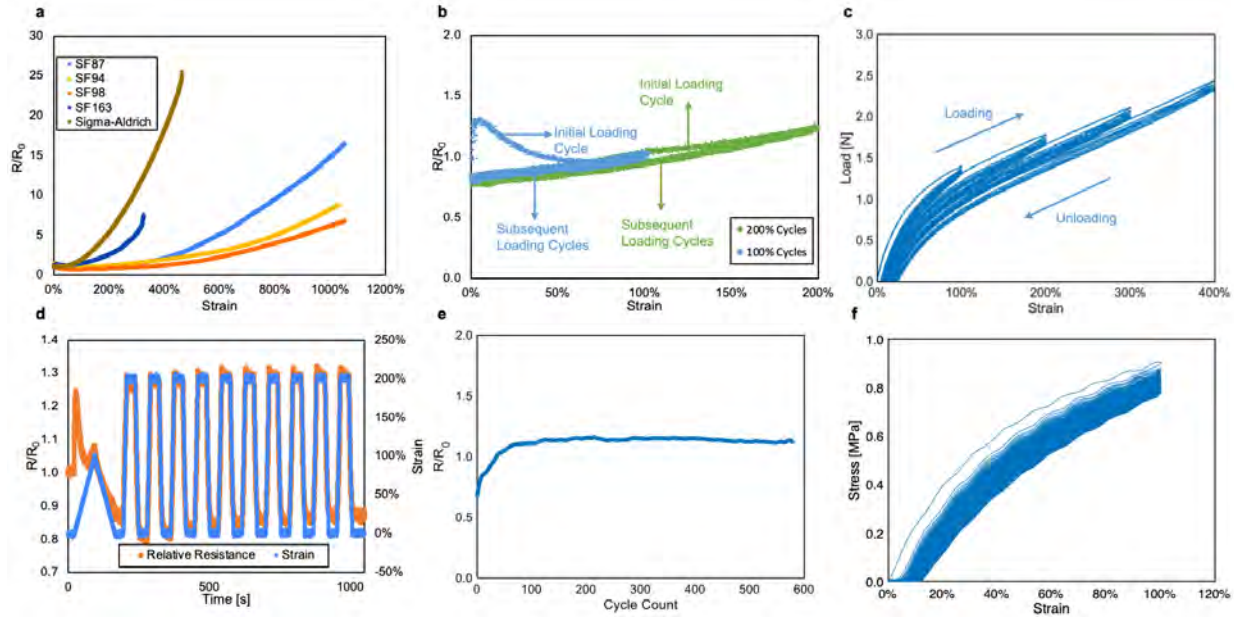
Figure 2.7: Electromechanical characterization. **a**, Change in the resistance of the elastic conductors synthesized with different Ag flakes when stretched to different maximum strains. The subsequent plots are only for composites with SF94 Ag flakes. **b**, Change in relative resistance of SF94-based elastic conductor during cyclic loading test with 100% and 200% strains. **c**, The load change from 0 to 400% of strain during cyclic loading test. **d**, Change in relative resistance during rapid loading at 600 mm min^{-1} for 10 cycles. **e**, Change in relative resistance during more than 500 cycles under 100% of strains at a rate of 300 mm min^{-1}. **f**, The stress change versus different strain of 100% under more than 500 cycles.
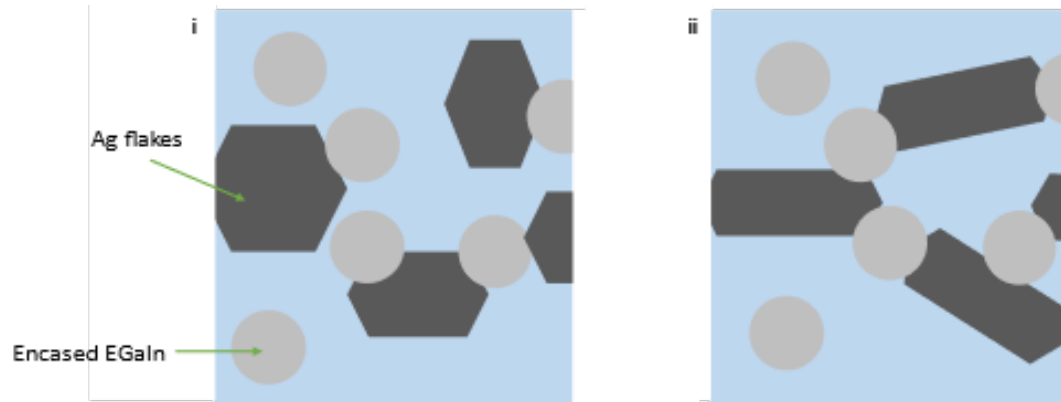
Figure 2.8: Schematic of Ag microflakes with different uniformities. **i**, Ag microflakes with low size uniformity and packing density. **ii**, Ag microflakes with higher size uniformity and packing density, resulting in more conductive pathways between the Ag flakes and EGaIn.

samples filled with different Ag flakes, which also shows a significant increase compared to our previous study that could reach to 600% [87]. At a strain of 400%, the relative resistance of elastic conductors with the Sigma-Aldrich 327077 Ag flakes increased significantly to
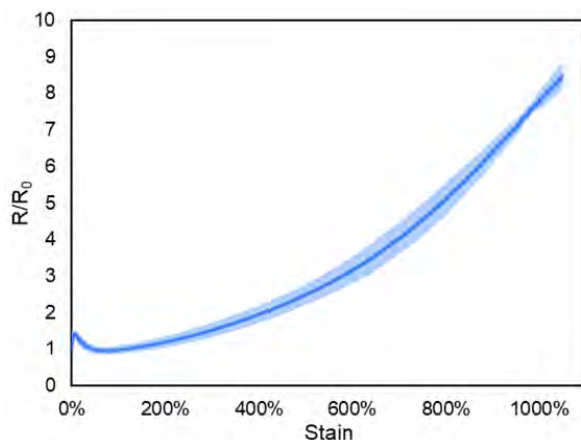
Figure 2.9: The electromechanical characterization test result of the elastic conductor with SF94 Ag flakes.

18.09. In comparison, at the same stretch state, that of SF98 was only 1.27. At 1000% strain, the samples filled with SF98 Ag flakes showed a relative resistance as low as 6.17. Such variation in electromechanical coupling indicates that the choice of Ag flakes does play an important role in determining how the electrical resistance of a printed conductive wire changes with strain. Referring to Table 2.2, we observe that the lower electromechanical coupling of the samples of SF87, SF94, SF98 Ag flakes correlates with a higher tapped density $(3.8 \sim 4.0$ g cm^{-3}). Tapped density is a parameter measuring the uniformity of particles determined by the weight of particles mechanically compressed to the same volume. In term of flake geometry, flatter and more uniform flakes have higher tapped density as they can be packed more compactly. As illustrated in Figure 2.8, we speculate that the flatter shape of flakes with higher tapped density contributes to a greater density of Ag-LM-Ag contacts and thereby improves the electrical connectivity of the percolating network and its integrity under mechanical strain. Because of its exceptional combination of high electric conductivity (6.38×10^5 S m^{-1}), high stretchability (>1000% strain), low electromechanical coupling (R/R_0 = 7.78 @1000% strain), and high consistency (Figure 2.9), SF94 Ag flakes were identified as the most promising filler material and is the focus of our subsequent measurements presented in Figure 2.7b-f.

Interestingly, even though the relative resistance increases in general as the strain

increases from 0% to 1000%, there is a variation in this increase in the range of very beginning 100% of strain (Figure 2.10). The relative resistance, R/R_0, tends to increase with steep curve first then slowly decreases for all the samples tested. For example, the relative resistance of the sample of SF94 Ag flakes first increased rapidly to 1.51 at 6% strain then decreased to 0.98 when reached the strain of 70%, and finally started to increase again slowly as the strain increases. This phenomenon could be attributed to the hysteresis of the particle-filled polymer architecture. We postulate that the EGaIn drops that are still enclosed in their oxidized layers prevent Ag flakes from fully mixing with these drops to form Ag-In alloys during the initial mixing step when synthesizing the ink. After mechanical loading, the oxidized layer breaks so that additional EGaIn drops rupture and react with Ag flakes to form new conductive pathways, resulting in a notable reduction in resistance. Referring to Figure 2.7b, subsequent loading cycles show negligible hysteresis and a more monotonic relationship between strain and resistance. Such measurements were obtained by applying 5 repeating cycles of strain from 0 to 100% and 0 to 200% at a constant rate of 50 mm min^{-1}. Corresponding stress-strain curves are shown in Figure 2.7c. Specifically, when we compare the first cycle of 100% strain to the second, there appears to be remarkable mechanical hysteresis. However, the hysteresis decreases for the remaining 4 cycles, as apparent by the overlap in the loading and unloading curves. Similar behavior was also noticed for the 200% strain loading cycles.

Another important requirement of soft conductors is that they should maintain stable conductivity under rapid loading. Referring to Figure 2.7d, we observed that through multiple strain cycles from 0 to 200% strain applied at a relatively fast rate of 600 mm min^{-1}, traces containing the SF94 Ag flakes demonstrated excellent stability. During each cycle, the sample was first stretched to 200% strain from the relaxed state at a 600 mm min^{-1} rate, then the sample was held in place for 30 seconds before releasing to the relaxed state with the same speed, and finally held at 0% strain for another 30 seconds before the next loading cycle. It should be noted that there is only 0.03 value difference in relative resistance for both
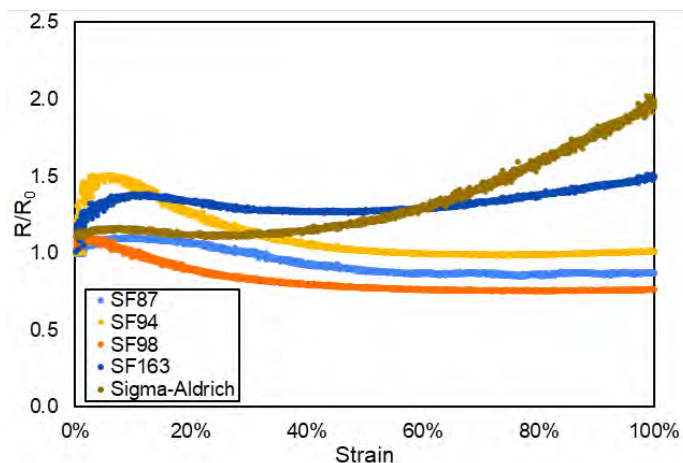
Figure 2.10: Electromechanical coupling during 100% strain. Change in the resistance of virgin samples containing different Ag flakes when initially stretched to a strain of 100%.

the relaxed and stretched state between the initial and final cycle. Moreover, more than 500 cycles of 100% strain at a rate of 300 mm/min were tested for the samples filled with SF94 Ag flakes. As Figure 2.7e and f show, the relative resistance and stress of the samples are very stable under hundreds of cycles. Such high consistency in the electromechanical coupling under consistent mechanical deformation illustrates that the elastic conductor includes desirable electromechanical properties, which are robustness, consistency, and instant electrical response to complex external mechanical deformation in short term.

2.4 Self-Healable Poly(vinyl alcohol)-Sodium Borate Composite Embedded with Silver and Liquid Metal

As has been discussed in this chapter, Ag flakes are widely used as the conductive fillers [96] in soft conductive composites since silver has high electrical conductivity (6.30×10^7 S m^{-1} at 20°C) and the high aspect ratio of the flakes is favorable in forming the electrically percolated pathways with a low volume fraction. Eutectic Gallium-Indium (EGaIn), which is liquid at room temperature, is highly deformable with negligible mechanical resistance while maintaining metallic electrical conductivity ($\sigma = 3.4 \times 10^6$ S m^{-1}) [97]. Many works have demonstrated successful applications of EGaIn as a conductive element in soft conductive material architectures with low Young's modulus, high stretchability, and moderate electromechanical coupling effect [21]. In addition, EGaIn is easy to adhere to metals such as Ag, which bridges the gaps between the Ag flakes using its deformability and provides a robust anchor while the Ag-EGaIn composite is being stretched. This interesting feature of EGaIn has boosted promising properties of the Ag-EGaIn-based composite, such as high electrical conductivity, low electromechanical coupling, and desired mechanical compliance [77, 98]. As observed in previous literature [99, 26], rigid particles can degrade the mechanical compliance and stretchability of the composite due to the inherent rigidity of the inclusions, which is exacerbated as the volume fraction of the rigid particle inclusion increases [100]. As a result, we take advantage of the unique properties of the hybrid inclusion architectures of Ag flakes and EGaIn in this work to achieve electrical conductivity without compromising mechanical compliance. We take the effort to keep the volume of Ag flakes and EGaIn embedded into the matrix initially low (∼ 12.5 vol% and ∼ 10.5 vol%, respectively) to minimize the degradation of the mechanical property of the organogel, such as stiffness, flexibility, and stretchability. However, the low inclusion fraction does not support conductive networks since the conductive particles are physically far away from each other. As a result, the composite is electrically insulating when the first synthesis. A partial dehydration process (see details in Chapter 3)
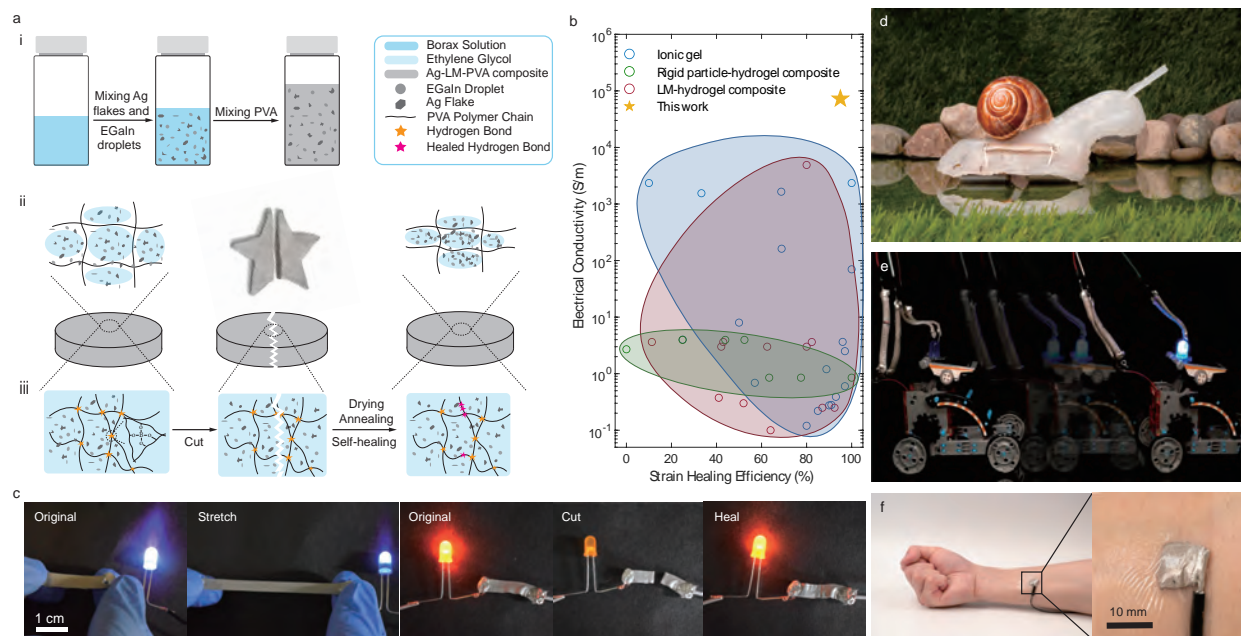
Figure 2.11: (**a**) Overview of Ag-LM-PVA composite: (i) Schematic illustration of the fabrication process, (ii) drying annealing, and (iii) self-healing mechanism. (**b**) Ashby-style plot highlights the combination of high electrical conductivity and high self-healing efficiency of this work. References of literature are listed in Supplementary Information. (**c**) Real image of the composite in its original state, under stretch, cut, and electrical self-healing. (**d**) Image of a snail-inspired crawling robot demonstrating the properties of the composite. (**e**) Image of reconfigured a toy car circuit demonstrating the properties of the composite. (**f**) Image of a bioelectronics application.

achieves high electrical conductivity at an elevated temperature (100°C), which removes a portion of EG and makes the conductive fillers connect to each other. PVA-Borax organogel is utilized due to its biocompatibility, tunable mechanical properties, and self-healing property. The mechanical healing efficiency is as high as 96% and is under huge influence of freezing time, which will be discussed in detail in the next section. The electrical healing efficiency is as high as 95% and is achieved instantaneously when the two breaking parts are connected together. Although the high liquid content renders the organogel desired properties such as high flexibility and biocompatibility, the dehydration of solvent makes the properties unstable and unreliable over time. For example, the water-based PVA-Borax organogel can lose 50% water within 5 hours in ambient conditions (23°C, air pressure), which alters the electrical and mechanical properties significantly. To overcome the dehydration issue and make the properties of the organogel system long-lasting, we use the polar solvent EG

instead of water to keep the solvent from drying in an ambient environment. The EG-based organogel composite will absorb water from the environment and increase slightly in weight (5%) due to the hygroscopicity of PVA [101]. After the adsorption of water saturation, the EG-based composite keeps a constant weight for more than 24 hours.

2.4.1 Contribution to Ag-LM-PVA composite

Yongyi Zhao has been leading this project and preparing for a manuscript to submit. I, as the second author to this project, designed the concept of this project with Yongyi. I helped Yongyi improve the fabrication of the material. I also participated in designing experiments related to characterization of the material and analyzing the result. I wrote and edited the manuscript as well. This conductive organogel is the last example of composite with multiphase inclusions.

2.4.2 Fabrication of Ag-LM-PVA composite

The Ag-LM-PVA composite is synthesized using the steps outlined in Figure 2.11a(i). A planetary centifugal mixer (AR-100; Thinky Corporation) is used to break up bulk EGaIn and form a suspension of LM microdroplets within an EG-based Borax solution. Next, Ag micro-flakes are added to the emulsion and dispersed by shear mixing with the planetary mixer. Lastly, an EG-based PVA solution is added and the material system and mixed at 120°C. Upon mixing, the PVA and Borax form hydrogen bond and gelation occurs. At this stage, the composite is a highly viscoelastic polymer and can be molded into desired shape. After molding, the composite is subject to the drying annealing process to achieve high electrical conductivity.

2.4.3 Material Characterization

After molding and drying annealing, we apply a one-cycle freeze-thaw treatment to the composite for varying time (10, 20, and 30 minutes). The freeze-thaw treatment alters the rheological property of the composite by introducing physical entanglement between polymer chains[102]. As shown in Figure 2.12a, the storage modulus (G') of the composite is approximately an order of magnitude higher than the loss modulus (G''), indicating the composite exhibits more solid property than liquid. To be mechanically compatible with soft biological tissues, the Ag-LM-PVA composite must be highly compliant and deformable. The stress-strain characteristics of the material are evaluated using an Instron 5969 materials testing machine as shown in Figure 2.12b. The degree of physical entanglement is impacted by the freezing time, which affects the mechanical properties of the composite such as Young's
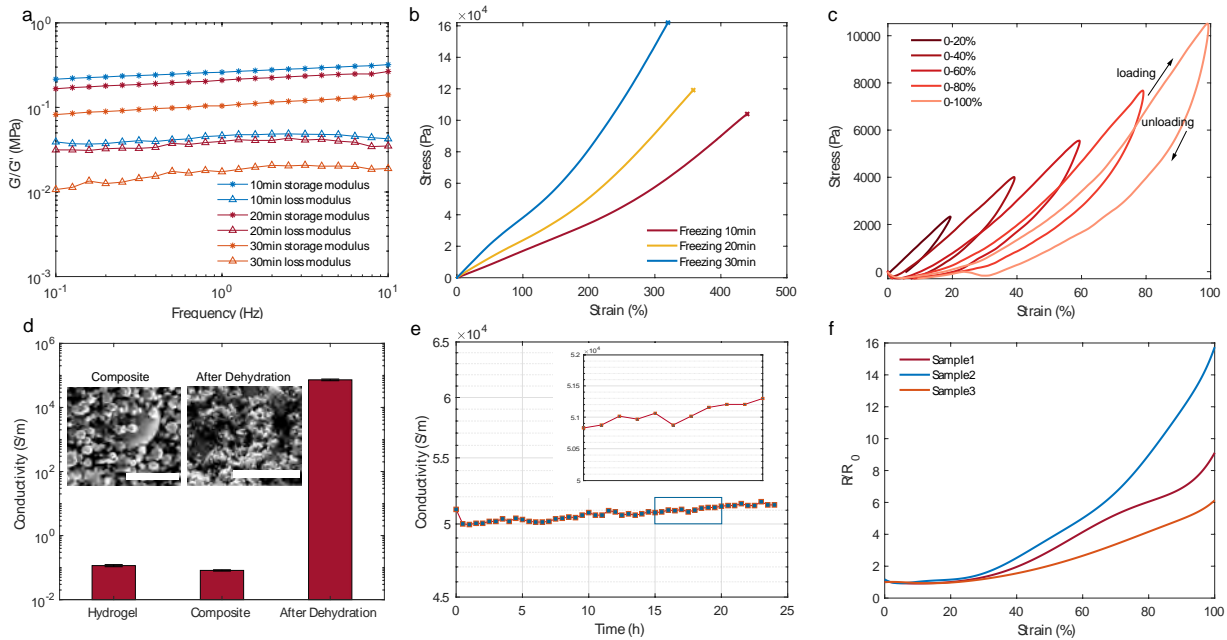
Figure 2.12: (**a**) DMA test of the composites after drying annealing of varying freezing time (10, 20, and 30 minutes). (**b**) Tensile test of the composites after drying annealing of varying freezing time (10, 20, and 30 minutes). (**c**) Cyclic test of the composite after drying annealing of freezing 10 minutes. (**d**) Electrical conductivity comparison of PVA-Borax organogel, Ag-LM-PVA composite, and Ag-LM-PVA composite after drying annealing. Insets are the Scanning Electron Microscope (SEM) images of the composite before and after drying annealing. Scale bar = 20 μm. (**e**) Electrical conductivity of Ag-LM-PVA composite after drying annealing evolving in 24 hours in ambient condition. (**f**) Electromechanical coupling of three Ag-LM-PVA composites after drying annealing.

modulus and stretchability. The longer freezing time leads to more physical entanglements, and thus the higher energy required to deform the polymer chains, which is reflected by the tensile modulus (tensile moduli of samples that are frozen for 10, 20, and 30 minutes are 17.1, 23.6, and 42.3 kPa, respectively). The physical entanglements also restrict the reconfiguration and straightening of the polymer chains, which degrades the stretchability (maximum strain of freezing 10, 20, and 30 minutes samples are 439.9, 358.1, and 319.8%, respectively). Importantly, the conductive and self-healing material is expected to undergo multiple loading cycles during usage, and robust mechanical property is essential to this requirement. To test the cyclic performance of the composite, it is first stretched by 20% strain and then relaxed to its original length, and the strain is increased by 20% up to 100% for each successive cycle as shown in Figure 2.12c. Hysteresis loop between loading and unloading cycles is observed, which is a typical feature of organo/hydrogels, indicating that the physical network formed by hydrogen bonds of the gel is broken.

2.4.4   Electrical & Electromechanical Characterization

Upon synthesis, the composite is ionically conductive due to the dissolution of ions from the Borax and the present of metal fillers. However, the conductivity is limited (0.082 S m^{-1}) due to the absence of electrically percolating pathways (left inset of Figure 2.12d). After performing the drying annealing, the conductive inclusions form electrically percolating pathways and the conductivity of the composite increases by a factor of 9.1×10^5 and reaches a value of 7.3×10^4 S m-1 (Figure 2.12d). We note that the conductivity of water-based conductive hydrogel changes naturally over time in ambient condition [96] due to the evaporation of water. In contrast, the conductivity of our composite is stable for the duration of greater than 24 hours, as shown in Figure 2.12e. The robust electrical property is resulting from the negligible evaporation rate of EG, which keeps the conductive fillers stable in position. In addition, we note that the evaporation of solvent happens nonuniformly through the thickness, i.e., the evaporation is more severely at the surface than the middle or bottom. As

a result, the electrical conductivity decreases from the top to the bottom surface through the thickness.

As shown in Figure 2.12f, we observe electromechanical coupling in which the electrical resistance of a strip of Ag-LM-PVA composite increases as it is stretched. We note that this electromechanical coupling is more pronounced than in other soft conductive materials that contain both LM and Ag inclusions[77, 98]. We attribute this to the relatively low volume fraction of conductive particles and the sparsity of the percolating network, although more study will be required to more fully understand this difference in electromechanical behavior.

2.4.5 Self-Healing Characterization

Next, we examine the mechanical and electrical self-healing properties of the Ag-LM-PVA composite. A key feature of the composite is that the PVA-Borax organogel matrix is crosslinked through the dynamic and reversible hydrogen bonding, which enables the rapid self-healing property and usually can achieve high efficiency (up to 100%) [103]. This results in mechanical self-healing, which is demonstrated by comparing the stress-strain characteristics of pristine and damaged composite after healing for 5 minutes in room temperature (Figure 2.13a). The elongation ratio of the pristine (δ_{b0}) and healed (δ_b) hydrogel composites are used to determine the efficiency (ϵ_H) of self-healing: $\epsilon_H = (\delta_b/\delta_{b0}) \times 100\%$. As shown in Figure 2.13a, the sample that is subject to freezing for 10 minutes achieved high mechanical self-healing efficiency (96.4%) and the freezing time makes significant impact on the healing efficiency. The sample that is frozen for 10 minutes has the highest mechanically self-healing efficiency whereas the longer freezing time degrades the mechanically self-healing efficiency (42.0% and 6.3% mechanically self-healing efficiency of the samples frozen for 20 and 30 minutes, respectively). We postulate that the physical entanglement formed during the freezing procedure restricts the free reconfiguration of the polymer chains, which then hinders the re-formation of hydrogen bond at the cut. As the freezing time increases, the physical entanglement increases, which causes more resistance to the hydrogen bonding.
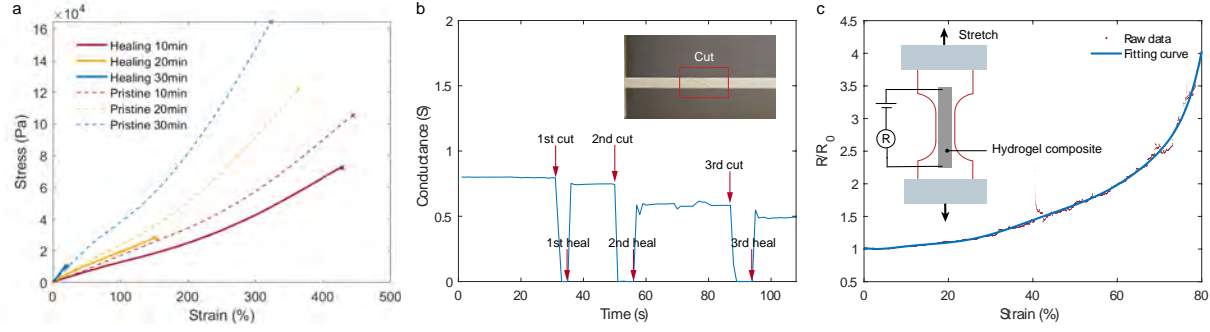
Figure 2.13: (**a**) Mechanical properties before and after the self-healing. (**b**) Self-healing of electrical properties while introducing several cut damages. Inset is showing the real image of the composite after self-healing around the damages spot. (**c**) Electromechanical coupling test after self-healing. Inset is the schematic illustration of the test method.

The electrical conductivity is achieved through the connection between neighboring conductive particles (Ag micro-flakes and/or EGaIn microdroplets). When the material is severed and then reconnected, the conductive particles on the opposing surfaces are connected through contact and wetting and restore the electrical percolation network. As a result, the electrical self-healing happens immediately after the two breaking parts are rejoined. As shown in Figure 2.13b, the electrical self-healing efficiency (θ_H), which is defined by $\theta_H = (\sigma_b/\sigma_{b0}) \times 100\%$, is as high as 95% for a single healing cycle, where σ_b is the electrical conductivity after self-healing, and σ_{b0} is the electrical conductivity before cutting. The average electrical self-healing efficiency (θ_H) reached to 86% out of three healing cycles. As mentioned earlier, during the drying annealing process, the enhancement in conductivity mostly occurs at the surface of the material (~ 0.3 mm thickness). As a result, it is important to align the conductive layers from the two breaking parts to achieve high electrical self-healing efficiency.

In addition, it is expected that the healed material can withstand some degree of stretch without breaking and losing the conductivity completely. Referring to Figure 2.13c, the healed material can withstand 80% strain without losing the electrical connection of the fillers. Moreover, the electromechanical coupling of the healed material is less than that of the pristine composite. We postulate that this is because the mechanical damage acts to

rupture the EGaIn droplets and facilitate the formation of more robust conductive pathways that can remain intact under strain. In this way, the activated EGaIn acts as a bridge between rigid particles over the crack when the overlap of rigid particles are reduced due to the stretch, and result in more moderate electromechanical coupling of the composite.

2.5 Silver-Coated Poly(dimethylsiloxane) Beads

2.5.1 Contribution to Phase-Segregated Silver-Silicone Composites

This project was led by Dr. Chengfeng Pan. I fabricated the phase-segregated composite by compositing with different types of silver particles. Then, I conducted and analyzed electromechanical characterization of the materials. This composite is an example of composites with heterogeneous material architectures in order to reduce the amount of conductive fillers.

2.5.2 Fabrication of Phase-Segregated Silver-Silicone Composites

Referring to Figure 2.14a, the thermally stable elastic conductor is made from a phase-segregated composite composed of core-shell silver-coated poly(dimethylsiloxane) (PDMS; Sylgard 184, Dow Corning) (PDMS@Ag) beads and silver flakes dispersed in an elastic PDMS matrix. To facilitate bonding between the PDMS core and Ag shell, a poly(dopamine) layer was coated on the PDMS beads prior to Ag deposition. The corresponding scanning electron microscopy (SEM) images (Figure 2.14b) show the Ag-coated PDMS microspheres (Figure 2.15) encased within a PDMS matrix. The Ag flakes are dispersed between the PDMS@Ag beads (Figure 2.14b), resulting in a local enhancement in Ag volumetric fraction and greater susceptibility to percolation. The incorporation of Ag-coated PDMS beads introduces an effective phase segregation in which Ag flakes are confined to the "grain boundaries" between the embedded beads. Henceforth, these phase-segregated silver-silicone material systems are referred to as PS3 composites. Moreover, the Ag shells on the PDMS@Ag beads establish additional sources of electrical connectivity between adjacent Ag flakes regions (alternatively,

the percolating Ag flakes can be treated as conductive bridges between the Ag shells). The combination of these two effects, that is, local enhancement of the Ag flake content and the flakes-bead shells-flakes connectivity, enables the PS3 composite to achieve a 2 orders of magnitude (139×) enhancement in electrical conductivity (σ), compared to the uniformly
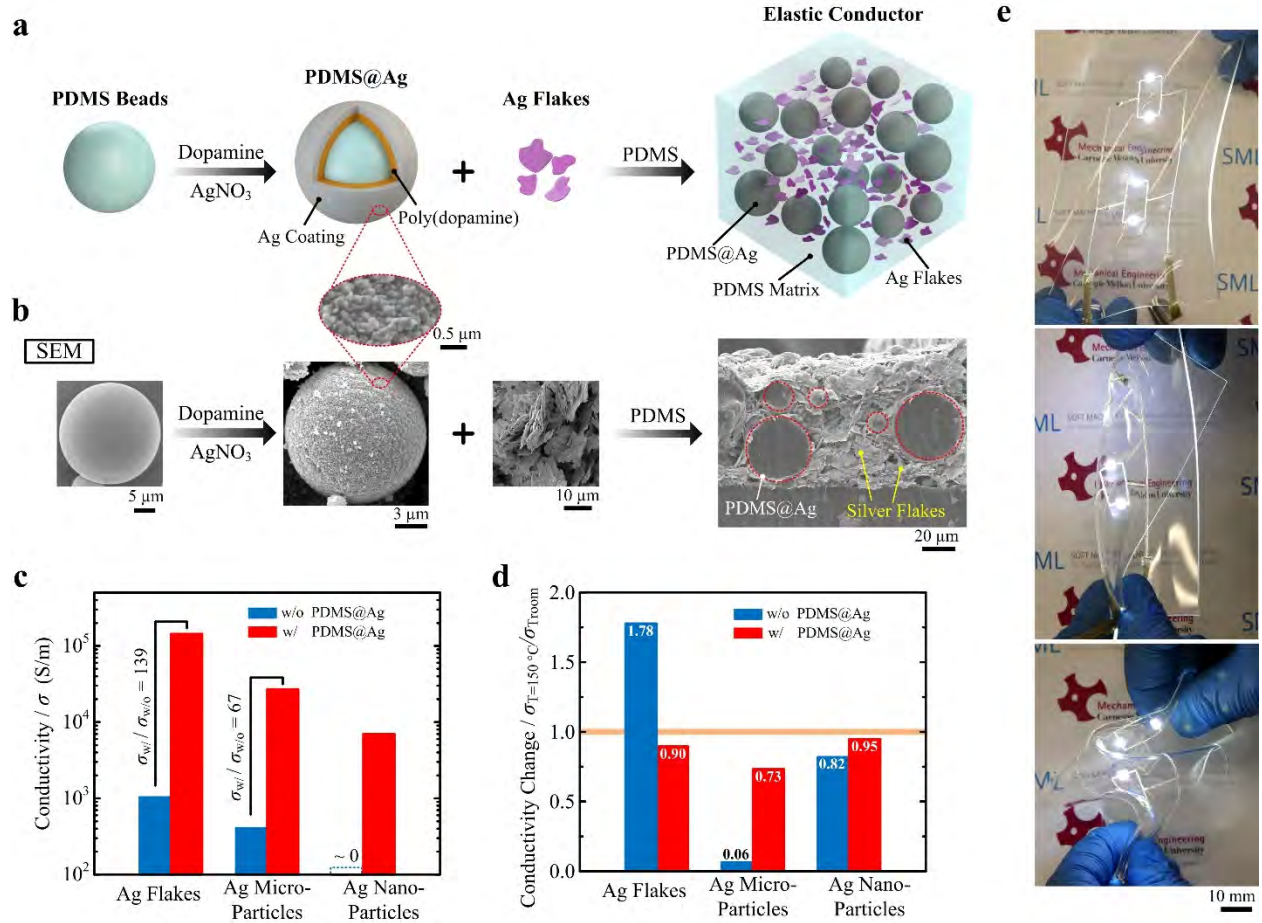
Figure 2.14: Thermally stable elastic conductors. **a**, Schematic of the fabrication process of the elastic conductor from composite of silver (Ag)-coated PDMS beads (PDMS@Ag), Ag flakes as an example filler, and the PDMS matrix. PDMS@Ag is a core–shell structure consisting of a poly(dopamine) and a Ag shell. **b**, Scanning electron microscopy (SEM) images corresponding to the previous illustration. The inset is the zoomed-in image of the Ag coating showing the Ag shell. **c**, Electrical conductivity of elastic conductors from composites with different Ag fillers (Ag flakes, Ag microparticles, and Ag nanoparticles) with/without PDMS@Ag at a volumetric fraction of 12 vol% Ag. Composites with PDMS@Ag have around 2 orders of magnitude higher conductivity relative to composites without PDMS@Ag. **d**, Electrical conductivity change of composites with/without PDMS@Ag between the temperature of 150°C and room temperature. Composites with PDMS@Ag are more thermally stable in electrical conductivity. **e**, Photographs of the stretchable LED circuitry made from a composite of PDMS@Ag and Ag flakes as the lead connection (red line in the inset) under stretching (top), folding (middle), and squeezing (bottom).
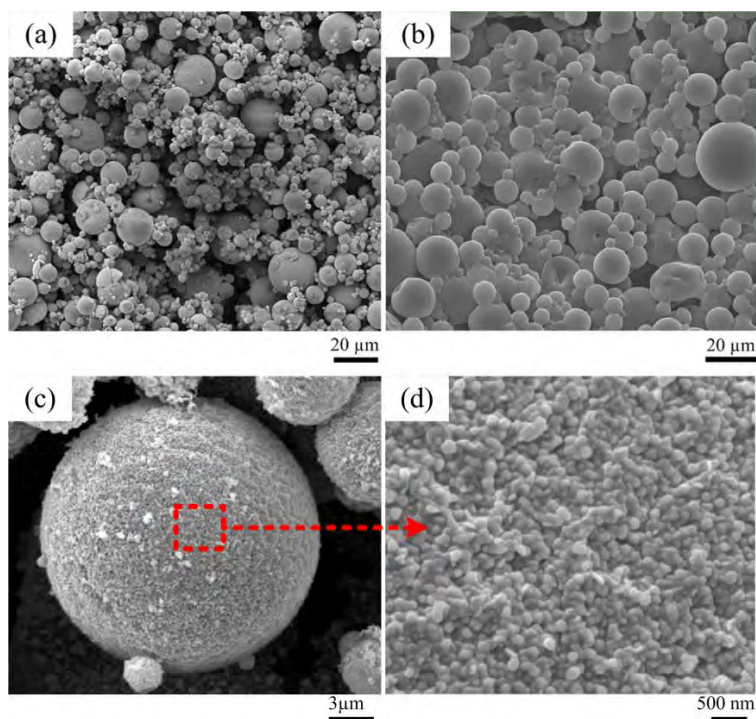
Figure 2.15: **(a)** Scanning electron microscope (SEM) image of polydisperse core-shell PDMS@Ag particles, **(b)** polydisperse PDMS particles, **(c)** single core-shell PDMS@Ag particle, and **(d)** zoomed-in image of Ag shell.
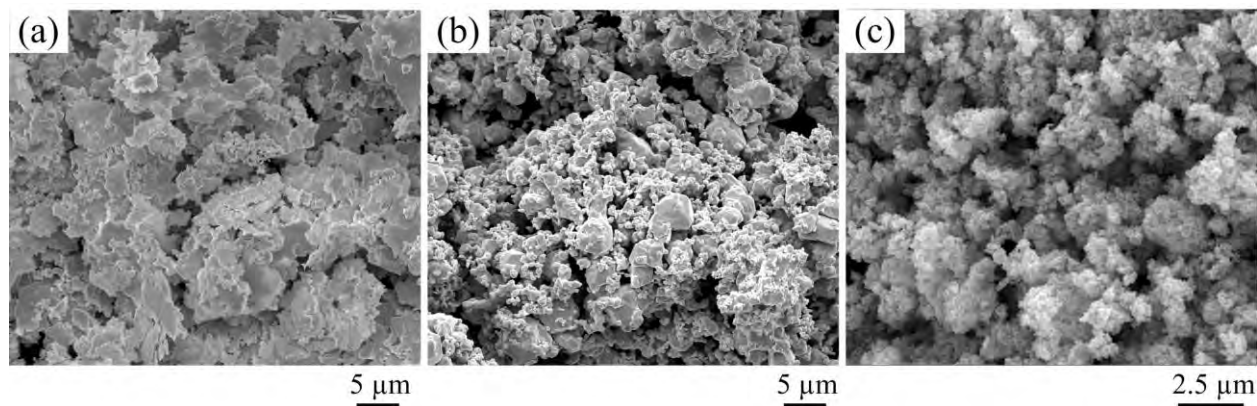
Figure 2.16: SEM image of Ag fillers. **(a)** Ag flakes, **(b)** Ag microparticles, and **(c)** Ag nanoparticles.

dispersed Ag flake/PDMS composites with the same Ag content (12 vol%) (Figure 2.14c). This material architecture also works for other types of Ag fillers (Figures 2.16 and 2.17). The conductivity of a composite with PDMS@Ag and Ag microparticles is 67 times higher than a composite with only Ag microparticle fillers with the same Ag content (12 vol%) B. The conductivity of a composite with PDMS@Ag and Ag nanoparticles goes from being
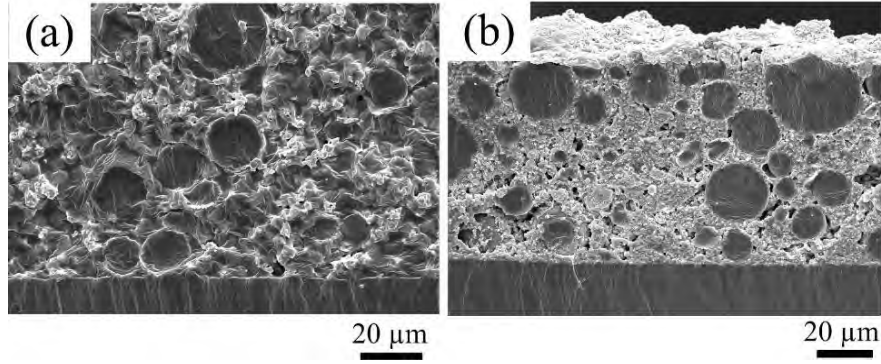
Figure 2.17: SEM image of sample cross sections. **(a)** PDMS@Ag/Ag microparticle/PDMS, and **(b)** PDMS@Ag/Ag nanoparticle/PDMS PS3 composite.

nonconductive ($\sigma \approx 0$) for a composite with only Ag nanoparticles to conductive ($\sigma = 6.94 \times 10^3$ S m^{-1}) (Figure 2.14c) at the same Ag content (12 vol%). Note that the total Ag content was determined by including the contribution from the PDMS@Ag shell. Since less Ag is needed to achieve the same electrical conductivity (1.4×10^5 S m^{-1}), this architecture enables a significant reduction in density compared to the uniformly dispersed Ag flake/PDMS composites (from 3.11 to 2.17 g cm^{-3}, i.e., 43.7% less). Last, the introduction of PDMS@Ag beads improves thermal stability of the conductivity (Figure 2.14d). We speculate that the similar thermal expansion of the PDMS beads and surrounding PDMS matrix results in a limited net impact on the percolating network of the Ag filler particles or their connectivity with the Ag shells. As shown in Figure 2.14e, a stretchable circuit powering an array of light-emitting diodes (LEDs) was fabricated using the PS3 composite with Ag flakes as the electrical leads (red lines in Figure 2.14e inset). The circuit maintained electrical functionality under mechanical deformation, for example, stretching, folding, and squeezing.

2.5.3   Electromechanical Properties of PS3 Composite

We studied the electromechanical properties of the elastomer composite. For the results presented in Figure 2.18a–d, we used a PDMS@Ag content of 40 vol% and a Ag flake content of 15 vol% for all samples. A representative evolution of the relative change in resistance (R/R_0) of the PDMS@Ag/Ag flake/PDMS composite as a function of the tensile strain (ϵ) for 11
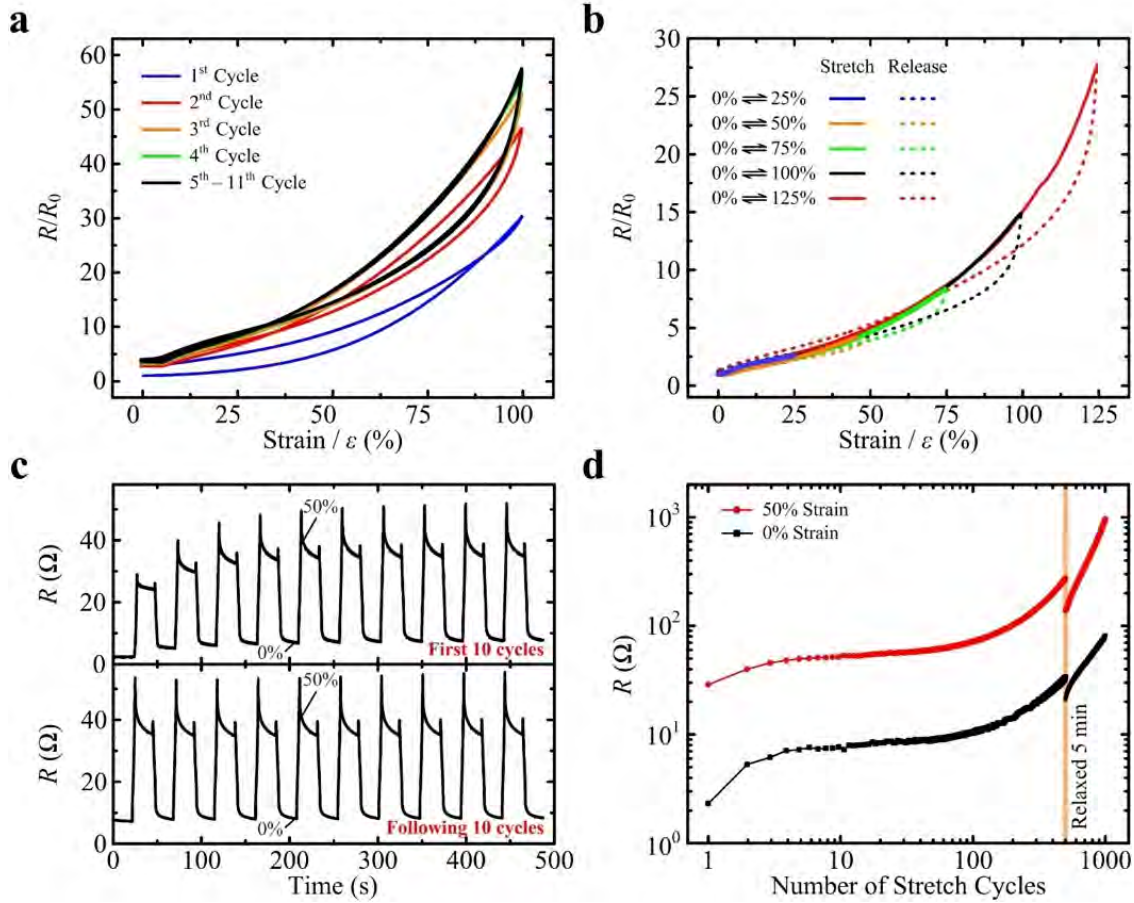
Figure 2.18: Electromechanical response of composites with PDMS@Ag beads and Ag flakes. **a**, Normalized resistance as a function of strain up to 100% strain showing differences during the first four cycles and then convergence to the same curve for the 5th to 11th cycles. **b**, Normalized resistance as a function of strain under different strain ranges. The data is collected after the conductor was precycled by stretching 10 times up to 100% strain. The results show negligible difference in the loading curves between stretching cycles but some hysteresis between loading and unloading within a stretching cycle. **c**, Electromechanical response of the conductor when cyclically strained to 50% over 20 cycles (first 10 cycles-top following 10 cycles-bottom). **d**, Resistance of the conductor at 50% elongation and relaxed states for over 1000 cycles. When the composite was held at a relaxed state for 5 min, it recovered some conductivity.

cyclic stretching and releasing cycles up to $\epsilon = 100\%$ is presented in Figure 2.18a. The results show hysteresis in the electromechanical response for the first four cycles and then converge to identical responses from the 5th to 11th cycle. We measured the mechanical response under different tensile strain ranges (Figure 2.18b) after pre-cycling to $\epsilon = 100\%$ for 10 cycles. In the first cycle following pre-cycling, the sample was first stretched by 25% and then relaxed to its original length. In each consecutive cycle, the strain was increased by steps
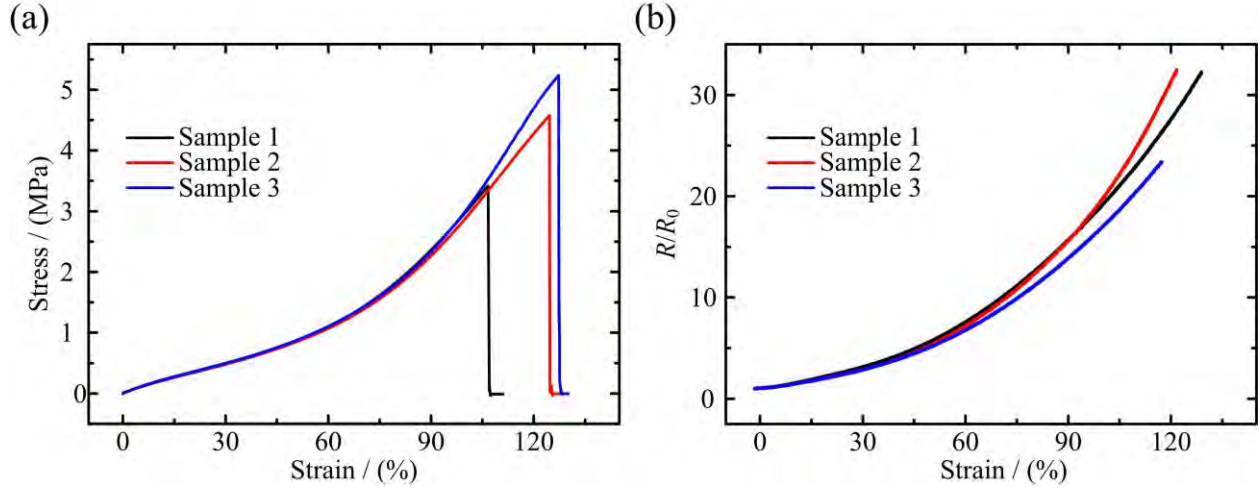
Figure 2.19: **(a)** Stress-strain curves of PS3 composites with Ag flakes. **(b)** Resistance change as a function of strain until to mechanical failure.

of 25% up to $\epsilon = 125\%$. The normalized resistance as a function of strain overlaps for each subsequent cycle with reasonable agreement. We observe some modest hysteresis between loading and unloading of each strain cycle. The representative stress-strain curves (Figure 2.19a) indicate that the strain limit of PS3 composites is larger than 100%. The composites will maintain electrically conductive until mechanical breakdown (Figure 2.19b). As shown in Figure 2.18c, the PS3 conductors demonstrate a largely consistent electromechanical behavior; that is, after an initial rise, the resistance profile is constant when cyclically strained between $\epsilon = 0$ and 50% over 20 loading cycles. The resistance profile converges to identical pulses after four cycles, which is consistent with the results in Figure 2.18a. The long-term use of this elastic conductor is evaluated by performing cyclic loading up to 50% strain (Figure 2.18d). After an initial break-in period (5 cycles), the electromechanical response stabilizes and is repeatable for the following 10 cycles. During subsequent stretching cycles, we observe that the resistance in both the relaxed and 50% elongated states begins to increase significantly after ~ 50 cycles. After 500 cycles, the conductor was held at a relaxed state for 5 mins (orange line), and the resistance is observed to decrease, suggesting some recovery of the conductivity due to the local stress release causing the reconfiguration of conductive pathways. This trend of resistance change during cyclic loading is common

for many particle-filled composites [13]. Nonetheless, there remains room to improve the performance of the PS3 composites for high cyclical loading, such as adding surfactants for better bonding between the conductive filler and matrix [69] or with the inclusion of liquid metal for reducing internal stress concentrations [77]. Despite the resistance increase during cyclic loading, the PDMS@Ag-based elastic conductors demonstrate high stretchability and relatively robust electromechanical performance.

2.6 Conclusions

2.6.1 EGain-Assisted Sintering of Silver Nanoparticles

We have introduced a technique to rapidly create soft and stretchable thin film electronics. The circuits are produced with ink-jet printed AgNP that interact with EGaIn at room temperature to form mechanically robust conductive traces. With the EGaIn coating, the traces exhibit a $\times 10^6$ increase in electrical conductivity and maintain low trace resistance under bending or when stretched to 80% strain. On a soft elastomer substrate (PDMS), the trace exhibits a moderate electromechanical response (e.g., 50% increase in electrical resistance with 50% strain; i.e., gauge factor ≈ 1) that is consistent over hundreds of loading cycles. EGaIn also functions as a room temperature solder that can be used to populate the circuit with surface mounted microelectronics. This is accomplished by placing the chips on the EGaIn-coated traces and then applying HCl vapor to remove surface oxide and allow the liquid metal to wet to the microchip pins.

When printed on temporary tattoo paper, the circuits can be placed on 3D surfaces using hydrographic transfer or worn on the skin as an electronic tattoo. Because the circuit is stretchable, it can be transferred to highly curved and nondevelopable (e.g., spherical) surfaces or placed over parts of the body that undergo significant strain. Moreover, unlike other approaches to stretchable electronics (e.g., conductive elastomers, wavy circuits, EGaIn microfluidics, etc.), thin-film circuits can be produced using a conventional inkjet printer.

This novel methodology leads to highly customized and feasible fabrication techniques of soft on-skin electronics that have never been demonstrated before. Future efforts will focus on further elemental and topographic characterization of AgNP-Ga-In circuits printed on various substrates, optimization of AgNP printing, deposition, and cleaning techniques for achieving highest stretchability and conductivity, optimization of the transfer techniques, and demonstration of a series of thin film e-skin circuits over the body for biomonitoring, and over 3D surfaces for interactive human-machine interfaces (HMIs).

2.6.2 Digitally Printable Elastomer Inks Embedded with Silver and Liquid Metal

We have studied the formulation of one especially promising class of printable conductive inks composed of LM alloy and Ag microparticles. Specifically, we examined the effect of Ag microflakes with difWferent physical properties including size, tapped density, and surface area on the conductivity and electromechanical properties of the bi-phasic AgInGa-SIS conductor. Through the systematic investigation of the conductive filler of the biphasic ink, it was demonstrated that the choice of Ag flakes has significant impact on the biphasic ink. More specifically, we postulated that the uniformity and flatness of Ag flakes, which are indicated by the tapped density, have direct impact on the electromechanical coupling of the composite.

Among the samples we examined, the composite filled with SF94 Ag flakes showed the highest electrical conductivity (6.38×10^5 S m^{-1}), extreme stretchability (>1000% strain), and low electromechanical coupling (R/R_0 = 7.78 @1000% strain). This specific formulation is suitable for various applications in soft electronics and robotics that require stable electrical connection under mechanical deformation. Our study also indicated the unique versatility of the ink. For example, filling the ink with Sigma-Aldrich 327077 Ag flakes would result in an elastic conductor with much higher electromechanical coupling, which could be suitable for specific applications in strain sensing.

With focus on rapid and scalable prototyping, this bi-phasic AgInGa-SIS ink represents an important step toward rapid and scalable manufacturing of printed stretchable circuits. The compatibility with a commercial extrusion-based printer and elimination of post-processing steps enable this composite to be widely utilized. To highlight the potential applications of this elastic conductor, we demonstrated a digitally printed circuit that is insensitive to mechanical deformation for wiring electronic devices. We also showed a tattoo-like bioelectronic circuit composed of electrical interconnects and bioelectrodes printed on an ultrathin polymer film and utilized as a fully wearable ECG monitoring system. Together, these demonstrations suggest that the bi-phasic ink could have widespread applications in stretchable electronics for personal computing and healthcare.

Moving forward, we see opportunities to further advance our understanding of these bi-phasic material systems. This includes future efforts to explore the influence of surface energy of different types of substrates on the width of printed traces under the same printing conditions. Furthermore, although this work provides empirical evidence for the influence of Ag flakes and tapped density on electrical and electromechanical properties, additional investigation is required to more fully understand this relationship. Such efforts could include combining recent efforts in theoretical modeling of electromechanical coupling in soft LM-polymer composites [104, 100] with previous computational studies on how the shape and aspect ratio of conductive particles influence their electrical connectivity within a particle-filled composite [105].

2.6.3 Self-Healable Poly(vinyl alcohol)-Sodium Borate based Hydrogel Composite Embedded with Silver and Liquid Metal

In this study, we reported an Ag-LM-PVA hydrogel composite that exhibits a high electrical conductivity (7×10^4 S m^{-1}), rapid and efficient self-healing property both electrically and mechanically (heal up to 96% maximum strain within 5 minutes, and instantaneously heal up to 86% of the conductivity), low tensile modulus (~ 20 kPa), high stretchability ($> 400\%$

strain), and anti-dehydration property (weight increases 2% within 24 hours in the ambient environment and keeps constant afterward). The material possesses huge potential in both engineering applications such as robotic applications and human-related systems such as bio-signal sensing. To illustrate the capabilities of the Ag-LM-PVA hydrogel, we fabricated a snail-inspired crawling robot where the conductive material acts as the flexible power line and can allow the robot to continue functioning using the self-healing property after physical damage. The recovery is fast thanks to the rapid mechanical and electrical self-healing properties. We also developed on-body electrodes out of the Ag-LM-PVA composite for EMG sensing, which showed satisfactory ability in obtaining high-quality signals. The self-healing ability of the material also enables the excellent signal quality for different sensing spots on the body of various shapes and/or sizes.

The partial dehydration technique enables a high electrical conductivity with a low inclusion volume fraction. The composite's rapid and efficient mechanical self-healing property is intrinsically achieved by the dynamic and reversible hydrogen bond of the PVA-Borax hydrogel. The hydrogen bonds will form automatically between the PVA chains at the crack that joins the two breaking parts. The self-healing is rapid since the hydrogen bonding formation is in the subpicosecond or picosecond time scale. Besides, the mechanical self-healing property is controllable via freezing time. The electrical self-healing is achieved by connecting the conductive fillers in the two breaking parts. The electrically percolating pathways recover immediately when the conductive fillers are in contact, and thus the recovery of electrical conductivity is instantaneous. The electrical self-healing can achieve high efficiency (86%) if the conductive layers are well aligned. In addition, the healed material demonstrates robust electromechanical coupling behaviors, i.e., remaining electrically conductive when stretched to 80%. Unlike water-based hydrogel composites, whose solvent dries rapidly at room temperature and leads to unstable electrical and mechanical properties, the EG-based hydrogel composite has robust and reliable mechanical and electrical properties over time due to the engineered anti-dehydration property.

Despite the hydrogel composite's promising properties, they can be further improved by overcoming the imperfections originate from the fabrication methods. First, since the composite is molded after crosslinking utilizing the fluidity of the viscoelastic hydrogel, it is difficult to mold it into small features due to the limited moldability of the composite. Besides, the low fluidity results in bubbles trapped in the composite. We conduct the degas process by settling the samples in the mold at room temperature for 15 minutes, which doesn't guarantee completely degassing. Increasing the fluidity of the composite by adjusting the PVA and/or Borax solution concentration can be helpful with the issues.

2.6.4   Silver-Coated Poly(dimethylsiloxane) Beads

We have introduced a new material architecture for elastic conductors that exhibit a combination of high electrical conductivity with low conductive filler (silver) content, robust thermal stability, and high mechanical compliance (strain limit > 100%). The conductive elastomers are made from composites composed of core-shell Ag-coated elastomer microspheres (PDMS@Ag), Ag fillers (Ag flakes, Ag microparticles, and Ag nanoparticles), and an elastic matrix (PDMS). The presence of PDMS@Ag beads improves the electrical conductivity for two reasons. First, Ag fillers that form percolation pathways are sterically confined to regions between adjacent PDMS@Ag beads, resulting in effective phase segregation and a highly localized increase in the density of Ag filler particles. Second, the Ag shells that coat the PDMS microspheres function as additional conductive pathways that connect the percolating networks formed within the surrounding Ag-rich domains. We postulate that the enhanced thermal stability is enabled by the presence of elastomer cores of the PDMS@Ag beads. With PDMS@Ag beads, additional Ag fillers are excluded from the volume that is occupied by the PDMS core of the bead. Thus, microstructural changes due to thermal expansion have less of an impact on percolation pathways in composites containing PDMS@Ag beads relative to those with only Ag fillers. The enhanced thermal stability of PS3 composites relative to composites without PDMS@Ag beads enables soft electronics to be used in high-temperature

environments that arise in manufacturing, materials handling, and cooking. We demonstrated specific examples where the PS3 composite could be used by fabricating a sensorized furnace glove and a soft gripper for use in high-temperature environments. Further efforts could extend this phase-segregated material architecture to other types of polymers, filler particles, and coatings while focusing on niche applications where high-temperature stability, electrical conductivity, and deformability are necessitated.

2.6.5 Lesson Learned

From the four projects introduced in this chapter, we learned that silver is a promising conductive filler to fabricate stretchable conductors. And we can reduce the number of silver particles required to reach the percolation threshold by adding another conductive filler, such as EGaIn, or by introducing microstructural changes to the host elastomers. As examples of composites with multiphase conductive inclusions, we presented AgNP-Ga-In composites, AgInGa-SIS conductive inks, and self-healable Ag-LM-PVA organogels. We also showed PS3 composites made of PDMS, silver-coated PDMS, and silver flakes as an example of composites with heterogeneous material microstructures. We calculated the compositions of the stretchable conductors (AgNP-Ga-In composite, AgInGa-SIS conductive inks, Ag-LM-PVA organogels, and PS3 composites) introduced in this chapter. For the conductive fillers, the final composites contain 21.7, 83.3, 22.5, and 3% by volume, respectively. Based on the volume fraction of each composite, we can conclude that introducing microstructural changes could be more effective than the other method to reach the percolation threshold with a low concentration of conductive inclusions.

From the conclusion of this chapter, we thought that a material with variable components can be a good candidate to realize the microstructural modifications. We came up with the material composition of hydrogels, which is mostly filled with water. The water content in hydrogels can increase through rehydration and decrease if materials are dried. We hypothesized that we can affect microstructures of conductive fillers in hydrogels by controlling the

amount of water.

Chapter 3

Ag-hydrogel: An Electrically Conductive Hydrogel Composite for Soft Electronics

- **Y. Ohm**, C. Pan, M. J. Ford, X. Huang, J. Liao, and C. Majidi, "An electrically conductive silver–polyacrylamide–alginate hydrogel composite for soft electronics," *Nature Electronics*, vol. 4, no. 3, pp. 185-192, 2021.

3.1 Introduction

Soft electronics that exhibit high electrical conductivity and match the compliance of biological tissue are important in the development of wearable computing [106, 107], soft sensors/actuators [35, 108, 109], energy storage/generation devices [110, 111], and stretchable displays [50, 41]. A variety of material architectures have been used to create soft and stretchable electronics, including deterministic (e.g., wavy, serpentine) structures [112, 113], soft microfluidic channels [114, 115], and conductive composites or polymers [89, 84, 77]. However, these conductive materials have intrinsic limitations, such as relatively high Young's modulus ($\gg 1$ MPa in some cases) or limited deformability, and thus are not ideally suited for many emerging applications related to bioelectronic systems (e.g., interfacing with biological tissues). Recently, researchers have demonstrated conductive elastomers with enhanced stretchability and compliance by incorporating microdroplets of liquid metal alloys such as eutectic gallium indium (EGaIn) [14, 21]. In particular, a highly stretchable and conductive polymer composite has been developed using silver and EGaIn particles embedded in an ethylene vinyl acetate copolymer [77]. Although EGaIn-based polymer composites exhibit an encouraging combination of high conductivity, stretchability, and compliance, they require a large volume fraction of metallic filler and their Young's modulus (~ 0.1–1 MPa) is greater than the modulus of soft gels and biological materials (roughly 1–10 kPa), e.g., adipose (body fat) tissue [116]. In this respect, there remains to be a stretchable conductive polymer with enough electrical conductivity to support broad use in electronics combined with a sufficiently low Young's modulus to match the compliance of soft biological tissue.

Hydrogels are a promising candidate for soft electronics since they have similar mechanical properties to a range of biological materials and soft tissues [24, 27], including epidermal skin [60], brain [117], spinal cord [118], and cardiac tissue [119]. Recent research has highlighted various aspects of hydrogels, including their high fracture toughness, tissue-like Young's modulus ($< 10^2$ kPa), high-water content ($> 75\%$), ionic conductivity, bioactivity, and biocompatibility [24, 28]. These properties enable unique applications in bioelectronics [29]
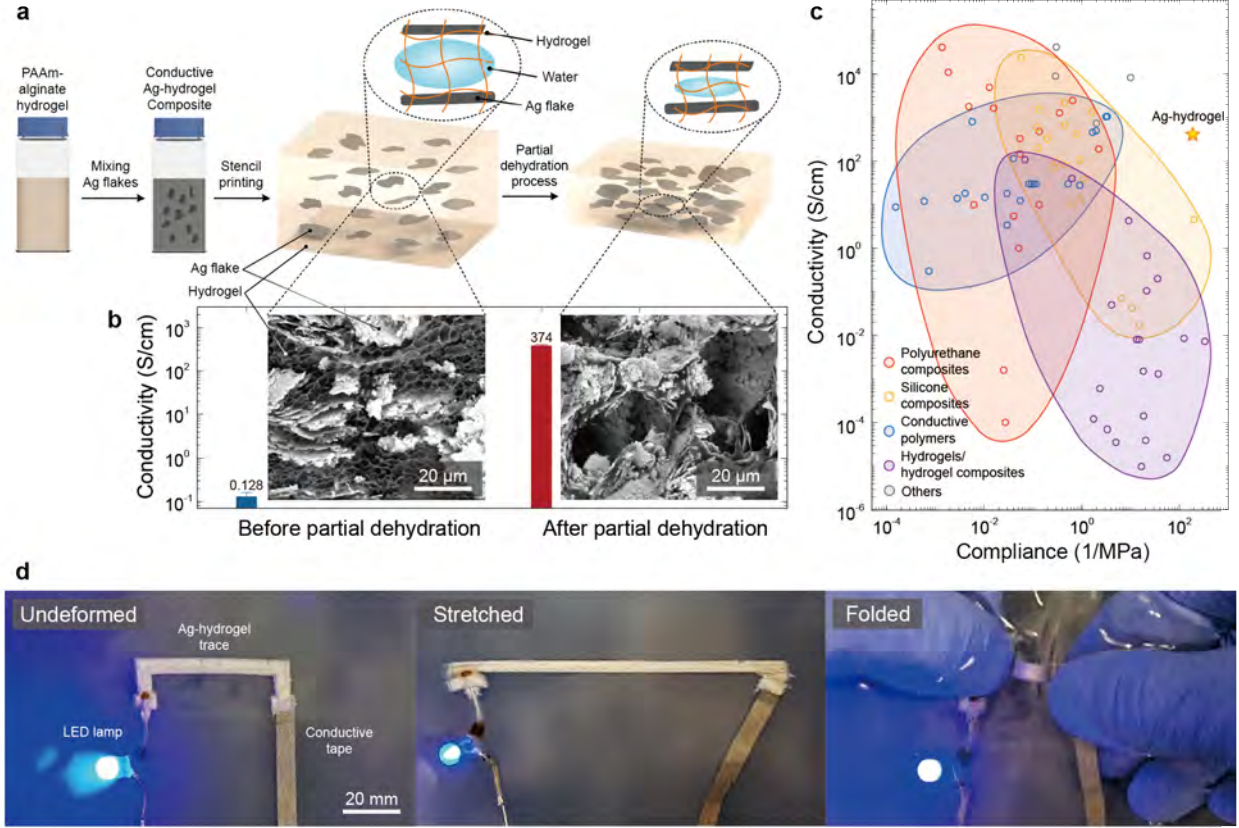
Figure 3.1: Soft, stretchable, and electrically conductive hydrogel composite. **a**, Composition and synthesis of the conductive hydrogel composite composed of micron-scale silver (Ag) flakes and polyacrylamide (PAAm)-alginate hydrogel (Ag-hydrogel). **b**, Conductivity of the Ag-hydrogel composite and micrographs of the composite before and after the controlled partial dehydration process. The error bars are the standard deviation for $N = 3$ samples. **c**, An Ashby-style plot comparing conductivity and compliance of the Ag-hydrogel with other soft conductors. **d**, Undeformed (left), stretched (centre), and folded (right) circuitry made of the stencil-printed Ag-hydrogel to power LED lamp.

and soft robotics [30], including soft-matter sensors [41, 120] and actuators [121]. However, hydrogels have an intrinsic ionic conductivity (10^{-5} to 10^{-1} S cm^{-1}) [122, 123, 124] that is 6–9 orders of magnitude lower than the conductivity of metals), and is inadequate for digital and power electronics [15].

To improve their electrical properties, hydrogel matrices have been filled with conductive materials such as metallic fillers (e.g., nanowires or micro/nanoparticles) [31, 32, 25, 33], carbon-based conductive materials (e.g., carbon nanotubes or graphene) [34, 26], and intrinsically conducting polymers (e.g., PEDOT:PSS or PANI) [35, 15, 36, 37]. These composites demonstrate the potential for engineering hydrogels that are both electrically conductive

($\sim 10^{-5}$–10^1 S cm^{-1}) and have tissue-like mechanical compliance. However, there is a trade-off between improved electrical conductivity and lowered compliance and deformability in these conductive hydrogel composites. For instance, a pure PEDOT:PSS hydrogel [15] has been developed with electrical conductivity (~ 40 S cm^{-1}) but high Young's modulus (~ 2 MPa) and low maximum strain limit ($< 35\%$ strain), while a soft graphene hydrogel [26] has been synthesized with favourable mechanical properties (Young's modulus of 50 kPa) but low electrical conductivity ($\sim 10^{-4}$ S cm^{-1}).

In this chapter, we report a method for creating an electrically conductive hydrogel composite that has high electrical conductivity (374 S cm^{-1}), low Young's modulus (< 10 kPa) that matches soft biomaterials like adipose tissue [116], and high stretchability (250% strain). We use a polyacrylamide (PAAm)-alginate hydrogel that is embedded with a low concentration of silver (Ag) flakes. Electrical conductivity is created via a partial dehydration process [15] in which a moderate portion of water is removed in order to induce percolation and create electrically conductive pathways (Figure 3.1a and 3.1b). Because the composite has a low concentration of metallic filler, it exhibits only modest hysteresis between loading and unloading cycles. The combination of high conductivity, low Young's modulus, high electrical stability, and high stretchability enables the hydrogel composite to occupy a unique place in the design space of electrically conductive soft materials for applications in soft robotics, bioelectronics, and wearable electronics (Figure 3.1c). To highlight potential applications of this soft conductor, we demonstrated a LED circuitry that shows high mechanical compliance (Figure 3.1d), a stingray-inspired soft swimmer where the shape-memory alloy (SMA) muscle was actuated with power transmitted through the conductive hydrogel composite, and a neuromuscular electrical stimulation electrode that can successfully deliver high frequency electrical signals generated by a commercial stimulator.

3.2 Ag-hydrogel Composite

The highly conductive hydrogel composite was fabricated by controlling assembly and percolation of silver (Ag) flakes within a polyacrylamide (PAAm)-alginate hydrogel matrix. Ag flakes were utilized since silver has high electrical conductivity and the high aspect ratio of the flakes permits morphologies that allow for greater electrical conductivity compared to networks of other conductive particles with similar volume concentration. The key step in achieving high electrical conductivity is to perform a partial dehydration of the hydrogel matrix, which enables the Ag flakes to form percolation pathways that remain stable when the composite is stretched or rehydrated (Figure 3.1a). The composition and synthesis of the PAAm-alginate gel matrix was adopted from previous work by Sun et al. [125]. However, for our system, we did not replace the sodium ion (Na^+) of the alginate with other multivalent cations, such as calcium ion (Ca^{2+}) as had been previously done. Although the material isn't ionically crosslinked by multivalent cations, it shows enhanced stretchability and toughness through the formation of a double-network hydrogel matrix enabled by mechanical and chemical interactions between two hydrogel matrices [125, 126].

After stencil printing (Figure 3.2) and before performing the partial dehydration, the Ag-hydrogel is ionically conductive with a low conductivity (~ 0.13 S cm^{-1}). At this stage of
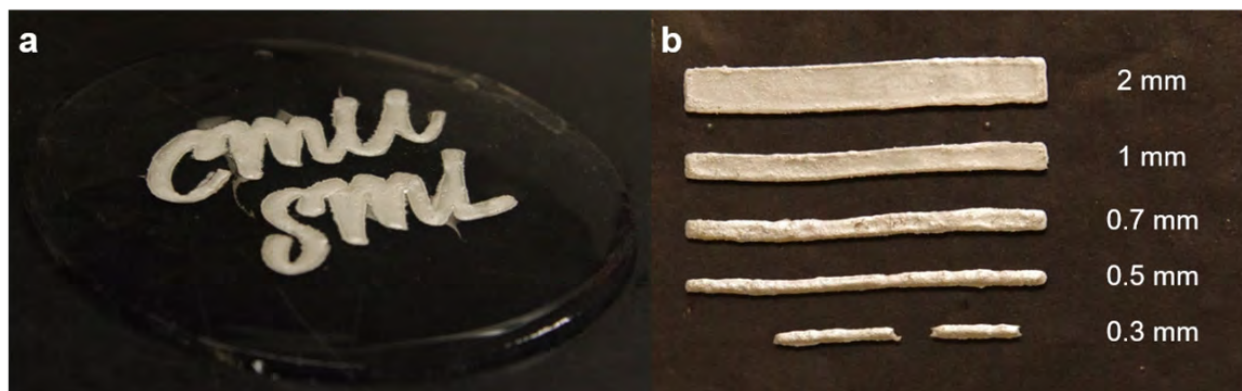
Figure 3.2: Printability. **a**, Ag-PAAm-alginate hydrogel "CMU SML" in cursive fonts printed by using stencil method. **b**, Printing resolution of current stencil printing method using the conductive Ag-hydrogel composite.

the fabrication process, the volume fraction of the Ag filler (5 vol%) is insufficient for percolation. The reason for using such a low volume fraction of Ag flakes instead of adding enough Ag fillers to exceed percolation threshold is that the presence of a large amount of Ag will suppress the double crosslinking process of the hydrogel matrix. As observed in cross-section images taken by scanning electron microscopy (SEM), adjacent Ag flakes are separated by the surrounding hydrogel matrix and don't form a connected network (Figure 3.1b left inset). Given that the hydrogel matrix is composed of a hydrophilic polymer network with ∼ 90 vol% of water, partial dehydration reduces the water content and allows for the formation of a percolating network of Ag flakes (Figure 3.1b right inset and 3.3). Concomitantly, we
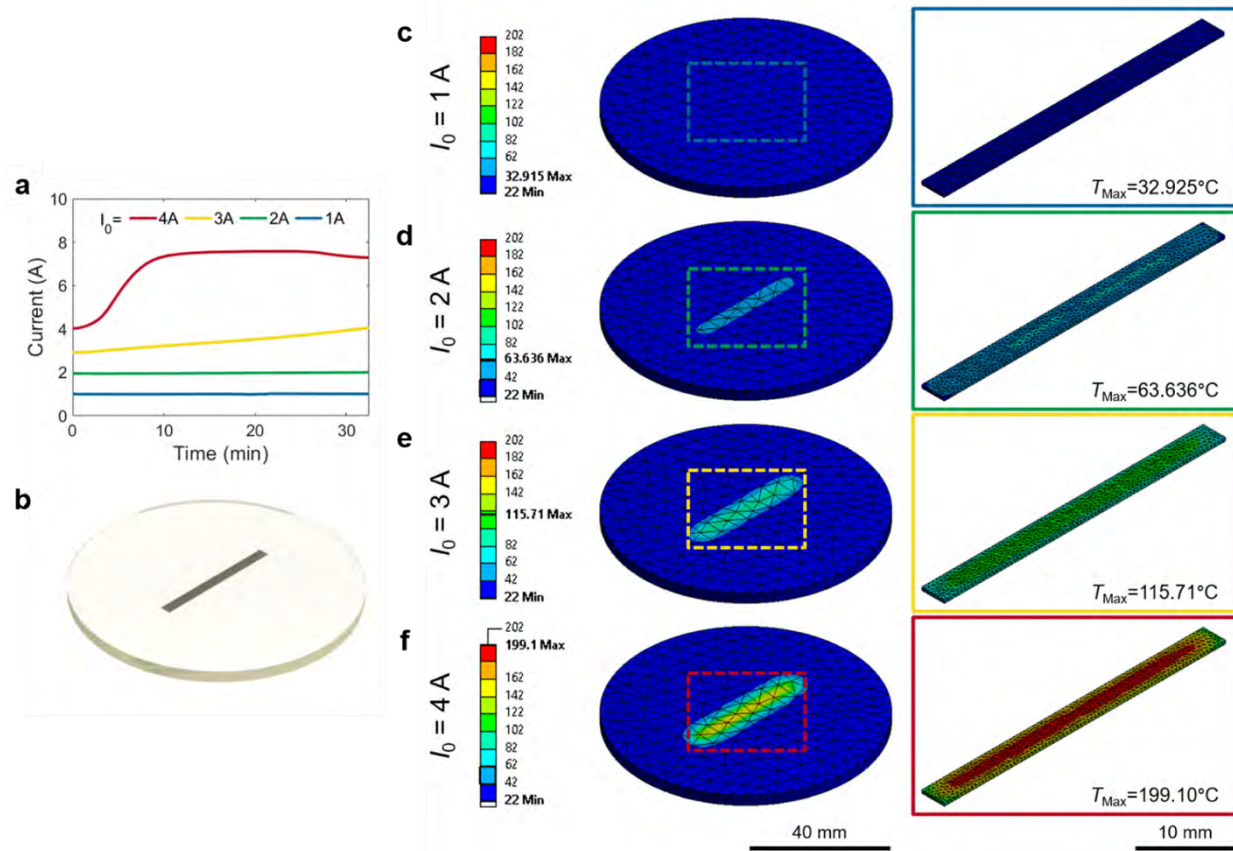
Figure 3.3: Frozen-SEM images of Ag-hydrogel before and after partial dehydration process. **a–b**, SEM images of freeze-dried PAAm-alginate hydrogel. **c–d**, SEM images of freeze-dried Ag-hydrogel composite before partial dehydration process. **e–f**, SEM images of freeze-dried Ag-hydrogel composite after partial dehydration process. The Ag flakes and hydrogel matrix are labelled in **d**. A blue line has been drawn in **d** and **f** to indicate possible percolation pathways for Ag flakes before and after rehydration. Note that before dehydration, percolation pathways do not exist.

observed that the electrical conductivity of the composite increased from 0.128 S cm^{-1} to 374 S cm^{-1} after dehydration (Figure 3.1b). The partial dehydration process enables the hydrogel composite to achieve high electrical conductivity, while maintaining tissue-like mechanical properties, i.e., low Young's modulus and high stretchability (Figure 3.1c).

3.2.1 Percolation and Conductivity

We measured electrical resistance changes of the Ag-hydrogel composites with different amounts of Ag content in-situ during the partial dehydration to better understand the effect of drying (Figure 3.4a and 3.5). The Ag-hydrogel composite specimens (40 mm $\times$ 3 mm $\times$ 0.7 mm) were stencil-printed on a PAAm-alginate hydrogel substrate using a polydimethylsiloxane (PDMS) mask (Sylgard 184; Dow Corning). Figure 3.4a shows the evolution in resistance as a function of partial drying time and the volumetric conductivity of the composites at 0 min and 90 min for the specimen with Ag content of 5 vol%. Initially, the resistance was on the order of kiloohms, with a corresponding conductivity of 0.128 $\pm$ 0.0348 S cm^{-1} for $N = 3$ samples, which indicates no electrical conductivity but ionic conductivity as the value of conductivity was more similar to an unfilled hydrogel [127]. The resistance of the Ag-hydrogel decreased exponentially after 10–15 minutes of drying, as electrically conductive paths began to form (Figure 3.3). As we described previously, Ag flakes do not initially form conductive pathways due to the high initial water content. The evaporation of water in the hydrogel matrix may facilitate intimate contact and adhesion between adjacent Ag flakes aggregates, thereby allowing for the formation of electrically conductive pathways. After exceeding the percolation threshold, the electrical conductivity reaches a saturation plateau. At this stage, the resistance is decreased to 1.14 $\pm$ 0.359 Ω after 90 minutes, and the corresponding volumetric conductivity reaches 374 $\pm$ 30.8 S cm^{-1} for $N = 3$ samples. Higher volumetric Ag content after partial dehydration was observed as the cross-section area of the specimen decreased from 1.76 mm^2 to 1.38 mm^2 after 90 minutes of drying (Figure 3.5b), which corresponds to an increase in the effective Ag content from 5.00 vol% to 6.07 vol%
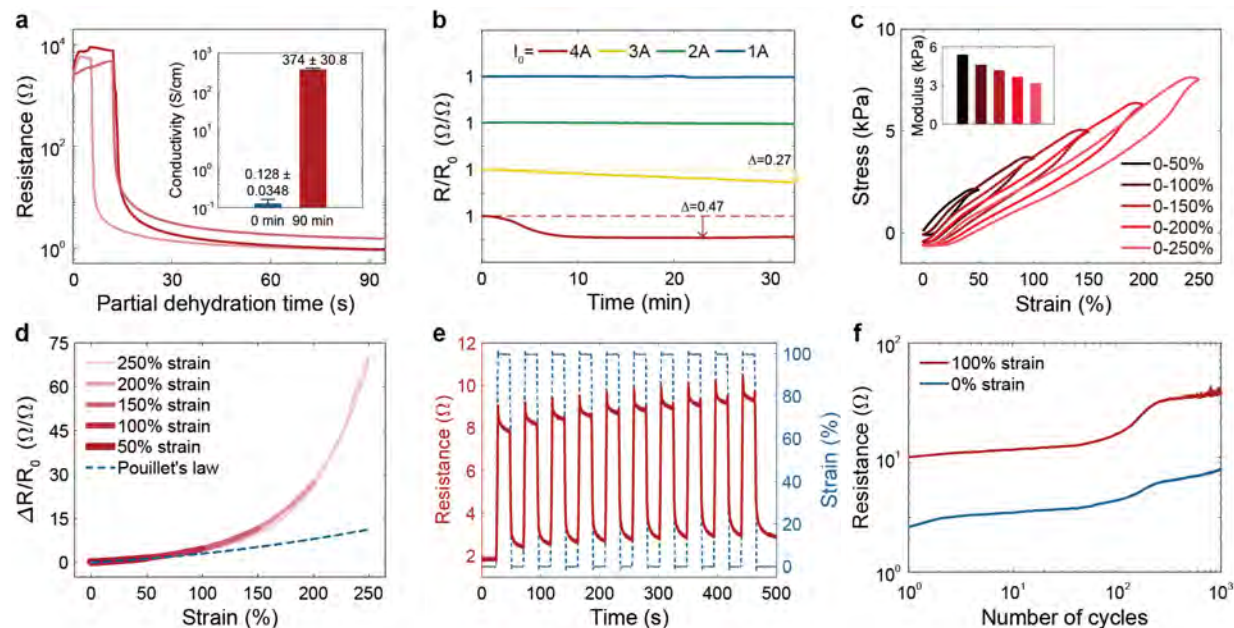
Figure 3.4: Material characterization. **a**, Absolute change in resistance as a function of time for partial dehydration process and (inset) the volumetric conductivity at 0 min and 90 min. The error bars are the standard deviation for $N = 3$ samples. This is for a composite with an initial Ag content of 5 vol%; plots for composites with other initial volume fractions are presented in Figure 3.5. **b**, Normalized change in resistance as a function of time with different initial currents and corresponding constant voltages; note, the y-axis offset is applied to each curve to assist in visualization of the data. Here, Δ is defined as the change in R/R_0 compared to its inital value of 1. **c**, Stress versus strain of the conductive hydrogel composite under different uniaxial loading conditions from 0% to 50%, 100%, 150%, 200%, and 250% strain, and effective elastic moduli as a function of loading condition (inset). **d**, Normalized change in resistance as a function of strain (gradient of red solid lines) along with the theoretical prediction using Pouillet's law for an incompressible elastomer with constant volumetric resistivity (dashed blue line). **e**, Electromechanical response as a function of time under uniaxial cyclic loading to 100% strain up to the first 10 cycles. For each cycle, the sample was stretched at 10 mm s^{-1}, held for 20 seconds, released at 10 mm s^{-1}, and held for 20 seconds. **f**, Cycling stability of the resistance under uniaxial cyclic loading to 100% strain up to 1,000 cycles. The sample was stretched and released at the speed of 10 mm s^{-1}.

and a decrease in the effective water content from 81.9 vol% to 78.1 vol%. Similar trends in resistance during the partial dehydration step were observed for Ag-hydrogel composites with different Ag contents (Figure 3.5c–f). As the initial Ag content increased, the exponential decrease in resistance occurred more quickly, demonstrating the effect of drying on the electrical conductivity.

Importantly, the percolation network appears to be permanently formed as a result of the dehydration step. When the resistance was recorded in an aqueous environment
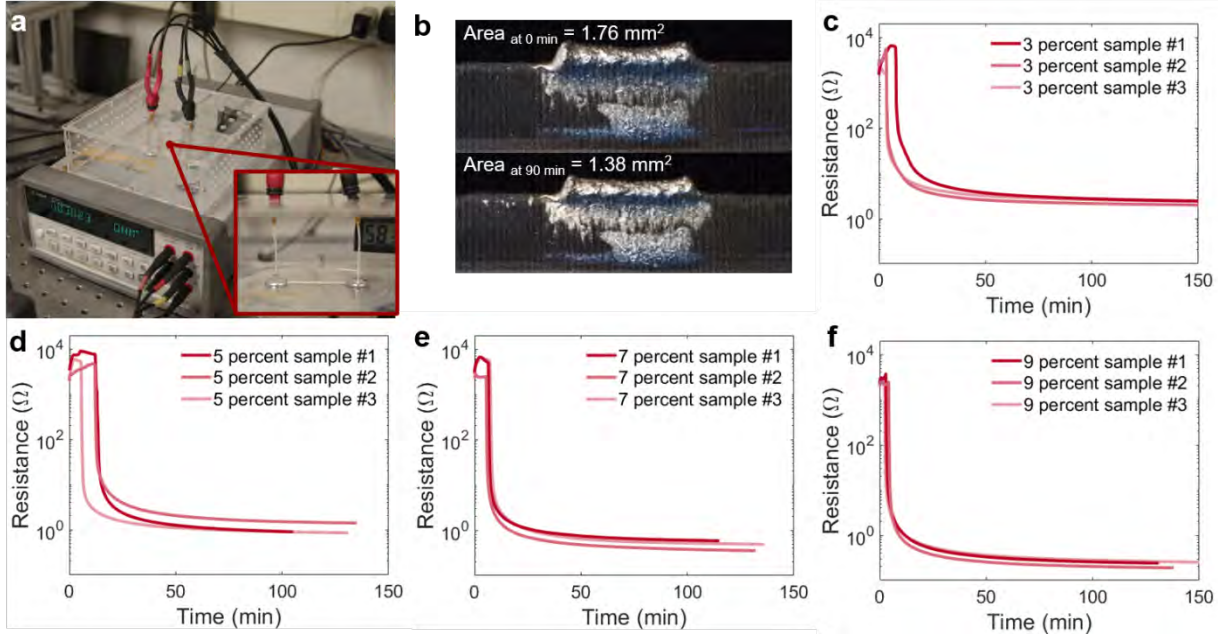
Figure 3.5: Partial dehydration process. **a**, Experimental setup of partial dehydration process measuring resistance change over drying time, which includes an acrylic box with an environmental monitor and a multimeter. An acrylic box was designed to minimize the effect of random air flow around the Ag-hydrogel for controlling the humidity and evaporation rate. These tests were conducted in a lab room with an air conditioner that sets the room temperature around 22 °C. **b**, A representative cross-sectional area change of the printed Ag-hydrogel during partial dehydration process. **c–f**, Resistance as a function of partial dehydration time for the Ag-hydrogel composites filled with different amount of Ag flakes. **c**, 3 vol%. **d**, 5 vol%. **e**, 7 vol%. **f**, 9 vol%. Each curve in **c–f** corresponds to a different sample.

where it could rehydrate (Figure 3.6), the Ag-hydrogel composite maintained high electrical conductivity. The resistance was observed to increase after three days in water due to
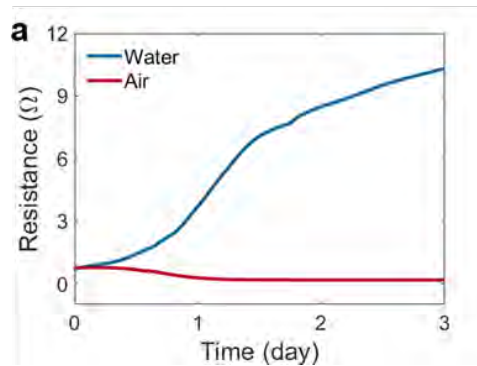
Figure 3.6: Environmental stability test. **a**, Resistance of a conductive hydrogel trace as a function of time under long-term exposure to ambient air (blue) and water (air) environment.

57
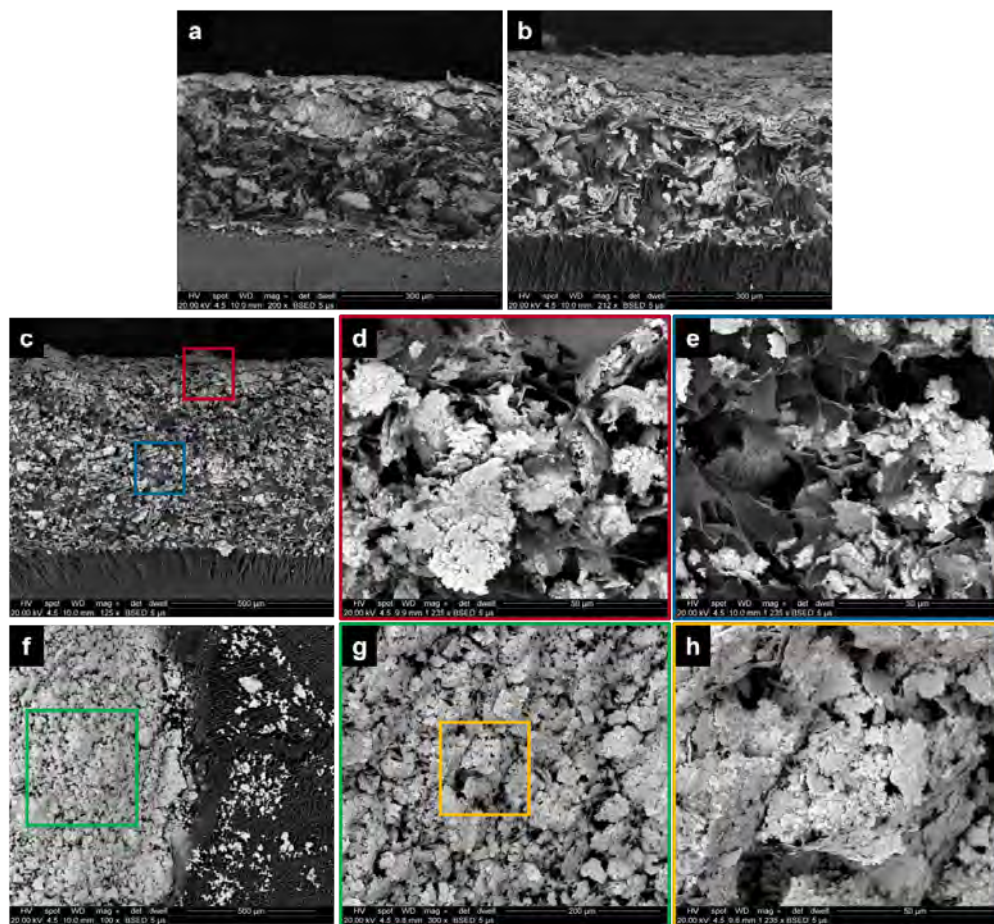
Figure 3.7: Frozen-SEM images of the rehydrated Ag-hydrogel. **a**, SEM image of freeze-dried Ag-hydrogel composite before rehydration. **b**, SEM image of a sample after 1.5 hours of rehydration. **c**–**h**, SEM images of a sample after 3 days of rehydration. **c**–**e**, SEM images of cross-section of the rehydrated Ag-hydrogel whose top part is shown in **d** and centre part is shown in **e**. **f**–**h**, SEM images of the rehydrated Ag-hydrogel from top view which is close to the edge of the trace. The image is magnified in **g** and **h**.

swelling of the hydrogel matrix. However, the percolating network remained largely intact and the absolute resistance was on the same order of magnitude as prior to rehydration. The absorbed water imposed capillary force that disrupted weak conductive pathways of Ag flakes. However, the main percolating network remained due to the comparatively stronger adhesion between contacting flakes (Appendix C.2). In this way, the material was still able to show high electrical conductivity even after being submerged in an aqueous environment for three days (Figure 3.6 and 3.7). The results could be compared to an Ag-hydrogel composite that was left in ambient air after partial dehydration, where the resistance decreased slightly

(Figure 3.6). These results highlight the importance of controlled assembly by dehydration to fabricate the soft conductor.

3.2.2 Response to Direct Current

High electrical conductivity enables the Ag-hydrogel composite to deliver high direct current at low voltages. We first applied a constant voltage and monitored direct current over time for a printed Ag-hydrogel trace which became electrically conductive after the partial
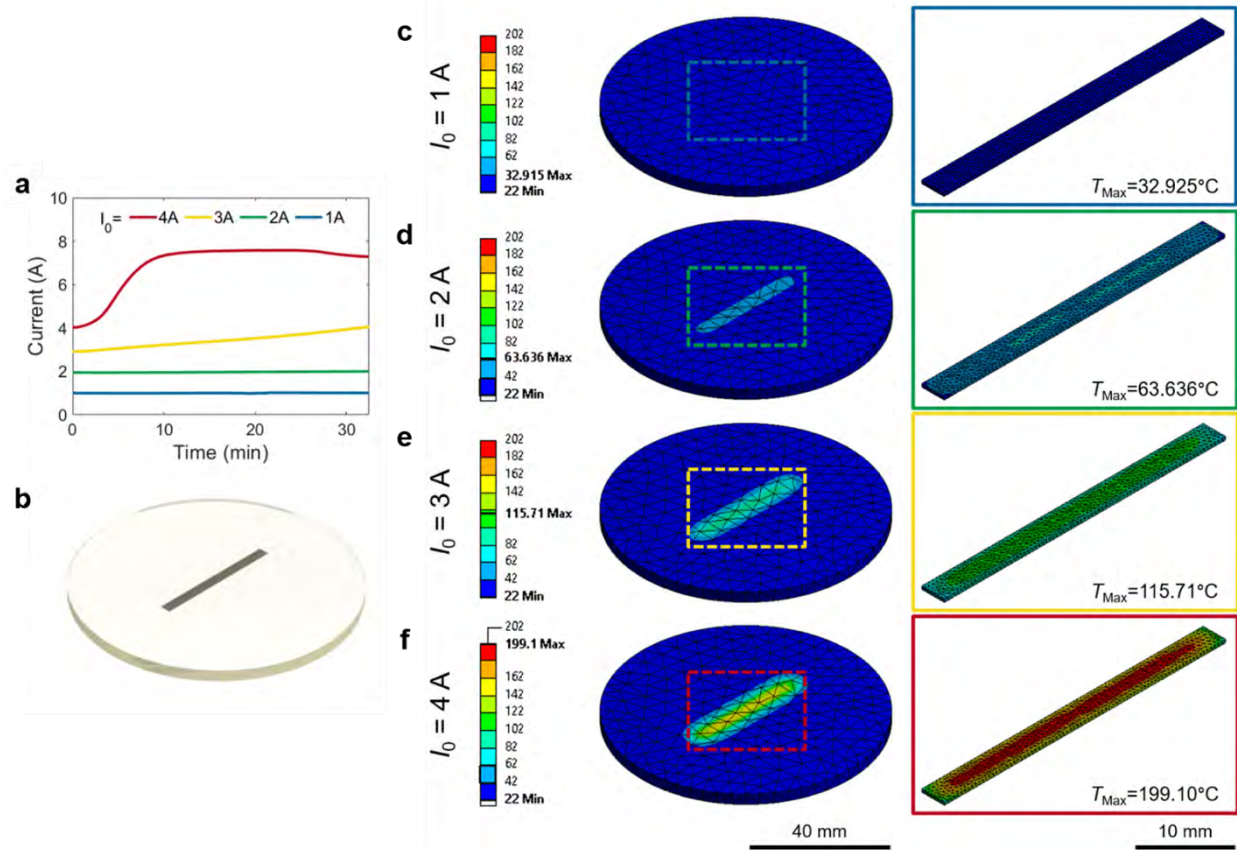
Figure 3.8: Response to direct current generated by fixed voltage and results of simulation of Joule heating. **a**, Current evolution as a function of time with different initial currents and corresponding constant voltages. This data was used to calculate the normalized resistance change shown in Figure 3.4b. **b**, 3D model of sample created by SOLIDWORKS (Dessault Systèmes) for simulation. The geometry of Ag-hydrogel trace is 40 mm × 3 mm × 0.7 mm. The Ag-hydrogel is encapsulated between two layers of PAAm-alginate hydrogel with diameter of 83 mm and thickness of 1.6 mm. The voltage was applied at the end of the trace. **c–f**, Results of Joule heating on the trace using a commercial steady-state thermal solver (2020 R1, Ansys Thermal-Electric toolbox). The unit of temperature is Celsius. **c**, Initial current (I_0) = 1 A. **d**, I_0 = 2 A. **e**, I_0 = 3 A. **f**, I_0 = 4 A.
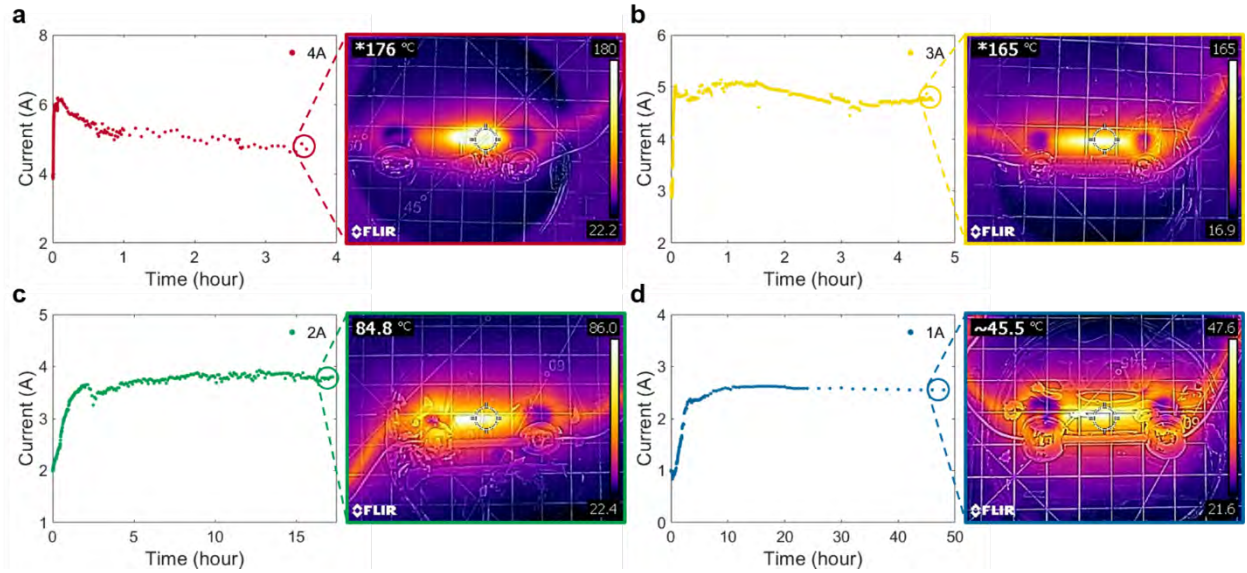
Figure 3.9: Long-term response to direct current in air. **a–d**, Current evolution as a function of time for Ag-hydrogel composites subjected to a long-term electrical power along with IR images near the end of each experiment. For the cases of electrical power with an initial current of 4 A (**a**) and 3 A (**b**), the IR images were taken right before the samples' electrical breakdown. For the case of 2 A (**c**), the IR image was taken when the current started to drop from the steady state. **a**. Initial current = 4 A and an IR image was taken in 3.5 hours. **b**. Initial current = 3 A and an IR image was taken in 4.5 hours. **c**. Initial current = 2 A and an IR image was taken in 17 hours. **d**. Initial current = 1 A and an IR image was taken in 48 hours.

dehydration process (Figure 3.8a). Voltages were applied to give initial current values (I_0) of 1, 2, 3, and 4 A, and the corresponding normalized resistance was also monitored over time (Figure 3.4b). For lower currents (I_0 = 1 or 2 A), the resistance profiles are stable, which demonstrates the electrical stability of the Ag-hydrogel. The resistance gradually decreased when subjected to an initial current of 3 A. When initial direct current of 4 A was applied, we observed a substantial decrease of resistance within 10 minutes. The decreased resistance saturated at the end of the test. We attribute this resistance decrease to further evaporation of water (beyond the intentional partial dehydration) between adjacent Ag flakes as the composite was heated by Joule heating at high current.

Finite element analysis (FEA) of Joule heating at steady-state and the long-term response to high current were compared. The results of simulation (Figure 3.8c-f) and long-term response to high current (Figure 3.9) show that the maximum temperature exceeds the
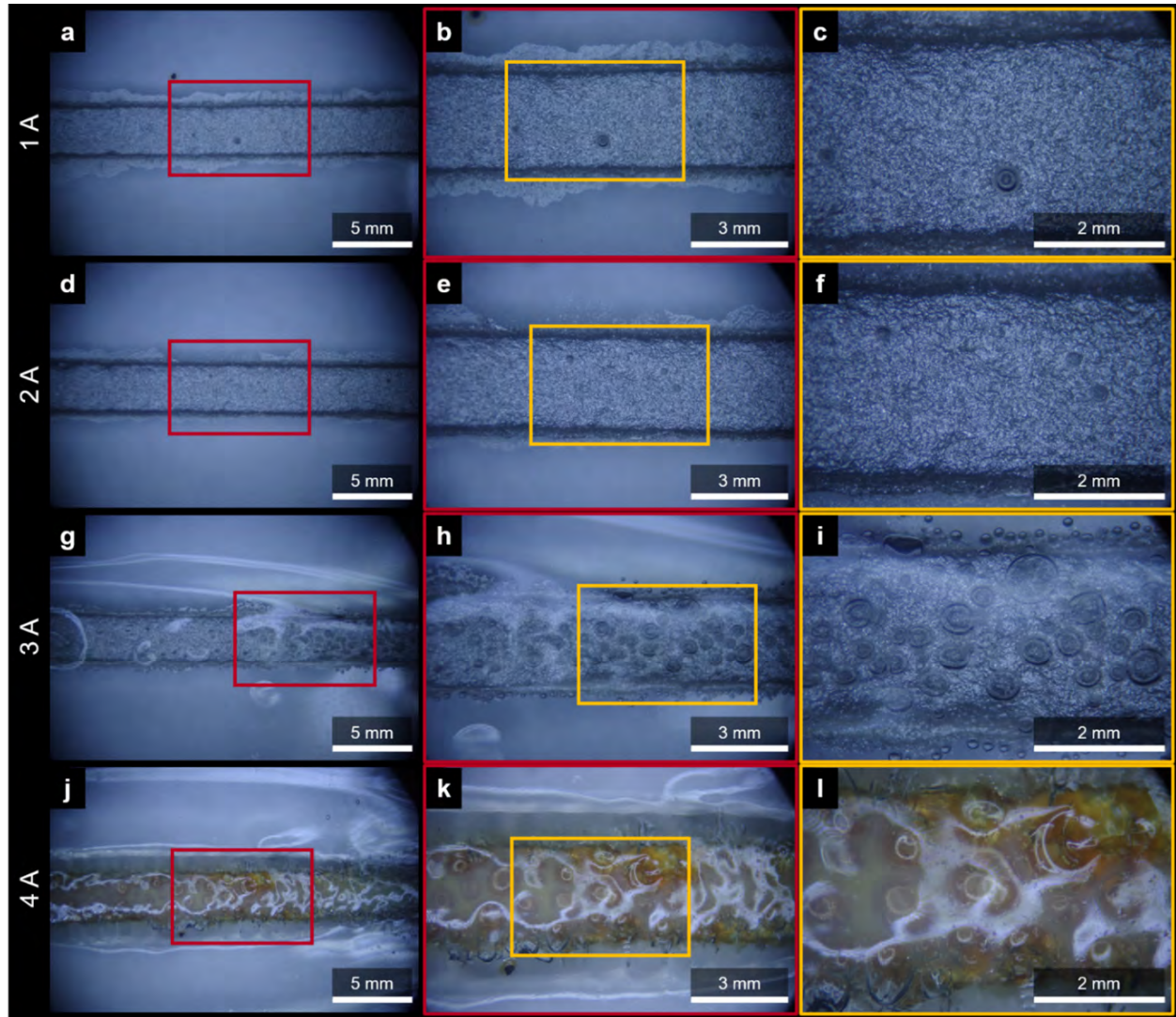
Figure 3.10: Micrographs of the traces of Ag-hydrogel composites after 30 minutes of Joule heating. **a–c**, Initial current (I_0) = 1 A. **d–e**, I_0 = 2 A, **g–i**, I_0 = 3 A, j-l, I_0 = 4 A. The localized high temperature at 4A results in the discoloration of hydrogel near Ag-hydrogel trace.

boiling point of water (100 °C) when the composite is subjected to an electrical power with an initial current of 3 A and 4 A. This localized high temperature produces bubbles (Figure 3.10g-l) near the Ag-hydrogel trace and can result in thermal degradation of the hydrogel at 4 A (i.e., the discoloration of the hydrogel as shown in Figure 3.10j-l). In contrast, Ag-hydrogel traces subjected to lower electrical currents (I_0 = 1 and 2 A) retain their original appearance (e.g., minimal bubbles and no discoloration) due to the lower localized temperature (< 100 °C, Figure 3.8c-d and 3.9c-d). We further investigated the long-term response of the Ag-hydrogel
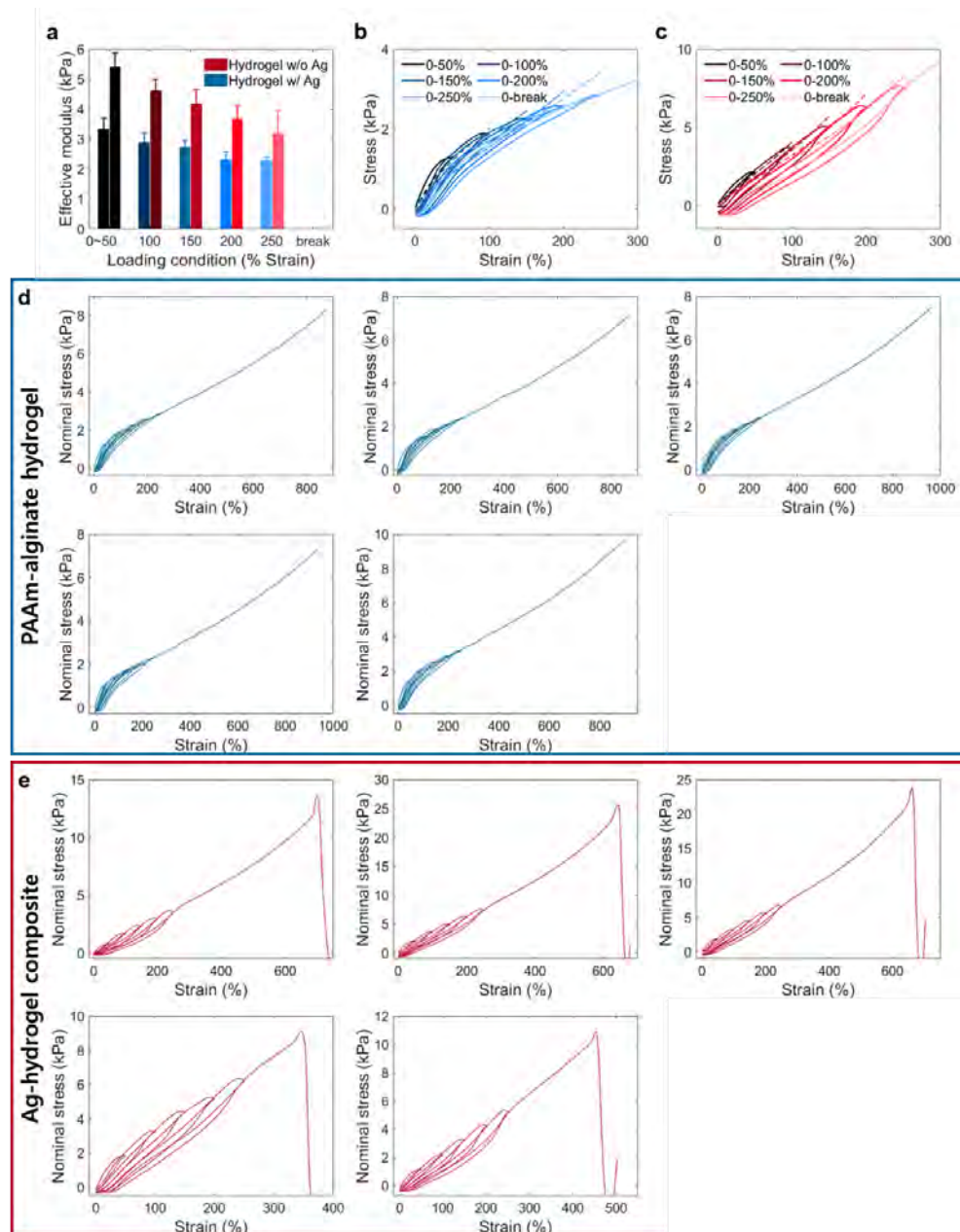
Figure 3.11: Mechanical characterization. **a**, Effective elastic modulus comparison between PAAm-alginate hydrogel and Ag-hydrogel composite as a function of loading condition. **b**, A representative plot of stress versus strain of the PAAm-alginate hydrogel under different uniaxial loading conditions from 0% to 50%, 100%, 150%, 200%, and 250% strain. **c**, A representative plot of stress versus strain of the Ag-hydrogel under different uniaxial loading conditions from 0% to 50%, 100%, 150%, 200%, and 250% strain. The dotted lines in **b** and **c** are a statistical fit (R-squared = 0.95) of data to a 2-parameter Ogden solid model [128]. **d**–**e**, Plots of stress versus strain of samples under the same cyclic loadings of **a**. The samples were prepared as free-standing samples. **d**, PAAm-alginate hydrogels. **e**, Ag-hydrogel composites.

composite to direct current while underwater. The results in Appendix C.3 show that the Ag-hydrogel can maintain high electrical conductivity in an aqueous environment during long-term usage. These results demonstrate the potential of the Ag-hydrogel composite as a power line for applications in digital electronics that require high direct current and can retain functionality in various environments.

3.2.3   Mechanical Properties

To be mechanically compatible with soft biological tissue, the Ag-hydrogel composite must be highly compliant and deformable. The stress-strain characteristics were evaluated using an Instron 5969 materials testing machine (Figure 3.4c). We calculated the effective elastic modulus (Figure 3.4c inset) by adopting the hyperelastic constitutive model C.1 for a 2-parameter Ogden solid [128] and performing a statistical fit ($R^2 = 0.95$). The 5 vol% Ag-hydrogel composite has a modulus of 5–6 kPa after performing partial dehydration (Figure 3.11), while the unfilled PAAm-alginate hydrogel's modulus is about 3–4 kPa. As observed with other conductive composites [21, 127], the introduction of metallic fillers into the soft matrix typically results in a composite with increased Young's modulus relative to the unfilled matrix. However, since the Ag content is kept low by controlling assembly through partial dehydration, the Ag-hydrogel composite has tissue-like softness and minimal hysteresis between mechanical loading and unloading.

3.2.4   Electromechanical Properties

Conductors that interface with biological tissues typically undergo complex and repetitive deformations and so it is crucial to understand the electromechanical coupling of the soft conductor. Electromechanical coupling of the Ag-hydrogel was measured by monitoring the change in resistance of a stencil-printed composite trace as a function of uniaxial strain. The printed composite was encapsulated with another layer of PAAm-alginate hydrogel after the partial dehydration to prevent further dehydration. We first examined changes in electrical
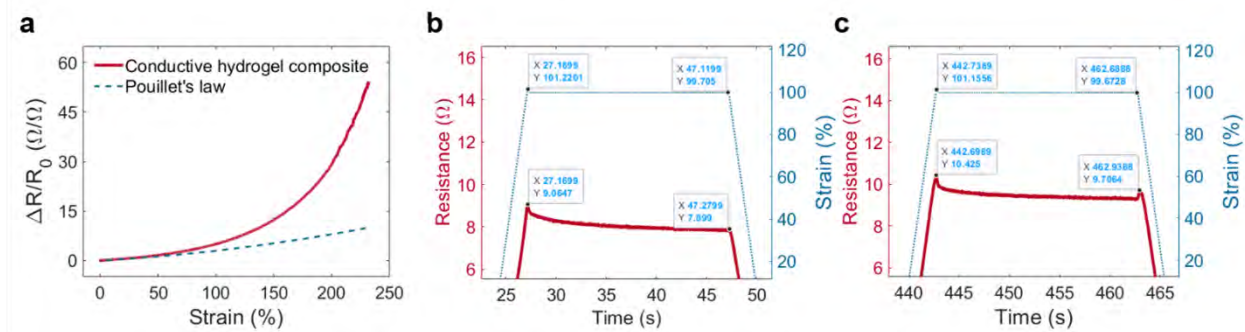
Figure 3.12: Electromechanical characterization. **a**, Normalized resistance change as a function of strain up to the electrical breakage of conductive hydrogel trace (Mechanically, the sample can stretch more). **b**, Magnified plot at 1st cycle of Figure 3.4e. **c**, Magnified plot at 10th cycle of Figure 3.4e.

resistance while subsequently imposing different tensile strains ($\epsilon = 50, 100, 150, 200$, and 250%; Figure 3.4d). The Ag-hydrogel was first stretched by 50% strain and then relaxed to its original length, and the strain was increased by 50% up to 250% for each successive cycle. The stretching and releasing curves overlapped, highlighting negligible hysteresis in resistance under different mechanical loading conditions. Since the conductive hydrogel composite shows small mechanical hysteresis, the resistance of the composite also shows small changes under cyclic loadings (Figure 3.12). In addition, the resistance change at small strain ($0 \sim 100\%$) agrees well with Pouillet's law [129], i.e., $\Delta R/R_0 = (1+\epsilon)^2 - 1$, where ϵ is strain, R is resistance, and R_0 is the initial resistance at small strain ($0 \sim 100\%$). Moreover, these tests demonstrate that the Ag-hydrogel is highly stretchable while maintaining electrical conductivity at strains up to 250%.

Importantly, the composite should be electromechanically robust to multiple strain cycles. Through multiple strain cycles between 0% and 100% strain, the resistance of the Ag-hydrogel remains low enough for practical purposes, such as digital circuit functionality or bioelectronics (Figure 3.4e). Through 10 cycles, the resistance remained relatively constant, with less than $1\ \Omega$ change in the relaxed state. When stretched, the electromechanical response was fast, changing according to the mechanical deformation within 0.1 seconds (Figure 3.12b-c). While being held right after stretching for 20 seconds, the resistance exponentially drops at first and the changes in resistance are about $1.2\ \Omega$ which are consistent

throughout the 10 cycles. These experiments illustrate the desirable electromechanical features of the Ag-hydrogel, which include fast electrical response (20 ~ 40 ms when stretched and 160 ~ 250 ms when released) to external mechanical stimuli and a robust percolating network for repeatable and consistent elastic response.

To validate long-term use, the Ag-hydrogel was also characterized for 1,000 cycles of tensile loading between 0% and 100% strain (Figure 3.4f). The resistance at 0% and 100% strain was bounded within stable boundaries for the first one hundred cycles, then slightly increased from 2.5 Ω to 4.2 Ω at 0% strain and from 10 Ω to 16 Ω at 100% strain. For subsequent loading cycles, the resistance of the conductive hydrogel composite at 100% strain was observed to increase and then fluctuate when approaching 1,000 cycles. The reason for this fluctuation was that the experiment was conducted in air with a relatively rapid speed of 10 mm s^{-1}, which led the sample to become drier and stiffer over the duration of the experiment (> 100 minutes). This could be avoided by performing the experiment in a humid environment. Nonetheless, the results of electromechanical characterization demonstrate the composite's high conductivity, low electromechanical hysteresis, and repeatable electrical response to mechanical deformation.

3.3 Stingray-Inspired Soft Swimmer

The tissue-like compliance and deformability of the Ag-hydrogel composite—along with its electrical conductivity—permit its use as a soft conductive material in soft robotics. To demonstrate its potential in soft robotics, we fabricated a stingray-inspired soft swimmer that was composed of a pair of hydrogel pectoral fins and a streamlined backbone made with a soft foam. Two sets of Ag-hydrogel traces formed compatible interfaces with the hydrogel pectoral fins. The soft and conductive traces served as power lines to deliver high current (~ 3.3 A) from a benchtop power supply (KPS3010D, Eventek) to a pair of shape memory alloy (SMA) actuators without interfering with the natural deformability and compliance
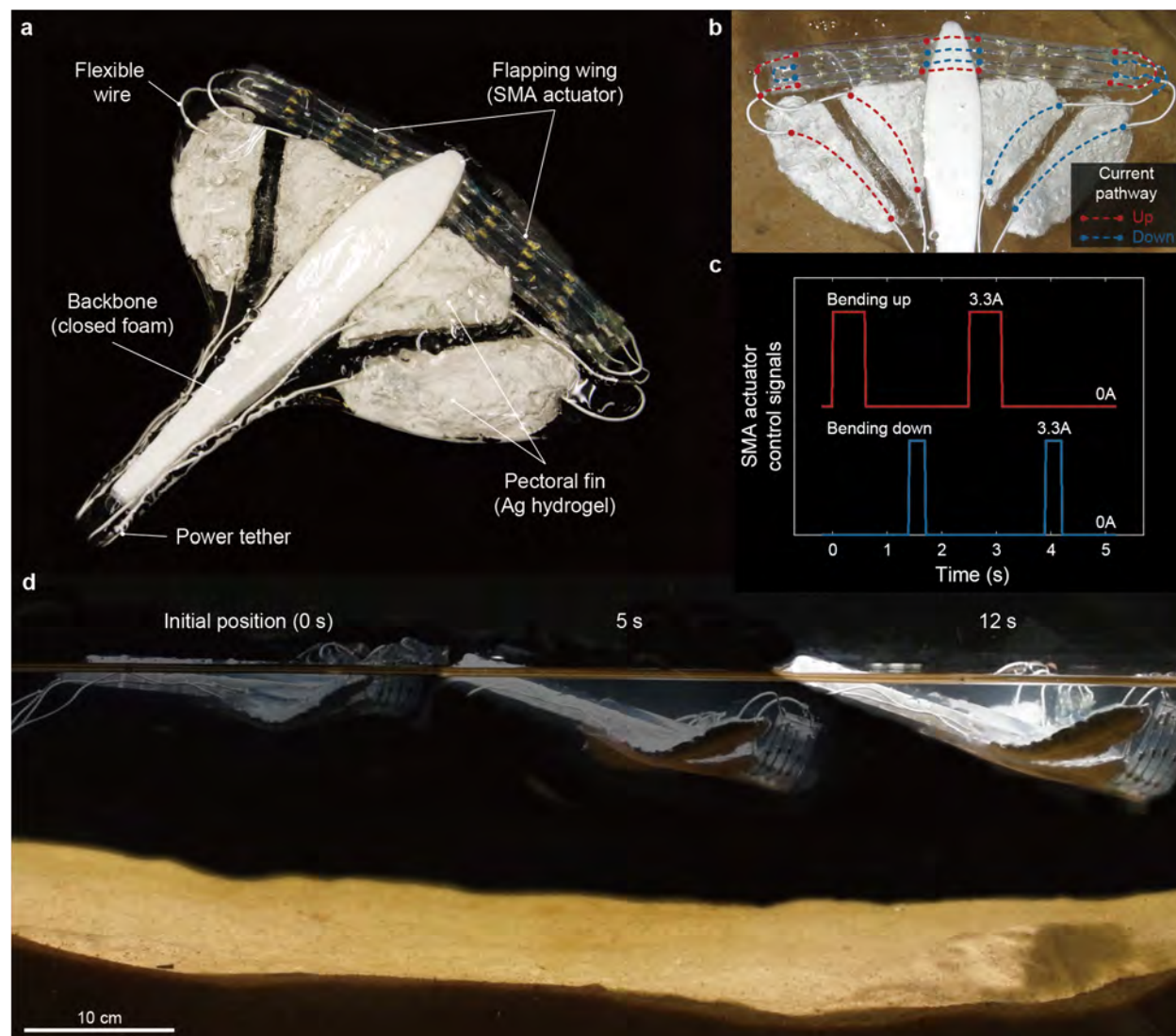
Figure 3.13: Stingray-inspired soft swimmer. **a**, A soft stingray-inspired swimmer with the conductive hydrogel composite. The soft swimmer is propelled by shape-memory alloy (SMA) wires, which require high current (3.3 A) to be actuated and are connected to the tethered power through the conductive hydrogel composite. **b**, Schematic of high-current signal routing, connecting the SMA wires and the power; the trace is color-coded with reference to **c**. **c**, Actuation sequence and required current for the soft swimmer. **d**, Sequential images of the soft swimmer from the side view.

of the hydrogel pectoral fin (Figure 3.13a). The soft actuators were composed of two SMA wires sandwiched by three layers of VHB tapes (4905, 3M), which enabled the actuators to bend upward and downward alternatively through direct Joule heating [130]. To induce a forward swimming motion, the top pair of SMA wires were activated for 0.6 seconds and then cooled for 1.9 seconds while the other pair were activated and cooled for 0.3 and 2.2

seconds, respectively (Figure 3.13b and 3.13c). Referring to Figure 3.13c, the upward and downward actuation cycles were staggered with a 0.9 second offset period. The stingray-inspired swimmer is capable of swimming at an average speed of 0.2 body lengths per second (40 mm s^{-1}) (Figure 3.13d). This demonstration highlights the electrical conductivity and stability of the Ag-hydrogel by carrying high currents (3.3 A) to activate the embedded SMA actuators.

3.4   Neuromuscular Electrical Stimulation Electrode

The soft and highly conductive Ag-hydrogel composite also has the potential to broaden the utilization of hydrogels as electrodes in the field of epidermal electrical stimulation
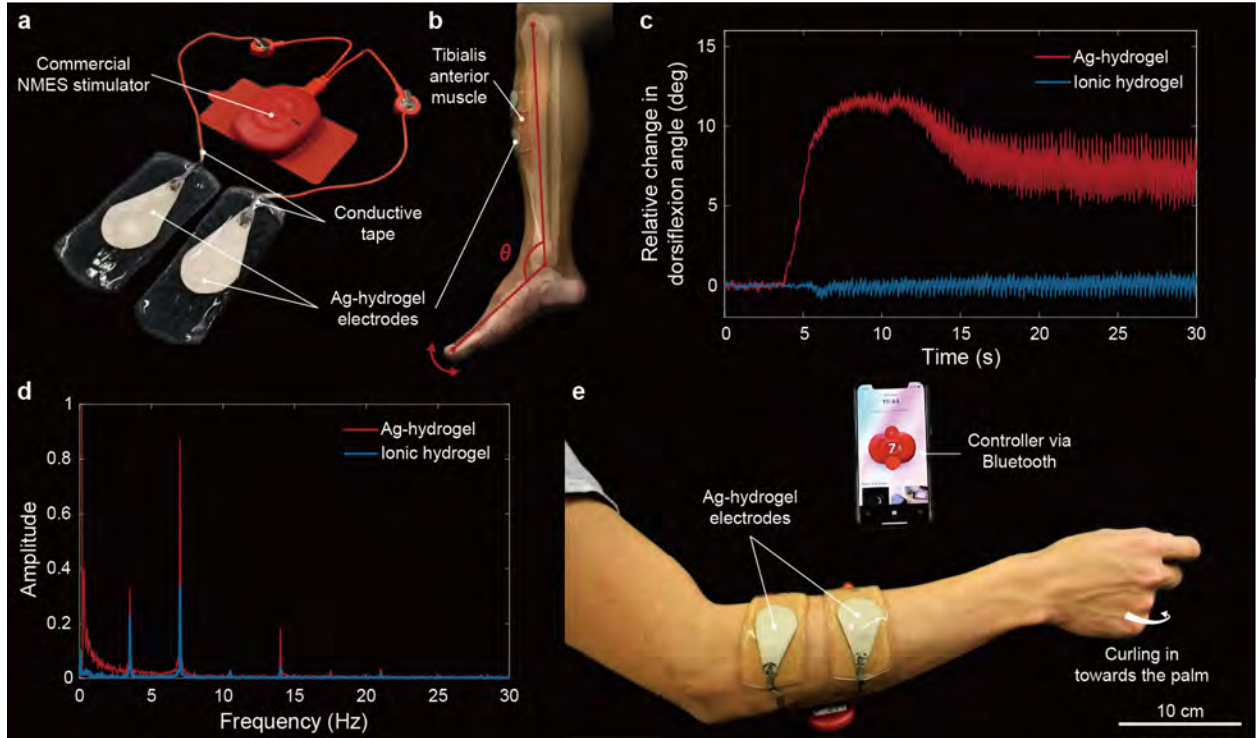
Figure 3.14: Neuromuscular electrical stimulation (NMES) electrode. **a**, NMES electrodes made of the Ag-hydrogel composite are assembled with a commercial electrical muscle stimulator. **b**, The electrodes are placed on the tibialis anterior muscle of the subject's leg to cause dorsiflexion. The red lines are used to track the relative change of the angle (θ) which is measured in **c**. **c**, Relative change in dorsiflexion angle as a function of stimulation time. **d**, Amplitude as a function of frequency, which is the result of fast Fourier Transform (FFT). **e**, The electrodes are placed on the arm and delivering electrical signals from the stimulator to the muscles in the posterior of the forearm.

67

and recording, which requires electrodes with adequate electrical conductivity [27, 131]. Here, we fabricated Ag-hydrogel electrodes to deliver high frequency electrical signals for neuromuscular electrical stimulation (NMES) [132] to demonstrate the enabling bioelectronic properties of the composite. As shown in Figure 3.14a, a pair of Ag-hydrogel electrodes is connected to a commercial electrical muscle stimulator (PowerDot 2.0 Uno, PowerDot), where the strength and frequency of the pulses are controllable using a smartphone via Bluetooth.

Figure 3.15: Neuromuscular electrical stimulation electrodes. **a**, The NMES electrodes made of the electrically conductive Ag-hydrogel (top) and ionically conductive PAAm-alginate hydrogel (bottom). **b**, The electrodes are placed on posterior of the forearm: Ag-hydrogel (top) and ionic hydrogel (bottom). **c**, The electrodes are placed on the tibialis anterior muscle: Ag-hydrogel (left) and ionic hydrogel (right). **d**, The side view of the subject's leg before (left) and after (right) electrical signal delivered by the electrodes made of the Ag-hydrogel. The red lines were used to track the change in dorsiflexion angle. **e**, The side view of the subject's leg before (left) and after (right) electrical signal delivered by the electrodes made of the ionic hydrogel. The blue lines were used to track the change in dorsiflexion angle.
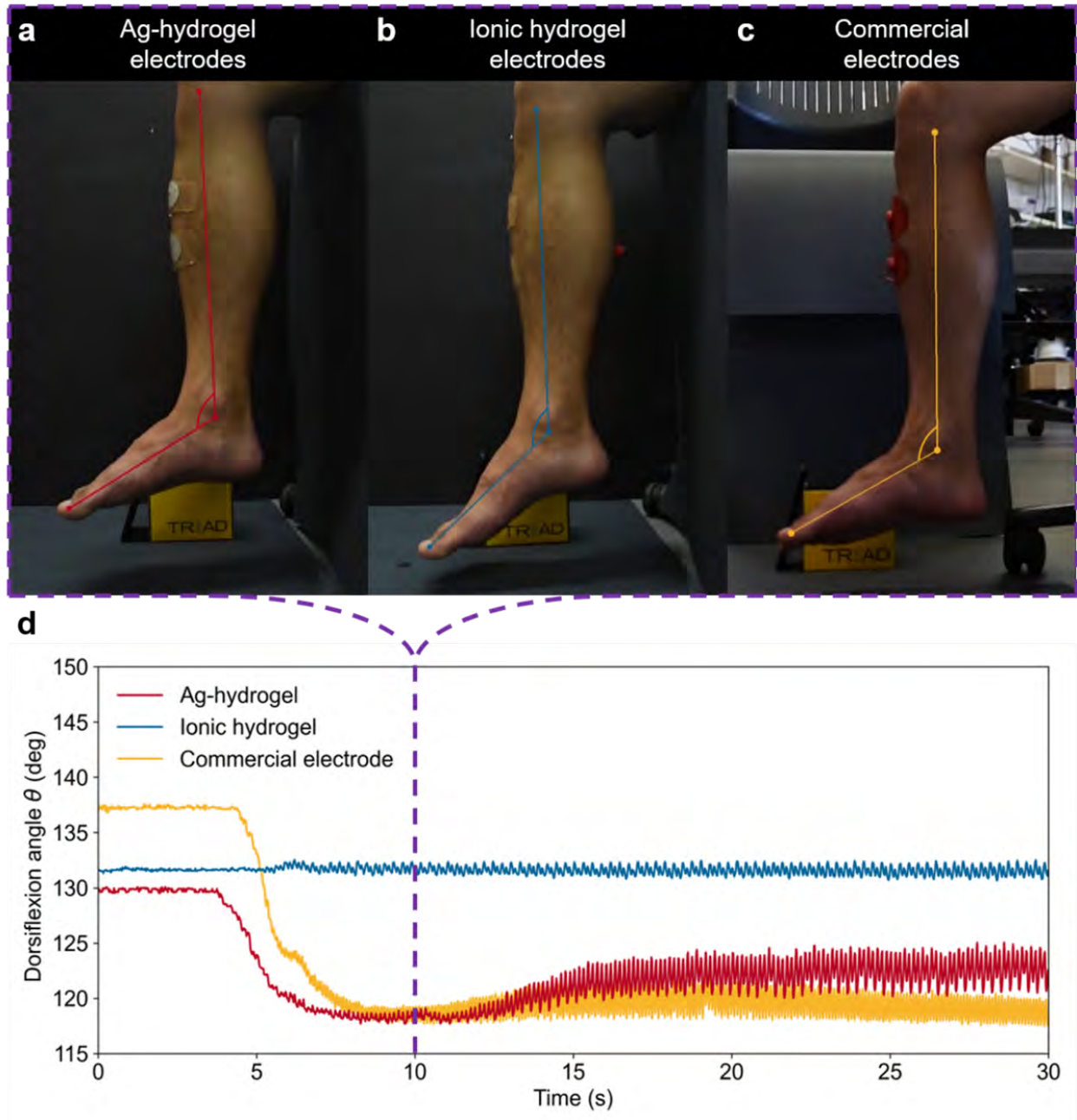
Figure 3.16: Comparison of the performance of neuromuscular electrical stimulation electrodes. **a–c**, Snapshot of the subject's calves which was taken in 10 seconds after turning on the NMES device. **a**, Electrodes made of Ag-hydrogel composites. **b**, Electrodes made of PAAm-alginate ionic hydrogel. **c**, Commercially available electrodes made by PowerDot. **d**, Absolute change in dorsiflexion angle as a function of stimulation time. The initial dorsiflexion angles were different in three cases, which can be hard to be controlled because of multiple variables (for example, posture of other body parts, muscle status, etc.). However, when the NMES device is stimulating the muscle, the dorsiflexion angle is mainly dependent on which muscle is contracted and how strong the stimulation is delivered.

For comparison, we also made unfilled hydrogel electrodes with ionic conductivity and performed NMES under the same conditions (Figure 3.15). First, the electrodes stimulate the tibialis anterior muscle of the leg, which dorsiflexes the foot when stimulated (Figure 3.14b). With the same stimulation intensity, we measured the relative change in dorsiflexion angle from the side view (Figure 3.14c) and the frequency of vibration (Figure 3.14d). Figure 3.14d shows that the frequencies of muscle stimulation in both cases are almost identical because the signal was generated by the same device and power. However, as shown in Figure 3.14c, the relative changes in dorsiflexion angle are different in both cases: the Ag-hydrogel electrodes were able to deliver sufficient current to induce dorsiflexion in foot, whereas the electrodes made of ionic hydrogel appeared ineffective to conduct enough current to contract the muscle. We also compared the performance of the Ag-hydrogel electrodes and commercial electrodes (made by PowerDot) along with the NMES device, which shows that the Ag-hydrogel electrodes have comparable performance to the commercially available NMES electrodes (Figure 3.16). The next experiment was conducted on the muscles in the posterior of the forearm, which results in tremors in the wrist and the fingers curling in towards the palm (Figure 3.14 and 3.15). The result shows that the stimulation driven by Ag-hydrogel electrodes exhibits more significant angle change between the proximal phalange and the metacarpus of the ring and little finger compared to the case of ionic hydrogel electrodes. This demonstration suggests that the Ag-hydrogel composite has the potential to improve bioelectronic interfacing of tissue-electrode contacts due to its high electrical conductivity and soft conformability.

3.5   Conclusions

We have reported an Ag-hydrogel composite that is based on two materials with disparate mechanical properties—Ag flakes and hydrogel matrix—and exhibits high electrical conductivity (> 300 S cm^{-1}), electrical stability under repeated mechanical loading, low Young's

modulus (< 10 kPa), and high stretchability (up to 250% strain without electrical failure). To illustrate the capabilities of the Ag-hydrogel, we fabricated a stingray-inspired swimmer driven by SMAs that require high current, high compliance, and high stretchability for actuation. We also developed skin-mounted electrodes made of the Ag-hydrogel for neuromuscular electrical stimulation, which require conformal contact and high conductivity in order to deliver electrical impulse with high frequency.

This combination of both high electrical conductivity and high compliance is achieved by controlling the assembly of Ag inclusions when dispersing the micron-sized Ag flakes in the polyacrylamide and alginate hydrogel. A key step in the fabrication process is the partial dehydration step, which allows intimate contact between Ag flakes and the formation of a percolating network that remains intact and stable even as the gel is fully rehydrated. The conductive hydrogel composites also have robust and reliable electromechanical coupling, which facilitates applications in soft robotic systems, wearable electronics, and bioelectronic interfacing. The combination of electrical and mechanical properties of the Ag-hydrogel composite occupies a unique place in the design space of electrically conductive soft materials (Figure 3.1c) and could be of use in the development of soft robotics, bioelectronics, and wearable electronics.

3.6 Lesson Learned

This chapter introduced a conductive hydrogel composite made of silver (Ag) flakes and a polyacrylamide (PAAm)-alginate hydrogel matrix. The material has an electrical conductivity that is adequate for powering digital electronics, a low Young's modulus that is comparable to biological tissues, and resilience to mechanical deformation, such as stretching, compression, bending, or twisting. Possible applications of the composite were shown with the following demonstrations: (i) A stingray-inspired soft swimmer and (ii) on-skin neuromuscular stimulation electrodes. However, these two applications are not sufficient to demonstrate the

material's potential in bioelectronics. In the field of bioelectronics or wearable electronics, materials should be not only mechanically compliant and highly conductive but also resilient to mechanical/electrical transformation since biological tissues, such as brains or natural nervous systems, are prone to change gradually and suddenly. This requires the ability of restoration, reprogrammability, self-healing, or self-repairing. In the next chapter, I will explore how the Ag-hydrogel composite is able to perform electrical reconfiguration thanks to its microstructural changes while being dehydrated and rehydrated. This can broaden the potential of the Ag-hydrogel composite in bioelectronics.

Chapter 4

A Reconfigurable Conductive Hydrogel Composite

- **Y. Ohm**, J. Liao, M. J. Ford, and C. Majidi, "Reconfigurable eletrical networks within a conductive hydrogel composite by controlling water amount," *Manuscript in preparation*.

4.1 Introduction

Wearable technology has is increasingly focused on utilizing soft materials for creating seamless interfaces with the human body [133, 134, 135]. To achieve this mechanically, we need soft materials that are deformable as the human body moves [136, 137]. Additionally, the material should be conductive to convey digital information for communication [138, 139, 120]. Researchers throughout the world have been inventing promising material architectures that are suitable for the integration of electronics into the human body [140, 141, 142, 143, 144]. Soft conductors play a key role in wearable electronics and soft robotics. There is an acute need for highly conductive materials that can maintain reliable electrical connections under mechanical deformations, such as compression, stretch, and bending [69, 13, 145]. Matsuhisa *et al.* introduced a composition of an elastic rubber matrix and silver flakes with an initial conductivity of 738 S cm^{-1} and a stretchability of 215% while maintaining electrical conductivity [69]. However, the conductive pathways discussed here cannot be modified without rebuilding the entire material or sample, resulting in static circuit functionality. The ability to reconfigure conductive networks within soft materials can close the gap with neuroplasticity in natural nervous tissue by allowing for the controlled and reversible transition between conductive and non-conductive states [38, 39, 146, 40, 14]. For example, a silicone composite with liquid metal droplets showed a reversible transition between an insulator and a conductor by simply controlling temperature [38]. This material functions as a conductor with a resistivity of 1.78×10^{-5} ohms m at temperatures (T) lower than 212 K ($\sim -61°C$ or $-78°F$) and has infinite resistivity in a warm environment where $T > 212$ K. Park *et al.* demonstrated a poly(ethylene glycol) diacrylate (PEGDA) hydrogel embedded with eutectic gallium indium (EGaIn) particles [39]. Mechanical stimuli (e.g., friction) can activate percolating pathways in the composite by rupturing native oxide layers of the EGaIn particles. Moreover, the conductive networks can be erased when the hydrogel matrix is rehydrated and swollen by water. Although these unique materials show potential for reconfigurable and reversible electrical pathways in soft materials, there are clear limitations
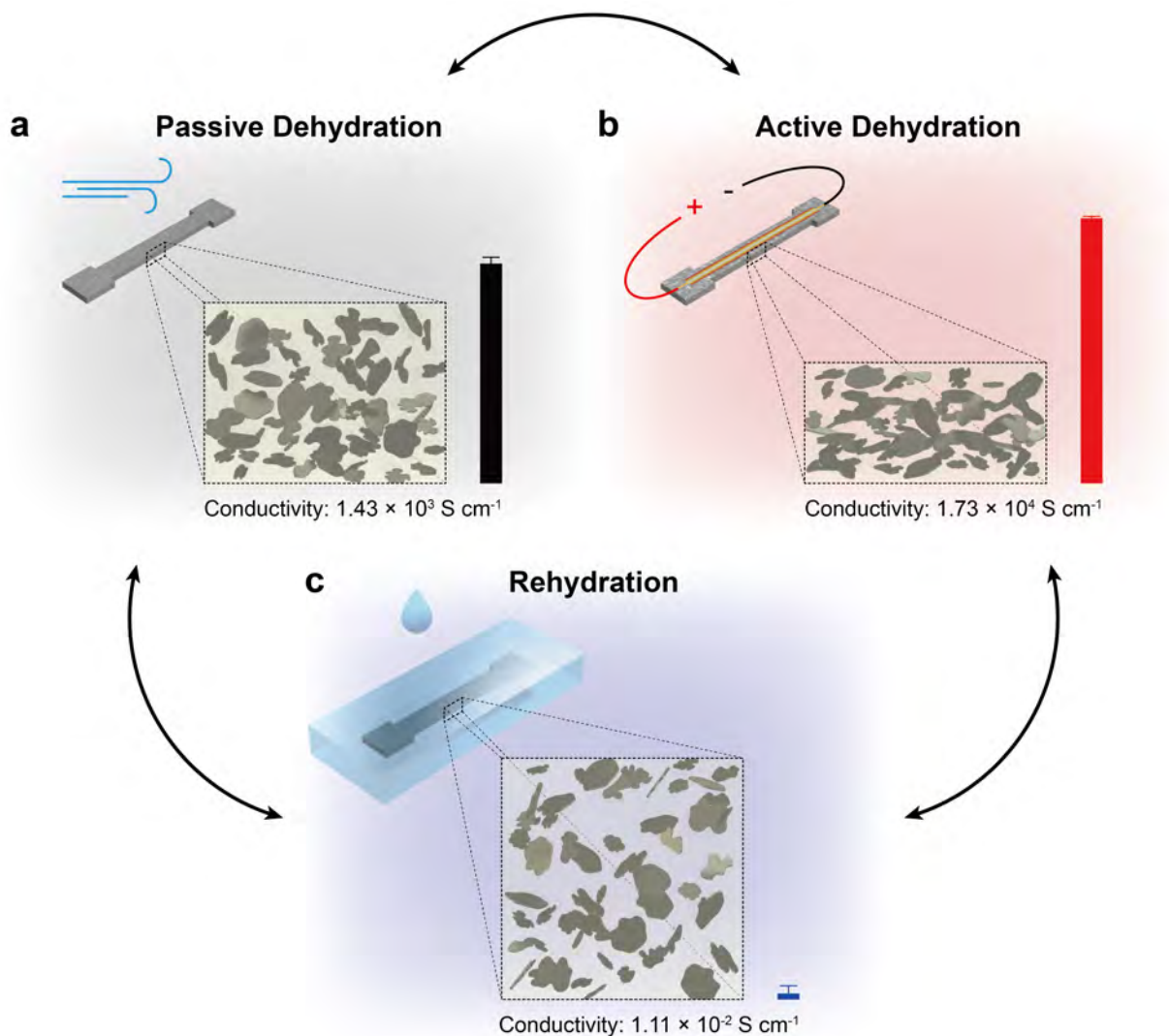
Figure 4.1: Overview of reconfigurable and reversible electrical networks in conductive hydrogel composites. (**a**) Passive dehydration is a process to dehydrate water content in the composite without any factitious operations except relative humidity and ambient temperature of the surrounding environment. The samples that undergo the passive dehydration process have a conductivity (σ) of 1.43×10^3 S cm^{-1}. (**b**) Active dehydration can evaporate more water from the composite by using Joule heating or electric power. After the active dehydration process, the conductive networks composed of silver flakes can be stronger than those from the passive dehydration. The conductivity in this case is 1.73×10^4 S cm^{-1}. (**c**) By introducing water externally, the composite can be rehydrated. The rehydrated composite has a larger volume than other dehydration cases since water particles are positioned between polymer networks and silver flakes. This causes the conducting networks to be weaker; therefore, the conductivity of the composite decreases ($\sigma = 1.11 \times 10^{-2}$ S cm^{-1}). The processes introduced in this figure are reversible, which allows reversible electrical networks in the hydrogel composite.

in terms of practical cases. First, the thermal environment for the insulator-conductor

transition is usually difficult to maintain while the device is on the human body since it requires temperatures either below the freezing point of water [38, 146] or close to the boiling point of the water [40]. For the conductors that can be reconfigured through mechanical activations [39, 14], the materials should be physically accessible to recreate the conductive pathways, which could not always be the option when a device is placed in the human body. To overcome the abovementioned limitations, we need a new material architecture whose electrical networks can be reconfigured or reversible through non-mechanical sintering in safe environments for the human body.

In this chapter, I propose a hydrogel composite whose conductive pathways are reversible and reconfigurable by controlling the amount of water within the composite. The material is composed of a polyacrylamide (PAAm) and alginate hydrogel [125], and a low concentration of micron-sized silver (Ag) flakes [96]. Since the composite contains only a small portion of Ag flakes (3% by volume), water is still the largest component of the material's composition. The amount of water in the composite can be changed through dehydration or rehydration. There are two different types of dehydration used in this article to decrease the water content: i) passive dehydration (Figure 4.1a), which does not have any other factitious processes except relative humidity and ambient temperature of the surrounding environment, and ii) active dehydration (Figure 4.1b), which uses Joule heating or electric power. Conductive hydrogel traces have a conductivity (σ) of $1,430 \pm 607$ S cm^{-1} after the passive dehydration process. Samples can become more conductive after going through the active dehydration or Joule heating process. Their conductivity is $17,300 \pm 1,860$ S cm^{-1} which is around 12 times larger than for the passive dehydration case. This is because Joule heating causes more evaporation of water from the composite by increasing the localized temperature of the material. Loss of water accelerates the composite to reach the percolation threshold by enabling physically closer and thus more robust networks between the conductive fillers. However, the electrical networks can be degraded (damaged or broken) by an increased amount of water within the composite, which can happen through the rehydration process by submerging samples in

a water bath or dropping water directly on top (Figure 4.1c). In this case, the rehydrated samples have an attenuated conductivity of 0.0111 ± 0.00590 S cm^{-1}. More importantly, the transition between high and low conductivity of the composite happens back and forth by increasing or decreasing the water amount. By utilizing this material's behavior over the dehydration and rehydration processes, we can successfully create, reinforce, erase, or reconfigure conductive pathways on the hydrogel composite.

4.2 Reconfigurable conductive hydrogel composite

The conductive hydrogel composite was composed of silver flakes and a double network hydrogel matrix made of polyacrylamide (PAAm) and alginate polymer networks, which originates from previous work. According to Ohm *et al.* [96], this material architecture has a stretchability of up to 250% without completely losing the percolation networks within the composite. The Young's modulus was reported to be less than 10 kPa which is comparable to biomaterials, such as adipose tissue [116]. As discussed in Chatper 3, this work hypothesized partial dehydration that enables high electrical conductivity in the composite, although there is a very low volumetric portion of conductive fillers (as the initial volume fraction of silver flakes was reported as 5% by volume) inside the composite. The dehydration process is directly related to the amount of water within the composite matrix because only water is the variable component in the composite. However, the previous work didn't conduct a deeper study about the change of components over the dehydration or rehydration process. Moreover, it was not clear whether the material could show consistent results or not after going through more than one of the processes. The work we introduce here is focused on the relationship between the volumetric conductivity of the composite according to the changes of each component in the composite during the dehydration and rehydration processes. In addition, we discuss how to accelerate the evaporation of water using Joule heating, which can result in the faster formation of conductive networks with higher conductivity than the

samples from the normal dehydration process. Lastly, this study shows consistent results over multiple cycles of passive/active dehydration and rehydration processes.

4.2.1 Active Dehydration Using Joule Heating

To further evaporate the remaining water within the composite, we applied Joule heating to the conductive hydrogel composite. For the material's composition and testing conditions for Joule heating, we used 3 vol% of silver flakes in polyacrylamide-alginate hydrogel and 1.5 W of electric power. The conductive hydrogel composites were patterned using a stencil printing method with a mask made of polydimethylsiloxane (PDMS). We tested the composites with different volume fractions of silver flakes (1, 2, 3, 4, and 5% by volume) using a fixed electric power input of 1.5 W for 30 minutes (Figure 4.2). The gain in conductance after 30 minutes of Joule heating was measured and used as a decision factor. For the cases of smaller volume fractions than 3 vol%, samples have higher resistances than those of other cases; therefore, higher direct voltages were applied across the samples with the fixed amount of input power according to Joule's first law, $P = VI = V^2/R$, where P is power, V is voltage, I is current, and R is resistance. Composites with 1 vol% of silver flakes were not able to survive with
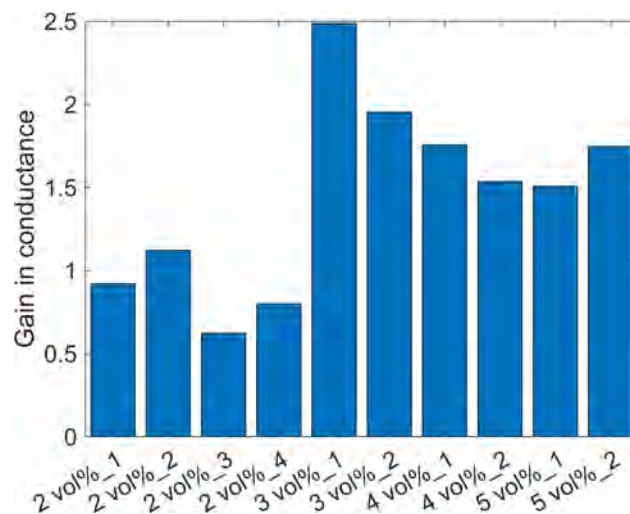
Figure 4.2: Conductance increases after 30 minutes of Joule heating with a fixed electric power input (1.5 W) based on different initial amounts of volume fraction of conductive fillers in hydrogel composites.

high amounts of direct voltage. On the other hand, we were able to measure the conductance gain for the samples fabricated with 2 vol% of silver flakes; however, the gains are lower than those of the 3 vol% samples. For the samples with higher volume fractions than 3 vol%, higher direct currents passed through the samples since they have lower resistance values than other cases ($P = VI = I^2R$). All the samples with 4 and 5 vol% of conductive fillers didn't show obvious breakdowns during the experiment, but the gain in conductance is smaller than the case of 3 vol%. Therefore, we decided to use the initial conductive filler amount as 3 vol% because we expected conductance gain after Joule heating as much as possible and didn't want a harsh environment for the repeatability of performance.

With the fixed initial amount of conductive fillers, we conducted an experiment to decide the amount of input power for Joule heating. We tested five electric power inputs for 30 minutes, including 1, 1.5, 2, 2.5, and 3 W (Figure 4.3). The result shows that samples under 2.5 and 3 W of electric power cannot survive after 30 minutes of Joule heating. This means that 2.5 and 3 W produce excessive heat that leads to some breakdowns or damage to the composites. The cases of 1 W show around 50% increase in conductance after Joule heating,
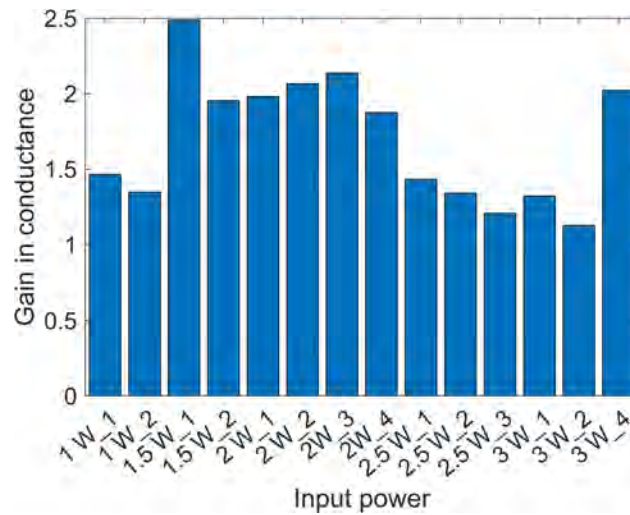
Figure 4.3: Conductance increases after 30 minutes of Joule heating applied to conductive hydrogel traces with 3 vol% of initial conductive filler concentration based on different power inputs for Joule heating. The samples under 2.5 W and 3 W were not able to survive the 30 minutes of Joule heating; therefore, the gains were calculated by using the last stable resistance values and initial resistance values of the samples.

which is lower than the cases of 1.5 and 2 W. Out of those two input parameters, we chose to use 1.5 W of electric power for characterization since the samples' gain in conductance is comparable to that of the samples under 2 W. Moreover, we postulated that less electric power is generally beneficial to the longevity of samples and repeatability of performance.

With these two characterization parameters (3 vol% of initial silver flakes in the composite and 1.5 W electric power as input), we monitored the evolution of electrical properties under 30 minutes of Joule heating training, as shown in Figure 4.4. We recorded voltage and current values displayed on the benchtop power supply and maintained power close to 1.5 W. Then, we calculated the resistance of the tested trace from voltage and current information ($R = V/I$). The resistance of the composite trace keeps going down during the training as the voltage applied across the sample decreases and the current increases with the fixed amount of power. Towards the end of 30 minutes of Joule heating, all the electrical properties tend to be saturated, which can also be seen in other characterization plots. We attribute this evolution of properties to percolating networks which can be strengthened during the training. Eventually, we conclude that Joule heating through electric power on the conductive hydrogel composite will enhance the electrical conductivity of the composite.
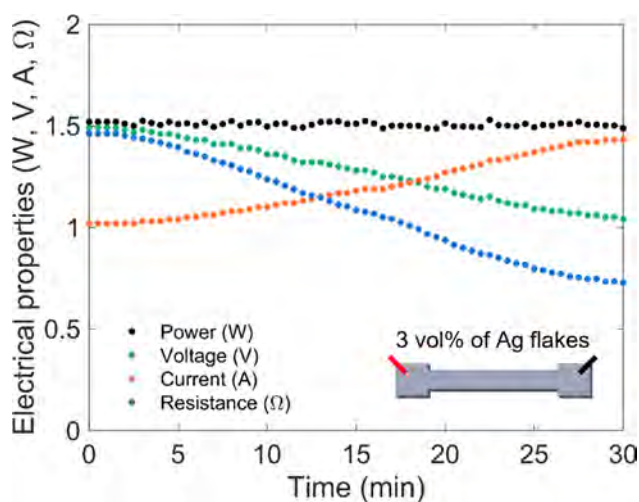
Figure 4.4: (**a**) Electrical properties used for the active dehydration using Joule heating. 1.5 W of power from a benchtop power supply was applied to the composite (inset) with 3 vol% of initial conductive fillers.

4.2.2   Evaporation of Water

The amount of remaining water within the conductive hydrogel composites plays a key role in the material's properties. There are three main components in the composites: water, polymer matrix, and silver flakes. Among the three, we assume that water is the only component whose amount can be changed within the composite. Surrounded by unsaturated air, water molecules can evaporate at the exposed surface with enough energy to overcome the vapor pressure [147]. The evaporation of water happens naturally, which we named passive dehydration to distinguish this from active dehydration through Joule heating. During the evaporation period, the water amount in the composite keeps decreasing. On the other hand, the portion of other unchanged components in the composite is relatively increasing. Therefore, the effective volume fraction of silver flakes gradually grows, which contributes to the increase in the conductivity of the composite.

To validate the hypothesis suggested above, we measured the absolute change in weight of conductive hydrogel traces using an analytical balance (HR-250AZ; A&D Company Ltd) designed for measuring mass with high precision. In Figure 4.5, the plot shows the absolute
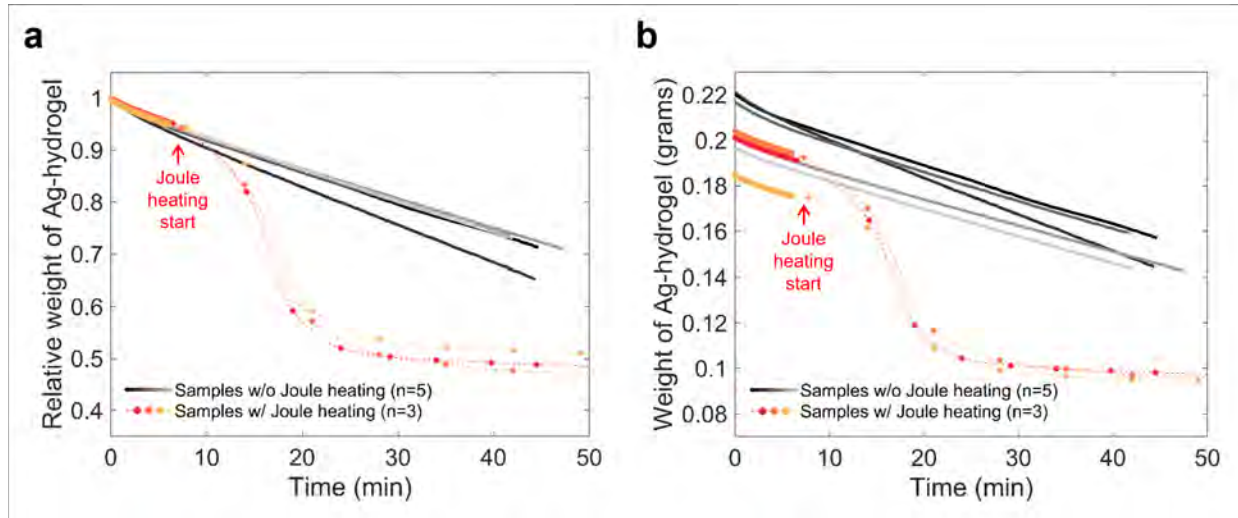
Figure 4.5: (**a**) Absolute weight changes of conductive hydrogel composites under the normal dehydration process (without Joule heating) and Joule heating. (**b**) Relative weight changes of conductive hydrogel composites under the passive dehydration process (without Joule heating) and the active dehydration through Joule heating.
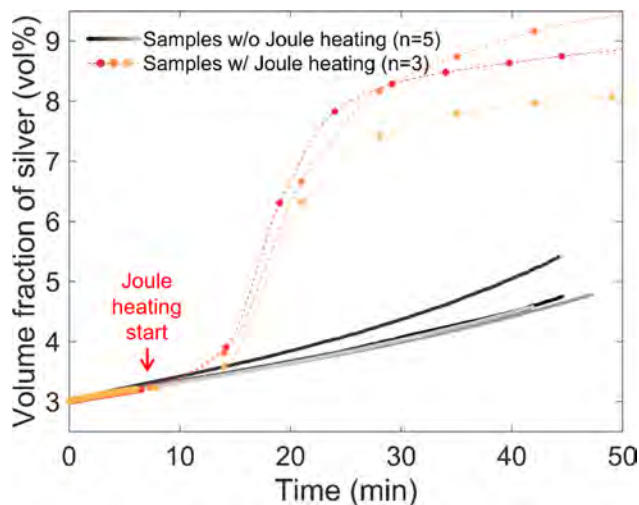
Figure 4.6: Effective volume fraction of silver flakes in the hydrogel composites with or without Joule heating as a function of time.

and relative weight evolution of the patterned traces over time (Detailed experimental conditions are described in Appendix D. There were two types of traces tested in this experiment: i) samples without Joule heating ($n = 5$) and ii) samples with Joule heating ($n = 3$). The case of Joule heating has fewer and discontinuous data points compared to the other case since the weight measurement cannot be conducted accurately while Joule heating was applied to the traces. The result shows that the weight of samples with passive dehydration remain relatively stable as water within hydrogel networks and silver flakes naturally evaporates. However, when Joule heating was applied, samples showed a dramatic decrease in their weight around 10 minutes after Joule heating was started. We confirmed that the active dehydration process through Joule heating accelerates the evaporation of water within hydrogel composites.

As the amount of water decreases, the volume portion of silver flakes relatively increases. In Figure 4.6, we calculated the volume fraction of silver flakes in the composites over time using the weight information from Figure 4.5. All the samples tested in this experiment were initially fabricated using 3 vol% of silver flakes. For the comparison of the two cases with or without Joule heating, we used data points at 37 minutes which is 30 minutes after the start of Joule heating. The result shows that the samples with the passive dehydration
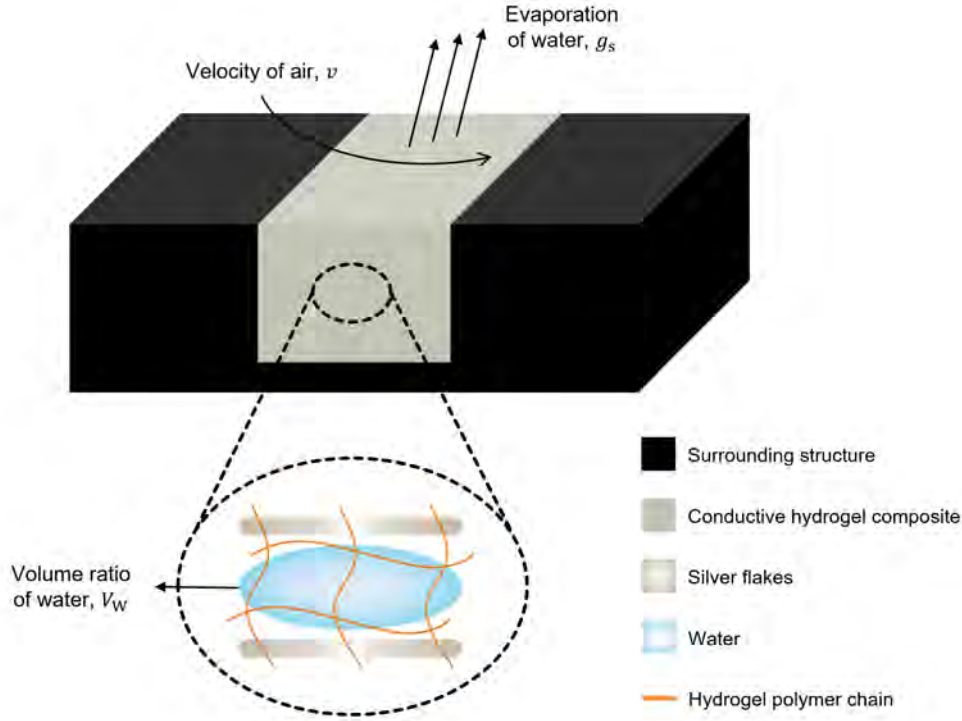
Figure 4.7: A cartoon of a model to predict the amount of water evaporated at the surface of the composite. The composite is surrounded by a structure that doesn't change its properties over time.

process contain 4.43 ± 0.225 vol% of conductive fillers in composites at 37 minutes, which is $47.6 \pm 7.50\%$ increase in volume fraction compared to the initial volume fraction. However, the samples under Joule heating show 8.42 ± 0.524 vol% ($281 \pm 17.5\%$ increase in volume fraction) of silver flakes after 30 minutes of electric power inputs.

To verify the experimental data, we set a simple model to predict the amount of water evaporated (Figure 4.7). In the model, the amount of evaporated water per second is calculated as $g_s = \theta V_w A(x_s - x)/3600$, where $\theta = 25 + 19v$ is the evaporation coefficient, v is the velocity of air above the water surface, V_w is the volume ratio of water in the composites, A is the surface area of water that exposed to the air, x_s is the maximum humidity ratio of saturated air at the same temperature as the water surface, and x is the humidity ratio in the air. v is assumed as 0 because the experiment happened in the chamber or the analytic balance; therefore, θ is 25 kg m^{-2} h^{-1}. V_w can be obtained from Figure 4.5 and Figure 4.8. The surface area A is set to be a constant of 120 mm^2 based on the dimensions of the

patterned trace. To decide x_s and x, we need information about the temperature at the sample's surface, the temperature of the air surrounding the sample, and the humidity of the surrounding air. For an easy calculation, we made another assumption that the temperature and humidity in the chamber didn't change in order to fix the humidity ratio x as 0.0037 kg kg^{-1}, which is the value at the temperature of 24°C and the relative humidity of 20%. A thermal imaging camera (A35; Teledyne FLIR LLC) was used to capture the surface temperature of the composite while Joule heating was applied. With the temperature information (Figure 4.9), x_s can be decided by using Mollier diagram (Figure 4.10). Energy from Joule heating increases the overall temperature of the hydrogel composite, resulting in higher temperature of water at the surface of the trace. With high surface temperature, the samples under Joule
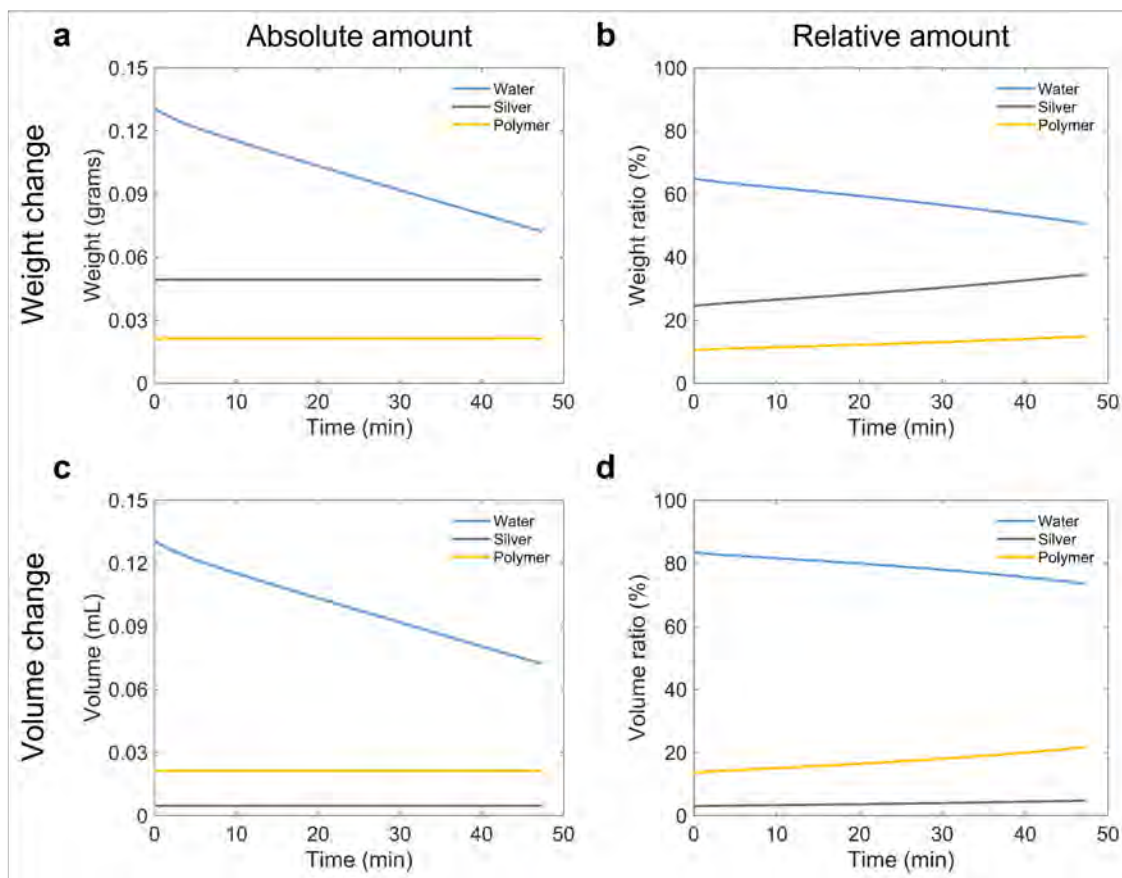
Figure 4.8: A representative result of weight and volume changes of each component within the hydrogel composite over time without Joule heating. (**a**) Absolute weight change, (**b**) relative weight change, (**c**) absolute volume change, and (**d**) relative volume change.
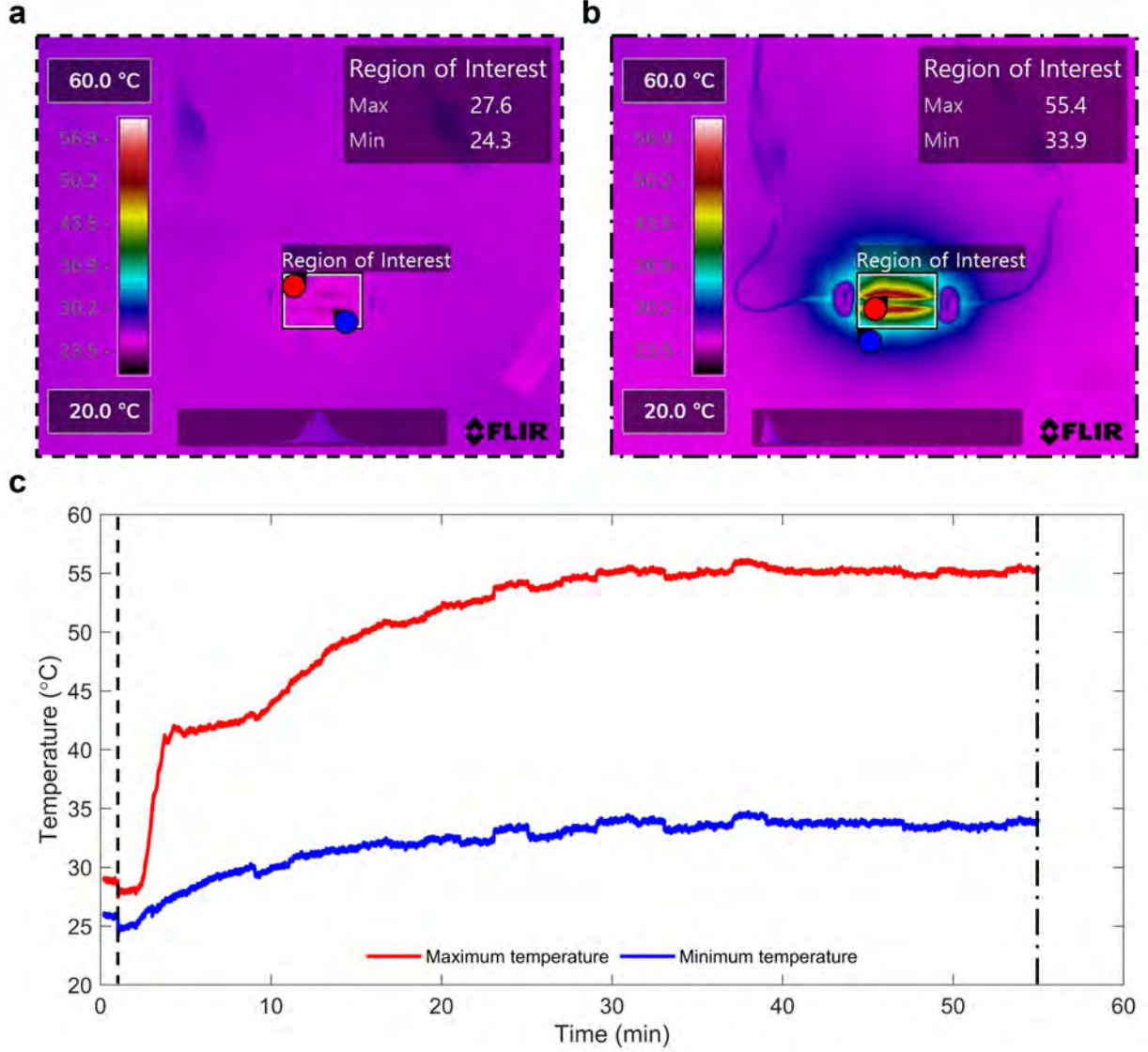
Figure 4.9: Temperature of the composite under Joule heating (1.5 W of electric power). (**a**) A thermal image of the sample at the lowest temperature. (**b**) A thermal image of the sample at the last time frame. (**c**) Maximum and minimum temperature evolution of the region of interest around the patterned composite over time. Joule heating was directly and continuously applied to the sample during the experiment.

heating have higher x_s than that of the other case; therefore, the evaporated amount of water is larger. This is shown in Figure 4.11, which depicts the results of the simulated water evaporation superposed on the experimental data. Due to a number of assumptions used to simplify the model, there are mismatches between the modeling results and actual data from the experiment; however, the result generally captures the similar tendency of evolution for
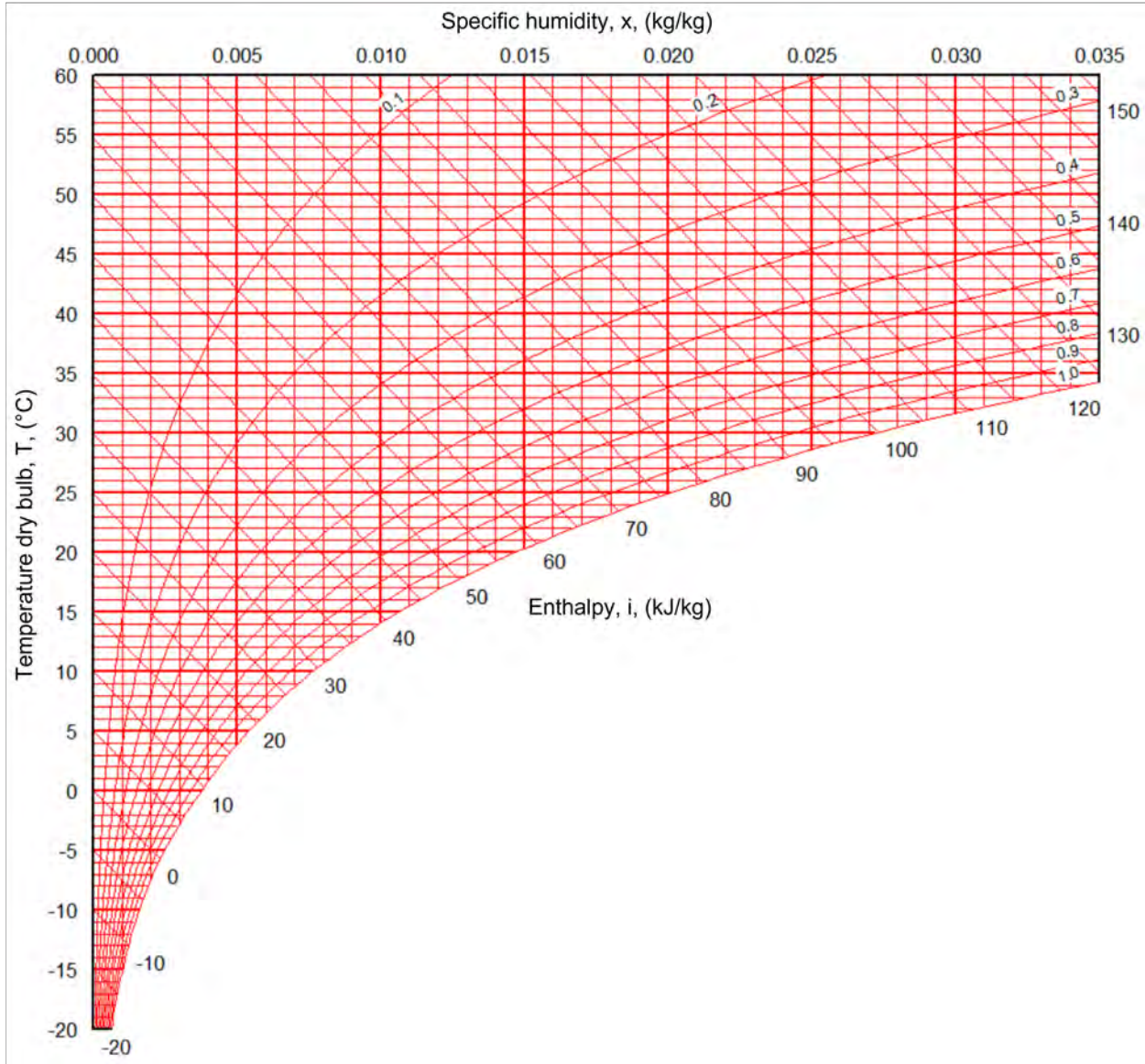
Figure 4.10: Mollier chart that shows the relationship between temperature of dry air, enthalpy, and moisture in the air. This graph was created by using a software called Mollier Sketcher version 2.1b distributed by IV Produkt Ltd.

each case of dehydration.

The effective volume fraction of conductive fillers affects the conductivity of composites [148]. As water evaporation happens, the volume portion of silver flakes in the composite relatively increases. In Figure 4.12, the resistance of the hydrogel composite decreases as the passive/active dehydration process goes on. The samples show plummets in resistance around 10 ~ 20 minutes after the initial patterning process, representing percolation thresholds in

86
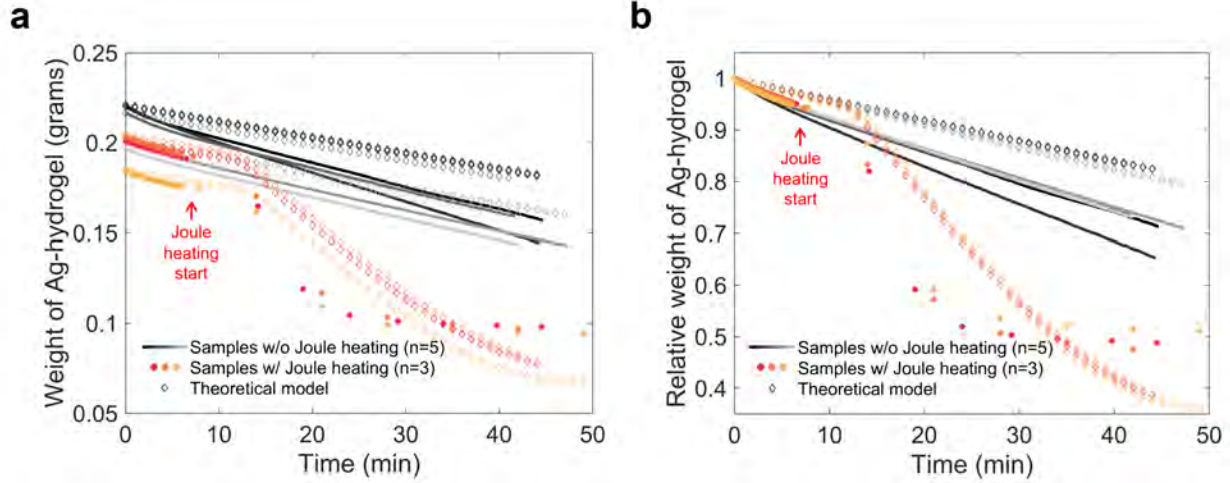
Figure 4.11: Simulated modeling results to predict (**a**) absolute and (**b**) relative changes of weight of the conductive hydrogel composites over time. All theoretical modeling results for the samples from passive or active dehydration processes, which are formatted in dashed lines, are superposed on the original experimental data.
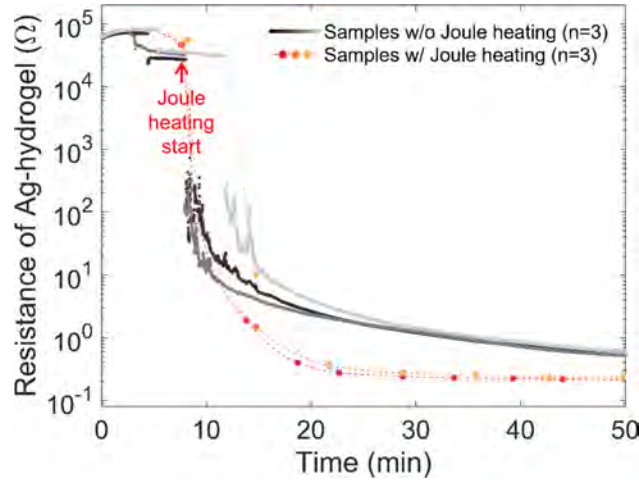
Figure 4.12: Absolute changes in resistance as a function of time for samples with or without Joule heating.

the composites. We can evaluate the effect of Joule heating in terms of enhancing percolating networks within the composites by simply comparing the resistance values at 37 minutes which is 30 minutes after the continuous electric power inputs. The samples without the active dehydration procedure have 0.890 ± 0.0739 ohms. On the other hand, the resistance of the Joule heated samples is 0.240 ± 0.0111 ohms, which is 3.17 times lower than the other case. In conclusion, the increase in volumetric content of conductive fillers by the dehydration
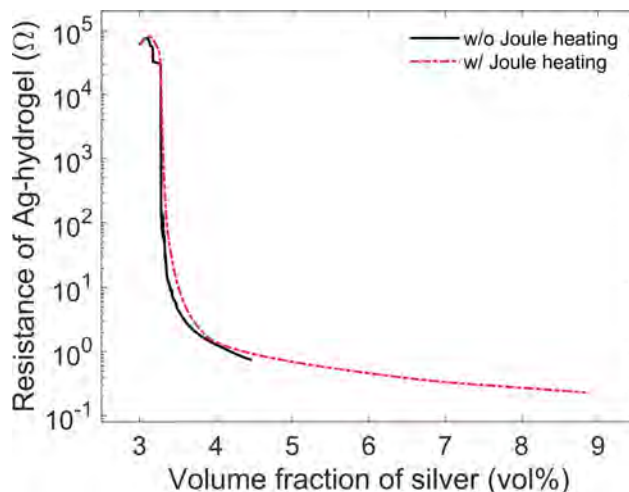
Figure 4.13: Resistance of the conductive hydrogel composite trace based on the effective volume fraction of silver flakes.

process causes the decrease in resistance, as shown in Figure 4.13. In addition, the further and faster evaporation of water through Joule heating contributes to an additional and quicker gain in conductivity of the composite.

4.2.3   Rehydration

We now confirmed that the amount of water within the conductive hydrogel composite is variable, and the conductivity of the composite increases when the material loses some portion of water. What if the composite gains more water during some processes? We hypothesized that an increase in the amount of water in the composite would decrease the conductivity by decreasing the volume fraction of silver flakes and introducing swelling to the hydrogel matrix. We attribute the result to a combination of two possible reasons. First, water can penetrate percolating networks in the composite by exerting capillary forces [96]. While the composite was under the dehydration process, percolating networks get enhanced by attractive forces, such as van der Waals forces, between silver flake particles. On the other hand, if the networks are surrounded by an excessive amount of water, repulsive forces (e.g., capillary forces) generated by water can overcome the attractive forces. This may result in sudden increases in resistance when water is applied. The second reason can be the volume

88
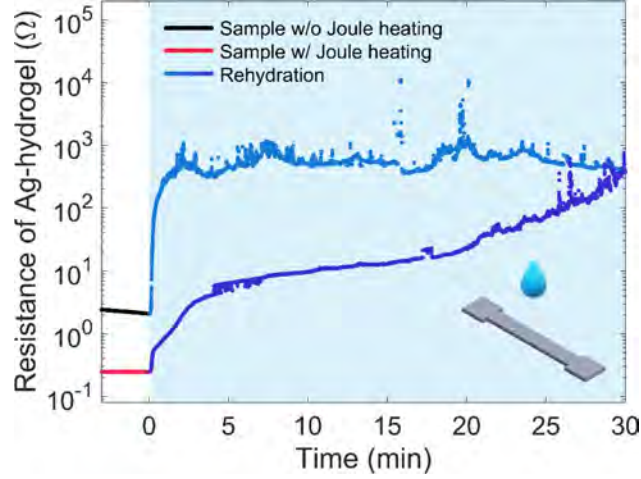
Figure 4.14: Absolute changes in resistance conductive hydrogel composites under the effect of rehydration. Water was directly applied on the composites at 0 minutes.

fraction of silver flakes within the composite, which might cause more gradual results than the first reason. As rehydration goes on, the composite will absorb more water from the surrounding environment. Then, the volume fraction of conductive fillers in the material will relatively decrease. This results in a gradual increase in resistance which is the opposite effect of the dehydration process. The water absorption by the hydrogel matrix made of polyacrylamide and alginate networks happens gradually [149].

To verify the speculation, we rehydrated the samples that had already gone through the passive or active dehydration by submerging them in water. Figure 4.14 shows absolute resistance evolutions of two samples when they were rehydrated, which represent each case of the passive dehydration or Joule heating. For the sample without Joule heating, we covered the trace with water when it had a resistance of 2.09 ohms, and the sample after the active dehydration was at 0.246 ohms before applying water. Both cases show sudden increases in resistance, which we consider the capillary forces dominantly affected. The conductive pathways that had already been formed were interrupted by the penetration of water all over the composite matrix resulting in the sudden change in resistance of the material. However, the sample that went through the Joule heating process shows a less sudden change in resistance. This may be attributed to the remaining amount of water after the
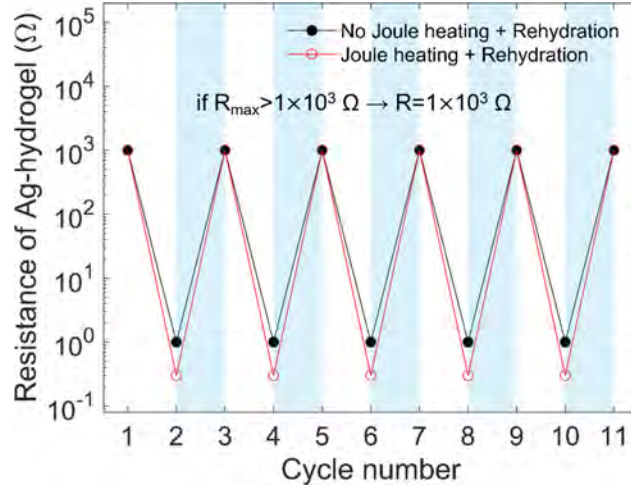
Figure 4.15: Resistance evolution of Ag-hydrogel composites under multiple cycles of normal dehydration/Joule heating and rehydration. Data points that are higher than 1,000 ohms are capped by 1,000 ohms.

dehydration process. Joule heating causes more loss in water than the passive dehydration process, which allows silver flake particles to be physically closer to each other. Proximity in physical distance tends to increase the attractive forces between the conductive particles, including van der Waals forces [150, 151, 152]. The percolating networks composed of particle connections with higher attractive forces are hard to be interrupted by the repulsive forces generated by water. This speculation proves that the sample with Joule heating shows a less sudden increase in resistance and still higher conductivity than the sample without Joule heating when the rehydration process is applied. If there are remaining dominant conductive networks after the initial introduction of water, they can be slowly weakened through the gradual absorption of water by the hydrogel matrix. We think the sample with the passive dehydration shows only the sudden change at the beginning of the rehydration process, and the plot of the sample with Joule heating captures the gradual increase in resistance after the sudden increase. We conclude that the introduction of water to the conductive hydrogel composite weakens the conductive networks.

By simply controlling the amount of water, the composite can function as an electrical conductor or insulator. This electrical transition can happen in the same material without adding or replacing any other components. However, it is important to check whether the

transition causes any permanent damage or changes in the material or not. Therefore, we conducted an experiment to show how repeatable the transition can be and how consistent the result can be through more than one cycle of dehydration and rehydration. In Figure 4.15, we recorded resistance values of samples under alternating dehydration and rehydration processes. For the case of the sample without Joule heating, we stopped the dehydration process when the resistance decreased to 1 ohm and rehydrated the sample until it reached 1,000 ohms. For the other case, we applied Joule heating to the composite up to 0.3 ohms; then, we submerged the trace in water until the resistance reached 1,000 ohms. The result proves that the material shows consistent electrical behaviors throughout multiple cycles of dehydration and rehydration. In addition, the experiment shows that the transition between conductor and insulator is repeatable.

4.3   Demonstrations

We have presented the material's behaviors through passive dehydration, active dehydration (Joule heating), and rehydration. To examine further possibilities of the material's usages, we conducted several demonstrations that show reconfigurability of conductive pathways under severe damages, reversibility of conductivity based on the amount of water within the composite, and a walker that shows three different gaits reconfigured by dehydrating or rehydrating the composite traces connected to DC motors. In Figure 4.16, Thermal images taken by a compact thermal camera (C2, Teledyne FLIR) were used to visualize activated conductive pathways within the composite. The assumption here is that an element with lower resistance has more current flow under the same amount of voltage than the other elements with higher resistances, which generates more Joule heating and increases localized temperature according to $P = VI = I^2R$. From this assumption, we can deduce that area with higher temperature in thermal images has higher electrical conductivity.
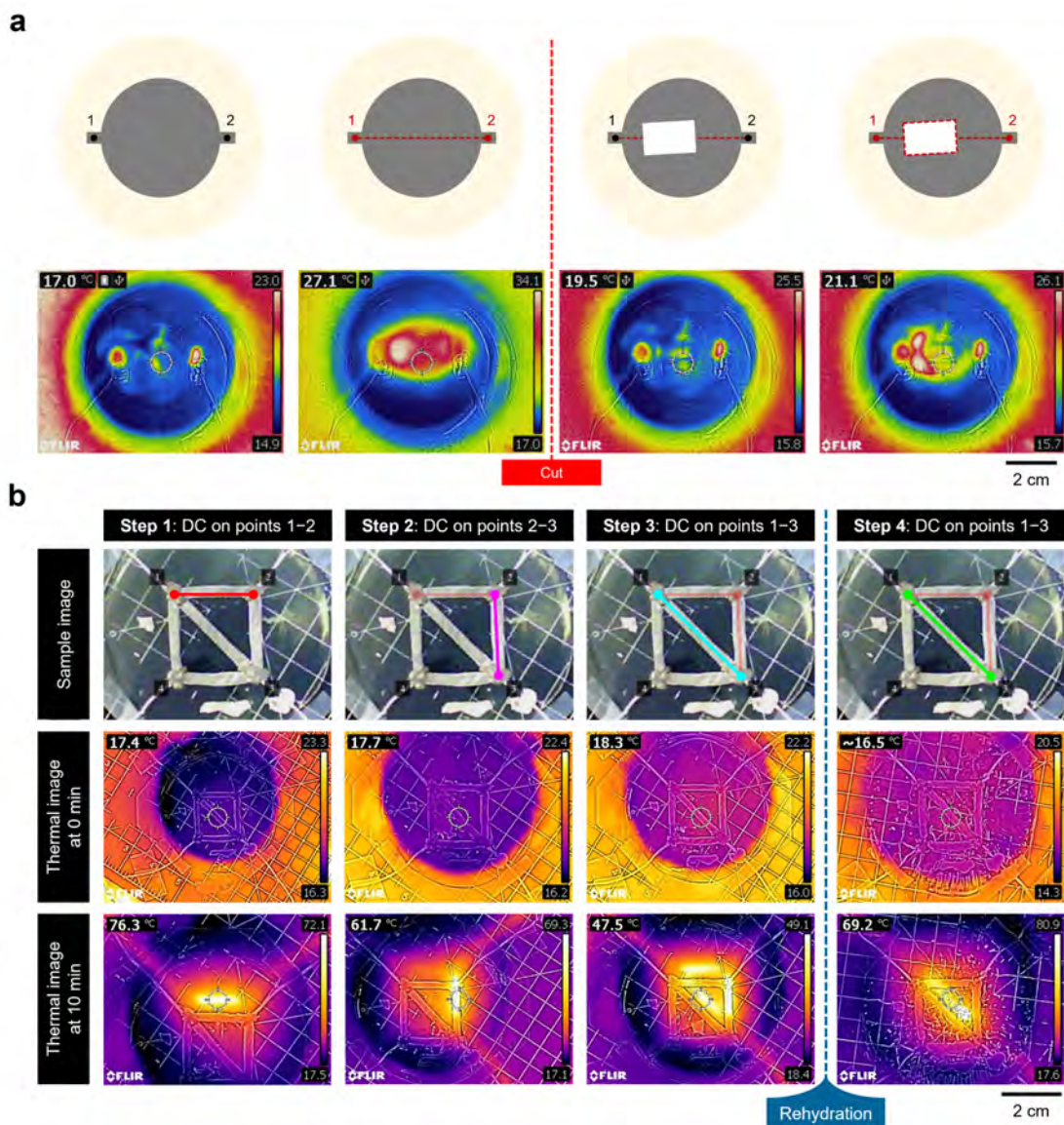
Figure 4.16: Demonstration of reconfigurable and reversible conductors made of the conductive hydrogel composite. (**a**) Reconfigurable conductive traces before and after the 'cut' damage on the activated conductive pathways. Two points of interest, 1 and 2, are highlighted as red when they were electrically conductive through the conductive hydrogel composite. The two points are marked as black, which means that there were no activated conductive pathways between. Conductive paths are illustrated as red dashed lines for the purpose of visualization. The damage was induced by a razor blade. (**b**) Reversible conductive hydrogel composite before and after rehydration. Each step highlights where Joule heating was applied for 30 minutes in red, pink, cyan, and green colors. Thermal images are also presented to visualize which trace was generating heat from Joule heating. The sample went through rehydration process for 4 hours after step 3 by being fully submerged in water bath. After the rehydration process and before applying the additional Joule heating, all water was removed.

4.3.1 Reconfigurability Before and After Damage

With Joule heating, the Ag-polyacrylamide-alginate hydrogel composite can reconfigure its electrically conductive pathways even under severe damage. We patterned the composite on top of a layer of a polyacrylamide-alginate hydrogel, as shown in Figure 4.16a. There are two points of interest at the end of the patterned composite. The two points were highlighted with red color when they are electrically connected by strong percolation pathways; on the other hand, they were marked as black, showing that they are connected with weak conductive pathways. After patterning, we applied either 2 V of direct voltage or 1.5 W of power to the composite using a benchtop power supply during the whole demonstration. As shown in the second thermal image in Figure 3a, we confirmed that there were activated conductive regions between points 1 and 2. Then, we inflicted a severe through cut using a ceramic blade around the area with the highest temperature. Right after the cut, the thermal image shows that there were no conductive pathways between points 1 and 2. As time passed, there was a gradual propagation of localized high temperatures around the cut. This means that the composite was reconfiguring new conductive pathways between points 1 and 2 when electrical power was applied. Furthermore, those pathways tend to be the shortest paths that connect the points of interest, which generally have low resistance as possible. We can conclude that the material that we proposed can recreate its percolating networks after a severe environment change, such as a through cut, with the help of Joule heating.

4.3.2 Reversibility Before and After Rehydration

The conductive pathways in the composite are reversible by the amount of water within the polymer matrix and silver flakes. To show the reversibility of the material, we patterned the composite in a shape of a hollow square with four points of interest (1, 2, 3, and 4) with a diagonal trace that connects points 1 and 3. In each step, the sample image and thermal images at 0 mins and 10 mins of Joule heating (1.5 W or power) are shown in Figure 4.16b. Without any further operations, the diagonal trace should have a higher temperature than

93

other traces when Joule heating was applied to points 1 and 3. This is because the diagonal trace has the shortest path between the two points, so it should have the lowest resistance compared to the trace that connects points 1-2-3 and the trace connecting points 1-4-3, given the same patterned width and thickness. However, if we apply Joule heating on the detouring trace of points 1-2-3 through steps 1 and 2, the conductivity of the detouring trace will be enhanced through the evaporation of localized water. Therefore, we can see multiple hotspots in step 3, which are not only on the diagonal trace but also on the edge traces that connect points 1, 2, and 3. After step 3, we submerged the whole sample in a water tank for 4 hours to rehydrate the sample. During this rehydration process, we hypothesized that the enhanced detouring traces would be removed by introducing water between the polymer matrix and silver flakes. In step 4, we took out the sample from the water bath and removed all remaining water from the sample. To prove our hypothesis, we applied direct voltage on points 1 and 3, and thermal images show that only the diagonal trace has hotspots, which means that the diagonal trace has higher conductivity than other traces. This demonstration shows that the electrical conductivity of the composite can be enhanced by Joule heating or lowered by rehydration. In other words, the material is a reversible conductor based on the amount of water between the composite's material architecture.

4.3.3   A Walker Powered and Controlled through the Composite

The conductivity of the conductive hydrogel composite is high enough to power electric motors from direct current power sources. We chose to use motors to demonstrate the reconfigurability of the composite in practical applications, where electronic devices can be powered through the material that can retain electrical information (an insulator or a conductor) by selectively absorbing or dehydrating water. We constructed a robot leg (Figure 4.17a-c) that used Jansen's linkage mechanism [153, 154] with a simple rotary input (DC geared motor) to mimic the motion of walking and kicking. Figure 4.17d shows a characterization of the motor speed with different resistance values (0.1, 1.5, 1.0, 2.2,
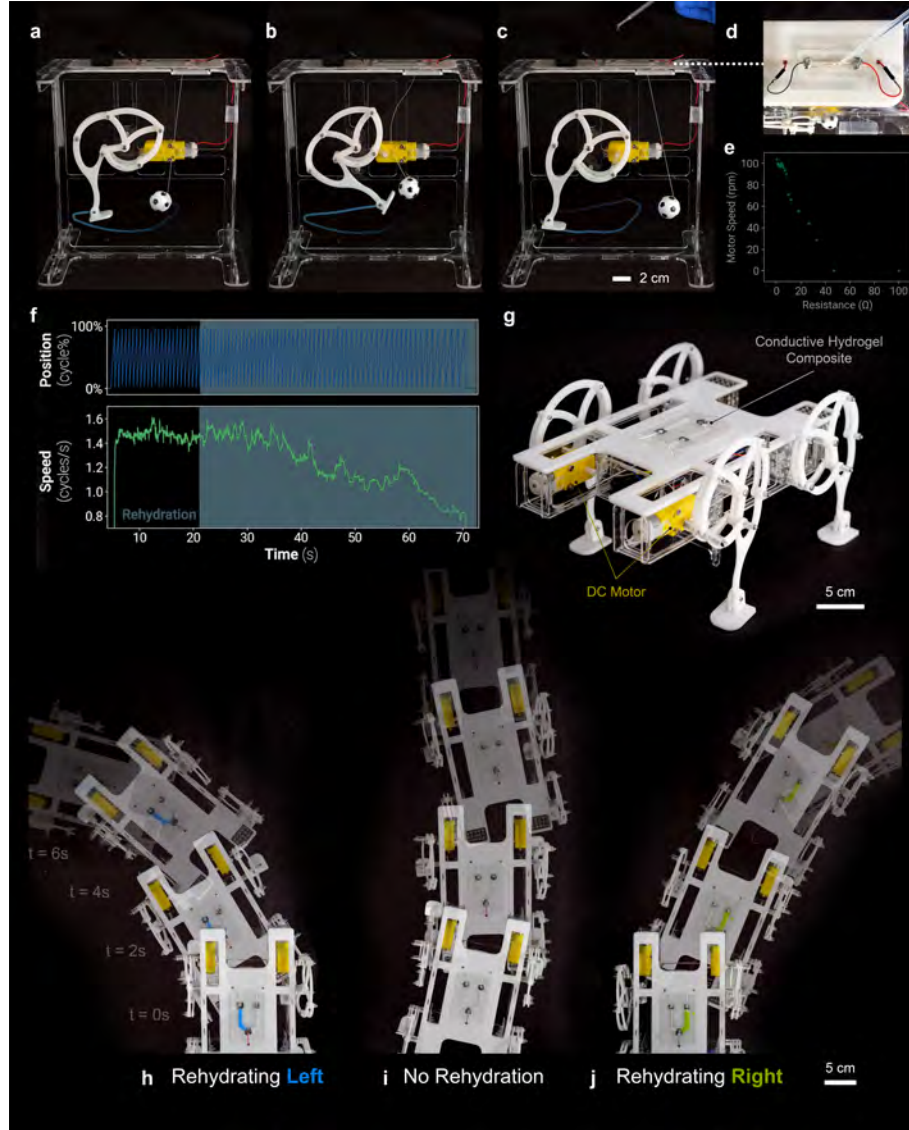
Figure 4.17: Motor reconfiguration for robotic legged locomotion. (**a-c**) A motorized robot leg mimics the motion of walking and kicking by using Jansen's linkage mechanism [153, 154] with a geared DC motor in series with the conductive hydrogel composite connection (top view magnified in **d**). A miniatured football is included for visualization of the overall kicking motion. (**e**) The motor speed characterization using different values of through-hole resistors (0.1, 1.5, 1.0, 2.2, 3.3, 3.9, 4.7, 5.6, 6.8, 8.2, 10, 12, 18, 27, 33, 47, and 100 ohms (**f**) The positions in cycles (blue trajectories in **a-c**; blue curve in **f**) and overall speed (green curve in **f**) of foot motion are analyzed. The motor completely stops 48 seconds after rehydrating the composite. (**g**) A quadruped robot demonstrates the reconfigurability of the conductive hydrogel composite by achieving reprogrammable locomotion behaviors shown in (**h-j**). Only two front legs are actuated while the rear legs are fixed. When both two traces of the composite are dehydrated (**i**), the two legs move at similar speed causing the robot to walk forward. By selectively rehydrating the left (the trace with water dyed with blue, **h**) or the right (the trace with green-colored water, **j**), the gait of the robot can be reconfigured to turn as one leg becomes slower than the other.
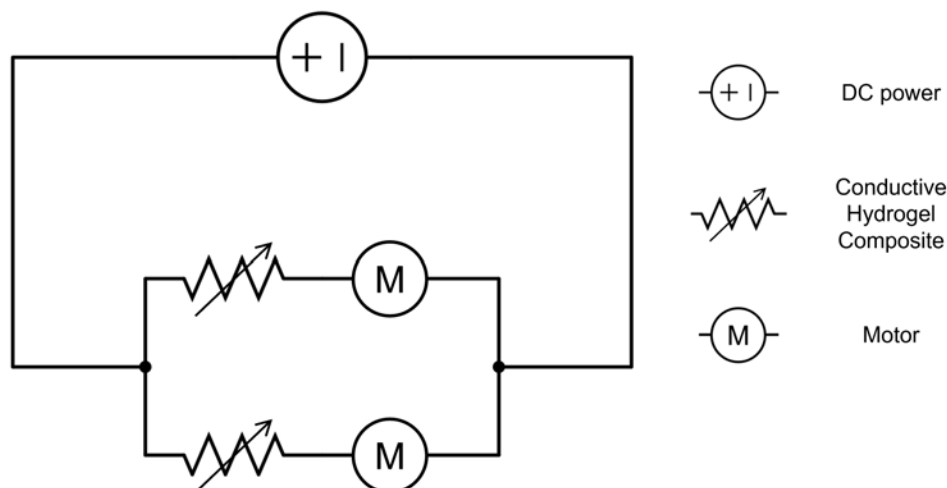
Figure 4.18: A circuit diagram related to the demonstration of the robotic legged locomotion in Figure 4. A portable 5 V battery was used as a DC power source. There are two DC motors used in this demonstration. Each motor is connected to a trace of the conductive hydrogel composite whose resistance is variable based on the dehydration or rehydration processes.

3.3, 3.9, 4.7, 5.6, 6.8, 8.2, 10, 12, 18, 27, 33, 47, and 100 ohms) by connecting through-hole resistors with a motor in series. The motor speed decreased as the series resistance increased, and the motor did not operate anymore with the resistance over 47 ohms. To visualize the performance of the motor and the effect of rehydrating the composite, we recorded the position in one cycle of the foot in the leg and calculated the speed (Figure 4.17f). Before rehydration, the robot leg cycled at higher speeds due to a lower resistance across the conductive trace connection. When rehydrated with the presence of water drops (highlighted in blue in Figure 4.17f), the resistance of the connection increased, which caused the leg to slow down. Then, the motor completely stopped 48 seconds after the rehydration.

We then demonstrated a quadruped robot whose gait can be reprogrammed by reversibly changing the conductivity of the composite (Figure 4.17g). The robot had four limbs; however, only the two front legs can be actuated while the rear legs were fixed. Each leg in the front was connected in series to a trace made of the composite and powered by a portable power bank (UE5044; Energizer) with a capacity of 5,000 mAh and a rated output of 5 V. Based on the circuit diagram of the connection (Figure 4.18), the motor can operate at full speed

when the resistance of the composite is low. However, the motor's speed gets slower with higher resistance of the composite. When the two trace connections were dehydrated by the passive or active dehydration process, the two legs moved at a comparable speed and caused the robot to walk forward (Figure 4.17i). By selectively rehydrating the left trace (blue color in Figure 4.17h) and the right trace (green color in Figure 4.17j), the robot can be reconfigured to walk to the left and right, respectively. Through the reprogrammable robotic walker demonstration, we confirm that the conductive hydrogel composite can pass direct current to power electric motors with its unique properties by reconfiguring intrinsic properties of the material.

4.4 Conclusions

We have reported a conductive hydrogel composite with reconfigurable and reversible percolation networks. The material's conductive properties can vary based on the amount of water inside. The two dehydration methods can increase the conductivity by evaporating water from the material. The composite achieved a conductivity of 1,430 S cm^{-1} after the passive dehydration process. To further evaporate water, we utilized Joule heating by applying a direct current across the patterned composite. The localized heat generated during the active dehydration can accelerate the water evaporation, enhancing conductive networks with an increased effective volume fraction of silver flakes. After the active dehydration, the conductivity was 17,300 S cm^{-1}, around 12 times higher than that of the passive dehydration. On the other hand, introducing rehydration into percolating networks can attenuate the electrical properties of the material, resulting in a dramatic decrease in conductivity (0.0111 S cm^{-1} after the rehydration). More importantly, this transition between high and low conductive states can repeatedly happen. We demonstrated the unique properties by showing reconfigured electrical connections after severe damage or rehydration to the dominant percolating networks. In addition, we built a quadruped robot whose motors were powered

97

through the conductive hydrogel. In this demonstration, the robot's gait was reprogrammed to three different states by reconfiguring the conductivity of the composite. This material, coupled with reconfigurable and reversible conductive properties, contributes to the diversity of soft reconfigurable conductors for wearable electronics or soft robotics.

Chapter 5

Conclusions

5.1 Future Directions

5.1.1 Biocompatibility Evaluation

One of the conductive hydrogel composite's strengths is its mechanical stiffness comparable to biological tissues. This can make the composite a candidate for material options in bioelectronics without the problems related to the mismatch in mechanical properties. However, it should not be used in biological environments without systematic and clinical-grade bioelectronic evaluations. In terms of the host hydrogel material, researchers have examined cell viability and metabolic activity of stem cells in different gel-conditioned media, including no gel, alginate gel, polyacrylamide gel, and polyacrylamide-alginate gel. Based on the results, there was no significant difference in cell viability. They concluded that there are minimal effects of polyacrylamide and alginate hydrogels on cells *in-vitro* and *in-vivo* [155]. However, cell viability is not the only one crietria to decide materials' biocompatibility. According to the international standard ISO 10993, to biologically evaluate medical devices, lots of tests are required, for example, skin sensitization, risk management processes, *in-vitro/in-vivo* cytotoxicity.

Using silver particles as the conductive component could be a problem related to bio-

compatibility. Zhang *et al.* questioned the cytotoxicity of silver ions and nano-sized silver particles. They concluded that both silver particles and dissolved silver ions have unique toxic effects on the cells [156]. On the other hand, Ipe *et al.* reported that no cytotoxicity was observed with a low concentration ($\leq 1\ \mu\text{g mL}^{-1}$) of silver nanoparticles [157]. Since there are mixed opinions about using silver particles in biological environments, the conductive hydrogel composite needs to be tested *in-vitro* and *in-vivo* in terms of biocompatibility.

5.1.2 Anti-Drying

Water, the major component of most hydrogels, can dry out over time, significantly affecting the materials' original properties. For example, the conductive hydrogel composite presented in this Dissertation can become stiffer and less deformable but more conductive after completely drying. The material's properties should not change while in operation; otherwise, the performance of devices is not consistent with the original intention. There have been several attempts to prevent hydrogels from drying or swelling. Yuk *et al.* [158] introduced a method to assemble hydrogels and elastomers through physical anchors activated by UV radiation. Mredha *et al.* [159] presented a non-swellable and non-dryable hydrogel by introducing a method to coat hydrogels with double hydrophobic layers to construct robust permeability barriers. As shown in both works, covering hydrogel with materials that are resistant to drying could keep the hydrogel composite from further drying.

Another way to prevent further evaporation of water can be found in the self-healable conductive composite introduced in Chapter 2. Hydrogel composites may not dry if water in the composites is replaced with some other materials that do not evaporate. Ethylene glycol is one of the candidates for this method since it has almost negligible evaporation rate at room temperature [160, 161]. This could cover one of the most significant limitations of hydrogel-based composites. However, it is unclear whether we can still define the materials as hydrogels or not after replacing water. Additionally, the replacement might disable reversible and reconfigurable conductive networks in the conductive hydrogel composite.

5.1.3 Printability

The conductive hydrogel composites introduced in Chapters 3 and 4 are patterned by stencil printing methods with polydimethylsiloxane (PDMS) masks. These patterning methods using masks usually limit high resolution and size of patterns. Moreover, there is a limited time window for patterning due to the composite's crosslinking process governed by fast radical substitution reactions [162].

One way to overcome the patterning issues is to replace the original initiator, Ammonium persulfate or APS, with another initiator that can be initiated with less time-dependent mechanisms. A water-dispersible TPO-based photoinitiator (906806; Sigma-Aldrich) is a good candidate for the solution. This chemical can be dissolved in water and activated when the particles are exposed to ultraviolet (UV) radiation with specific wavelengths (ranging from 385 to 420 nm) [163]. There are very few UV-curable conductive composites with conductive fillers because a large amount of fillers tend to block the UV radiation; thus, the composite cannot be fully cured. However, the conductive hydrogel composite introduced in this dissertation has a low volume fraction of conductive fillers inside. It allows UV light to penetrate through the composite, resulting in successful cross-linking reactions all over the matrix. The detailed fabrication method, and preliminary results of mechanical properties, electrical properties, and printability are presented in Appendix E.

This new cross-linking method can open up possibilities of using popular 3D printing techniques, including direct ink writing (DIW) or digital light processing (DLP) methods. This may allow the composite to be patterned without using any masks to shape. Moreover, it may enhance the resolution of patterning quality and complexity of the printability (out-of-the-plane) [164].

5.2   Contributions and Lessons Learned

As technologies evolve, we need materials that can perform more than one function simultaneously. Unlike conventional conductors (e.g., copper wires), materials are now required to deform their shape through stretching, compression, bending, or even fracture and self-healing while maintaining adequate electrical conductivity to connect electronic devices. This thesis work introduces one category of those multi-functional materials: a soft and stretchable conductor. More specifically, this dissertation presents how to fabricate the materials, test their mechanical, electrical, and electromechanical properties, and demonstrate them in practical use cases.

One of the most facile and reliable ways to create these material architectures is to introduce conductive fillers into stretchable polymer networks. In this dissertation, all the introduced composites used silver as the conductive component on account of its high electrical conductivity ($\sigma = 6.3 \times 10^7$ S m^{-1}) [73]. Other functions besides electrical conductivity vary based on the type of binding materials. Chapter 2 showed an anchoring mechanism between stretchable and hydro-transferrable film and alloy of silver nanoparticles and eutectic gallium-indium. With a bi-phasic host material (stable in two states, e.g., liquid and solid), I presented a conductive ink that can pattern any shape of digital circuits using a direct ink writing method. It is also possible to enable the material to heal itself after damage by utilizing dynamic hydrogen bonding between polymer chains. However, the abovementioned materials require a large volume fraction of conductive fillers to achieve percolating networks within the composites. To reduce the silver inclusions, introducing microscopic structural changes could be helpful. For example, silicone beads whose surface is covered by a thin conductive layer can confine silver particles in the composite, decreasing in conductive filler amount while maintaining dominant percolating pathways.

Another way to achieve electrical conductivity with a small amount of silver is to utilize the intrinsic features of hydrogels. Hydrogels are cross-linked polymeric networks mostly filled with water. In Chapter 3, I presented how to form percolating networks in a conductive

hydrogel composite through the partial dehydration process. The water evaporation enables the formation of electrical connections between silver flakes within a short amount of time. One of the lessons learned from this work is that controlling water content in a conductive hydrogel composite can affect the electrical properties of the material. As shown in Chapter 4, I showed reconfigurable electrical networks by increasing or decreasing the amount of water in the hydrogel composite. These processes are reversible and repeatable, allowing the composite to function either as an insulator or a conductor.

Throughout the works presented in this dissertation, I learned how to introduce specific functionalities into host materials through various fabrication methods. Then, I conducted experiments to characterize the functions, including mechanical, electrical, and electrome-chanical characterizations. Lastly, I built mechanical systems to demonstrate the applications of the materials in soft robotics, wearable technologies, and bioelectronics. With this knowl-edge and experience, I hope to keep contributing to the building blocks for multi-functional soft materials.

Appendix A

A.1   Detailed Fabrication Process of EGaIn-Assisted Sintering of Silver Nanoparticles Ink

Conductive silver nanoparticle (AgNP) ink (NBSIJ-MU01-MITSUBISHI) was used as dispersed nanoparticle ink in inkjet printer after filtering with a 5 µm sized membrane filter prior to filling the cartridge. In order to produce eutectic gallium indium (EGaIn), the gallium and indium precursors were purchased from (Gallium Source). EGaIn was obtained by stir mixing 75 wt% gallium and 25 wt% indium at 190 °C on a hotplate for 12 hours. The Polydimethylsiloxane (PDMS) materials used as packaging materials for electronic tattoos and tensile samples are Sylgard 184 (Dow Corning). The 2-part PDMS as mixed with 10:1 ratio and cured at 60 °C for 1 hour, then post-cured at 100 °C for 3 hours. Step-by-step guide for fabrication and interfacing process is depicted in Table A.1 and A.2.

A.2   Material Characterization

Scanning electronic microscopy (SEM) and energy dispersive X-ray spectroscopy (EDS) are used to examine the features and composition of the AgNP-Ga-In mixture. Micrographs of the conductive ink before and after EGaIn treatment are shown in Figure A.1A and A.1B, respectively. At lower magnification, a large number of small cracks within the conductive

Table A.1: Step-by-step fabrication process of electrically conductive traces on temporary tattoo papers
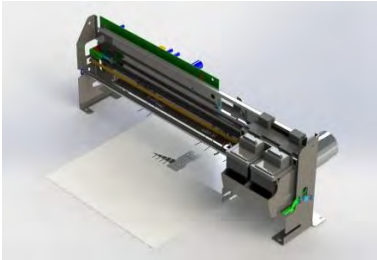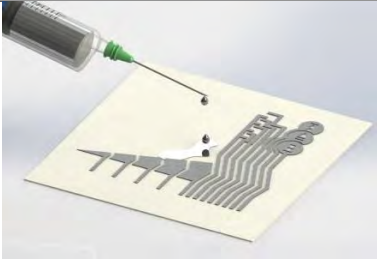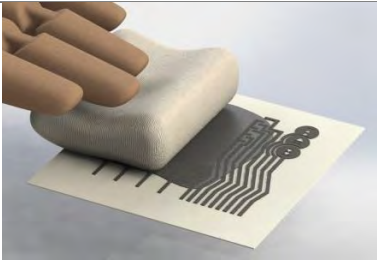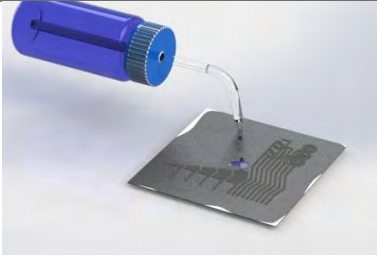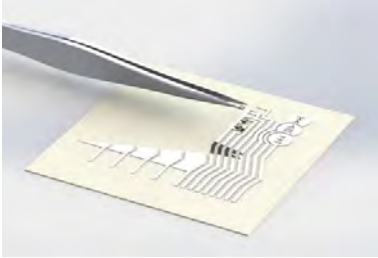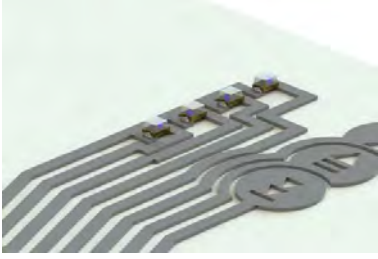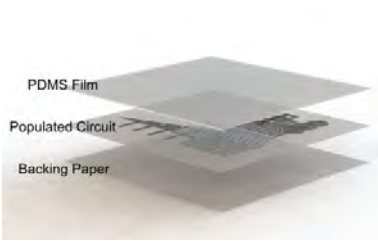
Step	Description	Illustration
1	Two desktop inkjet printers were used to printthe conductive traces using silver nanoparticle(AgNP) ink. We used both thermal drop-on-demand (HP, 840C) and piezo-electric drop-on-demand (Canon, MX922) print heads. Settingsfor Canon MX922: Media Type: Glossy PhotoPaper, Print Quality: High, Grayscale Printing,Brightness: Dark.	
2	A few drops of eutectic gallium indium (EGaIn, 75% gallium, 25% Indium Eutectic alloy) are deposited on the printed AgNP circuit to form a thin layer of EGaIn on the print.	
3	The added EGaIn is rubbed on to the printed circuit using a lint-free cloth or a cotton swab. A new cloth or cotton swab should be used, if needed.	
4	The excess EGaIn is removed by applying a weak aqueous solution of acetic acid (2 wt%) as a reducing agent for 5 to 10 seconds, followed by rinsing with water. Increasing the duration of this process will create defects in the traces and reduce their conductivity.	
5	In the last step, the cleaned traces are dried in the oven at 60 °C for 30 to 45 minutes. Now these electrically conductive traces can be used in different types of electronic circuits and be transferred to skin like a regular temporary tattoo or be transferred over complex 3D surfaces using a hydrographic technique.	

Table A.2: Step-by-step fabrication process of electronic tattoos with mounted microelectronic chips

Step	Description	Illustration
1	The prepared conductive AgNP-Ga-In traces are populated with microelectronic chips. First two drops of EGaIn are added to the prepared traces, where the electronic terminals of the chips will be in contact with the circuit.	
2	In this step, the microelectronic chips are placed carefully in the designed locations. This step should be repeated until all the microchips are placed in the proper location between conductive traces.	
3	The microelectronic chips are finally soldered to AgNP-Ga-In traces chips by Gently blowing HCl vapor to the terminals [92]. The HCl vapor removes the ~ 0.5–2 nm thick Ga_2O_3 skin layer on EGaIn drops and brings the electronic terminals and traces in full contact.	
4	The populated circuit is coated with a thin layer of PDMS to encapsulate the entire electronic circuit. The PDMS (Sylgard 184) is diluted in hexane with a mass ratio of 1:3.	

trace are clearly visible. These cracks are formed on the tattoo film because of solvent evaporation and consequent contraction of silver ink after printing. However, most of the small cracks are completely filled with the liquid metal after the treatment as shown in Figure A.1B. As observed at higher magnification micrographs, in Figure A.1C and A.1D, the liquid metal also causes the AgNP to cluster into aggregates that are at least 5 × larger than the individual particles. These aggregates (Figure A.5) form connected agglomerates with increased surface roughness (Table A.3) may contribute to the improved global conductivity.
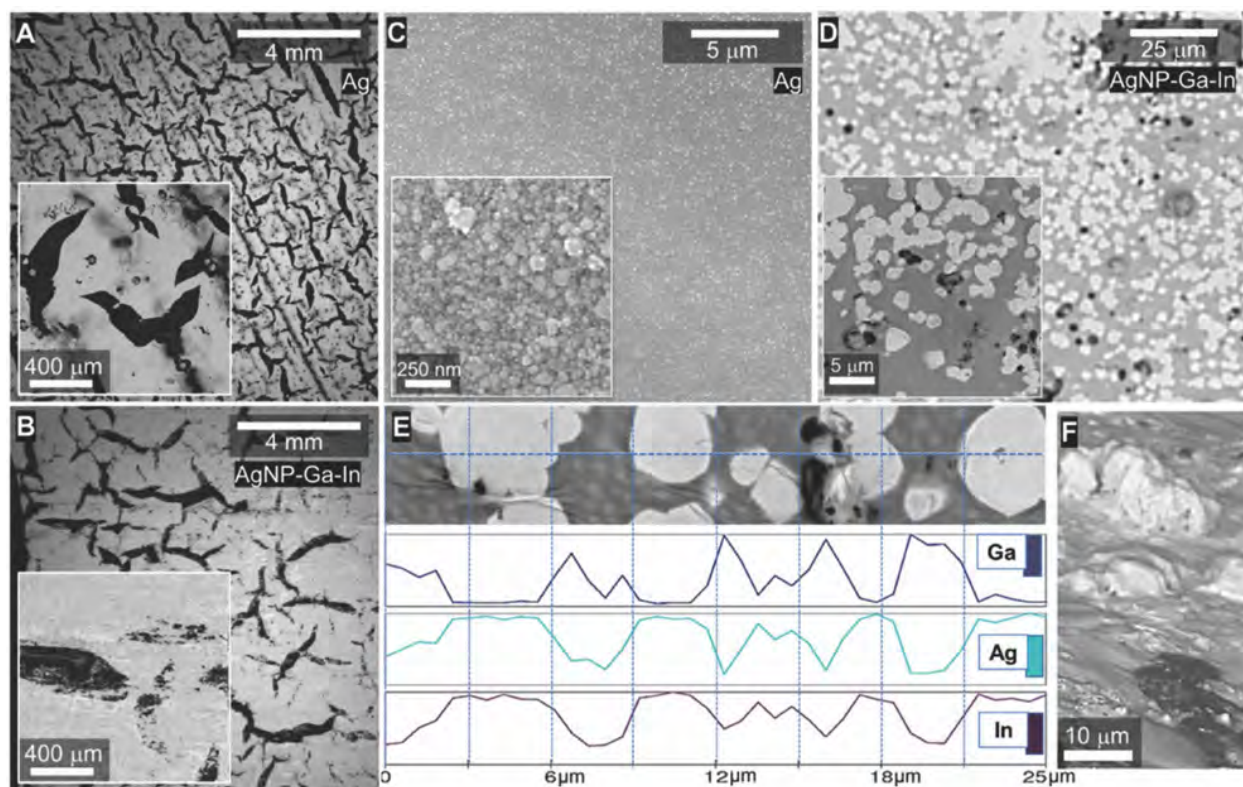
Figure A.1: Characterization of printed AgNP and AgNP-Ga-In traces. **A**, microcracks in printed AgNP, **B**, reduced crack density after EGaIn deposition, microscopy images of: **C**, printed AgNP and **D**, EGaIn-coated AgNP on temporary tattoo film. **E**, Energy-dispersive X-ray spectroscopy (EDS) line analysis of the conductive traces with bright and Gray coating regions. **F**, Formation of Ag-Ga-In "mountains" over Ga rich areas.

Referring to Figure A.1E, EDS analysis performed over a 25 µm long scanning line shows that Ag and In concentration profiles are similar to each other but opposite with respect to the Ga profile. In particular, higher amounts of Ag and In and low amounts of Ga are found on the white areas, which correspond to the location of AgNP-Ga-In clusters. In contrast, higher concentrations of Ga are detected in the gray areas outside the clusters. Note that both the white and gray areas in these images are located within the printed AgNP-Ga-In trace. Additional EDS analysis (Figure A.6), confirms that within the Ga-rich regions, the Ga:In ratio is $\approx 3:1$ (i.e., similar to that of the original EGaIn alloy), while on the AgNP-Ga-In clusters it is $\approx 1:2$. Referring to Figure A.1F, an isometric view of the sample shows that "mountains" of nanoparticle clusters protrude out of the surface (Figure A.6).

A.3 Conductivity Measurement

In order to determine the volume conductivity of traces composed of AgNP and AgNP-Ga-In, the resistance of traces were first measured with a digital multimeter (Agilent 34401A). Considering the known length (80 mm length) and width (1.5 mm) of the printed traces, thickness of each sample was measured through capturing the cross-section through scanning electron microscopy. As shown in Figure A.2, the thickness of the AgNP layer is approximately 450 nm while the thickness of AgNP-Ga-In traces varies between 500 nm and 1 μm. The large range of thickness for the AgNP-Ga-In traces is due to the formation of aggregated "mountains" on the surface of the traces (see Figure Figure A.5 for full details). Here, 450 nm and 1 μm are estimated for the thicknesses of AgNP and AgNP-Ga-In traces, respectively. The estimated conductivity based on these geometric properties are 3.5 S m^{-1} for AgNP and 4.85×10^6 S m^{-1} for AgNP-Ga-In traces.
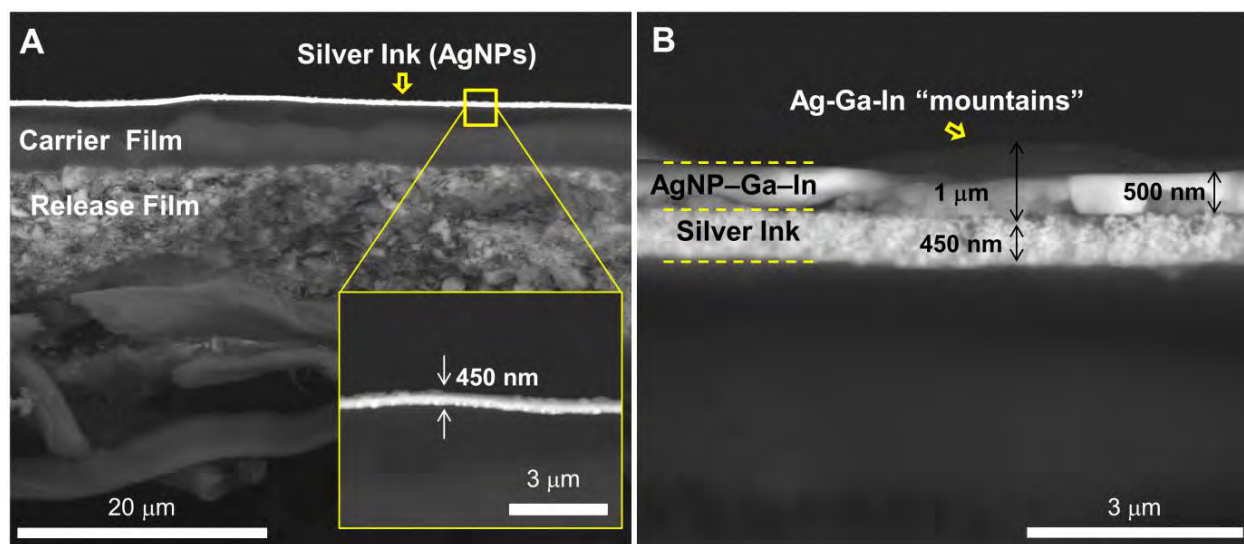
Figure A.2: Cross-section micrographs for estimating the electrical conductivity; **A**, printed silver ink composed of silver nanoparticles (inset: zoomed-in image shows the thickness of silver ink about 450 nm), **B**, crosssection of conductive AgNP-Ga-In traces along with measured thickness of each layer.

A.4 Effective Electrical Conductivity

Composite materials consisting of different electrically conductive phases result in a large scale effective conductivity. Since the arrangement of the phases with high and low conductivity is not known, it is challenging to predict the overall conductivity based on the electrical properties of each phase. However, it is possible to accurately predict the upper and lower bounds of electrical conductivity in a composite material [165, 166]. Using Equation A.1 and A.2, that were introduced by Hashin and Shtrikman [167], the conductivity bounds for a two-phase composite material can be estimated.

$$\sigma_{upper} = \sigma_h \frac{v_f}{\frac{1}{\sigma_l - \sigma_h} + \frac{1 - v_f}{3\sigma_h}} \tag{A.1}$$

$$\sigma_{lower} = \sigma_l \frac{v_f}{\frac{1}{\sigma_l - \sigma_h} + \frac{v_f}{3\sigma_l}} \tag{A.2}$$

Here, σ presents electrical conductivity values, while the subscripts h and l indicate the phases with high and low electrical conductivity, respectively. Also, v_f is the volume fraction of the integrated phase with the lower conductivity compared to the other phase in
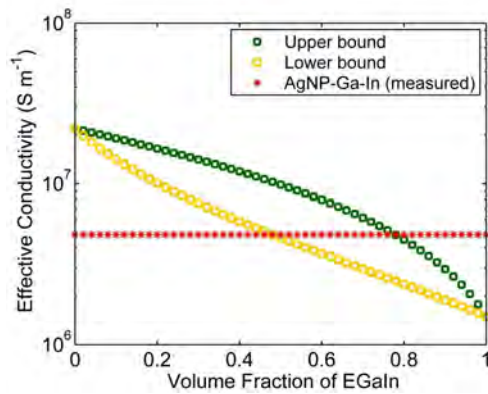
Figure A.3: Electrical conductivity bounds for AgNP-Ga-In based composites as a function of EGaIn volume fraction. The measured electrical conductivity of traces composed of AgNP-Ga-In alloy is shown on the plot which is closer to the lower bound of the predicted electrical conductivity.

composite. Here, the nominal conductivity of the silver nanoparticles as they are printed on Mitsubishi Resin Coated Papers NB-RC-3GR120 varies from 1.1 to 2.2×10^7 S m^{-1} and so we let $\sigma_h = 2.2 \times 10^7$ S m^{-1}. The measured conductivity of traces composed of pure EGaIn was found to be between 1.5×10^6 S m^{-1} and 1.8×10^6 S m^{-1} and so we let $\sigma_l = 1.5 \times 10^6$ S m^{-1}. These values are considered in order to predict the overall conductivity of the AgNP-Ga-In traces. As shown in Figure A.3, the effective conductivity is highly dependent on the volume fraction of EGaIn and varies from maximum conductive ($v_f = 0$, i.e., pure AgNPs) to the lowest conductivity ($v_f = 1$, i.e., pure EGaIn). As illustrated in this plot, the measured conductivity of the traces falls partially in this region. It should be mentioned that due to the presence of cracks and formation of particles (as seen in Figure Figure A.6), the lower bound of the conductivity is over predicting the effective electrical conductivity of AgNP-Ga-In traces. Furthermore, the conductivity of pure AgNPs cannot be reached to the nominal conductivity because of the presence of the crack in the prints. EGaIn bridges over the cracks and fills them while forming a new composition by alloying to the silver nanoparticles.

A.5 Smearing Test

In order to explore the resistance of AgNP-Ga-In circuits to smearing, we simulated a scenario with a "pin-on-disk" test with custom-designed equipment, at room temperature (20 °C). As shown in Figure A.4, the "pin-on-disk" equipment consists of two main components: a turntable with controlled rotation speed (here 50 rpm), where the material to be tested is fixed; and an auxiliary arm where a pin is fixed. A disk of 50 mm diameter from the TTP was used over which a 10×10 mm AgNP-Ga-In square was deposited with the aforementioned method. The pin is a polytetrafluoroethylene (PTFE) ball with a 10 mm diameter. The tests were performed with different applied forces (0.1 N, 0.5 N, 1 N and 5 N) during 20 cycles with a radius of 12 mm. For the lowest force (0.1 N) a test of 250 cycles was also performed. The PTFE ball was observed under optical microscope (Axiolab from Zeiss, equipped with

CCD-Iris, Sony, and video cameras) before and after each test to assess the smearing of AgNP-Ga-In over the polymeric pin AgNP-Ga-In. As shown in Figure A.5, no significant sign of AgNP-Ga-In smearing is observed. Instead, the PTFE pin itself is worn out under forces over 0.5 N and for the case of 250 repetitions under 0.1 N applied force.
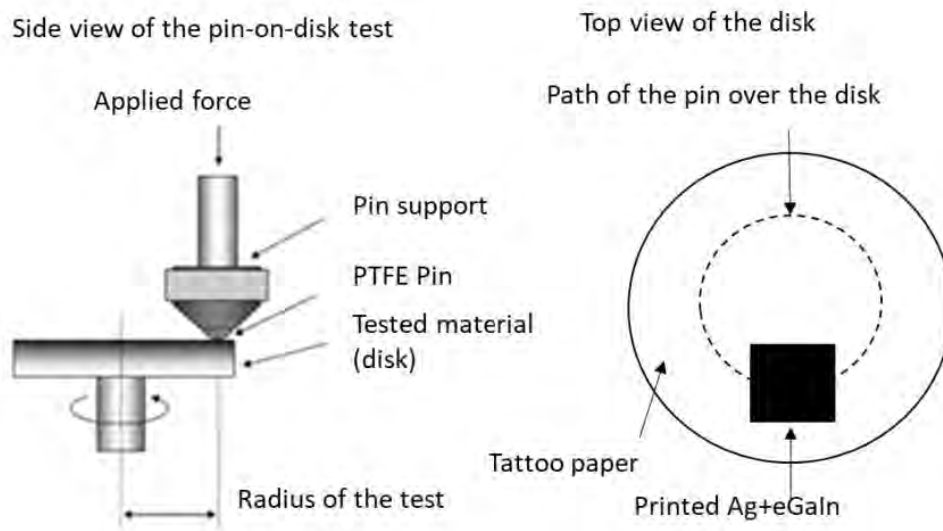
Figure A.4: Schematic of the pin-on-disk test setup composed of a turntable and a polytetrafluoroethylene (PTFE) pin.
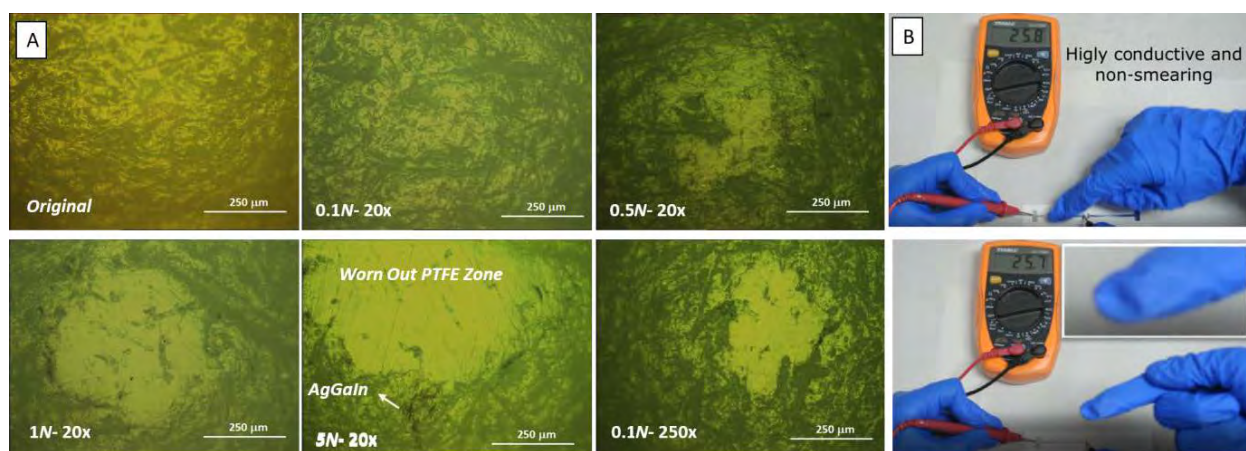
Figure A.5: Smearing test of silver nanoparticles sintered with EGaIn deposition. **A**, Optical images of the PTFE pin subjected to different level of forces and number of cycles to demonstrate the wearing and smearing behavior of printed AgNP-Ga-In traces. **B**, Snapshots of touching the trace without signs of smearing.

A.6 Elemental Analysis

Referring to Figure A.6A and A.6B, additional SEM images from different view of a AgNP-Ga-In circuit show mountain-like AgNP-Ga-In aggregates rising above a relatively flat Ga-rich film. A cross-sectional view is presented in Figure A.6C, which shows the distinct layers of the thin-film circuit. This includes (from bottom) (i) the backing paper, (ii) the release film (~ 12 µm), (iii) the carrier film (~ 5 µm), and (iii) the printed AgNP trace (~ 450 nm) which was taken into account when calculating the conductivity values. When in touch with water, the release film dissolves away and allows the carrier film to detach from the backing paper. The printed carrier film can be then transferred over an object or the skin. The cross-section measurement was performed on samples that were fractured after being frozen in liquid
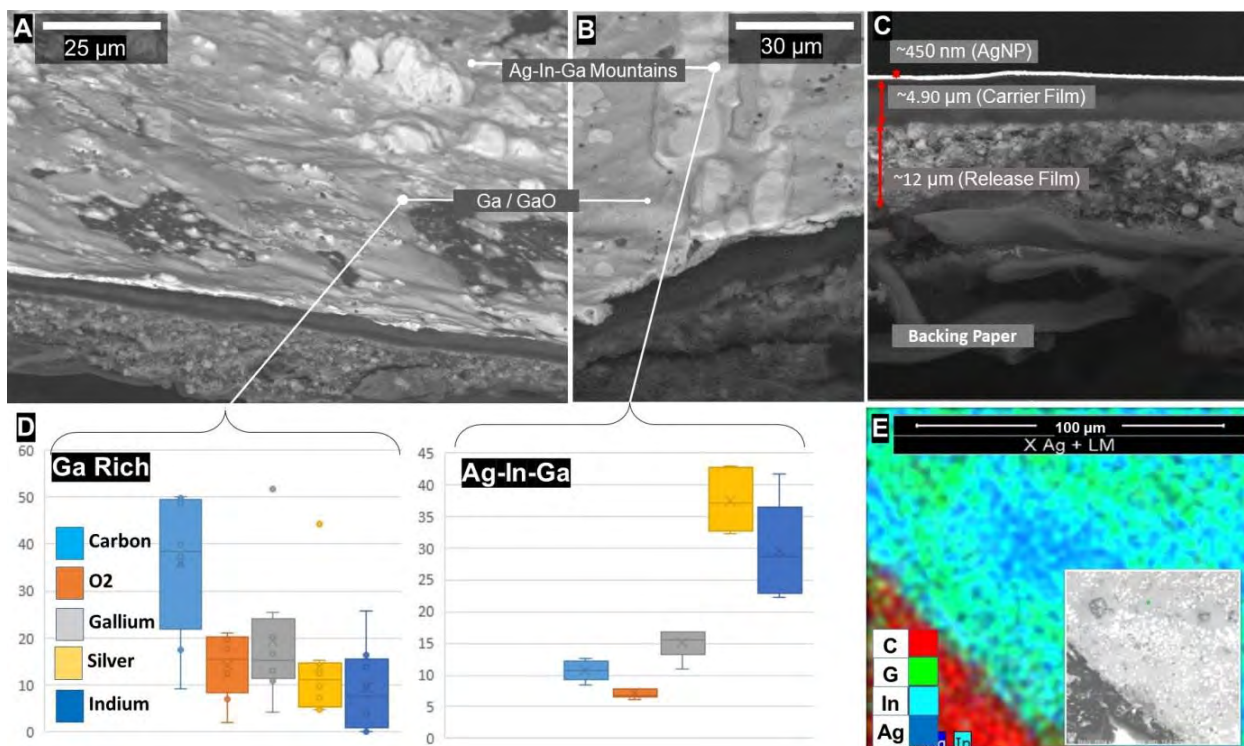
Figure A.6: Elemental analysis of AgNP-Ga-In traces. **A–B**, SEM images of the AgNP-Ga-In coating showing mountain-like aggregates of AgNP-Ga-In formed over a relatively flat Ga-rich film. **C**, SEM image of cross-section showing the different layers of the thin-film circuit; the cross-section is prepared by fracturing the sample after being frozen in liquid nitrogen. **D**, EDS analysis presenting relative elemental concentrations averaged over 12 measurement locations—6 each for Ga-rich (grey) and AgNP-Ga-In "mountain" regions (light grey). **E**, Elemental map taken near the edge of a EGaIn coated AgNP trace; the exposed (i.e., uncoated) tattoo paper corresponds to the carbon-rich region.

nitrogen.

Elemental measurements of the EGaIn-coated AgNP traces are presented in Figure A.6D. EDS analysis was performed on twelve points, six of them over the Ga-rich areas and the other six over the AgNP-Ga-In clusters. The average and standard deviation of Ag, Ga, In, C, O, elements are presented, which is in agreement with the linear EDS analysis presented in A.1E. The considerably higher concentrations of carbon detected in the Ga-rich areas may be due to the lower thickness of the coating in those regions. Since the AgNP-Ga-In aggregates rise hundreds of nanometers above the TTP substrate, the underlying C-rich substrate has less influence on the EDS measurements. An elemental map taken near the edge of a printed trace is presented in A.6E.

A.7   Surface Roughness

The surfaces of the tattoo paper at the different stages of the process, pristine, after AgNP printing and after liquid metal sintering, were characterized by Alicona Infinite Focus Microscopy (IFM) equipment, over 3259×3144 points in a 10×10 mm^2 area. The characterization allowed quantifying the surface roughness parameters: average height of selected area (S_a), root-mean-square height of selected area (S_q), average maximum peak height of selected area (S_p) and average maximum valley depth of selected area (S_v).

Table A.3: Surface roughness measurement conducted by Alicona Infinite Focus Microscopy

Sample	S_a (µm)	S_q (µm)	S_p (µm)	S_v (µm)
TTP	1.462	1.957	52.874	7.808
TTP + Ag	1.186	1.518	48.805	17.519
TTP + Ag + EGaIn	1.389	1.758	50.647	12.653

As demonstrated in Table A.3, the pristine tattoo paper is characterized by high peaks and comparatively not very deep valleys. This is a consequence of the morphology of the underlying paper which can be also seen in Figure A.5. After printing silver nanoparticles, the main feature is the increase in the valleys depth, due to the formation of cracks, as also observed in the SEM micrographs. After the EGaIn deposition, the valleys depth is decreased, since the EGaIn fills some of the formed cracks. But also there is a slight increase in peak height average, which can be explained by formation of AgNP-Ga-In mountains, as observed also in Figure A.5.

A.8   Multiple Depositions of AgNP

In order to find out the effect of thickness of AgNP layer on electrical properties, the printing process is repeated for desired number of times. First, line-shape samples (40 mm × 1 mm) with single, double, and triple prints of AgNPs were prepared, and then EGaIn was deposited on them to create conductive AgNP-Ga-In traces. The printing process was conducted using Fujifilm Dimatix material printer that allows precise multiple deposition of the silver ink without lifting the substrate as well as alignment with the integrated camera. Then EGaIn was simply deposited and cleaned by following the steps explained in the fabrication process (See Table A.1). Single, double, and triple depositions of AgNPs which indicated different layer thicknesses of the printed silver nanoparticle, resulted in average resistance of 190 MΩ, 180 MΩ, and 164 MΩ, respectively. After EGaIn deposition, the resistance of 17.6 Ω, 17.2 Ω, and 15.2 Ω was obtained for these specimens. This result implies that the thickness of the AgNP layer has minimal effect on the conductivity of the traces both before and after deposition. Moreover, these similar electrical properties after deposition of EGaIn can suggest that EGaIn only acts on the top surface of the printed AgNP ink. This result is consistent with SEM images (Figure A.1 and A.6), which shows the formation of AgNP-Ga-In mountains after the deposition of EGaIn on printed silver ink.

Appendix B

B.1 Electrical Conductivity

We first investigated the effects of PDMS@Ag on the conductivity of the composite by measuring conductivity as a function of total Ag content at fixed volumetric fractions of PDMS@Ag (ϕPDMS@Ag = 40 vol%) (Figure B.1a). Conductivity of composites with and without PDMS@Ag increases as the silver content increases (ϕAg). However, for the same silver content, the presence of PDMS@Ag leads to a significant increase in the electrical conductivity (up to 139 times). For example, with a low Ag content (3 vol%), we can engineer composites with PDMS@Ag inclusions that have an electrical conductivity greater than 10^3
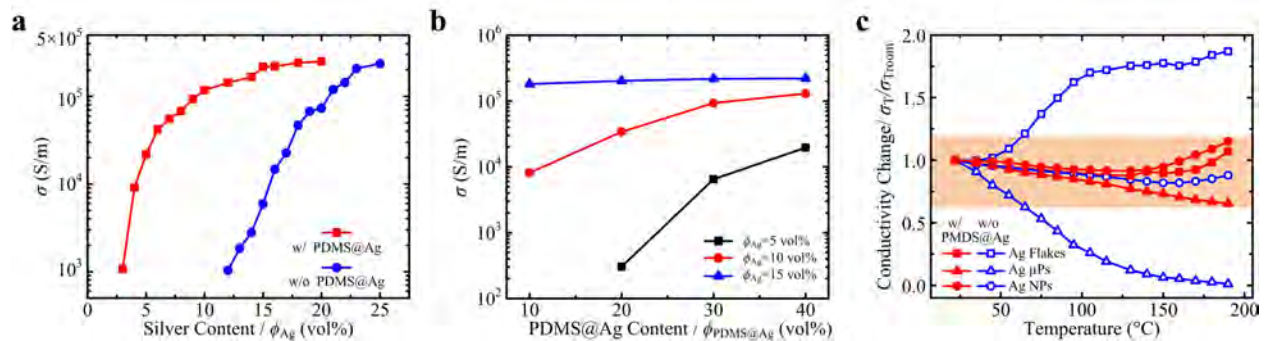
Figure B.1: Electrical conductivity. **a**, Conductivity of Ag-PDMS composites with/without PDMS@Ag beads as a function of total Ag content. The content of PDMS@Ag is fixed at 40 vol% for the composite with PDMS@Ag. **b**, Conductivity of PDMS@Ag/Ag flake/PDMS as a function of PDMS@Ag content. **c**, Electrical conductivity change of elastic conductors for composites with different Ag fillers (Ag flakes, Ag microparticles, and Ag nanoparticles) and with/without PDMS@Ag as a function of temperature. The shaded region highlights the relatively small deviation of conductivity as the temperature increases, which predominately occurs for composites with PDMS@Ag beads.

S m^{-1}, whereas the composite without PDMS@Ag needs a 12 vol% Ag content. Likewise, highly conductive (1.17×10^5 S m^{-1}) PS3 composites can be achieved with ϕAg = 10 vol%. For comparison, a Ag flake/PDMS composite with uniformly distributed filler particles requires ϕAg = 21 vol% to achieve a similar conductivity (1.19×10^5 S m^{-1}). The spatial confinement and phase segregation of Ag-rich portions observed for PDMS@Ag promote percolation in these composites. As illustrated in Figure B.2, the Ag flakes are confined to the grain boundaries between the PDMS@Ag inclusions. Thus, the actual volumetric fraction of Ag flakes in the PDMS matrix between PDMS@Ag beads is ϕAg/PDMS = ϕAg/$(1 - \phi$PDMS@Ag$)$, which explains the higher overall conductivity of the composite. In addition, the Ag shell layers that coat the PDMS@Ag beads provide continuous electrical connections between the percolating networks of Ag flakes that surround them. The distribution of PDMS@Ag beads aids in the formation of long-range conductive pathways throughout the entire composite. Figure B.1b shows the conductivity of PS3 composites as a function of the PDMS@Ag content (ϕPDMS@Ag) at fixed total volumetric fractions of silver (ϕAg = 5, 10, and 15 vol%).
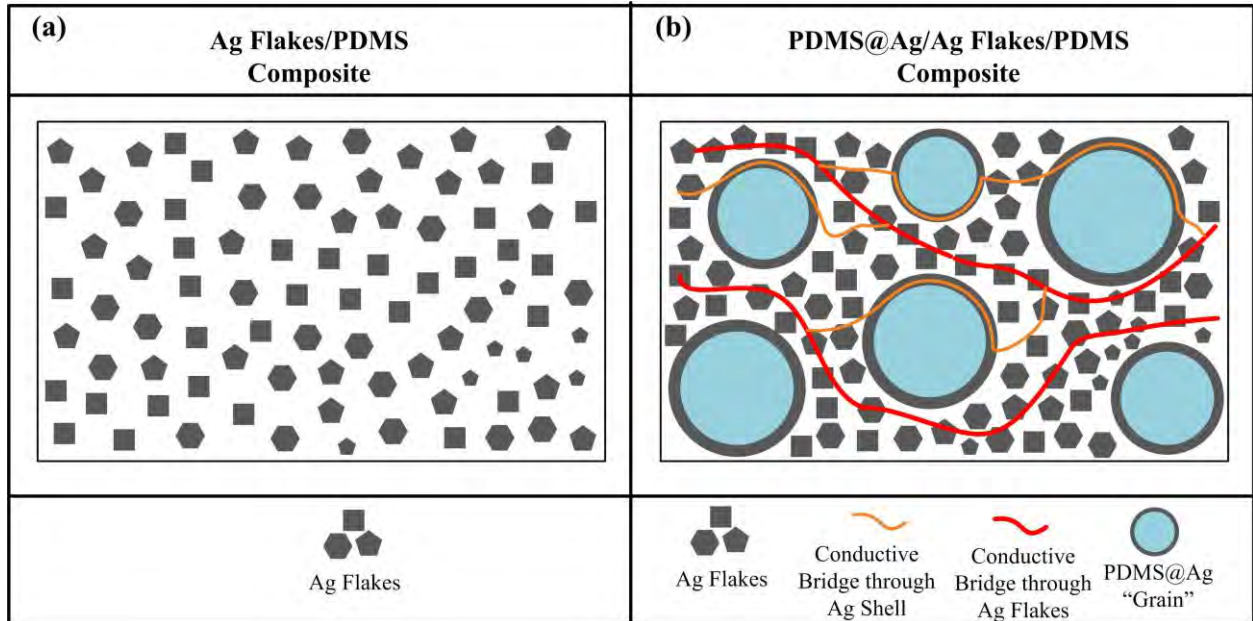
Figure B.2: 2D Schematic illustration of the comparison between **(a)** Ag flakes/PDMS and **(b)** PDMS@Ag/Ag Flake/PDMS PS3 composite. PS3 composite shows phase segregation of Ag flakes between "grains" (denser Ag flakes) and two types of conductive pathways helping enhancement in electrical conductivity.
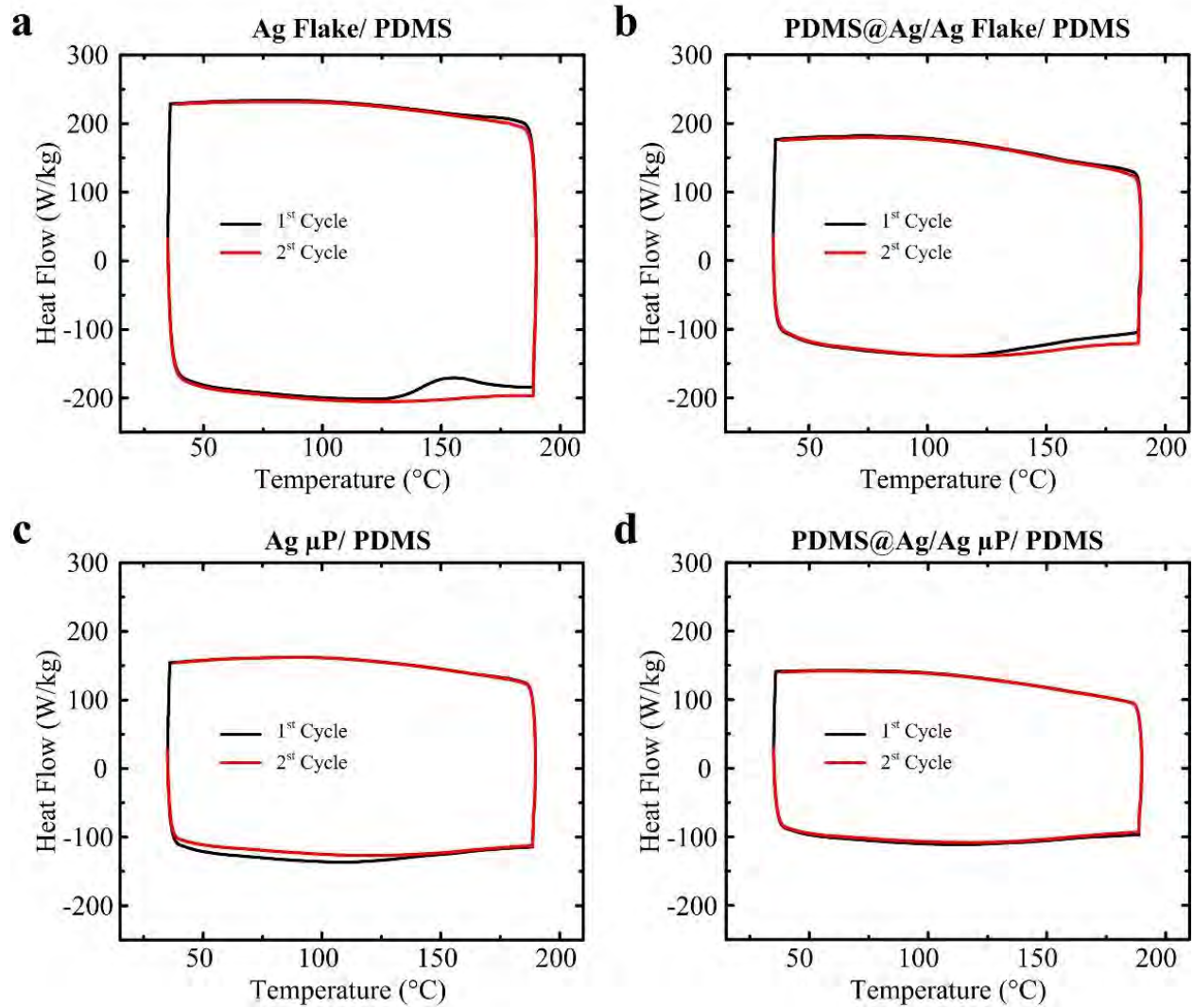
Figure B.3: Differential scanning calorimetry (DSC) measurements. **(a)** Ag flake/PDMS, **(b)** PDMS@Ag/Ag flake/PDMS PS3 composite, **(c)** Ag microparticle/PDMS, and **(d)** PDMS@Ag/Ag microparticle/PDMS PS3 composite.

For composites with low ϕAg = 5 or 10 vol%, the conductivities dramatically increase with increasing ϕPDMS@Ag. For ϕAg = 15 vol%, the conductivity exhibits only a slight increase when adding PDMS@Ag due to the saturation of percolation pathways.

We then measured the electrical conductivity change of composites with and without PDMS@Ag as a function of temperature for different Ag fillers, that is, Ag flakes, Ag microparticles, and Ag nanoparticles (Figure B.1c). We used 40 vol% PDMS@Ag along with 12 vol% total Ag content for all composites with PDMA@Ag inclusions. For each composite, we

adjusted the amount of Ag fillers (i.e., 23 vol% for Ag flakes and 22 vol% for Ag microparticles and nanoparticles) so that they would have similar initial conductivities at room temperature. Unlike significant negative or positive temperature coefficients of resistance measured for Ag flake/PDMS or Ag microparticle/PDMS, respectively, the conductivities of composites with PDMS@Ag vary across a comparatively small range (highlighted in the plot), demonstrating thermally stable conductivity in the PDMS@Ag composites. For example, the conductivity of the PS3 composites changes by 7% when heated to 190 °C, whereas the increase for the Ag flake/PDMS composites is 87%. Generally, as temperature increases, the PDMS matrix expands. For anisotropic particles like Ag flakes, the thermal expansion of the surrounding PDMS may create additional percolating pathways and subsequently increase electrical conductivity. For isotropic particles like Ag microparticles, the thermal expansion of the surrounding PDMS can disrupt these percolating pathways and subsequently decreases electrical conductivity. With PDMS@Ag beads, additional Ag fillers are excluded from the volume that is occupied by the PDMS core of the bead. Thus, microstructural changes due to thermal expansion have less of an impact on percolation pathways in composites containing PDMS@Ag beads relative to composites with only Ag fillers.

The small particle size of Ag nanoparticles (< 100 nm) results in low TCR for Ag nanoparticles/PDMS composites due to the close proximity between adjacent Ag nanoparticles, which
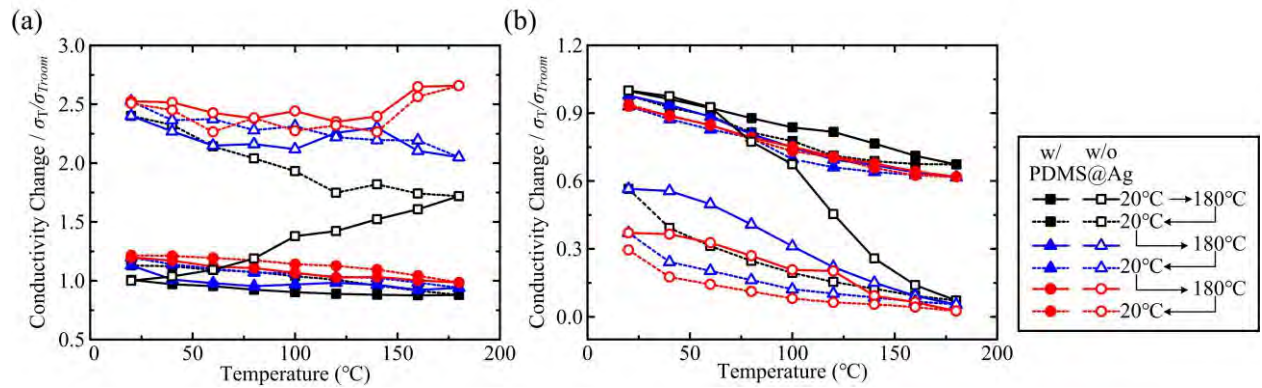
Figure B.4: Electrical conductivity change of elastic conductors for composites with/ without PDMS@Ag as a function of cyclic temperature loading for multiple temperature cycles for: **(a)** Ag flakes, and **(b)** Ag microparticles.
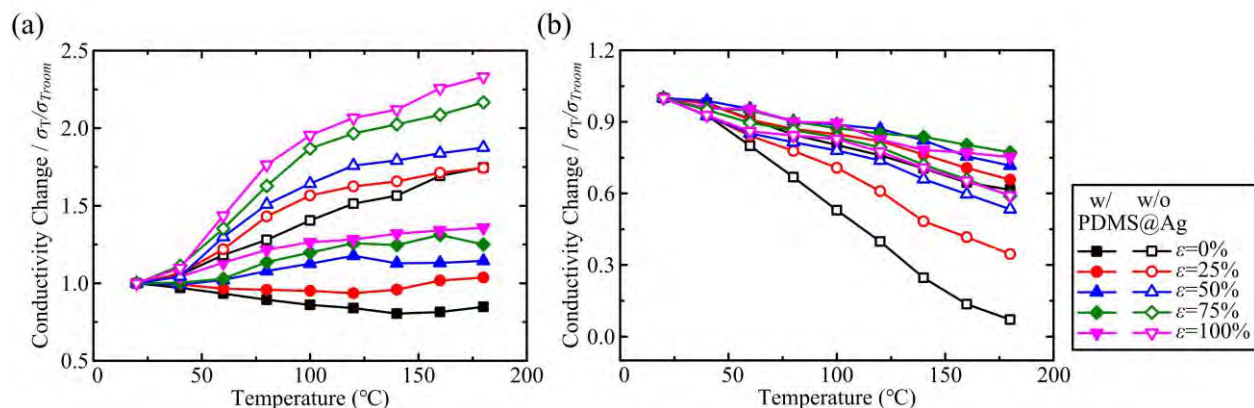
Figure B.5: Electrical conductivity change of elastic conductors for composites with/ without PDMS@Ag as a function of temperature at different strains: **(a)** Ag flakes, and **(b)** Ag microparticles.

limits the degradation of the percolating network from the thermal expansion of the surrounding PDMS matrix. Therefore, the addition of PDMS@Ag beads does not have a significant effect on further reducing the influence of temperature on electrical conductivity. Differential scanning calorimetry (DSC) (Figure B.3) confirms no phase change of silver fillers for the composites with and without PDMS@Ag. As shown in Figure B.4, the PS3 composites exhibit strong thermal stability (i.e., low change in electrical conductivity under cyclic heating and cooling). We also measured the conductivity change of elastic conductors with and without PDMS@Ag beads as temperature increased while the material was loaded in a stretched state. These results (Figure B.5) also demonstrate the suppression effect of the PDMS@Ag beads and their ability to maintain thermal stability. In summary, the results in Figure B.1 suggest that the material architecture of PDMS@Ag/Ag filler/PDMS composites exhibit a dramatic enhancement in electrical conductivity and robust thermal stability.

B.2   3D Percolation Theory of PS3 Composites

To evaluate the electrical properties of the core-shell silver-coated poly(dimethylsiloxane) (PDMS) bead-based composites (Phase-Segregated Silver-Silicone composites or PS3 composite), we fabricated samples with and without the PDMS beads with different silver contents and calculated conductivity based on their resistance information (Figure B.6a). We used the
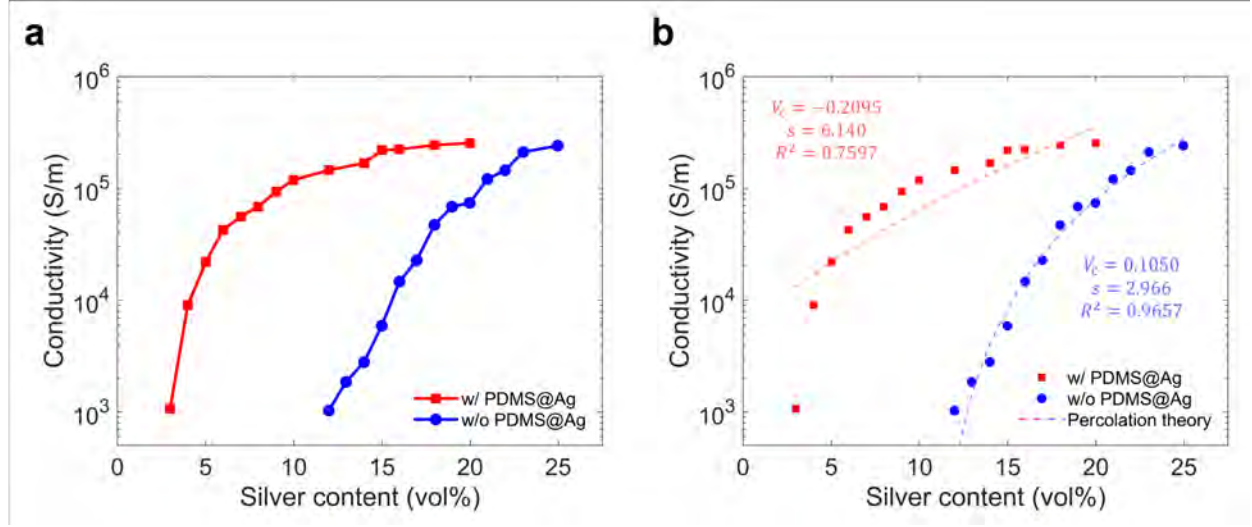
Figure B.6: **(a)** Experimental data of conductivity of PS3 composites based on volume fraction of silver flakes with/without Ag-coated PDMS beads. **(b)** The fitting curves based on the percolation theory of with/without Ag-coated PDMS beads in the composites are overlaid on experimental data.

3D percolation theory described in equation B.1 by fitting the experimental data, where σ and σ_0 refer to the conductivity of the composite and bulk silver, respectively [148]. V_f, V_c, and s denote the volume fraction of silver flakes, percolation threshold of the corresponding composite, and exponent factor, respectively. The electrical conductivity of bulk silver σ_0 is constant value of 8.5×10^7 S m^{-1} [13]. The percolation threshold V_c can be obtained by fitting the data for the composites with PDMS@Ag beads, and calculated using the theoretical percolation threshold model for the composites without PDMS@Ag beads. The exponent term s is changing by fitting the experimental data to the equation and comparing the result with the data.

$$\sigma = \sigma_0(V_f - V_c)^s \tag{B.1}$$

The equation of the theoretical percolation threshold model for silver flakes can be described in equation B.2, where V_{c_flake} is the percolation threshold for silver flakes, D is the diameter of silver flakes, t is the thickness of silver flakes, and D_{IP} is the tunneling distance [148]. The values of 35 μm, 15 nm, and 10 nm are used for D, t, and D_{IP}, respectively. Figure B.6b shows the result from the percolation theory overlaid on the experimental data.

The fitting curve of the equation 1 has a good agreement ($R^2 = 0.9657$) with the experimental data of composites without PDMS@Ag beads. However, the fitted curve based on the samples with PDMS@Ag beads does not match well with the experimental data. This is because the percolation theory isn't designed for microstructurally modified composites.

$$V_{c\_flake} = \frac{27\pi D^2}{4(D + D_{IP})^3}$$

(B.2)

B.3 Applications: Stretchable Antenna and Strain Sensor

To demonstrate the potential applications of the conductive PS3 composites, we present two representative use cases related to wearable computation and soft robotics. The first example (Figure B.7a–d) is a sensorized furnace glove that can withstand elevated temperatures. The PS3 composite functions as a stretchable radiofrequency (RF) antenna for measuring and transmitting strain information through coupling between antenna resonance and mechanical tensile strain. Two rectangular-shaped dipole antennas (53.9 mm × 3 mm × 0.14 mm) were fabricated on a PDMS substrate by stencil printing with a gap distance of 2.3 mm. A coaxial male connector (uFL SMT antenna connector, Adafruit) with a coaxial cable (RN-uFL-SMA6, Digi-key) was mounted to the antennas with silver epoxy. Another PDMS layer was applied to encapsulate and protect the antennas and the electrical contact between the antennas and connector (see Figure B.7b inset and Figure B.8). Representative measurements of the reflected power as a function of frequency under different strains are shown in Figure B.7a. We performed simulations in ANSYS and designed the antennas to have a resonance frequency of ~ 1.1 GHz at 0% strain (Appendix B.4). The simulation is in (green dashed line; Figure B.7a) good agreement with the experimental measurements (black line; Figure B.7a). Figure B.7a shows the shift of resonance frequency (valley point) and a similar level of high-quality radiation efficiency, that is, low enough reflected power,

as the elongation of antennas up to 80% strain. The resonant frequency of the antenna as a function of strain is presented in Figure B.7b. The resonant frequency (f_r) decreases linearly from 1.12 to 0.80 GHz as the sample was stretched to $\epsilon = 80\%$ with a linear fitting of $f_r = (-0.397\epsilon + 1.107)$ GHz with $R^2 = 0.99$. These results show the tunability of the stretchable antenna made from the PS3 composite over a wide range of frequencies. Since the resonant frequency of the antenna is linearly dependent on the strain, the antennas can function in a sensorized furnace glove.

To demonstrate the practical capabilities of the stretchable antenna for wearable devices, we produced an RFID-integrated smart furnace glove (Figure B.7c) for monitoring hand gestures in a high-temperature environment. The glove contains four stretchable antenna-integrated RFID tags over the metacarpophalangeal, proximal, and distal interphalangeal joints of each finger (excluding the thumb; find the design of the RFID tag in Figure B.9). We show the thermally stable functionality of this smart glove by recognizing a series of hand gestures in room temperature and high temperature (in a 100 °C furnace) (Figure B.7d). In these experiments, the fingers are cycled through different gestures where the signal strength of each individual RFID tag is captured by a far-field RFID antenna (LHCP far-field RFID antenna, Impinj) and reader system (speedway revolution R240 UHF RFID reader, Impinj) using an integrated RF chip. The scanning frequency is from 0.902 to 0.928 GHz. As shown in the left part of Figure B.7d (room temperature operation), the signal strength of the RFID tag will decrease from the baseline when the corresponding finger is bent. The high-temperature tests (Figure B.7d, right) were performed in an ~ 100 °C furnace and showed a similar decrease from the baseline when the corresponding finger was bent when compared to room-temperature measurements. The PS3 composites permit robust functionality of RFID tags, that is, gestures recognition, in a high-temperature environment.

The potential of the PS3 conductor in soft robotic applications is demonstrated with a strain sensor that is integrated into a robotic gripper that lifts food out of hot water. As shown in Figure B.7e, the gripper system is assembled on a 4 degrees of freedom robot arm
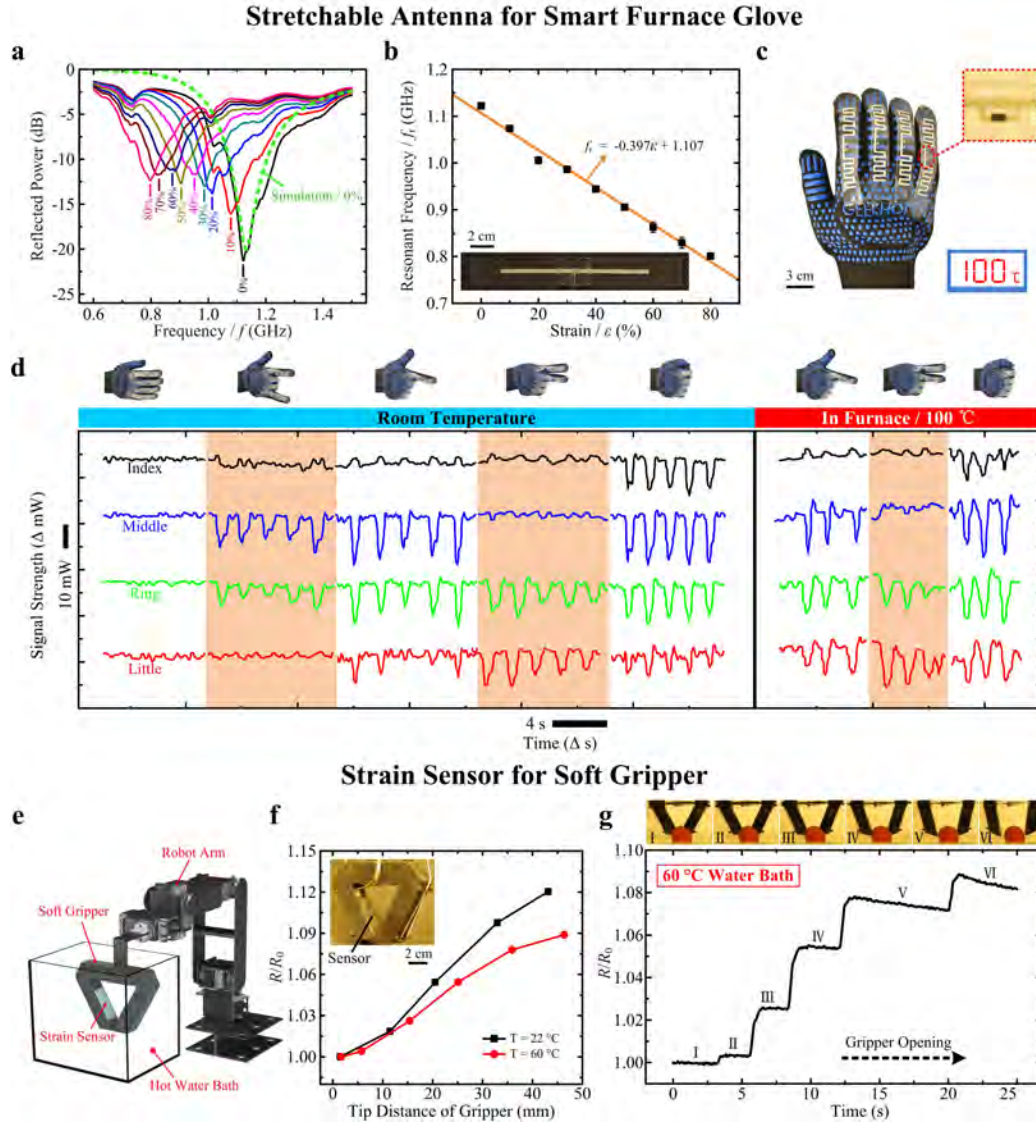
Figure B.7: Applications of thermally stable elastic conductors as a stretchable antenna and strain sensor for wearable devices and soft robotics. **a–d**, Stretchable antenna: **a**, frequency response of the reflected power from a representative antenna sample at different strains. The green dashed curve is the simulation result at the initial length, which is in strong agreement with the experimental result. **b**, Resonant frequency (fr) of the antenna as a function of strain. The inset is a photograph of the antenna. **c**, Photograph of the sensorized furnace glove with stretchable RF tags (white serpentine). The inset shows the integrated RF chip. **d**, Posture recognition of five different gestures of the hand in room-temperature (left) and furnace environment (high temperature) (right). The scale bars of axes are shown beside the axes. The photographs are the posture for each time window. **e–g**, Strain sensor for the soft gripper: **e**, schematic illustration of the strain sensor on a soft gripper-mounted robot arm. **f**, Resistance response of the strain sensor as a function of the tip distance of the gripper in room-temperature and hot water baths (~ 60 °C). The inset is the photograph of the sensor-integrated soft gripper. **g**, Resistance response of the strain sensor during the gripper opening for the task of food capture in hot water. The photographs of the gripper correspond to each opening state.
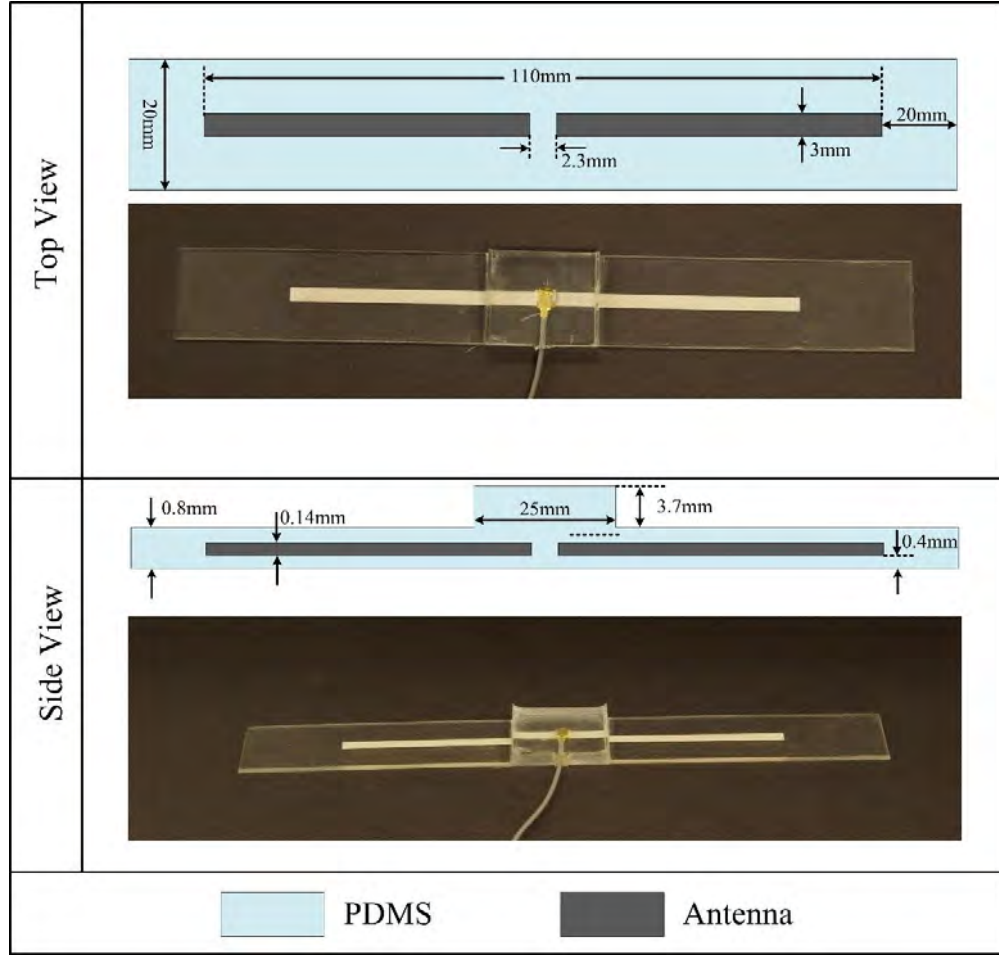
Figure B.8: Design schematic and photograph of stretchable antenna for vector network analyzing.

(UARM Swift Pro, UFactory). Two cables driven by stepper motors were used to open and close the soft gripper. We use the same soft gripper made of silicone rubber as in our previous work [168]. A strain sensor fabricated with a PDMS@Ag/Ag flake/PDMS composite (Figure B.10) was mounted on the inner side of the soft gripper to monitor the bending of the gripper jaw. The opening of the gripper jaw causes the strain sensor to elongate, increasing electrical resistance. The relative resistance (R/R_0) can be monitored as a function of the tip distance of the gripper in room-temperature and hot water bath (60 °C; Figure B.7f). As with the furnace glove, the results here show that the strain sensor works similarly in high-temperature and room-temperature environments. The process of grasping a food object (red potato) in a bath of hot water (60 °C) is presented. Figure B.7g shows the relative resistance change of
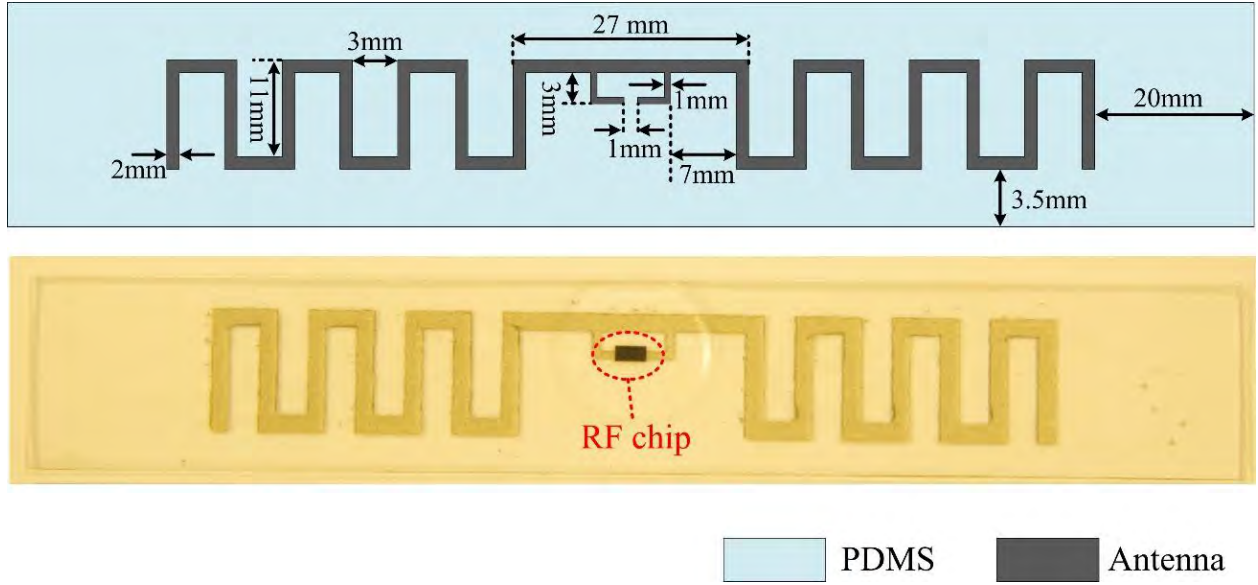
Figure B.9: Design schematic and photograph of RFID tag for smart glove.

the strain sensor during the gripper opening. Referring to the top of the figure, each signal increase corresponds to a turn of the stepper motor that is pulling the cable. Strain sensors for a robotic gripper along with the sensorized furnace glove demonstrate the potential of the PS3 composite in the applications of wearable computation and soft robotic in both mild- and high-temperature environments.

B.4   Antenna Design and Simulation

Our objective is to design antennas that resonate at desired frequencies and have high reflective performance. Doing so requires careful tuning of the antenna dimensions. We used ANSYS HFSS to simulate the antenna properties at zero strain, including the resonant frequency, Figure B.10 parameters, Z parameter, and antenna gain. We set the relative permittivity of PDMS to 3.11 and the bulk electrical conductivity of the antenna composite to 2,100 S cm^{-1} for the simulations. The input geometry of device for the HFSS simulation, i.e., the dimension of antenna and surrounding dielectric layer (PDMS), is shown in Figure B.8. We find excellent agreement between experimental results and simulation output (Figure
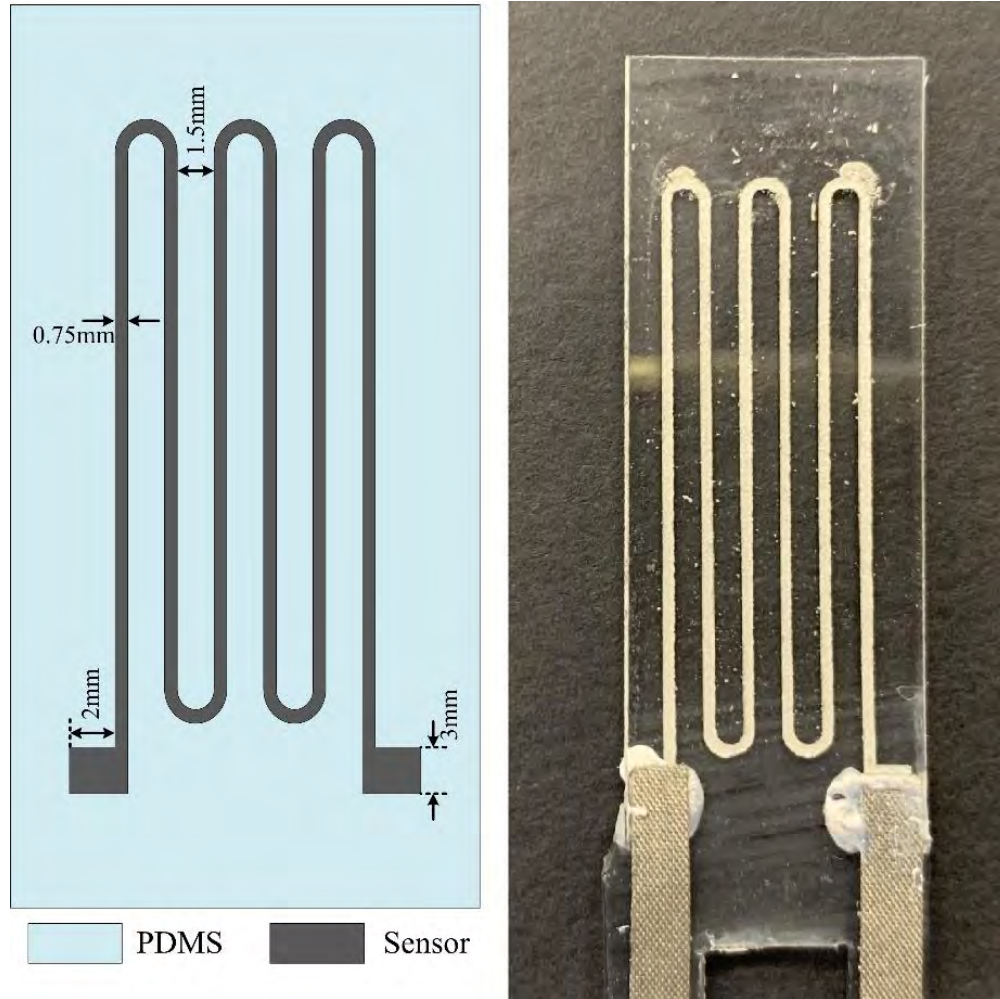
Figure B.10: Design schematic and photograph of strain sensor.

B.7a) at zero strain, which indicates the great potential of ANSYS HFSS in designing antenna made from PDMS@Ag/Ag flake/PDMS PS3 composite.

For the smart furnace glove application, we use a commercial RFID signal reading system consisting of a far field RFID antenna (LHCP far field RFID antenna, Impinj) and reader system (speedway revolution R240 UHF RFID reader, Impinj) to read the signal strength of RFID tags through RFID chips. This reading system has scanning frequency from 0.902 to 0.928 GHz. Thus, based on the same simulation solver (HFSS), we let the RFID system have a resonant frequency of 0.929 GHz by designing a serpentine dipole antenna with a loop (Figure B.9). We used a serpentine layout instead of a linear trace for antenna to reduce the length of the whole RFID tag so that it could fit into the glove fingers.

Appendix C

C.1 Hyperelastic Constitutive Model

A hyperelastic material, also called a Green elastic material, is an ideally elastic material that follows the stress-strain relationship derived from a strain energy density function [169]. One possible example of hyperelastic materials is an isotropic and incompressible rubber [170]. This type of materials follows non-linear elastic constitutive models. There are many constitutive laws to describe hyperelastic materials' mechanical behaviors, such as Neo-Hookean [171], Mooney-Rivlin [172, 173], Ogden [128], Gent [174], Arruda-Boyce [175], or Yeoh [176] hyperelastic models. According to Yuk *et al.* [158], the hyperelastic constitutive model for a two-parameter Ogden solid can be used to estimate the mechanical properties of the polyacrylamide-alginate hydrogel. For the incompressible and isotropic material, the strain energy density (W) can be defined as equation C.1, where C_i are material constants and λ_i are the principal stretches. If the material is under stretch of λ, $\lambda_1 = \lambda$ and $\lambda_2 = \lambda_3 = \lambda^{-1}$ because of the incompressibility ($\lambda_1 \lambda_2 \lambda_3 = 1$).

$$W = C_1(\lambda_1{}^2 + \lambda_2{}^2 + \lambda_3{}^2 - 3) + C_2(\lambda_1{}^4 + \lambda_2{}^4 + \lambda_3{}^4 - 3) \tag{C.1}$$

Then, we can calculate the total potential energy $\Pi = \Gamma + U = WV_0 - F\Delta L$, where Γ is the total elastic energy which can be defined as the multiply of the strain energy density (W) and the total initial volume (V_0), and U is the potential from mechanical work which can be

defined as the negative of the multiply of the applied force (F) and the uniaxial length change ($\Delta L = L_0(\lambda - 1)$). The Cauchy stress ($\sigma$) of a two-parameter Ogden solid can be obtained by setting the derivative of the total potential energy Π about the uniaxial stretch λ to zero, which is described in equation C.2.

$$\sigma = \frac{F}{A} = 2C_1\left(\lambda^2 - \frac{1}{\lambda}\right) + 4C_2\left(\lambda^4 - \frac{1}{\lambda_2}\right) \tag{C.2}$$

The engineering stress (σ_e) of a two-parameter Ogden solid can be described as equation C.3.

$$\sigma_e = \frac{\sigma}{\lambda} = 2C_1\left(\lambda - \frac{1}{\lambda^2}\right) + 4C_2\left(\lambda^3 - \frac{1}{\lambda_3}\right) \tag{C.3}$$

C.2   The Effect of Dehydration and Rehydration on the Conductive Paths

Electrical conductivity of the Ag-hydrogel composite is governed by a percolation network formed by the Ag flakes embedded within the hydrogel matrix. One of the most significant factors that can affect the percolation network of the Ag-hydrogel is de/rehydration. Here, we introduce how partial dehydration and rehydration of the conductive hydrogel composite affect the percolating paths around Ag particles by calculating the forces between Ag particles (Figure C.1a).

The partial dehydration process enables the Ag-hydrogel to achieve electrical conductivity. This also means that the distances between Ag particles in the hydrogel network are getting closer to each other by some adhesive forces. Among the general adhesion mechanisms, dispersive adhesion is relatively larger than other mechanisms [150]. In dispersive adhesion, also known as physisorption, two materials are held together by van der Waals force which is the attraction between two molecules [151]. An Ag flake can be modelled as a thin circular plate with smooth surfaces (Figure C.1b). Then, the van der Waals force between flakes can
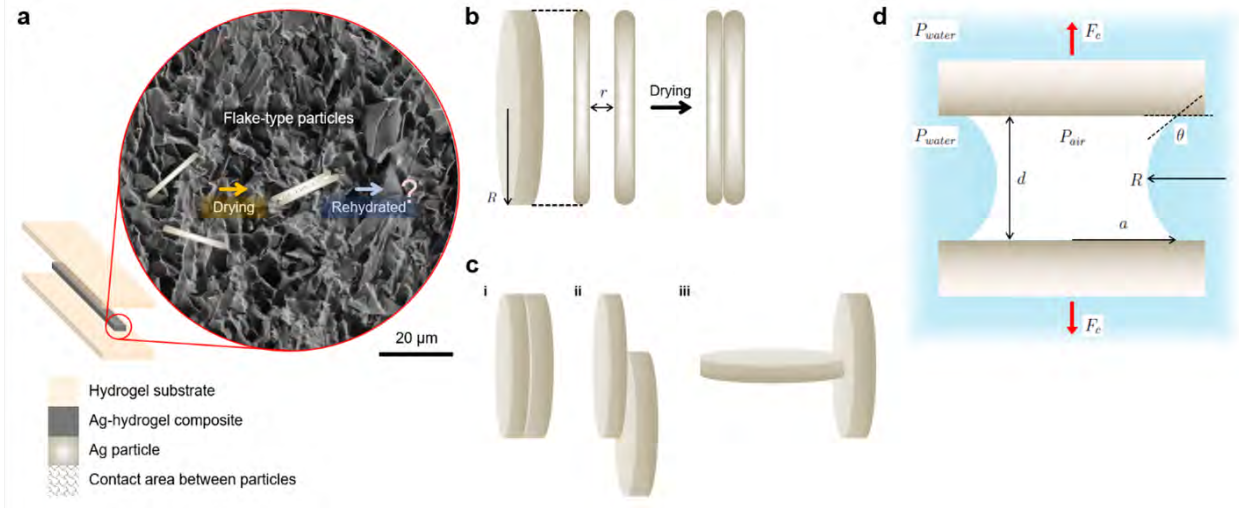
Figure C.1: Theoretical model of dehydration and rehydration effect on flake-type Ag particles in the Ag-hydrogel composite. **a**, The effect of dehydration and rehydration of the conductive hydrogel composite on the conducting paths between Ag particles. **b**, Flake-type Ag particles before and after the partial dehydration process. **c**, Three possible examples of contact of flake-type Ag particles: (i) in-plane ideal contact, (ii) in-plane partial contact, and (iii) off-plane partial contact. The size of Ag flakes can be modelled as thin circular plates with the radius of R_f and the thickness of each flake can be determined by different aspect ratios. **d**, Capillary penetration of water is shown in small gaps between particles when the conductive hydrogel composite is rehydrated with water. The shape of meniscus is determined by contact angle θ between water and the material of wall. Due to the capillary action, water is making pull-out force F_c against the adhesive forces. This force F_c is functioning a dominant repulsive mechanism.

be approximated by Safran et al. [152] as follows:

$$\frac{F_{VW,f}}{\text{Area}} = -\frac{A}{12\pi}\left(-\frac{2}{r^3} - \frac{2}{(r+h_1+h_2)^3} + \frac{2}{(r+h_1)^3} + \frac{2}{(r+h_2)^3}\right) \tag{C.4}$$

where A is the Hamaker coefficient [177] which is a constant that depends on the material properties and has units of energy (J), h_1 and h_2 are thicknesses of the surfaces that take part in interactions between two adjacent Ag flakes, and r is the distance between the surfaces. We considered three types of inter-particle contact between Ag flakes. First, we define "in-plane ideal contact", where one particle face is completely covered by the other particle face. The other two types of contacts are "in-plane partial contact", where the faces of the particles partially overlap, and "off-plane partial contact", where the edge of one particle touches the face of another particle (Figure C.1c). Based on the geometry, the van der Waals

force as an adhesive force can be calculated.

After forming conducting pathways, Ag hydrogel can be rehydrated under an aqueous environment. In that case, water can penetrate the hydrogel network and affect the percolation network by applying capillary forces which is dominant repulsive mechanism. Capillary action is the ability of a liquid to flow in narrow spaces without external forces [178]. This action is propelled by the combination of surface tension of the liquid and adhesive forces between the liquid and surrounding walls. Likewise, when the dried Ag hydrogel composite is rehydrated, water tends to penetrate the narrow gaps between Ag particles (Figure C.1d).

As shown in Figure C.1d, there is pressure gradient between trapped air and penetrating water caused by the capillary action. The pressure difference is referred as capillary pressure studied by Young-Laplace equation [179] as follows:

$$\Delta P = P_{air} - P_{water} = \frac{T}{R_c} \tag{C.5}$$

where P_{air} is the pressure of air, P_{water} is the pressure of water, T is the surface tension of the liquid, and R_c is the radius of the surface of the meniscus.

$$F_c = \Delta P \times \text{Area} = \frac{\pi a^2 T}{R_c} = \frac{2\pi a^2 T \cos(\pi - \theta)}{d} \tag{C.6}$$

where F_c is capillary force caused by capillary pressure, a is contact radius between two adjacent Ag particles, d is the distance between the two particles, and θ is the contact angle of meniscus formed by the liquid and the wall.

In Figure C.2a, van der Waals forces and capillary forces of Ag flakes are plotted as a function of the radius R_f of flakes. In general, adhesive forces due to van der Waals Forces and repulsive forces due to capillary forces increase as the dimension of flakes increase. The aspect ratio of flakes does not significantly affect the magnitude of forces. Van der Waals forces are generally larger than capillary forces ($R_f \geq 80$ nm), except for smaller particle radii ($R_f \leq 80$ nm).

Figure C.2b shows the effect of relative interaction thickness of flakes and the aspect ratio of flakes. The interaction thickness considers the thickness of a "skin" on Ag flakes that participates in van der Waals interactions. We considered a range of relative interaction thickness as it is unclear what the actual thickness of the flakes is or if surface interactions dominate over bulk interactions. If the interaction thickness is above a certain level of dimension (~ 1 μm), the change in the magnitude of the force is negligible when compared to smaller flakes. Capillary forces are less than van der Waals forces for all interaction thicknesses studied here when the radius R_f of Ag flakes is large. As shown in Figure C.2a, capillary forces can be dominant for smaller flakes ($\ll 1$ μm); however, van der Waals forces are dominant in general.
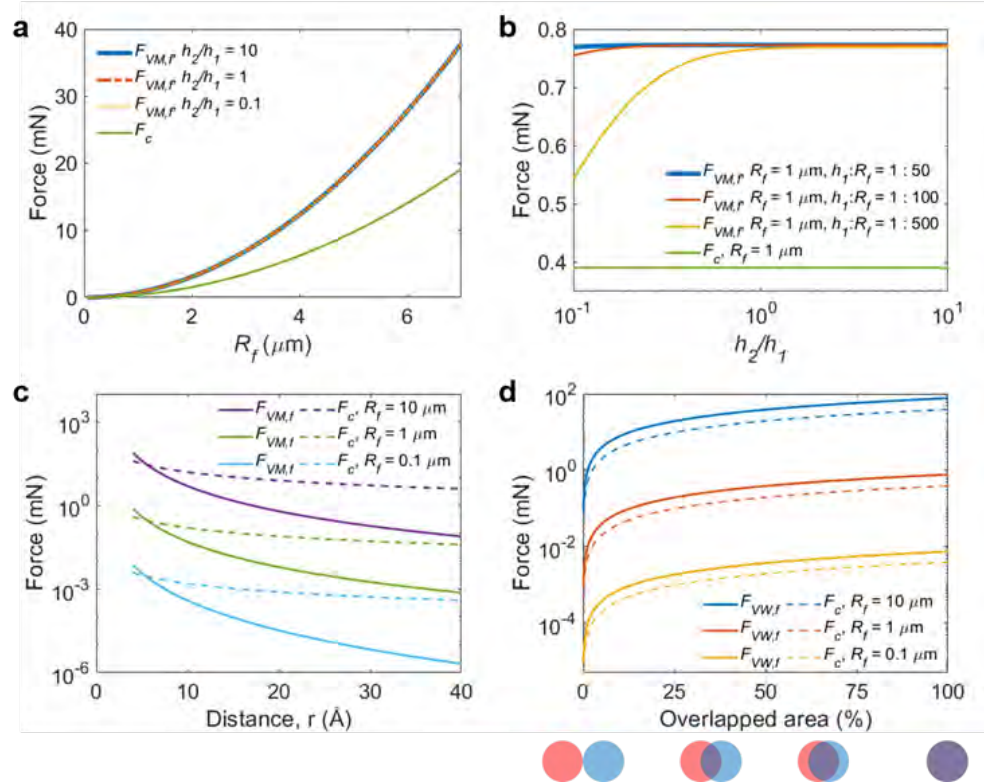
Figure C.2: Analytical comparison of adhesive forces and repulsive forces based on various dimensions of flake-type Ag particles. **a**, Van der Waals forces $F_{VW,f}$ and capillary forces F_c as a function of radius R_f of flake-type Ag particles. **b**, Van der Waals forces $F_{VW,f}$ and capillary forces F_c as a function of thickness h_1 and h_2 of flake-type Ag particles. **c**, Van der Waals forces $F_{VW,f}$ and capillary forces F_c as a function of distance r between flake-type Ag particles **d**, Van der Waals forces $F_{VW,f}$ and capillary forces F_c as a function of overlapped area between flake-type Ag particles.

Referring to Figure C.2c, van der Waals forces and capillary forces decrease when the distance between Ag particles increases. Capillary forces decrease at a smaller rate than van der Waals forces, so at larger inter-particle distances, capillary forces become dominant. When the particles are close enough ($r \leq 6$ Å), van der Waals forces are larger than capillary forces.

When using Ag flakes, the Ag-hydrogel composite can maintain high conductivity while being rehydrated if certain conditions are satisfied. These relate to the size of the Ag flakes, their aspect ratio, and the distance between the flakes. If the Ag flakes are too small, the capillary forces can be larger than van der Waals forces. For the flakes used in this work, which do not approach the high aspect ratios or small sizes that would allow water to disrupt percolation pathways, conducting paths remain after rehydration due to hysteresis of the van der Waals mediated interfacial adhesion. For these composites, the only factor that can affect the percolation network is the distance between the particles. After the drying process, water between particles partially evaporates. If the distance between the particles goes below a certain level (~ 6 Å), van der Waals forces become larger than capillary forces.

The stability of the conducting network can be affected by the different types of inter-particle contact between Ag flakes. If we consider Ag flakes with different radii ($R_f = 0.1$, 1, 10 µm), interaction thicknesses ($h = 0.001, 0.01, 0.1$ µm), and a fixed distance between flakes ($r = 4$ Å), we can evaluate the influence of partial overlap for "in-plane partial contact" (Figure C.1c (ii) and Figure C.2d). Figure C.2d shows van der Waals forces and capillary forces as a function of overlapped area of two Ag flakes. When two particles are in partial contact, variations in particle geometry will lead to differences in the magnitude of interfacial force. Generally, capillary and van der Waals forces increase when the dimensions of particles increase. As the extent of overlap increase, van der Waals forces and capillary forces increase as well. (The relationship between adhesive forces and repulsive forces is not changed unless the radius of flakes is large enough ($R_f \geq 80$ nm from Figure C.2a)).

The less common case of contact of out-of-plane contact between Ag flakes, in which one

plane is perpendicular to the other (Figure C.1c (iii)), is not studied in this model. It is expected that such contacts will form weak electrical contacts and adhesive bonds and not contribute as significantly to percolation, electrical conductivity under strain, or resistance to rehydration. Typically, flake-type particles have large aspect ratios from 1:50 to 1:500. Additionally, the sides of the flakes are not flat and so reliable electrical or mechanical contact is not anticipated. Therefore, we feel that it is reasonable to assume that out-of-plane partial contact is not expected to contribute to stable conductivity within the hydrogel composite.

C.3   Long-term Response to High Direct Current under Aqueous Environment

We recorded the current evolution of the Ag-hydrogel composite for additional specimens: (a) where input electrical power would differ due to differences in resistance and (b) while in a water bath that was initially at room temperature (Figure C.3). The material's response to high direct current can be influenced by the specimen's resistance and surrounding environment. Consistent with other batches, the conductive Ag-hydrogel composite can become more conductive when high electrical power was applied across the composite as
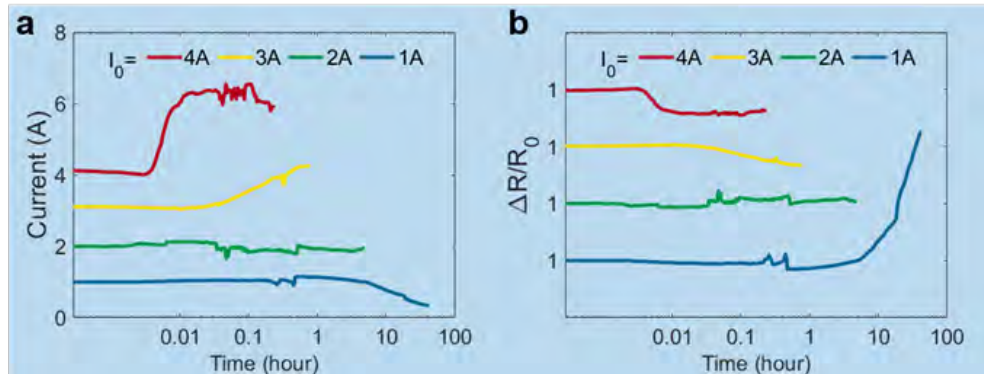
Figure C.3: Long-term response to direct current in water. **a**, Long-term current evolution as a function of time with different initial currents and corresponding constant voltages in aqueous environment. **b**, Long-term relative resistance evolution as a function of time with different initial currents and corresponding constant voltages in aqueous environment.

shown in Figure 3.8a and 3.9. Joule heating reduces the water content of the composite and subsequently increases the relative volume content of percolation pathways. However, when placed in a water bath, the composites are subjected to not only localized Joule heating but also heat dissipation by the external environment and rehydration by the surrounding aqueous environment. Based on the arguments in Appendix C.2, water that penetrates the matrix of the composite can pull the adjacent Ag particles apart, which results in disrupting weak percolating networks by imposing capillary forces. If the effect of Joule heating is stronger than rehydration, the resistance of the composite will decrease (for the cases of $I_0 = 3$ and 4 A); otherwise, the composite's resistance will increase (for the cases of $I_0 = 1$ and 2 A).

Appendix D

D.1 Detailed Experimental Conditions for Joule Heating

In Chapter 4, Joule heating was applied to the reconfigurable conductive hydrogel composites to accelerate the water evaporation of composites to increase their electrical conductivity. Figure D.1 shows the detailed timeline of experimental conditions for the hydrogel composites under Joule heating in two different measurement experiments. The composite was patterned using the stencil printing method at 0 minutes. The composites require $6-7$ minutes of crosslinking reactions to hold their shapes. After removing the PDMS molds, we apply electrical power directly to the composite traces using a benchtop power supply. As shown
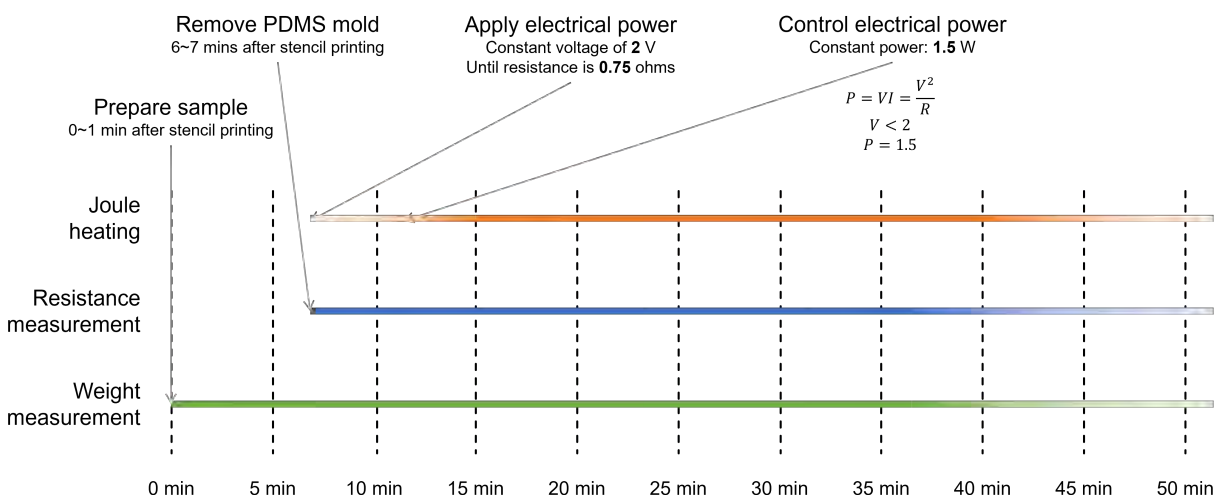
Figure D.1: Detailed timeline of experimental conditions for reconfigurable conductive hydrogel composites under Joule heating in resistance and weight measurement experiments.

135

in Figure 4.12, the traces' initial resistance values are very high ($> 10^4$ ohms). We set the experimental conditions of Joule heating as two stages. The first stage is a constant voltage of 2 V when the material's resistivity is high enough (resistance > 0.75 ohms). On the other hand, we apply a constant power of 1.5 W at the second stage when the material has a resistance lower than 0.75 ohms. If we apply the constant electrical power at the first stage, the required voltage might be too large, which results in mechanical and electrical damage to the composites.

Appendix E

E.1   Detailed Fabrication Process of UV-Hydrogel

For the material's composition, acrylamide (AAm, A8887; Sigma-Aldrich) and sodium alginate (16.7% of acrylamide by weight, W201502; Sigma-Aldrich) were used as hydrogel polymer matrix. N,N'-methylenebisacrylamide (0.6% of acrylamide by weight, MBAA, 146072; Sigma-Aldrich) and poly(ethylene glycol) diacrylate (2% of acrylamide by weight, PEGDA, 455008; Sigma-Aldrich) were used as crosslinker of the material system. Water-soluble TPO-based nanoparticle photoinitiator (2.5% of acrylamide by weight, 906808; Sigma-Aldrich) was used as a photoinitiator. Deionized water was used to dissolve the chemical before crosslinking. The water's initial weight ratio was kept 86% by weight.

Since the conductive hydrogel composite introduced in Chapter 3 has a low concentration of conductive fillers, the composite can be crosslinked using a photoinitiator that can be activated by UV radiation. For the source of UV radiation, we used UV flashlight (with a wavelength of 365 nm or 385 nm) and acrylic mold to pattern the UV-hydrogel. Digital light processing (DLP) printers with proper UV wavelengths, for example, PICO2 from Asiga America, can be used as well.

E.2 Printability of UV-Hydrogel

We used a DLP printer (PICO2; Asiga America) to pattern the UV-curable hydrogel composite. The material was successfully crosslinked and patterned in a shape of dogbones (Figure E.1a) and fine traces (Figure E.1b). The fine-tuning related to the duration of UV radiation is required to keep the printed patterns sharp.

Figure E.1: Printability of UV-curable conductive hydrogel composite using Asiga printer. **a**, Dogbone shapes. **b**, Resolution test. The traces' widths are starting at 1.4 mm (left) and decreasing to 0.1 mm (right) by 0.1 mm.

E.3   Mechanical Properties of UV-Hydrogel

To check whether the photoinitiator or PEGDA affects the mechanical properties of PAAm-alginate hydrogels or not, we conducted mechanical characterization of the UV-crosslinked hydrogel composites with and without silver flakes. We crosslinked the materials using a UV flashlight with a dimension of ASTM D412 Die C (the initial length is 80 mm). Figure E.2a shows the result of hydrogel without conductive fillers. The material's maximum strain is 175% with Young's modulus of 7 kPa. Introducing 1 vol% of silver flakes into the material can affect the mechanical properties. In Figure E.2b, the conductive hydrogel composite cured by UV radiation can stretch up to 142.5% of its original length and with Young's modulus of
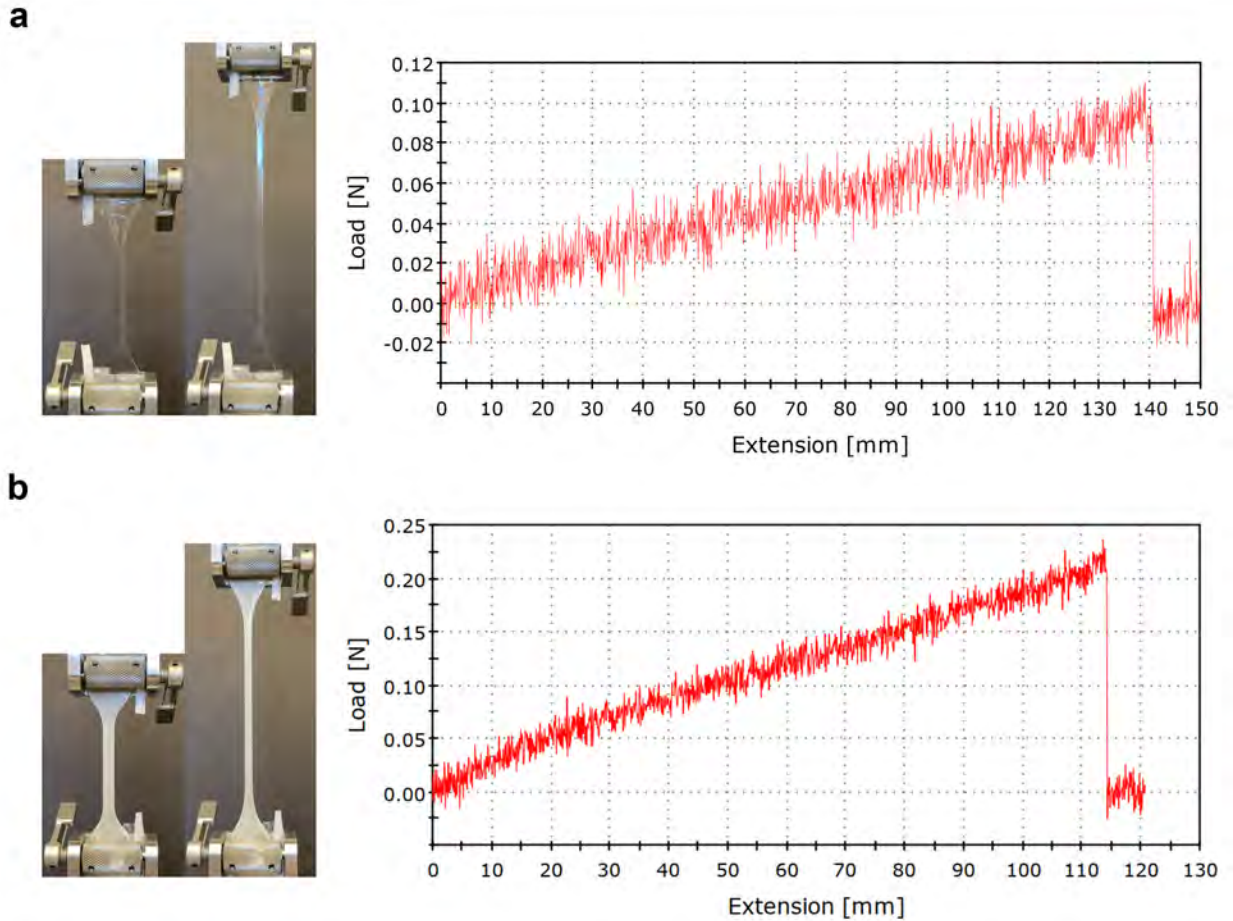
Figure E.2: Tensile test of UV-hydrogel. **a**, Polyacrylamide-alginate hydrogel without silver flakes. **b** UV-curable conductive hydrogel composite embedded with silver flakes.

19 kPa. Adding conductive fillers decreases the maximum strain limit while increasing the stiffness.

E.4   Electrical Properties of UV-Hydrogel

In Chapters 3 and 4, we introduced a partial dehydration process that enables percolation networks in the composite even though the volume fraction of conductive fillers is low. The UV-curable conductive hydrogel composite has more crosslinkers than the materials introduced in Chapters 3 and 4. The hydrogel polymer chains might be less free than the Ag-hydrogel or the reconfigurable hydrogel composite. However, the partial dehydration process should still work since it changes the microstructures of composites through water evaporation. Figure E.3 shows the resistance evolution of a UV-crosslinked composite trace over time. The resistance range and the evolution trend are the same as other materials' electrical properties. We can conclude that UV-hydrogel composite also forms percolation
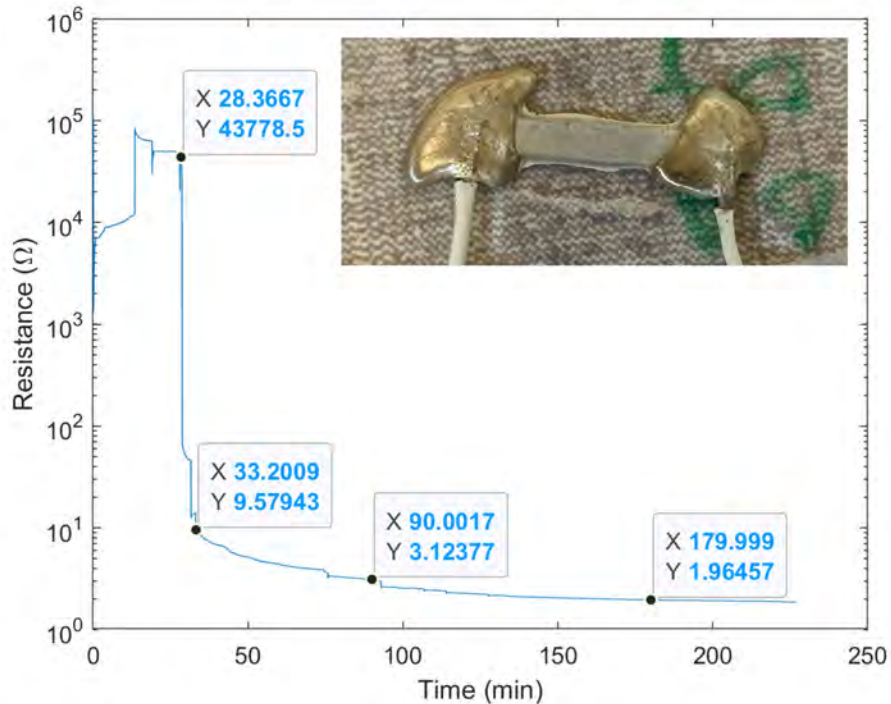
Figure E.3: Absolute resistance of UV-crosslinked conductive hydrogel composite over time.

networks through water evaporation.

Bibliography

[1] T. Someya, Z. Bao, and G. G. Malliaras, "The rise of plastic bioelectronics," *Nature*, vol. 540, no. 7633, pp. 379–385, 2016.

[2] C. Liao, M. Zhang, M. Y. Yao, T. Hua, L. Li, and F. Yan, "Flexible organic electronics in biology: materials and devices," *Advanced materials*, vol. 27, no. 46, pp. 7493–7527, 2015.

[3] D. Fitzpatrick, *Implantable electronic medical devices*. Elsevier, 2014.

[4] A. Lay-Ekuakille and S. C. Mukhopadhyay, *Wearable and autonomous biomedical devices and systems for smart environment*. Springer, 2010.

[5] H. U. Chung, A. Y. Rwei, A. Hourlier-Fargette, S. Xu, K. Lee, E. C. Dunne, Z. Xie, C. Liu, A. Carlini, D. H. Kim *et al.*, "Skin-interfaced biosensors for advanced wireless physiological monitoring in neonatal and pediatric intensive-care units," *Nature medicine*, vol. 26, no. 3, pp. 418–429, 2020.

[6] F. Molina-Lopez, T. Gao, U. Kraft, C. Zhu, T. Öhlund, R. Pfattner, V. Feig, Y. Kim, S. Wang, Y. Yun *et al.*, "Inkjet-printed stretchable and low voltage synaptic transistor array," *Nature communications*, vol. 10, no. 1, pp. 1–10, 2019.

[7] A. Chortos, J. Liu, and Z. Bao, "Pursuing prosthetic electronic skin," *Nature materials*, vol. 15, no. 9, pp. 937–950, 2016.

[8] J. Kim, M. Lee, H. J. Shim, R. Ghaffari, H. R. Cho, D. Son, Y. H. Jung, M. Soh, C. Choi, S. Jung *et al.*, "Stretchable silicon nanoribbon electronics for skin prosthesis," *Nature communications*, vol. 5, no. 1, pp. 1–11, 2014.

[9] A. Vásquez Quintero, R. Verplancke, H. De Smet, and J. Vanfleteren, "Stretchable electronic platform for soft and smart contact lens applications," *Advanced Materials Technologies*, vol. 2, no. 8, p. 1700073, 2017.

[10] Y. Qian, X. Zhang, L. Xie, D. Qi, B. K. Chandran, X. Chen, and W. Huang, "Stretchable organic semiconductor devices," *Advanced Materials*, vol. 28, no. 42, pp. 9243–9265, 2016.

[11] N. Bowden, S. Brittain, A. G. Evans, J. W. Hutchinson, and G. M. Whitesides, "Spontaneous formation of ordered structures in thin films of metals supported on an elastomeric polymer," *Nature*, vol. 393, no. 6681, pp. 146–149, 1998.

[12] D.-H. Kim, J. Song, W. M. Choi, H.-S. Kim, R.-H. Kim, Z. Liu, Y. Y. Huang, K.-C. Hwang, Y.-w. Zhang, and J. A. Rogers, "Materials and noncoplanar mesh designs for integrated circuits with linear elastic responses to extreme mechanical deformations," *Proceedings of the National Academy of Sciences*, vol. 105, no. 48, pp. 18 675–18 680, 2008.

[13] N. Matsuhisa, D. Inoue, P. Zalar, H. Jin, Y. Matsuba, A. Itoh, T. Yokota, D. Hashizume, and T. Someya, "Printable elastic conductors by in situ formation of silver nanoparticles from silver flakes," *Nature materials*, vol. 16, no. 8, pp. 834–840, 2017.

[14] E. J. Markvicka, M. D. Bartlett, X. Huang, and C. Majidi, "An autonomously electrically self-healing liquid metal–elastomer composite for robust soft-matter robotics and electronics," *Nature materials*, vol. 17, no. 7, pp. 618–624, 2018.

[15] B. Lu, H. Yuk, S. Lin, N. Jian, K. Qu, J. Xu, and X. Zhao, "Pure pedot: Pss hydrogels," *Nature communications*, vol. 10, no. 1, pp. 1–10, 2019.

[16] M. D. Dickey, "Stretchable and soft electronics using liquid metals," *Advanced Materials*, vol. 29, no. 27, p. 1606425, 2017.

[17] M. D. Dickey, R. C. Chiechi, R. J. Larsen, E. A. Weiss, D. A. Weitz, and G. M. Whitesides, "Eutectic gallium-indium (egain): a liquid metal alloy for the formation of stable structures in microchannels at room temperature," *Advanced functional materials*, vol. 18, no. 7, pp. 1097–1104, 2008.

[18] P. Surmann and H. Zeyat, "Voltammetric analysis using a self-renewable non-mercury electrode," *Analytical and bioanalytical chemistry*, vol. 383, no. 6, pp. 1009–1013, 2005.

[19] M. D. Bartlett, A. Fassler, N. Kazem, E. J. Markvicka, P. Mandal, and C. Majidi, "Stretchable, high-k dielectric elastomers through liquid-metal inclusions," *Advanced Materials*, vol. 28, no. 19, pp. 3726–3731, 2016.

[20] Y.-L. Park, C. Majidi, R. Kramer, P. Bérard, and R. J. Wood, "Hyperelastic pressure sensing with a liquid-embedded elastomer," *Journal of micromechanics and microengineering*, vol. 20, no. 12, p. 125029, 2010.

[21] A. Fassler and C. Majidi, "Liquid-phase metal inclusions for a conductive polymer composite," *Advanced Materials*, vol. 27, no. 11, pp. 1928–1932, 2015.

[22] J.-H. Kim, S. Kim, J.-H. So, K. Kim, and H.-J. Koo, "Cytotoxicity of gallium–indium liquid metal in an aqueous environment," *ACS applied materials & interfaces*, vol. 10, no. 20, pp. 17 448–17 454, 2018.

[23] C. Majidi, "Soft robotics: a perspective—current trends and prospects for the future," *Soft robotics*, vol. 1, no. 1, pp. 5–11, 2014.

[24] C. Keplinger, J.-Y. Sun, C. C. Foo, P. Rothemund, G. M. Whitesides, and Z. Suo, "Stretchable, transparent, ionic conductors," *Science*, vol. 341, no. 6149, pp. 984–987, 2013.

[25] C. Lim, Y. Shin, J. Jung, J. H. Kim, S. Lee, and D.-H. Kim, "Stretchable conductive nanocomposite based on alginate hydrogel and silver nanowires for wearable electronics," *APL Materials*, vol. 7, no. 3, p. 031502, 2019.

[26] H. Jo, M. Sim, S. Kim, S. Yang, Y. Yoo, J.-H. Park, T. H. Yoon, M.-G. Kim, and J. Y. Lee, "Electrically conductive graphene/polyacrylamide hydrogels produced by mild chemical reduction for enhanced myoblast growth and differentiation," *Acta biomaterialia*, vol. 48, pp. 100–109, 2017.

[27] H. Yuk, B. Lu, and X. Zhao, "Hydrogel bioelectronics," *Chemical Society Reviews*, vol. 48, no. 6, pp. 1642–1667, 2019.

[28] O. Erol, A. Pantula, W. Liu, and D. H. Gracias, "Transformer hydrogels: a review," *Advanced Materials Technologies*, vol. 4, no. 4, p. 1900043, 2019.

[29] L. Han, X. Lu, M. Wang, D. Gan, W. Deng, K. Wang, L. Fang, K. Liu, C. W. Chan, Y. Tang *et al.*, "A mussel-inspired conductive, self-adhesive, and self-healable tough hydrogel as cell stimulators and implantable bioelectronics," *Small*, vol. 13, no. 2, p. 1601916, 2017.

[30] S. Palagi, A. G. Mark, S. Y. Reigh, K. Melde, T. Qiu, H. Zeng, C. Parmeggiani, D. Martella, A. Sanchez-Castillo, N. Kapernaum *et al.*, "Structured light enables biomimetic swimming and versatile locomotion of photoresponsive soft microrobots," *Nature materials*, vol. 15, no. 6, pp. 647–653, 2016.

[31] T. Dvir, B. P. Timko, M. D. Brigham, S. R. Naik, S. S. Karajanagi, O. Levy, H. Jin, K. K. Parker, R. Langer, and D. S. Kohane, "Nanowired three-dimensional cardiac patches," *Nature nanotechnology*, vol. 6, no. 11, pp. 720–725, 2011.

[32] Y. Ahn, H. Lee, D. Lee, and Y. Lee, "Highly conductive and flexible silver nanowire-based microelectrodes on biocompatible hydrogel," *ACS applied materials & interfaces*, vol. 6, no. 21, pp. 18 401–18 407, 2014.

[33] X. Jing, X.-Y. Wang, H.-Y. Mi, and L.-S. Turng, "Stretchable gelatin/silver nanowires composite hydrogels for detecting human motion," *Materials Letters*, vol. 237, pp. 53–56, 2019.

[34] S. R. Shin, S. M. Jung, M. Zalabany, K. Kim, P. Zorlutuna, S. B. Kim, M. Nikkhah, M. Khabiry, M. Azize, J. Kong *et al.*, "Carbon-nanotube-embedded hydrogel sheets for engineering cardiac constructs and bioactuators," *ACS nano*, vol. 7, no. 3, pp. 2369–2380, 2013.

[35] L. Pan, G. Yu, D. Zhai, H. R. Lee, W. Zhao, N. Liu, H. Wang, B. C.-K. Tee, Y. Shi, Y. Cui *et al.*, "Hierarchical nanostructured conducting polymer hydrogel with high electrochemical activity," *Proceedings of the National Academy of Sciences*, vol. 109, no. 24, pp. 9287–9292, 2012.

[36] W. Zhao, Z. Han, L. Ma, S. Sun, and C. Zhao, "Highly hemo-compatible, mechanically strong, and conductive dual cross-linked polymer hydrogels," *Journal of Materials Chemistry B*, vol. 4, no. 48, pp. 8016–8024, 2016.

[37] V. R. Feig, H. Tran, M. Lee, and Z. Bao, "Mechanically tunable conductive interpene-trating network hydrogels that mimic the elastic moduli of biological tissue," *Nature communications*, vol. 9, no. 1, pp. 1–9, 2018.

[38] H. Wang, Y. Yao, Z. He, W. Rao, L. Hu, S. Chen, J. Lin, J. Gao, P. Zhang, X. Sun *et al.*, "A highly stretchable liquid metal polymer as reversible transitional insulator and conductor," *Advanced Materials*, vol. 31, no. 23, p. 1901337, 2019.

[39] J.-E. Park, H. S. Kang, J. Baek, T. H. Park, S. Oh, H. Lee, M. Koo, and C. Park, "Rewritable, printable conducting liquid metal hydrogel," *ACS nano*, vol. 13, no. 8, pp. 9122–9130, 2019.

[40] H. Liu, Y. Xin, H. K. Bisoyi, Y. Peng, J. Zhang, and Q. Li, "Stimuli-driven insulator–conductor transition in a flexible polymer composite enabled by biphasic liquid metal," *Advanced Materials*, vol. 33, no. 43, p. 2104634, 2021.

[41] C.-C. Kim, H.-H. Lee, K. H. Oh, and J.-Y. Sun, "Highly stretchable, transparent ionic touch panel," *Science*, vol. 353, no. 6300, pp. 682–687, 2016.

[42] D. Son, J. Kang, O. Vardoulis, Y. Kim, N. Matsuhisa, J. Y. Oh, J. W. To, J. Mun, T. Katsumata, Y. Liu *et al.*, "An integrated self-healable electronic skin system fabricated via dynamic reconstruction of a nanostructured conducting network," *Nature nanotechnology*, vol. 13, no. 11, pp. 1057–1065, 2018.

[43] H. Jin, N. Matsuhisa, S. Lee, M. Abbas, T. Yokota, and T. Someya, "Enhancing the performance of stretchable conductors for e-textiles by controlled ink permeation," *Advanced Materials*, vol. 29, no. 21, p. 1605848, 2017.

[44] K. K. Kim, S. Hong, H. M. Cho, J. Lee, Y. D. Suh, J. Ham, and S. H. Ko, "Highly sensitive and stretchable multidimensional strain sensor with prestrained anisotropic metal nanowire percolation networks," *Nano letters*, vol. 15, no. 8, pp. 5240–5247, 2015.

[45] D. J. Lipomi, M. Vosgueritchian, B. C. Tee, S. L. Hellstrom, J. A. Lee, C. H. Fox, and Z. Bao, "Skin-like pressure and strain sensors based on transparent elastic films of carbon nanotubes," *Nature nanotechnology*, vol. 6, no. 12, pp. 788–792, 2011.

[46] D. Kwon, T.-I. Lee, J. Shim, S. Ryu, M. S. Kim, S. Kim, T.-S. Kim, and I. Park, "Highly sensitive, flexible, and wearable pressure sensor based on a giant piezocapacitive effect of three-dimensional microporous elastomeric dielectric layer," *ACS applied materials & interfaces*, vol. 8, no. 26, pp. 16 922–16 931, 2016.

[47] M. Segev-Bar, A. Landman, M. Nir-Shapira, G. Shuster, and H. Haick, "Tunable touch sensor and combined sensing platform: toward nanoparticle-based electronic skin," *ACS applied materials & interfaces*, vol. 5, no. 12, pp. 5531–5541, 2013.

[48] Z. Liu, S. Fang, F. Moura, J. Ding, N. Jiang, J. Di, M. Zhang, X. Lepró, D. Galvao, C. Haines *et al.*, "Hierarchically buckled sheath-core fibers for superelastic electronics, sensors, and muscles," *Science*, vol. 349, no. 6246, pp. 400–404, 2015.

[49] L. Hines, K. Petersen, G. Z. Lum, and M. Sitti, "Soft actuators for small-scale robotics," *Advanced materials*, vol. 29, no. 13, p. 1603483, 2017.

[50] C. Larson, B. Peele, S. Li, S. Robinson, M. Totaro, L. Beccai, B. Mazzolai, and R. Shepherd, "Highly stretchable electroluminescent skin for optical signaling and tactile sensing," *Science*, vol. 351, no. 6277, pp. 1071–1074, 2016.

[51] T. Sekitani, H. Nakajima, H. Maeda, T. Fukushima, T. Aida, K. Hata, and T. Someya, "Stretchable active-matrix organic light-emitting diode display using printable elastic conductors," *Nature materials*, vol. 8, no. 6, pp. 494–499, 2009.

[52] F. Stauffer and K. Tybrandt, "Bright stretchable alternating current electroluminescent displays based on high permittivity composites," *Advanced Materials*, vol. 28, no. 33, pp. 7200–7203, 2016.

[53] J. Liang, L. Li, X. Niu, Z. Yu, and Q. Pei, "Elastomeric polymer light-emitting devices and displays," *Nature Photonics*, vol. 7, no. 10, pp. 817–824, 2013.

[54] S. Chiba, M. Waki, T. Wada, Y. Hirakawa, K. Masuda, and T. Ikoma, "Consistent ocean wave energy harvesting using electroactive polymer (dielectric elastomer) artificial muscle generators," *Applied Energy*, vol. 104, pp. 497–502, 2013.

[55] Q. Li, L. Chen, M. R. Gadinski, S. Zhang, G. Zhang, H. U. Li, E. Iagodkine, A. Haque, L.-Q. Chen, T. N. Jackson *et al.*, "Flexible high-temperature dielectric materials from polymer nanocomposites," *Nature*, vol. 523, no. 7562, pp. 576–579, 2015.

[56] Q. Li, G. Zhang, F. Liu, K. Han, M. R. Gadinski, C. Xiong, and Q. Wang, "Solution-processed ferroelectric terpolymer nanocomposites with high breakdown strength and

energy density utilizing boron nitride nanosheets," *Energy & Environmental Science*, vol. 8, no. 3, pp. 922–931, 2015.

[57] D. J. Lipomi and Z. Bao, "Stretchable, elastic materials and devices for solar energy conversion," *Energy & Environmental Science*, vol. 4, no. 9, pp. 3314–3328, 2011.

[58] Y. Xie, Y. Yu, Y. Feng, W. Jiang, and Z. Zhang, "Fabrication of stretchable nanocomposites with high energy density and low loss from cross-linked pvdf filled with poly (dopamine) encapsulated batio3," *ACS applied materials & interfaces*, vol. 9, no. 3, pp. 2995–3005, 2017.

[59] C. Pan, E. J. Markvicka, M. H. Malakooti, J. Yan, L. Hu, K. Matyjaszewski, and C. Majidi, "A liquid-metal–elastomer nanocomposite for stretchable dielectric materials," *Advanced Materials*, vol. 31, no. 23, p. 1900663, 2019.

[60] D.-H. Kim, N. Lu, R. Ma, Y.-S. Kim, R.-H. Kim, S. Wang, J. Wu, S. M. Won, H. Tao, A. Islam *et al.*, "Epidermal electronics," *Science*, vol. 333, no. 6044, pp. 838–843, 2011.

[61] J. Park, S. Choi, A. H. Janardhan, S.-Y. Lee, S. Raut, J. Soares, K. Shin, S. Yang, C. Lee, K.-W. Kang *et al.*, "Electromechanical cardioplasty using a wrapped elasto-conductive epicardial mesh," *Science translational medicine*, vol. 8, no. 344, pp. 344ra86–344ra86, 2016.

[62] S. Choi, S. I. Han, D. Jung, H. J. Hwang, C. Lim, S. Bae, O. K. Park, C. M. Tschabrunn, M. Lee, S. Y. Bae *et al.*, "Highly conductive, stretchable and biocompatible ag–au core–sheath nanowire composite for wearable and implantable bioelectronics," *Nature nanotechnology*, vol. 13, no. 11, pp. 1048–1056, 2018.

[63] S. H. Kim, S. Jung, I. S. Yoon, C. Lee, Y. Oh, and J.-M. Hong, "Ultrastretchable conductor fabricated on skin-like hydrogel–elastomer hybrid substrates for skin electronics," *Advanced Materials*, vol. 30, no. 26, p. 1800109, 2018.

[64] Z. Wang, Y. Huang, J. Sun, Y. Huang, H. Hu, R. Jiang, W. Gai, G. Li, and C. Zhi, "Polyurethane/cotton/carbon nanotubes core-spun yarn as high reliability stretchable strain sensor for human motion detection," *ACS applied materials & interfaces*, vol. 8, no. 37, pp. 24 837–24 843, 2016.

[65] J. A. Rogers, T. Someya, and Y. Huang, "Materials and mechanics for stretchable electronics," *science*, vol. 327, no. 5973, pp. 1603–1607, 2010.

[66] C. Pan, K. Kumar, J. Li, E. J. Markvicka, P. R. Herman, and C. Majidi, "Visually imperceptible liquid-metal circuits for transparent, stretchable electronics with direct laser writing," *Advanced Materials*, vol. 30, no. 12, p. 1706937, 2018.

[67] J.-Y. Sun, C. Keplinger, G. M. Whitesides, and Z. Suo, "Ionic skin," *Advanced Materials*, vol. 26, no. 45, pp. 7608–7614, 2014.

[68] Y. Kim, J. Zhu, B. Yeom, M. Di Prima, X. Su, J.-G. Kim, S. J. Yoo, C. Uher, and N. A. Kotov, "Stretchable nanoparticle conductors with self-organized conductive pathways," *Nature*, vol. 500, no. 7460, pp. 59–63, 2013.

[69] N. Matsuhisa, M. Kaltenbrunner, T. Yokota, H. Jinno, K. Kuribara, T. Sekitani, and T. Someya, "Printable elastic conductors with a high conductivity for electronic textile applications," *Nature communications*, vol. 6, no. 1, pp. 1–11, 2015.

[70] C. Cattin and P. Hubert, "Piezoresistance in polymer nanocomposites with high aspect ratio particles," *ACS applied materials & interfaces*, vol. 6, no. 3, pp. 1804–1811, 2014.

[71] C. Robert, J. F. Feller, and M. Castro, "Sensing skin for strain monitoring made of pc–cnt conductive polymer nanocomposite sprayed layer by layer," *ACS applied materials & interfaces*, vol. 4, no. 7, pp. 3508–3516, 2012.

[72] R. Xu, Y. Lu, C. Jiang, J. Chen, P. Mao, G. Gao, L. Zhang, and S. Wu, "Facile fabrication of three-dimensional graphene foam/poly (dimethylsiloxane) composites and their

potential application as strain sensor," *ACS applied materials & interfaces*, vol. 6, no. 16, pp. 13 455–13 460, 2014.

[73] D. J. Griffiths, "Introduction to electrodynamics," 2005.

[74] L. Li and Y.-J. Zhu, "High chemical reactivity of silver nanoparticles toward hydrochloric acid," *Journal of Colloid and Interface Science*, vol. 303, no. 2, pp. 415–418, 2006.

[75] J. S. Kim, E. Kuk, K. N. Yu, J.-H. Kim, S. J. Park, H. J. Lee, S. H. Kim, Y. K. Park, Y. H. Park, C.-Y. Hwang *et al.*, "Antimicrobial effects of silver nanoparticles," *Nanomedicine: Nanotechnology, Biology and Medicine*, vol. 3, no. 1, pp. 95–101, 2007.

[76] A. Larmagnac, S. Eggenberger, H. Janossy, and J. Vörös, "Stretchable electronics based on ag-pdms composites," *Scientific reports*, vol. 4, no. 1, pp. 1–7, 2014.

[77] J. Wang, G. Cai, S. Li, D. Gao, J. Xiong, and P. S. Lee, "Printable superelastic conductors with extreme stretchability and robust cycling endurance enabled by liquid-metal particles," *Advanced Materials*, vol. 30, no. 16, p. 1706157, 2018.

[78] K.-Y. Chun, Y. Oh, J. Rho, J.-H. Ahn, Y.-J. Kim, H. R. Choi, and S. Baik, "Highly conductive, printable and stretchable composite films of carbon nanotubes and silver," *Nature nanotechnology*, vol. 5, no. 12, pp. 853–857, 2010.

[79] T. Sekitani, Y. Noguchi, K. Hata, T. Fukushima, T. Aida, and T. Someya, "A rubberlike stretchable active matrix using elastic conductors," *Science*, vol. 321, no. 5895, pp. 1468–1472, 2008.

[80] J. Y. Oh, D. Lee, and S. H. Hong, "Ice-templated bimodal-porous silver nanowire/pdms nanocomposites for stretchable conductor," *ACS applied materials & interfaces*, vol. 10, no. 25, pp. 21 666–21 671, 2018.

[81] J. Liu, Q. Guo, S. Mao, Z. Chen, X. Zhang, Y. Yang, and X. Zhang, "Templated synthesis of a 1d ag nanohybrid in the solid state and its organized network for strain-sensing applications," *Journal of Materials Chemistry C*, vol. 6, no. 40, pp. 10 730–10 738, 2018.

[82] Y. Hu, T. Zhao, P. Zhu, Y. Zhu, X. Shuai, X. Liang, R. Sun, D. D. Lu, and C.-P. Wong, "Low cost and highly conductive elastic composites for flexible and printable electronics," *Journal of Materials Chemistry C*, vol. 4, no. 24, pp. 5839–5848, 2016.

[83] Y. Hu, T. Zhao, P. Zhu, Y. Zhang, X. Liang, R. Sun, and C.-P. Wong, "A low-cost, printable, and stretchable strain sensor based on highly conductive elastic composites with tunable sensitivity for human motion monitoring," *Nano Research*, vol. 11, no. 4, pp. 1938–1955, 2018.

[84] M. Tavakoli, M. H. Malakooti, H. Paisana, Y. Ohm, D. Green Marques, P. Alhais Lopes, A. P. Piedade, A. T. de Almeida, and C. Majidi, "Egain-assisted room-temperature sintering of silver nanoparticles for stretchable, inkjet-printed, thin-film electronics," *Advanced Materials*, vol. 30, no. 29, p. 1801852, 2018.

[85] J. J. Valeton, K. Hermans, C. W. Bastiaansen, D. J. Broer, J. Perelaer, U. S. Schubert, G. P. Crawford, and P. J. Smith, "Room temperature preparation of conductive silver features using spin-coating and inkjet printing," *Journal of Materials Chemistry*, vol. 20, no. 3, pp. 543–546, 2010.

[86] M. Grouchko, A. Kamyshny, C. F. Mihailescu, D. F. Anghel, and S. Magdassi, "Conductive inks with a "built-in" mechanism that enables sintering at room temperature," *ACS nano*, vol. 5, no. 4, pp. 3354–3359, 2011.

[87] P. A. Lopes, D. F. Fernandes, A. F. Silva, D. G. Marques, A. T. de Almeida, C. Majidi, and M. Tavakoli, "Bi-phasic ag–in–ga-embedded elastomer inks for digitally printed, ultra-stretchable, multi-layer electronics," *ACS Applied Materials & Interfaces*, vol. 13, no. 12, pp. 14 552–14 561, 2021.

[88] C. M. Hassan and N. A. Peppas, "Structure and morphology of freeze/thawed pva hydrogels," *Macromolecules*, vol. 33, no. 7, pp. 2472–2479, 2000.

[89] C. Pan, Y. Ohm, J. Wang, M. J. Ford, K. Kumar, S. Kumar, and C. Majidi, "Silver-coated poly (dimethylsiloxane) beads for soft, stretchable, and thermally stable conductive elastomer composites," *ACS applied materials & interfaces*, vol. 11, no. 45, pp. 42 561–42 570, 2019.

[90] A. Campbell and W. Reynolds, "The system silver–indium–gallium," *Canadian Journal of Chemistry*, vol. 40, no. 1, pp. 37–45, 1962.

[91] A. Hirsch, H. O. Michaud, A. P. Gerratt, S. De Mulatier, and S. P. Lacour, "Intrinsically stretchable biphasic (solid–liquid) thin metal films," *Advanced Materials*, vol. 28, no. 22, pp. 4507–4512, 2016.

[92] K. B. Ozutemiz, J. Wissman, O. B. Ozdoganlar, and C. Majidi, "Egain–metal interfacing for liquid metal circuitry and microelectronics integration," *Advanced Materials Interfaces*, vol. 5, no. 10, p. 1701596, 2018.

[93] J. W. Boley, E. L. White, and R. K. Kramer, "Mechanically sintered gallium–indium nanoparticles," *Advanced Materials*, vol. 27, no. 14, pp. 2355–2360, 2015.

[94] Y. Su, J. Zhao, W. Zhan, H. Yuan, L. Wu, G. Sui, and H. Zhang, "A multifunctional hydrogel fabricated via ultra-fast polymerization by graphene oxide-adsorbed liquid metal nanodroplets," *Chemical Engineering Journal*, vol. 435, p. 135018, 2022.

[95] J. Wen, Y. Tian, Z. Mei, W. Wu, and Y. Tian, "Synthesis of polypyrrole nanoparticles and their applications in electrically conductive adhesives for improving conductivity," *RSC advances*, vol. 7, no. 84, pp. 53 219–53 225, 2017.

[96] Y. Ohm, C. Pan, M. J. Ford, X. Huang, J. Liao, and C. Majidi, "An electrically conductive silver–polyacrylamide–alginate hydrogel composite for soft electronics," *Nature Electronics*, vol. 4, no. 3, pp. 185–192, 2021.

[97] R. K. Kramer, C. Majidi, and R. J. Wood, "Masked deposition of gallium-indium alloys for liquid-embedded elastomer conductors," *Advanced functional materials*, vol. 23, no. 42, pp. 5292–5296, 2013.

[98] A. Hajalilou, A. F. Silva, P. A. Lopes, E. Parvini, C. Majidi, and M. Tavakoli, "Biphasic liquid metal composites for sinter-free printed stretchable electronics," *Advanced Materials Interfaces*, p. 2101913, 2022.

[99] R. Tutika, S. H. Zhou, R. E. Napolitano, and M. D. Bartlett, "Mechanical and functional tradeoffs in multiphase liquid metal, solid particle soft composites," *Advanced Functional Materials*, vol. 28, no. 45, p. 1804336, 2018.

[100] Y. Zhao, P. Khandagale, and C. Majidi, "Modeling electromechanical coupling of liquid metal embedded elastomers while accounting stochasticity in 3d percolation," *Extreme Mechanics Letters*, vol. 48, p. 101443, 2021.

[101] B. Ying and X. Liu, "Skin-like hydrogel devices for wearable sensing, soft robotics and beyond," *Iscience*, vol. 24, no. 11, p. 103174, 2021.

[102] M. J. Ford, D. K. Patel, C. Pan, S. Bergbreiter, and C. Majidi, "Controlled assembly of liquid metal inclusions as a general approach for multifunctional composites," *Advanced Materials*, vol. 32, no. 46, p. 2002929, 2020.

[103] D. L. Taylor and M. in het Panhuis, "Self-healing hydrogels," *Advanced Materials*, vol. 28, no. 41, pp. 9060–9093, 2016.

[104] N. Zolfaghari, P. Khandagale, M. J. Ford, K. Dayal, and C. Majidi, "Network topologies dictate electromechanical coupling in liquid metal–elastomer composites," *Soft Matter*, vol. 16, no. 38, pp. 8818–8825, 2020.

[105] L. Vovchenko and V. Vovchenko, "Simulation of percolation threshold in composites filled with conducting particles of various morphologies," *Materialwissenschaft und Werkstofftechnik*, vol. 42, no. 1, pp. 70–74, 2011.

[106] S. Lin, H. Yuk, T. Zhang, G. A. Parada, H. Koo, C. Yu, and X. Zhao, "Stretchable hydrogel electronics and devices," *Advanced Materials*, vol. 28, no. 22, pp. 4497–4505, 2016.

[107] G. Schiavone, F. Fallegger, X. Kang, B. Barra, N. Vachicouras, E. Roussinova, I. Furfaro, S. Jiguet, I. Seáñez, S. Borgognon *et al.*, "Soft, implantable bioelectronic interfaces for translational research," *Advanced Materials*, vol. 32, no. 17, p. 1906512, 2020.

[108] L. Dejace, N. Laubeuf, I. Furfaro, and S. P. Lacour, "Gallium-based thin films for wearable human motion sensors," *Advanced Intelligent Systems*, vol. 1, no. 5, p. 1900079, 2019.

[109] T. Qiu, S. Palagi, J. Sachs, and P. Fischer, "Soft miniaturized linear actuators wirelessly powered by rotating permanent magnets," in *2018 IEEE International Conference on Robotics and Automation (ICRA)*.   IEEE, 2018, pp. 3595–3600.

[110] W. Zhang, P. Feng, J. Chen, Z. Sun, and B. Zhao, "Electrically conductive hydrogels for flexible energy storage systems," *Progress in Polymer Science*, vol. 88, pp. 220–240, 2019.

[111] Y. Shi and G. Yu, "Designing hierarchically nanostructured conductive polymer gels for electrochemical energy storage and conversion," *Chemistry of Materials*, vol. 28, no. 8, pp. 2466–2477, 2016.

[112] J. Kim, G. A. Salvatore, H. Araki, A. M. Chiarelli, Z. Xie, A. Banks, X. Sheng, Y. Liu, J. W. Lee, K.-I. Jang *et al.*, "Battery-free, stretchable optoelectronic systems for wireless optical characterization of the skin," *Science advances*, vol. 2, no. 8, p. e1600418, 2016.

[113] W. Lee, D. Kim, J. Rivnay, N. Matsuhisa, T. Lonjaret, T. Yokota, H. Yawo, M. Sekino, G. G. Malliaras, and T. Someya, "Integration of organic electrochemical and field-effect transistors for ultraflexible, high temporal resolution electrophysiology arrays," *Advanced Materials*, vol. 28, no. 44, pp. 9722–9728, 2016.

[114] Y. Lin, O. Gordon, M. R. Khan, N. Vasquez, J. Genzer, and M. D. Dickey, "Vacuum filling of complex microchannels with liquid metal," *Lab on a Chip*, vol. 17, no. 18, pp. 3043–3050, 2017.

[115] A. Koh, D. Kang, Y. Xue, S. Lee, R. M. Pielak, J. Kim, T. Hwang, S. Min, A. Banks, P. Bastien *et al.*, "A soft, wearable microfluidic device for the capture, storage, and colorimetric sensing of sweat," *Science translational medicine*, vol. 8, no. 366, pp. 366ra165–366ra165, 2016.

[116] K. Comley and N. A. Fleck, "A micromechanical model for the young's modulus of adipose tissue," *International Journal of Solids and Structures*, vol. 47, no. 21, pp. 2982–2990, 2010.

[117] D.-H. Kim, J. Viventi, J. J. Amsden, J. Xiao, L. Vigeland, Y.-S. Kim, J. A. Blanco, B. Panilaitis, E. S. Frechette, D. Contreras *et al.*, "Dissolvable films of silk fibroin for ultrathin conformal bio-integrated electronics," *Nature materials*, vol. 9, no. 6, pp. 511–517, 2010.

[118] I. R. Minev, P. Musienko, A. Hirsch, Q. Barraud, N. Wenger, E. M. Moraud, J. Gandar, M. Capogrosso, T. Milekovic, L. Asboth *et al.*, "Electronic dura mater for long-term multimodal neural interfaces," *Science*, vol. 347, no. 6218, pp. 159–163, 2015.

[119] L. Xu, S. R. Gutbrod, A. P. Bonifas, Y. Su, M. S. Sulkin, N. Lu, H.-J. Chung, K.-I. Jang, Z. Liu, M. Ying *et al.*, "3d multifunctional integumentary membranes for spatiotemporal cardiac measurements and stimulation across the entire epicardium," *Nature communications*, vol. 5, no. 1, pp. 1–10, 2014.

[120] P. A. Lopes, D. Vaz Gomes, D. Green Marques, P. Faia, J. Góis, T. F. Patrício, J. Coelho, A. Serra, A. T. de Almeida, C. Majidi *et al.*, "Soft bioelectronic stickers: Selection and evaluation of skin-interfacing electrodes," *Advanced healthcare materials*, vol. 8, no. 15, p. 1900234, 2019.

[121] H. Yuk, S. Lin, C. Ma, M. Takaffoli, N. X. Fang, and X. Zhao, "Hydraulic hydrogel actuators and robots optically and sonically camouflaged in water," *Nature communications*, vol. 8, no. 1, pp. 1–12, 2017.

[122] C. Yang and Z. Suo, "Hydrogel ionotronics," *Nature Reviews Materials*, vol. 3, no. 6, pp. 125–142, 2018.

[123] H.-R. Lee, C.-C. Kim, and J.-Y. Sun, "Stretchable ionics–a promising candidate for upcoming wearable devices," *Advanced Materials*, vol. 30, no. 42, p. 1704403, 2018.

[124] J. Rivnay, H. Wang, L. Fenno, K. Deisseroth, and G. G. Malliaras, "Next-generation probes, particles, and proteins for neural interfacing," *Science Advances*, vol. 3, no. 6, p. e1601649, 2017.

[125] J.-Y. Sun, X. Zhao, W. R. Illeperuma, O. Chaudhuri, K. H. Oh, D. J. Mooney, J. J. Vlassak, and Z. Suo, "Highly stretchable and tough hydrogels," *Nature*, vol. 489, no. 7414, pp. 133–136, 2012.

[126] C. H. Yang, M. X. Wang, H. Haider, J. H. Yang, J.-Y. Sun, Y. M. Chen, J. Zhou, and Z. Suo, "Strengthening alginate/polyacrylamide hydrogels using various multivalent cations," *ACS applied materials & interfaces*, vol. 5, no. 21, pp. 10 418–10 422, 2013.

[127] S. Mondal, S. Das, and A. K. Nandi, "A review on recent advances in polymer and peptide hydrogels," *Soft Matter*, vol. 16, no. 6, pp. 1404–1454, 2020.

[128] R. W. Ogden, "Large deformation isotropic elasticity–on the correlation of theory and experiment for incompressible rubberlike solids," *Proceedings of the Royal Society of London. A. Mathematical and Physical Sciences*, vol. 326, no. 1567, pp. 565–584, 1972.

[129] H.-J. Kim, C. Son, and B. Ziaie, "A multiaxial stretchable interconnect using liquid-alloy-filled elastomeric microchannels," *Applied Physics Letters*, vol. 92, no. 1, p. 011904, 2008.

[130] X. Huang, K. Kumar, M. K. Jawed, Z. Ye, and C. Majidi, "Soft electrically actuated quadruped (seaq)—integrating a flex circuit board and elastomeric limbs for versatile mobility," *IEEE Robotics and Automation Letters*, vol. 4, no. 3, pp. 2415–2422, 2019.

[131] H. Li, A. Erbaş, J. Zwanikken, and M. Olvera de la Cruz, "Ionic conductivity in polyelectrolyte hydrogels," *Macromolecules*, vol. 49, no. 23, pp. 9239–9246, 2016.

[132] D. A. Lake, "Neuromuscular electrical stimulation," *Sports medicine*, vol. 13, no. 5, pp. 320–336, 1992.

[133] M. Weigel, T. Lu, G. Bailly, A. Oulasvirta, C. Majidi, and J. Steimle, "Iskin: flexible, stretchable and visually customizable on-body touch sensors for mobile computing," in *Proceedings of the 33rd Annual ACM Conference on Human Factors in Computing Systems*, 2015, pp. 2991–3000.

[134] M. D. Bartlett, E. J. Markvicka, and C. Majidi, "Rapid fabrication of soft, multilayered electronics for wearable biomonitoring," *Advanced Functional Materials*, vol. 26, no. 46, pp. 8496–8504, 2016.

[135] X. Zhao, Y. Zhou, J. Xu, G. Chen, Y. Fang, T. Tat, X. Xiao, Y. Song, S. Li, and J. Chen, "Soft fibers with magnetoelasticity for wearable electronics," *Nature communications*, vol. 12, no. 1, pp. 1–11, 2021.

[136] F. Ershad, A. Thukral, J. Yue, P. Comeaux, Y. Lu, H. Shim, K. Sim, N.-I. Kim, Z. Rao, R. Guevara *et al.*, "Ultra-conformal drawn-on-skin electronics for multifunctional motion artifact-free sensing and point-of-care treatment," *Nature communications*, vol. 11, no. 1, pp. 1–13, 2020.

[137] H. Kim, E. Kim, C. Choi, and W.-H. Yeo, "Advances in soft and dry electrodes for wearable health monitoring devices," *Micromachines*, vol. 13, no. 4, p. 629, 2022.

[138] Z. Chen, J. Xi, W. Huang, and M. M. Yuen, "Stretchable conductive elastomer for wireless wearable communication applications," *Scientific reports*, vol. 7, no. 1, pp. 1–8, 2017.

[139] X. Liang, H. Li, J. Dou, Q. Wang, W. He, C. Wang, D. Li, J.-M. Lin, and Y. Zhang, "Stable and biocompatible carbon nanotube ink mediated by silk protein for printed electronics," *Advanced Materials*, vol. 32, no. 31, p. 2000165, 2020.

[140] M. Ku, J. Kim, J.-E. Won, W. Kang, Y.-G. Park, J. Park, J.-H. Lee, J. Cheon, H. H. Lee, and J.-U. Park, "Smart, soft contact lens for wireless immunosensing of cortisol," *Science advances*, vol. 6, no. 28, p. eabb2891, 2020.

[141] J. Park, J. Kim, S.-Y. Kim, W. H. Cheong, J. Jang, Y.-G. Park, K. Na, Y.-T. Kim, J. H. Heo, C. Y. Lee *et al.*, "Soft, smart contact lenses with integrations of wireless circuits, glucose sensors, and displays," *Science advances*, vol. 4, no. 1, p. eaap9841, 2018.

[142] Y. Song, J. Min, Y. Yu, H. Wang, Y. Yang, H. Zhang, and W. Gao, "Wireless battery-free wearable sweat sensor powered by human motion," *Science advances*, vol. 6, no. 40, p. eaay9842, 2020.

[143] M. Parrilla, T. Guinovart, J. Ferré, P. Blondeau, and F. J. Andrade, "A wearable paper-based sweat sensor for human perspiration monitoring," *Advanced Healthcare Materials*, vol. 8, no. 16, p. 1900342, 2019.

[144] J. Finnegan, B. Peterkin, H.-C. Han, J. M. Yentes, S. I. Rennard, and E. J. Markvicka, "Wireless, battery free wearable electronic nose," in *Frontiers in Biomedical Devices*, vol. 84815.   American Society of Mechanical Engineers, 2022, p. V001T04A005.

[145] R. Chen, X. Xu, D. Yu, C. Xiao, M. Liu, J. Huang, T. Mao, C. Zheng, Z. Wang, and X. Wu, "Highly stretchable and fatigue resistant hydrogels with low young's modulus as transparent and flexible strain sensors," *Journal of Materials Chemistry C*, vol. 6, no. 41, pp. 11 193–11 201, 2018.

[146] X. Ming, L. Shi, H. Zhu, and Q. Zhang, "Stretchable, phase-transformable ionogels with reversible ionic conductor–insulator transition," *Advanced Functional Materials*, vol. 30, no. 49, p. 2005079, 2020.

[147] J.-C. Bénet, S. Ouoba, F. Ouedraogo, and F. Cherblanc, "Experimental study of water evaporation rate, at the surface of aqueous solution, under the effect of a discontinuity of chemical potential–effect of water activity and air pressure," *Experimental Thermal and Fluid Science*, vol. 121, p. 110233, 2021.

[148] J. Li and J.-K. Kim, "Percolation threshold of conducting polymer composites containing 3d randomly distributed graphite nanoplatelets," *Composites science and technology*, vol. 67, no. 10, pp. 2114–2120, 2007.

[149] O. İsmail and Ö. Gökçe Kocabay, "Absorption and adsorption studies of polyacrylamide/sodium alginate hydrogels," *Colloid and Polymer Science*, vol. 299, no. 5, pp. 783–796, 2021.

[150] S. Joo and D. F. Baldwin, "Adhesion mechanisms of nanoparticle silver to substrate materials: identification," *Nanotechnology*, vol. 21, no. 5, p. 055204, 2009.

[151] F. London, "The general theory of molecular forces," *Transactions of the Faraday Society*, vol. 33, pp. 8b–26, 1937.

[152] S. Safran, *Statistical thermodynamics of surfaces, interfaces, and membranes*. CRC Press, 2018.

[153] S. Nansai, N. Rojas, M. R. Elara, R. Sosa, and M. Iwase, "On a jansen leg with multiple gait patterns for reconfigurable walking platforms," *Advances in Mechanical Engineering*, vol. 7, no. 3, p. 1687814015573824, 2015.

[154] L. Patnaik and L. Umanand, "Kinematics and dynamics of jansen leg mechanism: A bond graph approach," *Simulation Modelling Practice and Theory*, vol. 60, pp. 160–169, 2016.

[155] M. C. Darnell, J.-Y. Sun, M. Mehta, C. Johnson, P. R. Arany, Z. Suo, and D. J. Mooney, "Performance and biocompatibility of extremely tough alginate/polyacrylamide hydrogels," *Biomaterials*, vol. 34, no. 33, pp. 8042–8048, 2013.

[156] T. Zhang, L. Wang, Q. Chen, and C. Chen, "Cytotoxic potential of silver nanoparticles," *Yonsei medical journal*, vol. 55, no. 2, pp. 283–291, 2014.

[157] D. S. Ipe, P. Kumar, R. M. Love, and S. M. Hamlet, "Silver nanoparticles at biocompatible dosage synergistically increases bacterial susceptibility to antibiotics," *Frontiers in microbiology*, p. 1074, 2020.

[158] H. Yuk, T. Zhang, G. A. Parada, X. Liu, and X. Zhao, "Skin-inspired hydrogel–elastomer hybrids with robust interfaces and functional microstructures," *Nature communications*, vol. 7, no. 1, pp. 1–11, 2016.

[159] M. T. I. Mredha, H. H. Le, J. Cui, and I. Jeon, "Double-hydrophobic-coating through quenching for hydrogels with strong resistance to both drying and swelling," *Advanced Science*, vol. 7, no. 6, p. 1903145, 2020.

[160] H. Chen, X. Ren, and G. Gao, "Skin-inspired gels with toughness, antifreezing, conductivity, and remoldability," *ACS applied materials & interfaces*, vol. 11, no. 31, pp. 28 336–28 344, 2019.

[161] M. Rusdi, Y. Moroi, H. Nakahara, and O. Shibata, "Evaporation from water- ethylene glycol liquid mixture," *Langmuir*, vol. 21, no. 16, pp. 7308–7310, 2005.

[162] S. A. Shafiee, J. Aarons, and H. H. Hamzah, "Electroreduction of peroxodisulfate: A review of a complicated reaction," *Journal of The Electrochemical Society*, vol. 165, no. 13, p. H785, 2018.

[163] A. A. Pawar, G. Saada, I. Cooperstein, L. Larush, J. A. Jackman, S. R. Tabaei, N.-J. Cho, and S. Magdassi, "High-performance 3d printing of hydrogels by water-dispersible photoinitiator nanoparticles," *Science advances*, vol. 2, no. 4, p. e1501381, 2016.

[164] W. HuangáGoh, A. HoseináSakhaei *et al.*, "Highly stretchable hydrogels for uv curing based high-resolution multimaterial 3d printing," *Journal of Materials Chemistry B*, vol. 6, no. 20, pp. 3246–3253, 2018.

[165] D. S. McLachlan, M. Blaszkiewicz, and R. E. Newnham, "Electrical resistivity of composites," *Journal of the American Ceramic Society*, vol. 73, no. 8, pp. 2187–2203, 1990.

[166] Y. Lu, K. Sagara, Y. Matsuda, L. Hao, Y. R. Jin, and H. Yoshida, "Effect of cu powder addition on thermoelectric properties of cu/tio2- x composites," *Ceramics International*, vol. 39, no. 6, pp. 6689–6694, 2013.

[167] Z. Hashin and S. Shtrikman, "A variational approach to the theory of the effective magnetic permeability of multiphase materials," *Journal of applied Physics*, vol. 33, no. 10, pp. 3125–3131, 1962.

[168] T. Hellebrekers, K. B. Ozutemiz, J. Yin, and C. Majidi, "Liquid metal-microelectronics integration for a sensorized soft robot skin," in *2018 IEEE/RSJ International Conference on Intelligent Robots and Systems (IROS)*. IEEE, 2018, pp. 5924–5929.

[169] R. W. Ogden, *Non-linear elastic deformations*. Courier Corporation, 1997.

[170] A. Muhr, "Modeling the stress-strain behavior of rubber," *Rubber chemistry and technology*, vol. 78, no. 3, pp. 391–425, 2005.

[171] L. Treloar, "The elasticity of a network of long-chain molecules—ii," *Transactions of the Faraday Society*, vol. 39, pp. 241–246, 1943.

[172] M. Mooney, "A theory of large elastic deformation," *Journal of applied physics*, vol. 11, no. 9, pp. 582–592, 1940.

[173] R. S. Rivlin, "Large elastic deformations of isotropic materials iv. further developments of the general theory," *Philosophical transactions of the royal society of London. Series A, Mathematical and physical sciences*, vol. 241, no. 835, pp. 379–397, 1948.

[174] A. Gent, "Elastic instabilities in rubber," *International Journal of Non-Linear Mechanics*, vol. 40, no. 2-3, pp. 165–175, 2005.

[175] E. M. Arruda and M. C. Boyce, "A three-dimensional constitutive model for the large stretch behavior of rubber elastic materials," *Journal of the Mechanics and Physics of Solids*, vol. 41, no. 2, pp. 389–412, 1993.

[176] O. H. Yeoh, "Some forms of the strain energy function for rubber," *Rubber Chemistry and technology*, vol. 66, no. 5, pp. 754–771, 1993.

[177] H. C. Hamaker, "The london—van der waals attraction between spherical particles," *physica*, vol. 4, no. 10, pp. 1058–1072, 1937.

[178] N. R. Morrow, "Physics and thermodynamics of capillary action in porous media," *Industrial & Engineering Chemistry*, vol. 62, no. 6, pp. 32–56, 1970.

[179] P.-G. de Gennes, F. Brochard-Wyart, and D. Quéré, "Capillarity and gravity," in *Capillarity and wetting phenomena*. Springer, 2004, pp. 33–67.

[180] V. Arumugam, M. Naresh, and R. Sanjeevi, "Effect of strain rate on the fracture behaviour of skin," *Journal of Biosciences*, vol. 19, no. 3, pp. 307–313, 1994.

[181] N. Lu, C. Lu, S. Yang, and J. Rogers, "Highly sensitive skin-mountable strain gauges based entirely on elastomers," *Advanced Functional Materials*, vol. 22, no. 19, pp. 4044–4050, 2012.

[182] R. C. Webb, A. P. Bonifas, A. Behnaz, Y. Zhang, K. J. Yu, H. Cheng, M. Shi, Z. Bian, Z. Liu, Y.-S. Kim *et al.*, "Ultrathin conformal devices for precise and continuous thermal characterization of human skin," *Nature materials*, vol. 12, no. 10, pp. 938–944, 2013.

[183] W.-H. Yeo, Y.-S. Kim, J. Lee, A. Ameen, L. Shi, M. Li, S. Wang, R. Ma, S. H. Jin, Z. Kang *et al.*, "Multifunctional epidermal electronics printed directly onto the skin," *Advanced materials*, vol. 25, no. 20, pp. 2773–2778, 2013.

[184] M. Kaltenbrunner, T. Sekitani, J. Reeder, T. Yokota, K. Kuribara, T. Tokuhara, M. Drack, R. Schwödiauer, I. Graz, S. Bauer-Gogonea *et al.*, "An ultra-lightweight design for imperceptible plastic electronics," *Nature*, vol. 499, no. 7459, pp. 458–463, 2013.

[185] D. Wang, Y. Chang, Q. Lu, and Z. Yang, "Nano-organic silver composite conductive ink for flexible printed circuit," *Materials Technology*, vol. 30, no. 1, pp. 54–59, 2015.

[186] W. Dang, V. Vinciguerra, L. Lorenzelli, and R. Dahiya, "Printable stretchable interconnects," *Flexible and Printed Electronics*, vol. 2, no. 1, p. 013003, 2017.

[187] L. Bareket, L. Inzelberg, D. Rand, M. David-Pur, D. Rabinovich, B. Brandes, and Y. Hanein, "Temporary-tattoo for long-term high fidelity biopotential recordings," *Scientific reports*, vol. 6, no. 1, pp. 1–8, 2016.

[188] H.-H. Lee, K.-S. Chou, and K.-C. Huang, "Inkjet printing of nanosized silver colloids," *Nanotechnology*, vol. 16, no. 10, p. 2436, 2005.

[189] P. Smith, D.-Y. Shin, J. Stringer, B. Derby, and N. Reis, "Direct ink-jet printing and low temperature conversion of conductive silver patterns," *Journal of materials science*, vol. 41, no. 13, pp. 4153–4158, 2006.

[190] S.-P. Chen, Z.-K. Kao, J.-L. Lin, and Y.-C. Liao, "Silver conductive features on flexible substrates from a thermally accelerated chain reaction at low sintering temperatures," *ACS applied materials & interfaces*, vol. 4, no. 12, pp. 7064–7068, 2012.

[191] X. Nie, H. Wang, and J. Zou, "Inkjet printing of silver citrate conductive ink on pet substrate," *Applied surface science*, vol. 261, pp. 554–560, 2012.

[192] C.-L. Lee, K.-C. Chang, and C.-M. Syu, "Silver nanoplates as inkjet ink particles for metallization at a low baking temperature of 100 c," *Colloids and Surfaces A: Physicochemical and Engineering Aspects*, vol. 381, no. 1-3, pp. 85–91, 2011.

[193] J. Perelaer, C. E. Hendriks, A. W. de Laat, and U. S. Schubert, "One-step inkjet printing of conductive silver tracks on polymer substrates," *Nanotechnology*, vol. 20, no. 16, p. 165303, 2009.

[194] M. Okamoto, M. Kurotobi, S. Takeoka, J. Sugano, E. Iwase, H. Iwata, and T. Fujie, "Sandwich fixation of electronic elements using free-standing elastomeric nanosheets for low-temperature device processes," *Journal of Materials Chemistry C*, vol. 5, no. 6, pp. 1321–1327, 2017.

[195] K. Black, J. Singh, D. Mehta, S. Sung, C. J. Sutcliffe, and P. R. Chalker, "Silver ink formulations for sinter-free printing of conductive films," *Scientific reports*, vol. 6, no. 1, pp. 1–7, 2016.

[196] R. Guo, Y. Yu, Z. Xie, X. Liu, X. Zhou, Y. Gao, Z. Liu, F. Zhou, Y. Yang, and Z. Zheng, "Matrix-assisted catalytic printing for the fabrication of multiscale, flexible, foldable, and stretchable metal conductors," *Advanced Materials*, vol. 25, no. 24, pp. 3343–3350, 2013.

[197] Y. Yu, C. Yan, and Z. Zheng, "Polymer-assisted metal deposition (pamd): A full-solution strategy for flexible, stretchable, compressible, and wearable metal conductors," *Advanced Materials*, vol. 26, no. 31, pp. 5508–5516, 2014.

[198] Y. Yu, X. Xiao, Y. Zhang, K. Li, C. Yan, X. Wei, L. Chen, H. Zhen, H. Zhou, S. Zhang *et al.*, "Photoreactive and metal-platable copolymer inks for high-throughput, room-temperature printing of flexible metal electrodes for thin-film electronics," *Advanced Materials*, vol. 28, no. 24, pp. 4926–4934, 2016.

[199] N. Kazem, T. Hellebrekers, and C. Majidi, "Soft multifunctional composites and emulsions with liquid metals," *Advanced Materials*, vol. 29, no. 27, p. 1605985, 2017.

[200] C. B. Eaker and M. D. Dickey, "Liquid metal actuation by electrical control of interfacial tension," *Applied Physics Reviews*, vol. 3, no. 3, p. 031103, 2016.

[201] J. Wissman, M. D. Dickey, and C. Majidi, "Field-controlled electrical switch with liquid metal," *Advanced Science*, vol. 4, no. 12, p. 1700169, 2017.

[202] G. Li, X. Wu, and D.-W. Lee, "Selectively plated stretchable liquid metal wires for transparent electronics," *Sensors and Actuators B: Chemical*, vol. 221, pp. 1114–1119, 2015.

[203] X. Niu, S. Peng, L. Liu, W. Wen, and P. Sheng, "Characterizing and patterning of pdms-based conducting composites," *Advanced Materials*, vol. 19, no. 18, pp. 2682–2686, 2007.

[204] K. Chu, S.-C. Lee, S. Lee, D. Kim, C. Moon, and S.-H. Park, "Smart conducting polymer composites having zero temperature coefficient of resistance," *Nanoscale*, vol. 7, no. 2, pp. 471–478, 2015.

[205] S. Gong, D. Wu, Y. Li, M. Jin, T. Xiao, Y. Wang, Z. Xiao, Z. Zhu, and Z. Li, "Temperature-independent piezoresistive sensors based on carbon nanotube/polymer nanocomposite," *Carbon*, vol. 137, pp. 188–195, 2018.

[206] K. Chu and S.-H. Park, "Fabrication of a hybrid carbon-based composite for flexible heating element with a zero temperature coefficient of resistance," *IEEE Electron Device Letters*, vol. 36, no. 1, pp. 50–52, 2014.

[207] Y. Cao, T. G. Morrissey, E. Acome, S. I. Allec, B. M. Wong, C. Keplinger, and C. Wang, "A transparent, self-healing, highly stretchable ionic conductor," *Advanced Materials*, vol. 29, no. 10, p. 1605099, 2017.

[208] M. Foster, *A Text Book of Physiology*, ser. A Text Book of Physiology. Macmillan and Company, 1896, no. v. 4. [Online]. Available: https://books.google.com/books?id=5S44AQAAMAAJ

[209] A. E. Pereda, "Electrical synapses and their functional interactions with chemical synapses," *Nature Reviews Neuroscience*, vol. 15, no. 4, pp. 250–263, 2014.

[210] R. S. Zucker and W. G. Regehr, "Short-term synaptic plasticity," *Annual review of physiology*, vol. 64, no. 1, pp. 355–405, 2002.

[211] S. Herculano-Houzel, "The remarkable, yet not extraordinary, human brain as a scaled-up primate brain and its associated cost," *Proceedings of the National Academy of Sciences*, vol. 109, no. Supplement 1, pp. 10 661–10 668, 2012.

[212] K. D. Micheva, B. Busse, N. C. Weiler, N. O'Rourke, and S. J. Smith, "Single-synapse analysis of a diverse synapse population: proteomic imaging methods and markers," *Neuron*, vol. 68, no. 4, pp. 639–653, 2010.

[213] M. P. Wolf, G. B. Salieb-Beugelaar, and P. Hunziker, "Pdms with designer functionalities—properties, modifications strategies, and applications," *Progress in Polymer Science*, vol. 83, pp. 97–134, 2018.

[214] Z. Wang, A. A. Volinsky, and N. D. Gallant, "Crosslinking effect on polydimethylsiloxane elastic modulus measured by custom-built compression instrument," *Journal of Applied Polymer Science*, vol. 131, no. 22, 2014.

[215] J. C. Wingfield, J. P. Kelley, F. Angelier, O. Chastel, F. Lei, S. E. Lynn, B. Miner, J. E. Davis, D. Li, and G. Wang, "Organism–environment interactions in a changing world: a mechanistic approach," *Journal of Ornithology*, vol. 152, no. 1, pp. 279–288, 2011.

[216] B. D. Rabideau and A. E. Ismail, "Mechanisms of hydrogen bond formation between ionic liquids and cellulose and the influence of water content," *Physical Chemistry Chemical Physics*, vol. 17, no. 8, pp. 5767–5775, 2015.

[217] W.-L. Hung, D.-M. Wang, J.-Y. Lai, and S.-C. Chou, "On the initiation of macrovoids in polymeric membranes–effect of polymer chain entanglement," *Journal of Membrane Science*, vol. 505, pp. 70–81, 2016.

[218] M. Bercea, S. Morariu, and D. Rusu, "In situ gelation of aqueous solutions of entangled poly (vinyl alcohol)," *Soft Matter*, vol. 9, no. 4, pp. 1244–1253, 2013.

[219] R. B.-K. Wakshlak, R. Pedahzur, and D. Avnir, "Antibacterial activity of silver-killed bacteria: the" zombies" effect," *Scientific reports*, vol. 5, no. 1, pp. 1–5, 2015.